

**FUNCTIONALIZED POLYMERIC MATERIALS SUPPORTED
NOBLE METAL NANOPARTICLES FOR CATALYZING
INORGANIC AND ORGANIC REDOX REACTIONS**

By

SANKARARAO CHAPPA

CHEM01201304032

Bhabha Atomic Research Centre, Mumbai

A thesis submitted to the

Board of Studies in Chemical Sciences

In partial fulfillment of requirements

for the Degree of

DOCTOR OF PHILOSOPHY

of





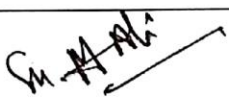

HOMI BHABHA NATIONAL INSTITUTE



August, 2018

Homi Bhabha National Institute
Recommendations of the Viva Voce Committee

As members of the Viva Voce Committee, we certify that we have read the dissertation prepared by Shri Sankararao Chappa entitled "Functionalized Polymeric Materials Supported Noble Metal Nanoparticles for Catalyzing Inorganic and Organic Redox Reactions" and recommend that it may be accepted as fulfilling the thesis requirement for the award of Degree of Doctor of Philosophy.

Chairman – Prof. R. C. Bindal.		Date: 31.08.18
Guide / Convener - Dr. Ashok K. Pandey		Date: 31.8.2018
Examiner – Dr. Vinod Kumar Shahi		Date: 31/08/18
Member 1- Dr. Manmohan Kumar		Date: 31/8/18
Member 2- Dr. Sk. Musharaf Ali		Date: 31/8/2018
Member 3- Dr. Virendra Kumar		Date: 31/08/18

Final approval and acceptance of this thesis is contingent upon the candidate's submission of the final copies of the thesis to HBNI.

I hereby certify that I have read this thesis prepared under my direction and recommend that it may be accepted as fulfilling the thesis requirement.

Date: 31.8.2018

Place: HBNI, Mumbai



Signature
Guide

STATEMENT BY AUTHOR

This dissertation has been submitted in partial fulfillment of requirements for an advanced degree at Homi Bhabha National Institute (HBNI) and is deposited in the Library to be made available to borrowers under rules of the HBNI.

Brief quotations from this dissertation are allowable without special permission, provided that accurate acknowledgement of source is made. Requests for permission for extended quotation from or reproduction of this manuscript in whole or in part may be granted by the Competent Authority of HBNI when in his or her judgment the proposed use of the material is in the interests of scholarship. In all other instances, however, permission must be obtained from the author.

Sankararao Chappa

DECLARATION

I, hereby declare that the investigation presented in the thesis has been carried out by me. The work is original and has not been submitted earlier as a whole or in part for a degree / diploma at this or any other Institution / University.

Sankararao Chappa

LIST OF PUBLICATIONS ARISING FROM THE THESIS

Journal

1. Self-reducing asymmetric polymer membrane for in situ formation and containment of noble metal nanocatalysts. **S. Chappa**, R.N. Shinde, A.K. Pandey, *Green Chem.* **2015**, 17 (8), 4157–4161.
2. Egg-shell membrane mimicking synthetic polymer membrane supported palladium nanoparticles for catalyzing reduction of uranyl (VI) ions. **S. Chappa**, A.M. Mhatre, V.C. Adya, A.K. Pandey, *Appl. Catal. B Environ.* **2017**, 203, 53-64.
3. Dual-function grafted electrospun polymer nanofibers scaffold hosted palladium nanoparticles for catalyzing the organic and inorganic redox reactions. **S. Chappa**, Bharath R. Sundar Ram, Charlie Oommen and A.K. Pandey, *Macromol. Chem. Phys.* **2017**, 218, 1600555.
4. Poly(ethylenimine) and poly(ethylene glycol methacrylate phosphate) anchored membranes hosted palladium nanoparticles for catalyzing U(VI) ions reduction and Mizoroki-Heck coupling reaction, **S. Chappa**, P.B. Rathod, A.K. Debnath, Debasis Sen and A.K. Pandey, *ACS Appl. Nano Mater.* **2018**, 1, 3259–3268.

Conferences

1. Nanocatalyst in synthetic polymer membranes for redox applications. **S. Chappa** and A.K. Pandey, "Proceedings of International conference on Recent Advances in Analytical Science" by Department of Chemistry, Indian Institute of Technology (IIT, BHU), April 7-9, 2016. (Best Paper award)
2. Poly (ethylene glycol methacrylate phosphate) anchored Fe₃O₄/membrane nanoparticles as a multipurpose material. **S. Chappa**, P.B Rathod and A.K Pandey "Proceedings of International Conference on Nanotechnology: Ideas, Innovations and Initiatives (ICN: 3I-2017)" by IIT Roorkee during 06-08, December 2017, 72. (Best paper award)
3. Presented "Functionalized polymeric materials supported noble metal nanoparticles for catalyzing inorganic and organic redox reactions." **S. Chappa** and A.K. Pandey, At 30th research scholars meet, by Indian chemical society (Mumbai branch) in association with Department of chemistry, Jai Hid college, Mumbai during 9-10, February 2018, 39.

Sankararao Chappa

Dedicated To.....

..... My Parents

ACKNOWLEDGEMENTS

I humbly grab this opportunity to express my profound gratitude to my supervisor, **Prof. Ashok Kumar Pandey** for his constant encouragement from finding a challenging research problem, how to approach a research problem, the need to be persistent to accomplish it, and to the process of writing thesis. His logical way of thinking, explaining things and his wide knowledge on the subject have created a lot of impact on me to learn things. He inspired me to become an independent researcher with his exceptional scientific knowledge, skills, and values.

I am thankful to **Dr. B S. Tomar** and **Prof. A K. Tyagi** former and present Deans, chemical sciences, HBNI for permitting me to register for my Ph.D. I would like to thank **Dr. P K. Pujari**, Associate director and Head, Radiochemistry division, BARC for his constant support and encouragement. My sincere thanks must go to members of my doctoral committee: **Prof. R C. Bindal** (chairman), **Prof. Manmohan Kumar**, **Dr. Sk. Musharaf Ali**, and **Dr. Virendra Kumar** for their valuable suggestions and comments.

I am grateful to all the teachers in my life who had taught me and encouraged me to achieve my goals. I am very much thankful to **Mr. K. Trinath**, **Mr. Chinni babu**, **Mr. Srinivas**, **Mr. Chakradhar**, **Mr. CH. Sivunnaidu**, **Mr. B. Venkataramana**, **Dr. N. Sivaraman** for their inspiration.

I express my sincere thanks to my fellow labmates: **Mr. Amol Mhatre**, **Mr. Prakash Rathod**, **Dr. Seraj Ansari**, **Dr. Rajesh gujar**, **Mr. D.R. Prabhu**, **Dr. Dhaval raut**, **Mr. Avinash Kanekar**, **Mr. Parveen Kumar Verma**, **Dr. B.N. Mohanty**, **Dr. C. Agarwal**, **Dr. Sanhita Chaudhury**, **Dr. Rakesh Shinde**, **Dr. V.R. Chavan**, **Ms. Apurna Naik**, **Dr. A. Bhattacharya**, **Dr. D. Dutta**, **Dr. K. Sudarsan**, **Dr. S. Sodaye**, **Dr. R. Tripathi**, **Dr. Priya Maheswari**, **Dr. S.**

Mukharjee, Dr. A. Sengupta, Dr. S.K. Gupta, Mr. N. Pathak, Mr. V. Telmore for their constant support and encouragement during the course of the present work.

I express my sincere thanks to my collaborators, who have contributed significantly to make my work complete in all aspects. I am very much grateful to **Dr. Charlie Oommen, Dr. Chandru, Mr. Bharath, Mrs. Rekha, Sri. Shashikumar** of Aerospace engineering, IISc, Bangalore. **Dr. R Gupta** and **Dr. V.C. Adya**, BARC for their help. I am also thankful to the operating personnel of sophisticated Analytical Instrumentation Facility (SAIF), IIT Bombay, Mumbai for providing FE-SEM facility on chargeable basis.

I am also thankful to my friends: **Mr. Satyanarayana, Mr. Praveen Kumar, Mr. Srinivasarao, Mr. Mohan, Mr. Parasuramu, Ms. Prasanna, Ms. Bharathi, Mr. Sudheer, Dr. Krishna, Mr. YA Naidu, Dr. Omkar, Mr. Raveendra Kumar, Dr. K. D Prasad, Dr. Guravaih, Dr. Parthiban, Dr. Raja. Mr. Murali, Dr. M. Naik, Dr. Chhillar, Mr. R. Mehta, Mr. GK. Mourya, Mr. SA. Khan, Dr. P. Maity, Mr. A. Sharma, Mr. A. Kaushik, Mr. T. Roy, Mr. Rahul, Mr. V. Belwanshi, Mr. R. Dhawan, Dr. V. Rastogi, Dr. N. Singh, Dr. S. Kumar** for their love and support.

It is very difficult to find the right words to express my gratitude to my parents for their love, care and support. I express my sincere gratitude to my brothers **Raju** and **Ramesh**, my sister in-laws **Radha** and **Lakshmi**, my niece **Gayatri, Harika**, and **Geeta**, my nephew **Ganesh** for their endless love and support. My sincere thanks to my family friends **Kiran, Mrs. Gowri, Satyam, Mrs. Simhachalam, Ms. Havanthi, Mrs. Lavanya, Mrs. Tulasi** for their endless love and support. And last, but certainly not least, my sincere thanks to all people who have helped directly or indirectly towards the completion of this thesis.

Sankararao Chappa

CONTENTS

SYNOPSIS	i
LIST OF FIGURES	xiii
LIST OF TABLES	xxii
LIST OF SCHEMES	xxiv
ABBREVIATIONS	xxv
CHAPTER1. INTRODUCTION	1
1.1 Introduction to nanoscience	2
1.1.1 Nanomaterials	3
1.1.2 Why nanomaterials are different.....	4
1.1.3 Properties of nanomaterials.....	7
1.2 Syntheses of nanomaterials	9
1.2.1 Bottom up approach: Mechanism of growth/formation of nanoparticles	9
1.2.2 Top down approach.....	18
1.3 Metal nanoparticles as catalyst	18
1.4 Immobilization of nanocatalyst on solid supports	25
1.4.1 Synthetic polymer membranes as host matrix	25
1.4.2 Bio-polymers as host matrix	27
1.4.3 Electrospun fibres mat	28
1.5 Scope of the thesis.....	30
CHAPTER2. EXPERIMENTAL	31
2.1 Nanoparticles synthesis.....	32
2.1.1 Experimental methods used for syntheses of noble metal NPs	32
2.2 Analytical techniques for characterization of nanoparticles	39
2.2.1 Electron microscopy	39
2.2.2 Inductively coupled plasma-atomic emission spectroscopy (ICP-AES)	42
2.2.3 Ultraviolet-Visible spectroscopy (UV-Vis)	43
2.2.4 X-ray diffraction (XRD)	47
2.2.5 Energy dispersive X-ray fluorescence (EDXRF)	49
2.2.6 Nuclear Magnetic resonance spectroscopy (NMR)	50
2.2.7 X-ray photoelectron spectroscopy (XPS)	52
2.2.8 Small angle X-ray scattering (SAXS).....	55

2.2.9	Capillary flow porometry (CFP).....	56
2.2.10	Electrospinning technique.....	59
2.3	Application of nanoparticles for catalysis.....	61
2.3.1	Reduction of <i>p</i> -nitrophenol (PNP).....	62
2.3.2	Reduction of methylene blue (MB).....	64
2.3.3	Hexavalent chromium reduction.....	65
2.3.4	Reduction of uranium (VI to IV).....	66
CHAPTER3. SELF-REDUCING ASYMMETRIC POLYMER MEMBRANE FOR IN SITU FORMATION AND CONTAINMENT OF NOBLE METAL NANOCATALYSTS.....		67
3.1	Introduction.....	68
3.2	Experimental.....	70
3.2.1	Synthesis of self-reducing membrane.....	70
3.2.2	Formation of noble metal NPs in self-reducing membrane.....	71
3.2.3	Reduction of <i>p</i> -nitrophenol (PNP) and methylene blue (MB).....	71
3.2.4	Reduction of Cr(VI) ions.....	72
3.3	Results and discussion.....	73
3.4	Conclusions.....	86
CHAPTER4. PALLDIUM NANOPARTICLES HOSTD IN HYDRAZINE/SULFONATE ANCHORED MEMBRANES FOR CATALYZING REDUCTION OF URANYL(VI) IONS.....		87
4.1	Introduction.....	88
4.2	Experimental.....	91
4.2.1	Formation of Pd NPs embedded neutral membrane.....	92
4.2.2	Formation of Pd NPs embedded cation-exchange membrane.....	93
4.2.3	Determination of Pd ⁰ content loaded in membranes.....	94
4.2.4	Characterizations of membranes.....	94
4.2.5	Reduction of U(VI) ions.....	95
4.3	Results and discussion.....	98
4.3.1	Characterizations of Pd NPs embedded membranes.....	98
4.3.2	Comparison of catalytic activities of Pd NPs embedded membrane.....	107
4.3.3	Quantification of U(VI) ions reduction with formic acid.....	112
4.3.4	Kinetics of reduction.....	116
4.3.5	Enhancement of kinetics of reduction using sonication.....	117
4.4	Conclusions.....	118

CHAPTER5. GRAFTED-ELECTROSPUN POLYMER MICROFIBER SCAFFOLD HOSTED PALLADIUM NANOPARTICLES FOR CATALYZING REDOX REACTIONS	120
5.1 Introduction.....	121
5.2 Experimental.....	124
5.2.1 Preparation of electrospun PES microfibers mat.....	124
5.2.2 Chemical treatments.....	126
5.2.3 Reductions of U(VI), Cr(VI) and <i>p</i> -nitrophenol.....	127
5.3 Results and discussion.....	128
5.3.1 Formation of Pd NPs embedded PES fibers mat.....	128
5.3.2 Catalytic reduction of U(VI) ions.....	133
5.3.3 Catalytic reduction of Cr(VI) anions.....	135
5.3.4 Catalytic reduction of <i>p</i> -nitrophenol.....	137
5.4 Conclusions.....	142
CHAPTER6. PALLADIUM NANOPARTICLES HOSTED IN POLY(ETHYLENIMINE) AND POLY(ETHYLENE GLYCOL METHACRYLATE PHOSPHATE) ANCHORED MEMBRANES FOR CATALYZING U(VI) IONS REDUCTION AND MIZOROKI-HECK COUPLING REACTION	144
6.1 Introduction.....	145
6.2 Experimental.....	147
6.2.1 Synthesis of Pd NPs on polyethylenimine (PEI) anchored membrane.....	147
6.2.2 Synthesis of Pd NPs in poly(ethylene glycol methacrylate phosphate) (EGMP) anchored membrane.....	148
6.2.3 Characterizations of membranes.....	148
6.2.4 Mizoroki-Heck coupling reaction.....	150
6.2.5 Reduction of U(VI) ions.....	151
6.3 Results and discussion.....	151
6.3.1 Catalytic activities of Pd NPs embedded PEI and poly(EGMP) in U(VI) ions reduction.....	162
6.3.2 Catalytic activities of Pd ²⁺ /Pd NPs loaded membranes for Mizoroki-Heck coupling reaction.....	166
6.4 Conclusions.....	173
CHAPTER7. SUMMARY AND FUTURE SCOPE	174
7.1 Summary of the present study and major conclusions.....	175
7.1.1 Chemical synthesis involved in synthesis of noble metal nanoparticles in polymer matrices.....	176

7.1.2	Catalytic applications of the metal nanoparticles hosted on polymer matrices	176
7.2	Future scope	178
REFERENCES		179

SYNOPSIS

Nanomaterial science is the intermediate domain between atoms/molecules and macro-world, where properties resemble neither to individual atoms nor bulk materials. In nanoscale region, neither quantum chemistry nor the classical laws of physics hold. Most of the emerging technologies of immense commercial importance such as catalysis, nanoelectronics, sensors, energy conversion and storage are based upon the application of the functional nanomaterials. The functional nanomaterials exhibit exceptional catalytic activity originating mainly from their size reduction and shape variation.

In catalysis, the ability to accept or donate charge plays a key role. The electrons are extensively delocalised and the extension of delocalisation varies with the size in nanoscale region. Similarly, surface energies and surface morphologies are also size dependant. There are always the questions of how the catalytic activity is affected by size in the regime between atoms and bulk, what is the minimum bulk-like lattice required for normal catalytic behaviour, or is there ideal size for which catalytic activity is maximized? The relationship between size and activity depends on choice of a catalyst and nature of a reaction. The catalytic properties of nanocatalyst would be influenced by at least two major factors: (1) changing the electronic structure of metallic nanocatalysts i.e. increasing the Fermi level of the nanocatalyst leading to a lower reduction potential of the metal on the surface of the nanocatalyst, and (2) increasing the number of chemically unsaturated and thermodynamically high-energy active surface atoms. It is also known that the type of exposed crystal planes (which can be controlled by the nanocatalyst shape) can influence the activity and selectivity of the nanocatalyst. In some cases, the nanocatalysts exhibit new properties due to plasmonic electromagnetic fields. However, the major problems in a large-scale application of the nanoparticles as catalysts originate from: (1) reshaping of the nanocatalyst during catalysis reaction, (2) products deposition on the surface could decrease the nanoparticle

stability and limit their recycling, (3) capping materials on the surface of colloidal nanocatalysts reduce their activity and can affect their Fermi energy, and (4) aggregation of the nanocatalysts.

It is interesting to note that the nanocatalysts are intermediate between conventional heterogeneous catalysts and homogeneous catalysts. The nanocatalysts may be considered either as heterogeneous catalyst or homogeneous catalyst depending upon the prevailing conditions. The common and acceptable definition of colloidal heterogeneous nanocatalysis is when the reaction occurs on the surface of nanoparticles. However, in homogeneous catalysis, the solvent can dissolve high-energy atoms or ions from the sharp edges or corners of the nanoparticle surface and form a complex that can catalyze the reaction in solution. With the help of molecular orbital (MO) theory, the interaction between an adsorbate and a metal catalyst can be explained. Noble metal nanoparticles show superior catalytic activity due to the formation of bonds between reactant molecules and the surface atoms of the nanoparticles, which weakens the bonds in the reacting molecules resulting to the lowering of activation barrier. Electronic structure and the geometry are the important considerations in the metal nanoparticles catalysts. From Bronsted-Evans-Polanyi (BEP) relation, the strong adsorption energies result in faster reaction rates for the first order surface reactions. The BEP relation shows the small energy barriers for the strong binding, and thus the catalytic performance is limited by desorption of products. However, in the case of weak binding, the reaction rate is limited by the large activation energies as predicted by BEP. Therefore, an optimum binding energy is needed for better performance of a catalyst.

Noble metal nanoparticles are most studied nanocatalysts because of their high surface area, under-coordinated surface sites, quantum confinement effects, and their chemical stability. However, because of their small size and high surface area, they often tend to agglomerate. Also, it is difficult to withdraw the nanoparticles from the system/solution leading to recyclability and

products contamination problems. In recent years, considerable efforts have been made to effectively stabilize and prevent the agglomeration of nanoparticles. The nanoparticles in the form of nanocomposites are extensively used in the optics, sensors and catalysis applications. Solid supports like carbon nanomaterials, superparamagnetic iron oxides particles, porous/non-porous inorganic nanoparticles (silica, titania, zirconia etc), natural and synthetic polymeric materials (resins/beads/films/membranes) have been explored to host the nanocatalysts. Among all these solid supports, the nanocatalysts immobilized on the magnetic nanoparticles and polymer films/membranes are easily retrievable from the process in which they act as nanocatalysts. The control over size and distribution of nanoparticles in the polymer matrix are the major issues in the polymer nanocomposites that have to be taken care of. Also, the immobilization of nanoparticles in the dense solid matrices may cause a diffusion resistance during the catalytic reaction. By immobilizing the nanoparticles in an open matrix like microfiltration membrane, the diffusion resistance can be minimised due to a high accessibility of the nanoparticles in porous matrix. Therefore, the porous structure of the support matrix has advantage for attaining highly efficient utilization of the available catalytic sites due to easy accessibility to the nanoparticles inside the interior matrix.

A synthetic or bio-polymer membranes have been studied extensively as the host matrices to stabilize nanoparticles. In general, the membranes provide an interphase that separates two phases and controls the selective transport of a component from one phase into the other. Membranes can be porous or homogeneous dense membranes. The transport in the dense membrane occurs through hopping between ion-exchange sites or functional groups. Structure of the membrane may be isotropic (symmetric: the structure is identical over the cross-section of the membrane) or anisotropic (asymmetric: the structure varies over the cross-section of the membrane). Membrane

supported transition/noble metal nanoparticles have shown the potential application in catalysis because of their special optical, electrical, and catalytic properties compare to bulk metal.

The present thesis is mainly focused on the functionalization of microporous membranes and microfibers by UV-initiator induced anchoring/grafting and subsequent chemical modifications to host the noble metal nanoparticles such as Ag, Au, Pd, Ru and Rh. In actual applications, these nanoparticles embedded membranes have not been used as the conventional membranes are defined. Based on the applications in the present thesis these membranes should have been termed as porous films or nanocomposite porous sheets. However, the “membrane” terminology has been retained due to their resemblance with the membranes such as egg shell membranes, and possibility of using them as the membrane in the “flow-through” catalysis. Thus prepared nanocomposites membranes have been studied for their potential applications in the organic and inorganic redox reactions. The functionalized polymeric membranes developed to host the metal nanocatalysts are of three types: (i) self-reducing membranes, (ii) cation-exchange membranes, and (iii) amine/phosphate functionalized membranes. For comparison, the self-reducing electrospun microfiber mat has also been synthesized to host the Pd nanocatalyst. All these membranes have been found to possess different noble metal nanoparticles loading capacities. The thesis is divided into seven chapters. The brief description of each chapter is given below:

Chapter 1: Introduction

This chapter describes a brief introduction about nanoscience and nanochemistry relevant to the present thesis, particularly how these nanomaterials are different compare to their bulk (size dependent properties). The literature on the immobilization of nanoparticles on the polymeric materials, relevant to the present work, and how their physical architecture influences the rate of the catalytic reaction have also been discussed. General introduction on the noble metal nanoparticles mediated catalysis has been discussed by using d-band centre model. Finally, the scope of the present thesis has been outlined.

Chapter 2: Experimental

The experimental procedures for syntheses of noble metal nanoparticles on the host membranes/electrospun microfiber mats and also the various instrumental techniques used for characterizing these nanocomposites have been discussed briefly. The electrospinning technique used for preparation of poly (ether sulfone) microfibers has also been explained. The details of UV-initiator induced grafting (poly (ether sulfone) fiber mat)/anchoring (poly(propylene) membrane) used for the functionalization of the polymeric materials are given. The characterization techniques include field emission scanning electron microscopy (FE-SEM), inductively coupled plasma-atomic emission spectroscopy (ICP-AES), UV-VIS spectrophotometry, X-ray diffraction (XRD), energy dispersive X-ray fluorescence (EDXRF), X-ray photoelectron spectroscopy (XPS) and capillary flow porometry (CFP).

Chapter 3: Self-reducing asymmetric polymer membrane for *in situ* formation and containment of noble metal nanocatalysts

In this chapter, the poly(propylene) membrane having an asymmetric physical structure, dense at the surface with fibrous interior, has been developed by anchoring glycidyl methacrylate in pores of the host poly(propylene) membrane and subsequently reacting with *N*-methyl-*D*-glucamine to host the Ag, Au, Ru, Rh and Pd nanocatalysts. These nanocatalysts are formed by *in situ* reductions in the precursor salt solutions without need of any external reducing agent. The polyol containing *N*-methyl-*D*-glucamine acts as the reducing agent and also stabilizes the nanoparticles formed on it. This functionalized membrane mimics the egg shell membrane in terms of reduction and stabilization of the nanoparticles. The catalytic activities of these nanocatalysts embedded polymer matrix have been tested for the organic redox reactions such as reduction of *p*-nitrophenol (PNP) to *p*-aminophenol, degradation of methylene blue (MB) by using Ag nanoparticles containing polymer matrices as a catalyst and borohydrate as a reducing agent. For inorganic redox reactions like Cr(VI) to Cr(III) and U(VI) to U(IV), the Pd nanoparticles embedded polymer matrix has been used as the catalyst and *in situ* hydrogen produced by the decomposition of formic acid as the reducing agent. It has been observed that the functionalized membrane developed in this work acts as a robust container of almost bare nanoparticles without affecting their accessibility, and it was also found that nanoparticles formed by this method have long shelf-life.

Chapter 4: Palladium nanoparticles hosted in hydrazine/sulfonate anchored membranes for catalyzing reduction of uranyl (VI) ions

Studies on the palladium nanoparticles hosted in the hydrazine/sulfonate anchored membranes have been described in this chapter. The functionalized membrane has been prepared by anchoring

of glycidyl methacrylate monomer by the UV-initiator induced polymerization in the pores of poly(propylene) membrane, and reacting subsequently with hydrazine hydrate. This functionalized polymer matrix has been found to form Pd nanoparticles by spontaneously reducing Pd^{2+} ions. The variation of Pd nanoparticles loading capacity of this polymer matrix with time has been studied. In addition to this self-reducing polymer membrane, a cation-exchange membrane has also been prepared by functionalizing with 2-acrylamido-2-methylpropane sulfonic acid monomer in pores of the host poly(propylene) membrane. These two functionalized membranes/matrices have been characterized for their ion-exchange capacities, porosity, Pd nanoparticles size distribution, and elemental mappings. Pd nanoparticles embedded in the hydrazine grafted membrane have exhibited excellent catalytic activity towards UO_2^{2+} ions reduction in the presence of formic acid. While, the Pd nanoparticles embedded in a cation-exchange membrane have not shown any catalytic activity towards UO_2^{2+} ions reduction under the similar conditions. The kinetics of reduction has also been analysed which shows that a threshold amount of Pd^0 in the hydrazine grafted membrane is required for a significant rate of reduction. It has been observed that the kinetics of reduction at lower amount of Pd^0 is controlled by pseudo-second-order kinetics. With increased amount of Pd^0 , the reduction process switches to diffusion controlled indicating matrix effect on the reduction kinetics. To improve mass transfer of reactants to the host polymer matrix and to overcome the diffusion barrier affecting the kinetics of UO_2^{2+} ions reduction, high intensity ultrasonication has been used. This has resulted in a switching kinetics of the reduction from diffusion-controlled process to pseudo-first-order kinetics leading to a very high catalytic activity of Pd nanoparticles. The Pd nanoparticles embedded in the host poly(propylene) matrix have shown long shelf-life and do not deteriorate during the successive cycles of reuse.

Chapter 5: Grafted-electrospun polymer microfiber scaffold hosted palladium nanoparticles for catalysing redox reactions

This chapter deals with the preparation of porous poly (ether sulfone) (PES) microfiber mat using the electrospinning technique, immobilization of Pd nanoparticles on to this fiber mat and its application in the organic and inorganic redox reactions. The microfiber mat as a host has been studied to explore the possibility of providing more accessibility of the Pd nanoparticles to the reactants. It is expected that the catalytic reduction in the microfiber mat would not be diffusion controlled. The reducing moiety has been attached covalently to the PES microfiber mat by UV-initiator induced graft polymerization of glycidyl methacrylate, and reacting subsequently with hydrazine via epoxy ring opening. The reduction of precursor Pd²⁺ ions by grafted hydrazine has lead to the nucleation and growth of Pd nanoparticles on the shell of microfiber itself. The organic reductions involving *p*-nitrophenol to *p*-aminophenol, degradation of methylene blue, and inorganic reductions involving Cr(VI) to Cr(III) and U(VI) to U(IV) have been examined. The normalised catalytic activities of the Pd nanoparticles hosted on electrospun PES microfiber mat have been found to be higher than earlier reported in literature, but lower than that given in previous chapter using Pd nanoparticles embedded membrane.

Chapter 6: Palladium nanoparticles hosted in poly(ethylenimine) and poly(ethylene glycol methacrylate phosphate) anchored membranes for catalyzing U(VI) ions reduction and Mizoroki-Heck coupling reaction

This chapter describes the development of amine functionalized membrane which can hold higher amount of nanoparticles, and also provides tertiary/secondary amine sites which are required for some of the C-C coupling reactions. To increase the amount of nanoparticles loading, the host

poly(propylene) membrane has been functionalized with polyethylenimine (PEI) by first anchoring of poly(glycidyl methacrylate) by UV-polymerization, and subsequently attaching PEI by the glycidyl ring opening reaction. Pd nanoparticles have been formed by reducing the Pd²⁺ ions-loaded PEI-membrane with sodium borohydride. The effect of porosity of PEI functionalized membrane on the catalytic activity of Pd nanoparticles has also been studied toward UO₂²⁺ ions reduction with formic acid. For comparison, the UO₂²⁺ ions reduction has also studied using Pd nanoparticles immobilized on poly(ethylene glycol methacrylate phosphate) (poly(EGMP)) anchored poly(propylene) membrane. The poly(EGMP)-membrane hosted Pd nanoparticles have been found to be less efficient compared to the Pd nanoparticles hosted in the PEI-membrane. This could be attributed to a fact that the amine groups on PEI enhance the formic acid decomposition, thereby increase the hydrogen production rate. The *in situ* H₂ produced from formic acid decomposition eventually leads to the reduction of UO₂²⁺ ions. The Pd nanoparticles loaded on PEI and EGMP functionalized membranes have also been tested in Mizoroki-Heck coupling reaction which is most efficient route for the vinylation of aryl/vinyl halides (C-C coupling). In a typical experiment, 1mmol of iodobenzene, 1.1 mmol of ethyl acrylate and 3 mmol of triethylamine have been taken. It has been found that, the coupling reaction is successful with reduced and unreduced palladium in both types of the membranes. However, the Pd nanoparticles embedded PEI-membrane gives better yield (76%) in comparison with the EGMP grafted membrane (70%). This could be due to the amine groups in the PEI-grafted membrane facilitating the reaction. It has been seen from mechanism that, in presence of a base, the Pd²⁺ ions get reduced first and then reaction proceeds. Since the functionalized membrane contains amine group, the reaction with Pd nanoparticles without external base has been found to be successful to some extent.

Chapter 7: Summary and Future Scope

In this chapter, the conclusions drawn from the work carried out in the present thesis and future scope related to this topic of research have been given. The major conclusions include:

(i) The noble metal nanocatalysts embedded on polymer membranes provide the physical stability (by preventing agglomeration), chemical stability (by inhibiting chemical corrosion), and makes it easy to withdraw from the system which helps in recyclability and prevents contamination of the products.

(ii) The self-reducing membranes developed in this work provide an easy route to host noble metal nanocatalysts without using any external reducing agents. These membranes mimic the egg-shell membrane in terms of formation and stabilization of nanoparticles.

(iii) These functionalized membranes developed in the present work also provide control over nanoparticles growth/size. This can be achieved by controlling the amount of monomers anchored in the membranes or keeping the functionalized membranes in a precursor salt solution for a predetermined time.

(iv) The self-reducing membranes developed in the present work have an asymmetric structure, dense at the surface and fibrous interior. The nanoparticles formed in the interior of the matrix have shown remarkable enhancement in the catalytic activity compared to surface immobilized nanoparticles.

(v) The nanocatalysts formed on the polymer membranes/microfiber mats have been found to catalyse both organic and inorganic redox reactions. As part of inorganic redox reactions,

reductions of Cr(VI) to Cr(III) and U(VI) to U(IV) have been studied. Reduction of *p*-nitrophenol and degradation of methylene blue have been studied as the examples of the organic reductions.

(vi) *In situ* generated hydrogen from formic acid decomposition could be used as a reducing agent for the inorganic ions reduction, which is produced by the decomposition of formic acid on Pd nanoparticles surface. The Pd nanoparticles loaded cation-exchange membranes have been found to be unsuccessful in reducing UO_2^{2+} ions under similar conditions.

(vii) The $\text{Pd}^0/\text{Pd}^{2+}$ -loaded PEI/poly(EGMP) functionalized poly(propylene) membrane has been studied for catalysing Mizoroki-Heck coupling reaction. The model reaction has been successful with both reduced and unreduced palladium embedded membranes.

LIST OF FIGURES

Figure 1.1 Lycurgus Cup in transmitted (a) and reflected (b) light (Freestone et al. 2007).	5
Figure 1.2 Illustration of the increased surface to volume ratio provided by nanostructured materials.	6
Figure 1.3 Illustrations of the density of states vs. energy for bulk material, quantum well, quantum wire and quantum dot (atom like behavior when the particle size is reduced). (Redrawn from Xu 2005).....	7
Figure 1.4 The general approaches used for synthesis of the nanoparticles.	9
Figure 1.5 The schematic graph represents the principle of NP nucleation due to Mer's mechanism of (sulfur) nucleation derived from CNT (Polte 2015).	11
Figure 1.6 Change in the Gibbs free energy as a function of the nucleus radius (r) as a sum of the volume and surface free energies (Camargo et al. 2015).....	13
Figure 1.7 The Schematic representation of electric double layer (EDL) formed around a nanoparticle (according to Gouy-Chapman model) which consists of inner Stern layer and the outer diffusive layer, and (b) corresponding decrease of the counter and co-ion concentration with respect to the distance from the particle surface(Polte 2015).	16
Figure 1.8 Schematic representation of electrostatic and steric stabilization of the Ag nanoparticles (Tüzüner and Demir 2015).....	18
Figure 1.9 A scatter plot of the d-band centre of the metal surface versus the adsorption strength of p-nitrophenol (Pozun et al. 2013).	22
Figure 1.10 The possible reaction pathway of formic acid decomposition by Pd on basic groups containing membrane/resin (Mori et al. 2013).....	23

Figure 1.11 Plot of rates of formic acid decomposition versus d-band centre (Tedsree et al. 2011).	24
Figure 1.12 Various applications of the functionalized polymer membranes.	27
Figure 1.13 Various applications of electrospun fibres.	29
Figure 2.1 Schematic representation of the steps involved in synthesis of pore-filled precursor membranes.	35
Figure 2.2 The different types of pore-filling membranes prepared by controlling the amount of polymer anchored/grafted on the pore walls of the membrane.....	36
Figure 2.3 Schematic comparison of optical/light microscope (LM), transmission electron microscope (TEM) and scanning electron microscope (SEM).....	40
Figure 2.4 A representative FE-SEM image of poly(propylene) membrane.....	42
Figure 2.5 The schematic representation of ICP-AES instrument.....	43
Figure 2.6 The excitation process.	43
Figure 2.7 Electronic energy level and transitions.....	44
Figure 2.8 Electronic transitions with vibrational transitions superimposed. (Rotational levels, which are very closely spaced within the vibrational levels, are omitted for clarity.)	45
Figure 2.9 Schematic representation of a typical UV-Visible spectrophotometer.	47
Figure 2.10 A typical XRD instrumental setup.	48
Figure 2.11 The direction of magnetic moment due to spinning of proton (a) and the difference in energy of the two spin states (b).	52
Figure 2.12 The schematic diagram of XPS.	54
Figure 2.13 A representative survey spectrum of Pd NPs embedded in PEI functionalized PP host membrane.....	54

Figure 2.14 Schematic representation of the experimental setup for a SAXS experiment and representation of the scattering vector (q) on the detector surface (Kikhney and Svergun 2015).....	55
Figure 2.15 The schematic representation of principles of CFP of a membrane.....	57
Figure 2.16 The plots showing flow rates as a function of applied pressure across dry and wet poly(propylene) membrane.	59
Figure 2.17 A schematic representing the electrospinning apparatus.....	61
Figure 2.18 A typical electrospun fiber mat produced by electrospinning technique.	61
Figure 2.19 Reduction scheme of p-nitrophenol to p-aminophenol.	63
Figure 2.20 The mechanism involved in PNP reduction with borohydride in presence of Ag NPs (Baruah 2016).	63
Figure 2.21 The UV-Vis spectra of p-nitrophenol to p-aminophenol conversion.	63
Figure 2.22 Chemical structure of methylene blue in its oxidized and reduced forms.	64
Figure 2.23 The UV-Vis spectra of methylene blue degradation.	64
Figure 2.24 UV-Vis spectra showing reduction of Cr(VI) to Cr(III) with formic acid at 45 °C as a function of time in the presence of Pd NPs loaded membrane.	65
Figure 2.25 UV-Vis spectra showing reduction of U (VI) to U(IV).	66
Figure 3.1 FE-SEM images showing surface (a) and cross-section (b) of the host poly(propylene) membrane, and surface (c) cross-section (d) of the same host membrane after anchoring with poly(GMA) and subsequent treatment with NMDG.	73
Figure 3.2 The representative FE-SEM image of the surface of Rh NPs loaded membrane (a), and corresponding elemental mappings of nitrogen(b) and Rh (c) by EDS.	75

Figure 3.3 FE-SEM images showing Au NPs having geometries of cubes and prisms at the surface (a), spherical at the porous surface (b), Silver NPs (c), Palladium NPs (d) and Ru NPs (e) formed at the surfaces of membrane samples equilibrated with 0.1 mol L ⁻¹ HAuCl ₄ /AgNO ₃ /PdCl ₂ /RuCl ₃ solutions for overnight.....	77
Figure 3.4 EDXRF spectra of Rh (a) and Ru NPs (b) loaded membrane.	78
Figure 3.5 FE-SEM images of cross-section of the Ag ⁰ loaded membrane samples (a), elemental mappings of nitrogen (b), Silver (c), and mixed elemental mapping image of nitrogen and silver (d).	79
Figure 3.6 Variations in loading of Ag ⁰ and Pd ⁰ in the membrane as a function of equilibration time at room temperature in 0.05 mol L ⁻¹ solutions of AgNO ₃ and PdCl ₂	80
Figure 3.7 FE-SEM images showing Ag NPs formed on the surfaces of the membrane after 1 min (a) and 60 min (b) equilibration in 0.05 mol L ⁻¹ AgNO ₃ solution.	81
Figure 3.8 XRD pattern of Ag NPs loaded membrane stored for three months under ambient conditions.	82
Figure 3.9 Successive UV-Vis spectra showing reduction of Cr(VI) to Cr(III) at 45°C using formic acid as a function of time in the presence of a Pd NPs loaded membrane (a), and corresponding variation of logarithm of A _t /A ₀ as a function of reduction time (b). A _t and A ₀ represent absorbance at 350 nm corresponding to concentration of Cr(VI) at time t and initial respectively.	83
Figure 3.10 UV-Vis spectra showing the absence of significant reductions of Cr(VI) with formic acid at 45°C as a function of time in the presence of NMDG-membrane sample without Pd NPs.....	83

Figure 3.11 Successive UV-Vis spectra showing the reduction of methyl blue with BH_4^- ions at room temperature as a function of time in the presence of Ag NPs loaded membrane (a), and corresponding variation of logarithm of A_t/A_0 as a function of reduction time (b)..... 85

Figure 3.12 Successive UV-Vis spectra showing the reduction of p-nitrophenol to p- aminophenol reduction with BH_4^- ions at room temperature as a function of time in the presence of Ag NPs loaded membrane (a) , and corresponding variation of logarithm of A_t/A_0 as a function of reduction time (b). 85

Figure 4.1 The experimental setup of Z-flow cell spectrophotometry used for on-line monitoring of UV-Vis absorption spectra during U(VI) to U(IV) ions reduction..... 92

Figure 4.2 Successive UV-Vis spectra showing reduction of UO_2^{2+} to U^{4+} ions using formic acid: (a) in the presence of Pd NPs embedded hydrazine-grafted PP membrane at room temperature and (b) in the presence of hydrazine-grafted membrane without Pd NPs at 50°C as a function of time. 96

Figure 4.3 Comparison of pore-size distributions obtained by capillary flow porometry in the pristine poly(propylene) membrane, hydrazine-grafted poly(propylene)membrane, and Pd NPs embedded membrane samples..... 100

Figure 4.4 Variation of Pd0 content in the hydrazine-grafted membrane sample as a function of equilibration times in the aqueous solution containing $0.01 \text{ mol L}^{-1} \text{ PdCl}_2$ at $\text{pH} = 2$ 101

Figure 4.5 The representative FE-SEM images of surface of pristine PP membrane (a & b), cross-section of pristine PP membrane (c & d), surfaces of Pd NPs embedded hydrazine grafted membrane (e & f), cross-section of Pd NPs embedded hydrazine-grafted

membrane (g & h), and EDS elemental mappings of nitrogen (i), Pd (j) and mixture of N and Pd at cross-sections (4×4 μm) of the same Pd NPs embedded hydrazine-grafted membrane (k).....	105
Figure 4.6 Representative FE-SEM images of surface (a & b), cross-section (c & d) of PP based cation-exchange membrane, and elemental mappings of Pd (e), N (f), and mixture of Pd and N along the cross-sections of the same PP membrane (g).	106
Figure 4.7 Variation of logarithm of $[U(VI)]_t/[U(VI)]_0$ as a function of reduction time with formic acid in the presence of Pd embedded PP membrane at 40, 50, 60°C temp. $[U(VI)]_t$ and $[U(VI)]_0$ represent conc. of UO_2^{2+} ions at time t and initial, respectively.	108
Figure 4.8 Variation of catalytic activity of the Pd NPs embedded in hydrazine-grafted membrane as a function of Pd^0 content in the reduction of U(VI) ions by formic acid to U(IV) ions at 50°C.	109
Figure 4.9 UV–Vis spectra showing no reduction of U(VI) with formic acid in the presence of Pd NPs immobilized in the cation-exchange membrane at 50°C. Figures. a & b present the experiments carried out using the cation-exchange membrane loaded with Pd NPs in one cycle and four cycles, respectively.....	110
Figure 4.10 The successive UV–Vis spectra obtained online after every 5 min intervals during 70 min reduction of U(VI) ions with formic acid in the presence of Pd NPs embedded hydrazine-grafted PP membrane at 50°C.	112
Figure 4.11 UV-Vis spectra showing the stability of absorbance peaks of U(IV) ions stored at -4°C (a) and at room temperature (25°C) (b).	114

Figure 4.12 UV–Vis spectra showing the absorbance peaks corresponding to U(IV) ions after 1 h successive cycles of the reduction of U(VI) ions with formic acid in the presence of Pd embedded PP membrane.....	115
Figure 5.1 FE-SEM images of electrospun nanofiber mats formed by using the solutions having: (a) 20 wt. % of PES in DMAc, (b) 28 wt. % of PES in DMAc, (c) 30 wt. % of PES in DMAc, and (d) 28 wt. % of PES in DMAc: acetone in 80:20 ratio under lower and higher magnifications.....	126
Figure 5.2 FE-SEM images of the pristine PES nanofibers mat (a,b), and same nanofibers mat after the chemical modifications shown in Scheme 1 (c,d) under higher and lower magnifications.....	130
Figure 5.3 The C, N, Pd elemental mappings of Pd NPs loaded PES microfibers mat (70x70 μm) by EDS showing the presence of nitrogen from residual hydrazine and Pd NPs. ...	131
Figure 5.4 Cross-sectional FE-SEM image of Pd NPs loaded microfiber.....	131
Figure 5.5 Elemental mappings of Pd and N on the cross-section of Pd NPs loaded PES microfibers Fiber@Pd using FE-SEM/EDS.....	132
Figure 5.6 The increase in the concentration of U(IV) ions as a function of reduction time of U(VI) ions with formic acid at 50°C was monitored from the f-f transition peaks in successive UV-Vis spectra recorded from the samples taken from reaction solution.....	134
Figure 5.7 Successive UV-Vis spectra obtained during reductions of Cr(VI) with formic acid at 50°C (a) and 25°C (b) and corresponding variation of $\ln [A]_t/[A]_0$ vs reduction time (t) in the presence of Fiber@Pd. The UV-Vis spectra shown in (c) indicate no reduction of Cr(VI) under similar conditions (50°C) in absence of the catalyst along with comparisons of reduction rate profiles at room temperature and at 50°C.....	136

Figure 5.8 The successive UV-Vis spectra showing quantitative conversion of PNP to PAP with borohydride in the presence of Fiber@Pd (a) and corresponding variation of $\ln [A]_t/[A]_0$ vs. reduction time (b).....	138
Figure 5.9 The successive UV-Vis spectra showing no reduction of p-nitrophenol to p-aminophenol with borohydride (a) and hydrazine (b) in the absence of catalyst Fiber@Pd.	139
Figure 5.10 The kinetic rate profile showing variation of $\ln [A]_t/[A]_0$ vs. time in the reduction of p-nitrophenol to p-aminophenol with hydrazine at room temp.....	140
Figure 5.11 The kinetic rate profiles showing variations of $\ln [A]_t/[A]_0$ vs. time in the reductions of p-nitrophenol to p-aminophenol with borohydride (a) and hydrazine (b) at room temperature in recycles of catalyst Fiber@Pd.	142
Figure 6.1 The comparison of obtained pore-size distributions of pristine membrane and PEI functionalized membrane (PP2, PP3 and PP4) by capillary flow porometry.	154
Figure 6.2 A representative SEM images of the PP membranes anchored with different amounts of polymer PP2 (a & b), PP3 (c & d) and PP4 (e & f), respectively, under two different magnifications.....	155
Figure 6.3 The representative SEM image of the Pd NPs formed on the PP2 membrane (a), and corresponding elemental mappings of nitrogen (b) and Pd (c) by EDS.	156
Figure 6.4 The surface morphology of Pd NPs embedded membrane (PP1) (a) and cross-sectional image of the same membrane (b) under same magnification.	157
Figure 6.5 (a) Scattering profile from blank membrane, Pd ²⁺ ions loaded and Pd NPs loaded membrane, (b) Scattering contribution solely from the nanoparticles as obtained from the subtraction of scattering profile of blank and Pd ²⁺ ions loaded membrane.	158

Figure 6.6. Size distribution of the Pd NPs in the PEI-membrane PP1 (a), PP3 (b), and PP4 (c) as obtained from the SAXS data analysis.	159
Figure 6.7 The EDS elemental mappings of nitrogen (a), palladium (b) across the cross-section of the PP1 membrane.	160
Figure 6.8 Representative FE-SEM images of surface (a & b) and corresponding elemental mappings of phosphorus (c) and palladium (d) by EDS of poly(EGMP)- membrane.	161
Figure 6.9. UV– Vis spectra showing growth of U(IV) ions absorption peaks (a), variation of logarithm of $[U(VI)]_t/[U(VI)]_0$ as a function of reduction time with formic acid in the presence of Pd NPs embedded PEI (PP3) membrane at 50°C, (b) and no reduction of U(VI) ions with formic acid in absence of Pd catalyst (c).....	164
Figure 6.10 UV–Vis spectra showing less efficient growth of absorption peaks of U(IV) ions during reduction of U(VI) ions with formic acid in the presence of Pd NPs immobilized in the EGMP anchored membrane at 50°C.....	166
Figure 6.11 Deconvoluted XPS spectra of binding energies peaks of $3d_{5/2}$ and $3d_{3/2}$ obtained before using Pd^{2+} ions loaded PEI-membrane (a), and after coupling reaction (b).	170
Figure 6.12 The 1H NMR (a) and ^{13}C NMR spectra of ethyl cinnamate (b).	171
Figure 6.13 The LC-MS spectra of ethyl cinnamate.....	172
Figure 6.14 The bar diagram of catalyst (Pd NPs embedded PEI-membrane) cycle with yield (%).	172

LIST OF TABLES

Table 2.1 The primary beam filters used in EDXRF.	50
Table 4.1 Comparison of absorption energy levels for U(IV) ion in solution (Misbah and Iftikhar 2013) and observed in the present work due to its complex formation with formate.	113
Table 4.2 Analyses of the kinetics of U(VI) ions reduction with formic acid in the presence of Pd NPs hosted in the hydrazine-grafted PP membrane. The chemical conditions were kept constant and varied either temperature or catalyst.	117
Table 5.1 Comparison of the catalytic activities of Fiber@Pd with Pd/C during the reduction of UO_2^{2+} ions with formic acid at 50°C temp. The conditions were kept same in all the experiments as 0.1 mol L ⁻¹ $UO_2(NO_3)_2$ at pH=2 and 1 mol L ⁻¹ formic acid.	134
Table 5.2 Comparison of catalytic activity of Pd NPs hosted in different matrices for the reduction of Cr(VI) anions with formic acid.	137
Table 5.3 Comparison of the catalytic activity of Fiber@Pd in the reduction of p-nitrophenol with borohydride at room temp. with the catalytic activities of Pd, Au and Ag NPs reported in literature under similar conditions.	141
Table 6.1 The comparisons of the amount of polymer anchored, percentage of water uptake (hydrophilicity) and amount of Pd ⁰ loading in PEI and poly(EGMP) anchored PP membranes.	153
Table 6.2 The comparisons in catalytic activities of Pd NPs immobilized on PEI functionalized PP membranes.	165
Table 6.3 The outcome of Mizoroki-Heck coupling reaction examined in different experimental conditions. Triethylamine was used as external base.	168

Table 6.4 Comparison of Mizoroki-Heck coupling reaction yield carried out with Pd NPs hosted in different matrices and conditions.....	169
---	-----

LIST OF SCHEMES

Scheme 2.1 Formation of free radicals (1R, 2R, 3R) from photolysis of α' - α -dimethoxy- α -phenyl acetophenone (DMPA).	36
Scheme 2.2 Mechanism of formation of free radicals from photolysis of poly (ether sulfone). ..	36
Scheme 3.1 The chemical reaction involved in the anchoring of NMDG on to the poly(GMA) anchored membrane that reduces noble metal precursor ions and stabilizes the thus formed NPs.	74
Scheme 4.1 Chemical modifications involved in the formation of Pd NPs in the neutral PP membrane.....	99
Scheme 4.2 Representative steps involved in the formation of Pd NPs in the cation-exchange membrane.....	102
Scheme 4.3 Preferential UO_2^{2+} ions interactions with sulfonic acid groups in a pore of Pd NPs embedded cation-exchange membrane (a), and with Pd NPs in hydrazine-grafted membrane (b).	111
Scheme 5.1 Chemical modifications involved in the covalent attachment of reducing hydrazine groups on the electrospun PES microfibers mat.	128
Scheme 6.1 Chemical modifications involved in formation of Pd NPs on the PEI anchored PP membrane.....	152
Scheme 6.2 Formation of Pd NPs in the poly(EGMP)-membrane.....	161
Scheme 6.3 Formation of Pd NPs from Pd^{2+} ions by the amine groups in the PEI functionalized membrane.....	167
Scheme 6.4. Mizoroki-Heck coupling reaction between iodobenzene and ethyl acrylate.	170

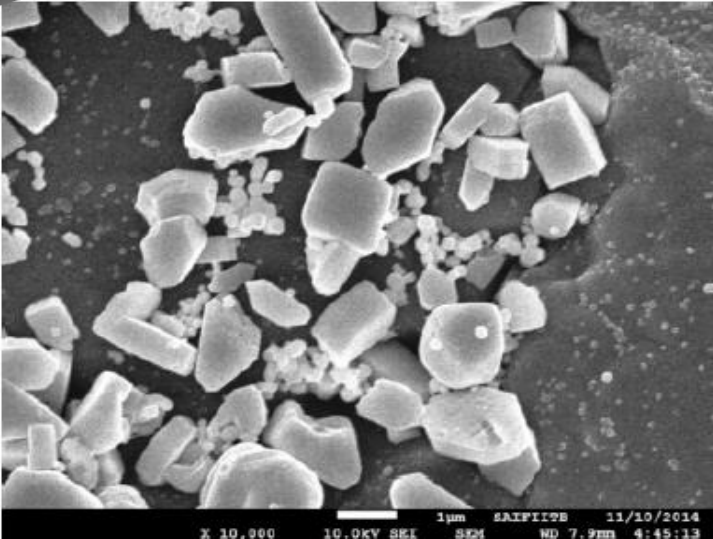
ABBREVIATIONS

AFM	: Atomic force microscopy
AMPS	: 2-acrylamido-2-methyl-1-propane sulfonic acid
APTMS	: (3-acryloxy propyl) trimethoxysilane
BEP	: Bronsted-Evans-Polanyi
BET	: Brunauer-Emmentt-Teller
CCD	: Charge coupled device
CFP	: Capillary flow porometry
CNT	: Classical nucleation theory
CTAB	: Cetyltrimethylammonium bromide
DFT	: Density functional theory
DLVO	: Derjaguin-Landau-Verwey-Overbeek
DMF	: <i>N-N'</i> -dimethyl formamide
DMPA	: α,α' -dimethoxy- α -phenyl-acetophenone
DOS	: Density of states
EDL	: Electrical double layer
EDS	: Energy dispersive spectrometer
EDX	: Energy-dispersive X-ray spectroscopy
EDXRF	: Energy dispersive X-ray fluorescence
EGDM	: Ethylene glycol dimethacrylate
EGMP	: Ethylene glycol methacrylate phosphate
ESCA	: Electron spectroscopy of chemical analysis

ESM	: Egg-shell membrane
FE-SEM	: Field emission scanning electron microscopy
FTIR	: Fourier-transform infrared spectroscopy
HOMO	: Highest occupied molecular orbital
HRTEM	: High resolution transmission electron microscopy
ICP-AES	: Inductively coupled plasma atomic emission spectroscopy
LC-MS	: liquid chromatography - mass spectrometry
LUMO	: Lowest unoccupied molecular orbital
MB	: Methylene blue
MCA	: Multi channel analyzer
MO	: Molecular orbital
NCs	: Nanocatalysts
NFs	: Nanofibers
NHE	: Normal hydrogen electrode
NMDG	: <i>N</i> -methyl- <i>D</i> -glutamine
NMP	: N-Methyl-2-pyrrolidone
NMR	: Nuclear magnetic resonance
NPs	: Nanoparticles
PA	: Polyamide
PAA	: poly(acrylic) acid
PAN	: Poly(acrylonitrile)
PAP	: <i>p</i> - aminophenol
PEG	: Poly(ethylene glycol)

PEI	: Poly(ethylenimine)
PES	: Poly(ether sulfone)
PNP	: <i>p</i> - nitrophenol
PP	: Poly(propylene)
PU	: Poly(urethane)
PUREX	: Plutonium uranium reduction extraction
PVA	: Poly(vinyl alcohol)
PVAc	: Poly(vinyl acetate)
SAXS	: Small angle X-ray scattering
TEM	: Transmission electron microscopy
TLC	: Thin-layer chromatography
TMS	: Tetramethylsilane
UV-Vis	: Ultraviolet-Visible
WDXRF	: Wavelength dispersive X-ray fluorescence
XRD	: X-ray diffraction
XRF	: X-ray fluorescence
XPS	: X-ray photoelectron spectroscopy

CHAPTER1. INTRODUCTION



1.1 Introduction to nanoscience

The concept of nanoscience was first introduced about 55 years ago by the Nobel physicist Richard Feynman in his talk at American Physical society, Caltech on December 29, 1959 entitled **“There’s plenty of room at the bottom”**. The statement in his words *“The principles of physics, as far as I can see, do not speak against the possibility of maneuvering things atom by atom. It is not an attempt to violate any laws; it is something, in principle, that can be done; but in practice, it has not been done because we are too big”*. This was widely accepted as the spark that initiated the present ‘nano’ age. Till 1990’s, the talk went unnoticed and did not inspire the conceptual beginnings of the field and then it made a remarkable progress in the nanoscience and nanotechnology.

Nanotechnology is the branch of science which involves the manipulation of the matter to the nanoscale level whose properties are different from that of the bulk material. Nanotechnology promises the possibility of creating nanostructures of meta-stable phases with non-conventional properties including superconductivity and magnetism etc. Another important aspect of nanotechnology is the miniaturization of current and new instruments, sensors and machines that will greatly influence the world we live in. Nanoscience is one of the most active disciplines all over the globe and is considered to be the fastest growing revolutionary fields in the human history. Rapid developments of many advanced instruments such as field emission electron microscope (FE-SEM), high resolution transmission electron microscope (HRTEM), X-ray bound techniques, atomic force microscope (AFM) etc. for advance research in nanomaterials are the witness of global interest in the subject.

1.1.1 Nanomaterials

Nanomaterial science is a broad and interdisciplinary area of research which has been growing around the globe passionately. The term “nano” comes from the Greek prefix “nanos” meaning dwarf or extremely small. A nanometer (nm) is a measurement of length which is one billionth of a meter (10^{-9} m). Thus nanomaterials can be defined as *“the particles (crystalline or amorphous) of organic or inorganic materials having at least one dimension in the range of 1-100 nm (Edelstein and Cammaratra 1998), and whose physical and chemical properties are significantly different from that of the bulk material.* Nanomaterial science is the boundary between the atoms /molecules and the macro-world. To distinguish nanomaterials from bulk, it is very important to determine the unique properties of nanomaterials and their prospective impact on the science and technology. A well-known example is that the allotropes of carbon are diamond and graphite, both have different bonding and structural characteristics so their thermal, electrical, optical, and chemical properties. However, fullerenes (C₆₀, C₇₀, and others) the new forms of carbon show exceptional physical and chemical properties. These unique properties of nanomaterials are so different from the bulk that raises a question, “how big or small is the nanometer?” For example, size of a water molecule is 0.3 nm across whereas; the red blood cell is approximately 7,000nm wide.

Nanomaterials are classified on the basis of their origin, dimensions and structural composition (Cao 2004). Depending on their origin, they are categorized as natural and artificial. Viruses, bacteria, protein molecules etc. belong to natural nanomaterials, whereas artificial nanomaterials are made through mechanical or fabrication process. According to their dimensions, they are grouped as a zero, one, two and three-dimensional materials. Zero dimensional materials are quantum dots in which the movements of the electrons are restricted in all the three directions.

One dimensional material includes wire, ribbon, rod and tube-like shape, where the movements of electrons are restricted in the X and Y directions. In two dimensional materials such as thin films, sheets etc. the electrons can move freely in the X-Y plan. The three-dimensional material is constructed from the nanoparticles as building blocks, in which the electron can move freely in all the three directions (X, Y and Z) (Siegel 1993). Metal nanoparticles are extensively used in the catalytic applications and these have potential for the extensive industrial applications. Among the metal nanoparticles, the noble metal nanoparticles (Ag, Au, Pd, Pt, Ru and Rh) are mostly used because these possess the spectacular properties such as tunable surface plasmon and photo-thermal effects, excellent resistance to corrosion and air oxidation, and lesser cytotoxicity. The other examples are metal oxide nanoparticles such ZnO, TiO₂, NiO, Co₃O₄ and Fe₃O₄ nanoparticles. The present thesis mainly focuses on the noble metal nanomaterials such as Ag, Au, Pd, Ru and Rh nanoparticles which are extensively used as the industrial catalysts.

1.1.2 Why nanomaterials are different

Nanomaterials behave differently compared to bulk. For example, Gold is yellow in colour, non-magnetic and melts at 1336K when it is bulk. However, if the size of gold is reduced to around 10nm range then it appears red in colour and melts at lower temperature compare to bulk. If we reduce the size of the gold even lower then it acts as very good catalyst. In ancient times, the nanomaterials had been used to play with optical properties to decorate the object as shown in Figure 1.1 It is, therefore, the properties of nanomaterials are size dependent and their unusual properties are explained by two factors: (i) total fraction of atoms at the surface, and (ii) quantum confinement.

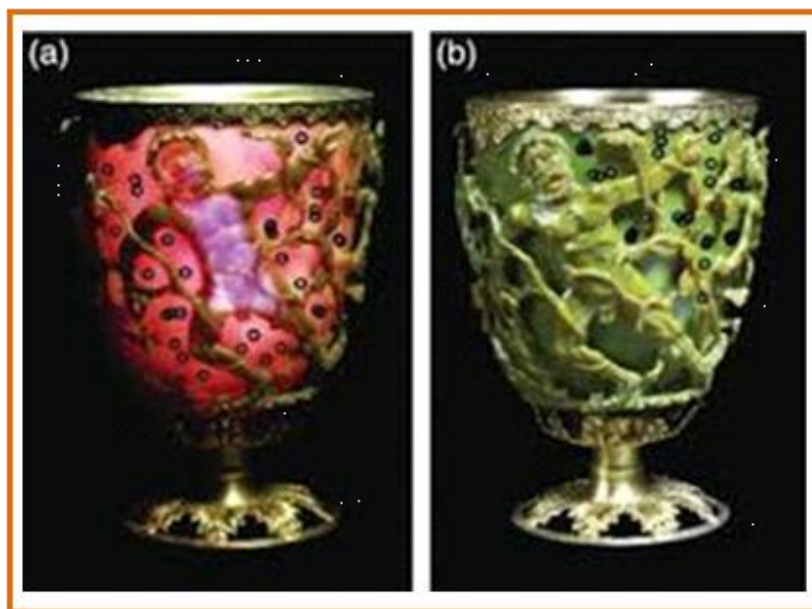


Figure 1.1 Lycurgus Cup in transmitted (a) and reflected (b) light (Freestone et al. 2007).

1.1.2.1 Total fraction of atoms at the surface

The physical and chemical properties of nanomaterials change drastically with the change in the surface to volume ratio. As the size of the material decreases, this ratio increases significantly. As shown in Figure 1.2, the total surface area of given particle with 1cm^3 cube in the size is 6cm^2 , whereas when the particle size is reduced to 1mm^3 then surface area increases to 60cm^2 , the proportion of number of surface atoms to bulk atoms has increased nearly 10%. If the particle size is further decreased to 1nm^3 then the surface area becomes $60,000,000\text{cm}^2$. This gives nearly 80% of atoms at the surface. This increase in the surface atoms alters the physical and chemical properties of the material, and is extremely important for the industrial applications such as catalytic processing and separation science.

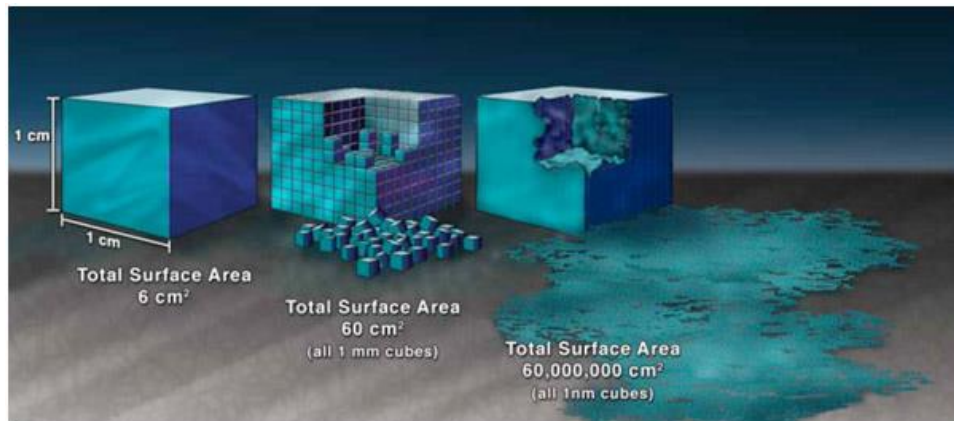


Figure 1.2 Illustration of the increased surface to volume ratio provided by nanostructured materials.

1.1.2.2 *Quantum confinement: Atom like behavior of nanoparticles*

The electron movements in nanomaterial depend on the dimension. Quantum size effects appear when the size of nanomaterials is closer to single atom or molecules compare to bulk materials. Based on dimensions these new materials can be divided as:(i) zero dimensional (Quantum dots) in which electron movement is confined in all three dimensions, (ii) quantum wires, which are one dimensional nanomaterial where electrons are free to move in X-direction, (iii) two dimensional material like thin films where, electrons are free to move in X-Y plane, and (iv) three dimensional material, where electron can move in X,Y and Z directions. As shown in Figure 1.3, the density of states in these nanomaterials ($g(E)$) are defined by the number of energy states between energy E and $E+dE$, which is derived by $dn(E)/dE$. When the particle size is reduced to nanometre range then discrete energy levels are formed and particles behave like individual atoms. Whereas, the energy levels are continuum in bulk material. When the particle size is less than 10nm diameter, the electrons in the conduction band are confined rather than continuum. The density of states $g(E)$, which is defined by the number of energy states between energy E and $E+dE$ and this energy

spacing between the electrons in a box quantum levels are greater than the thermal energy ($k_B T$) at low temperature, so the energy levels are considered as discrete. The discretization of the electronic states and widening in band gap makes some nanoparticles strongly fluorescent (CdS, PdS etc.).

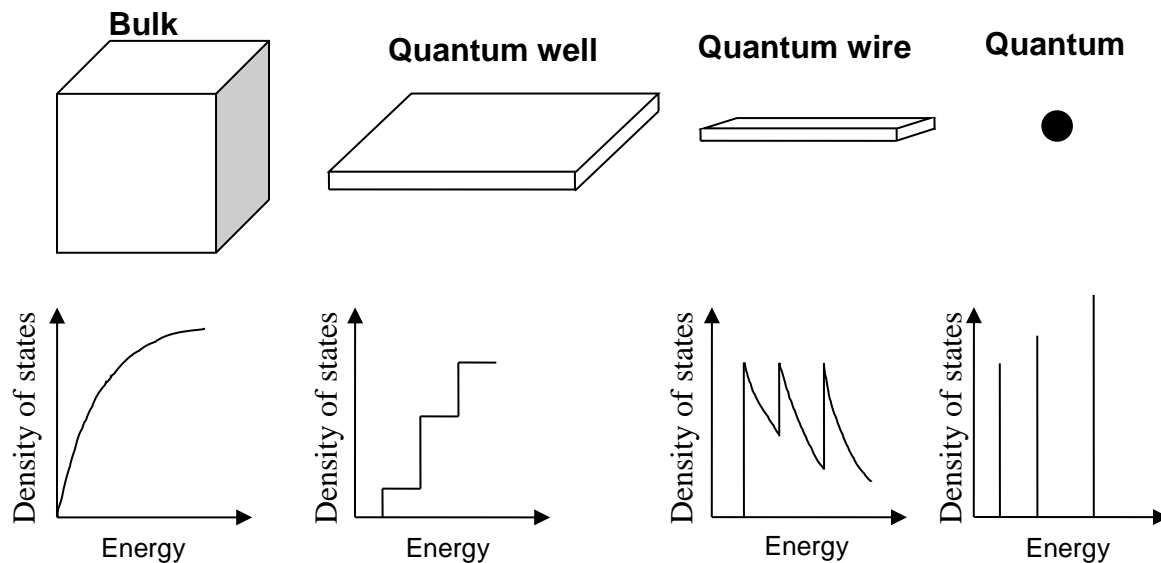


Figure 1.3 Illustrations of the density of states vs. energy for bulk material, quantum well, quantum wire and quantum dot (atom like behavior when the particle size is reduced). (Redrawn from Xu 2005).

1.1.3 Properties of nanomaterials

1.1.3.1 Optical properties

In case of bulk metal a continuous electronic states exist because overlapping of conduction and valance bands. When the particle size is reduced to nanometer range then these two band energy levels are well separated. This changes the light absorption property in the nanomaterials compare to bulk material. As an example, gold is yellow when it is in bulk but changes to red in colour when the size is reduced to around 10nm. The origin for this change in colour is surface plasmon.

This is described as the natural oscillation of the electrons inside in a given nanosphere. The surface plasmon resonance occurs when the frequency of the incident light is close to that of the natural oscillation of the electrons in the conduction band. The frequency of the surface plasmon depends on the shape, size and dielectric function of the material. This surface plasmon resonance can occur in the visible or ultraviolet region. Noble metals like copper, silver and gold have strong plasmon resonance in the visible light region. Whereas, most of the other transition metals show poorly resolved absorption band in the Ultraviolet region (Lavrich et al. 1998; Maier 1987).

1.1.3.2 Mechanical properties

Atomic density of the amorphous surface changes when size of the material approaches to nanoscale. In nanomaterials the crystal interfaces are incoherent, this mis-alignment causes modification of the grain boundary of the atomic structure. Due to these, many mechanical properties such as scratch resistance, fracture toughness and hardness are changed. For example, nanomaterials of titanium carbide and tungsten carbide are erosion-resistant, wear-resistant and harder as compared to the bulk.

1.1.3.3 Catalytic properties

The physical and chemical properties of the nanomaterials depend on the size, shape, surface functionality and composition. The catalytic activity of the metal ion increases orders of magnitude with increasing the surface area. Apart from the surface area, shape of the nanomaterials enables the exposure of specific surface facets that can be more catalytically active or selective for a reaction of interest. The increase in surface area increases the defective coordination environment of the atoms, which increases the adsorption of reactant molecule, and therefore, eventually increases the catalytic activity of the nanomaterials.

1.2 Syntheses of nanomaterials

There are various methods used to prepare the nanomaterials, goal of all these synthetic methods is to exhibit properties that are result of their characteristic length in one, two or three dimensions (~1-100 nm). These methods are categorized broadly into (i) Bottom up and (ii) Top down. Most chemists approach the “Bottom up” synthesis while nano-physicists operate from the “Top down” synthesis route. The general synthesis of metal nanoparticles are given in Figure 1.4.

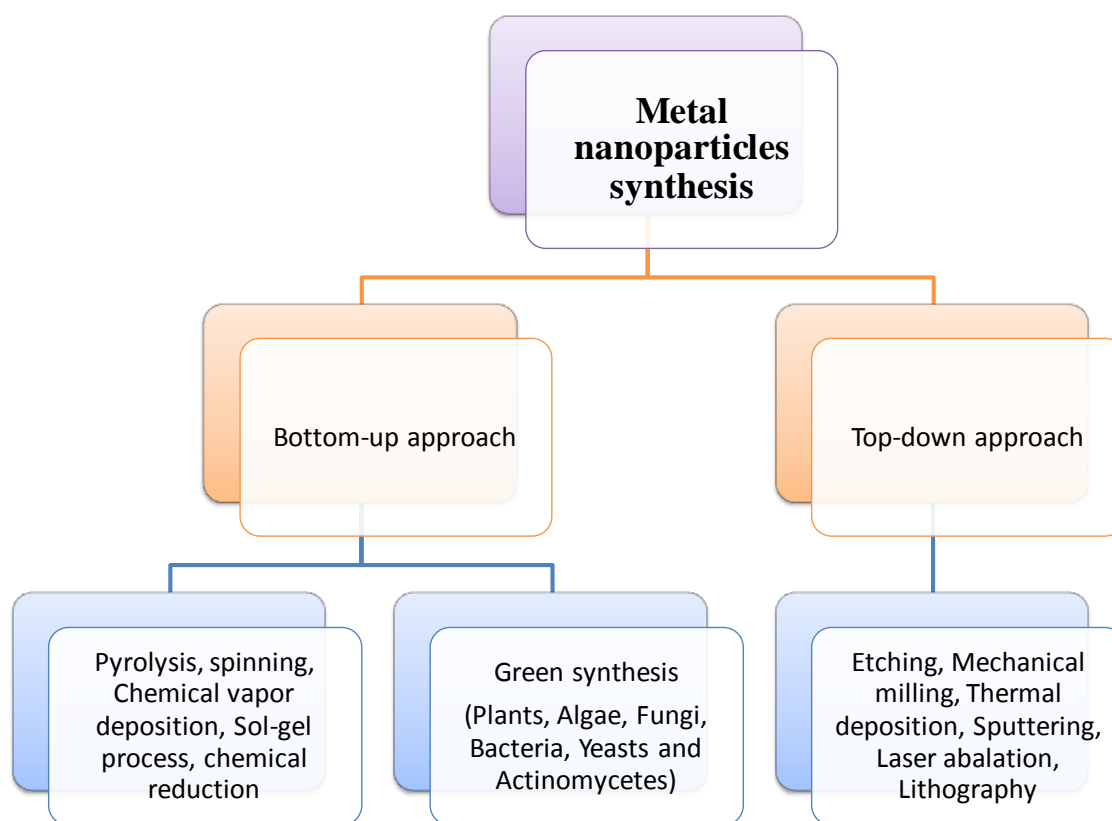


Figure 1.4 The general approaches used for synthesis of the nanoparticles.

1.2.1 Bottom up approach: Mechanism of growth/formation of nanoparticles

This approach involves assembling of atom -by- atom or molecule -by- molecule. The control over the nanoparticle formation depends on nucleation and growth. In nucleation process, the aggregation of atoms takes place. Therefore growth of nuclei results in the formation of larger

particles. The issues in synthesizing the nanoparticles by this approach are control of particle size, shape its composition and control of the interfaces. The nucleation is explained based on the thermodynamic model which describes the appearance of new phase “the nucleus” in the meta-stable primary phase. The most theoretical works on nucleation are based on the classical nucleation theory (CNT) which was developed by Becker and Doring more than 70 years ago. The CNT describes only the nucleation; particle growth is separated as a subsequent process. The further growth of nanoparticles is explained by using processes such as Oswald ripening and diffusion limited growth. In general, the growth of the nanostructures depends on:

- Nucleation kinetics and growth
- Concentration and structure of the stabilizing agent
- Nature of the capping/stabilizing agent
- Temperature and pH of the medium

The nucleation can be either homogeneous or heterogeneous. In homogeneous nucleation, all nuclei are formed simultaneously which results in mono-dispersed particles. While in heterogeneous nucleation poly-dispersed particles are formed.

Mer has proposed a concept called ‘burst nucleation’ which means a large number of nuclei form in a short period of time, and they grow without any further nucleation so that nanoparticles of same sizes are formed (Homogeneous nucleation). If nucleation and growth happen simultaneously, then nanoparticles differ in their sizes (Heterogeneous nucleation). The control over the size distribution of the particles can be achieved by separating of homogeneous to heterogeneous nucleation which is shown in Figure 1.5. In stage I, the monomers concentration increases and reaches critical super saturation (C_s) level, here homogeneous nucleation is possible after certain time but which is “effectively infinite” (Mer 1952). In stage II, burst nucleation

happens due to a rapid self-nucleation. In stage III, the nucleation period ends because the super saturation level lowers below the self-nucleation level. After that, the growth occurs by diffusion of further monomers in solution/matrix toward particle surfaces which can be interpreted as homogeneous nucleation and growth. The expected particle concentration is fast at stage II (the self-nucleation stage) and mostly constant at final growth stage (III).

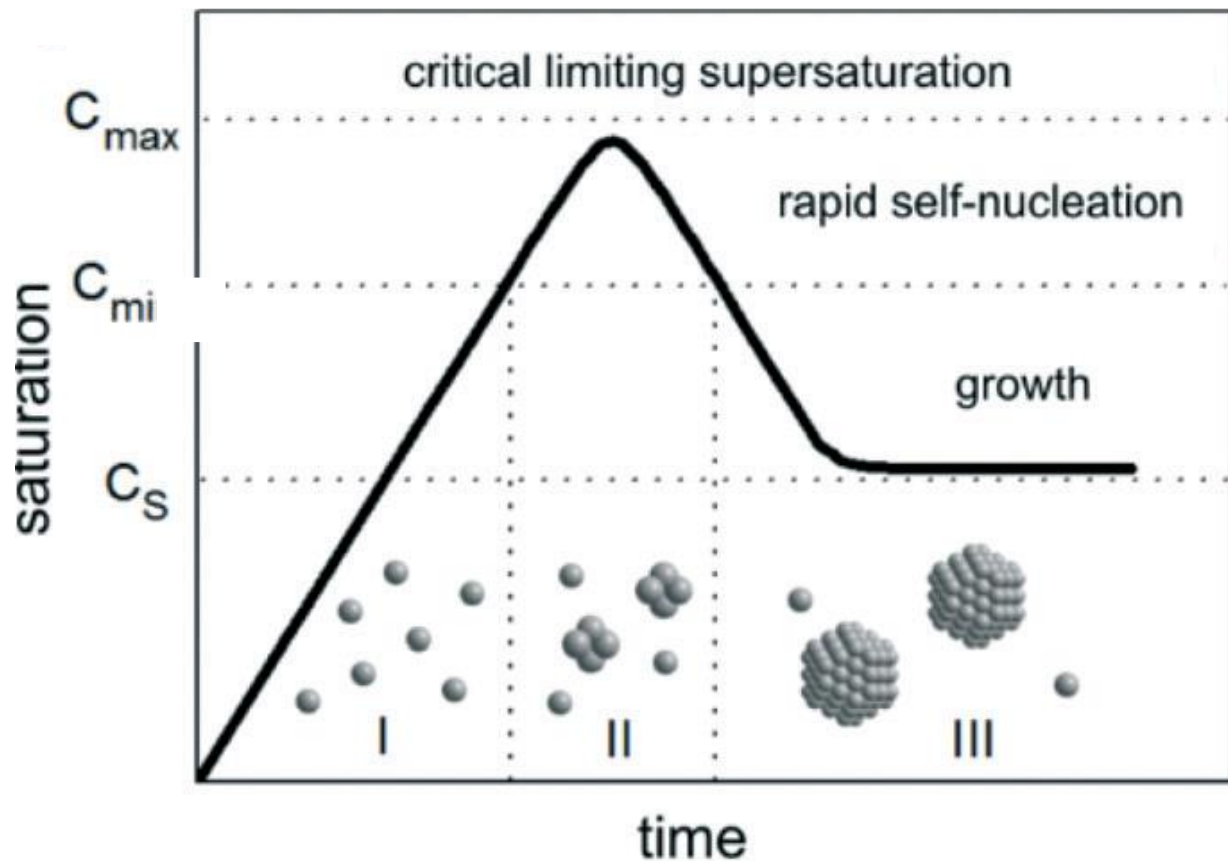


Figure 1.5 The schematic graph represents the principle of NP nucleation due to Mer's mechanism of (sulfur) nucleation derived from CNT (Polte 2015).

The formation of nanoparticles was also explained based on Gibbs free energy. During the formation of new solid phase (nanoparticles) from super saturated solution, the Gibbs free

energy decreases and this change in Gibbs energy depends on the concentration of the solute which is represented as:

$$\Delta G_V = -\frac{kT}{\Omega} \ln(C/C_0)$$

C is the concentration of the solute, C_0 is equilibrium concentration, T is temperature, and Ω is atomic volume. Spontaneous nucleation is favoured when ΔG_V becomes negative and concentration of the solute is higher than equilibrium concentration ($C > C_0$). The amount of decrease in Gibbs free energy is accompanied by increase in surface area of the newly formed particles per unit area (γ). The overall Gibbs free energy change for the formation of spherical particles of radius r from supersaturated solution is:

$$\Delta G = \left(\frac{4}{3}\right) \pi r^3 \Delta G_V + 4\pi r^2 \gamma$$

The two terms in the above equation represent change in volume free energy ($\Delta\mu_v$) and change in surface free energy ($\Delta\mu_s$) respectively. The variation of ΔG as a function of spherical nuclei with radius r (solid line) is shown in Figure 1.6. In the Figure, the surface and volume terms are shown in dashed lines. As long as the solution is super saturated, the term γ is positive and ΔG is negative. The ΔG reaches maximum at a critical radius of r^* which is minimum size at which a nucleus can survive in solution or minimum radius it must possess in order to spontaneously grow from supersaturated solution. If $r < r^*$, the surface term exceeds the volume term then any nucleus smaller than r^* will dissolve into the solution. In other words, the increase in the surface energy due to the nucleus formation is higher than the stabilization due to the formation of a new solid phase from the supersaturated solution, and hence nucleation is not favoured. On the other hand, if $r^* > r$, the contribution from the volume term exceeds the surface term so that the created nuclei is stable and undergoes subsequent growth.

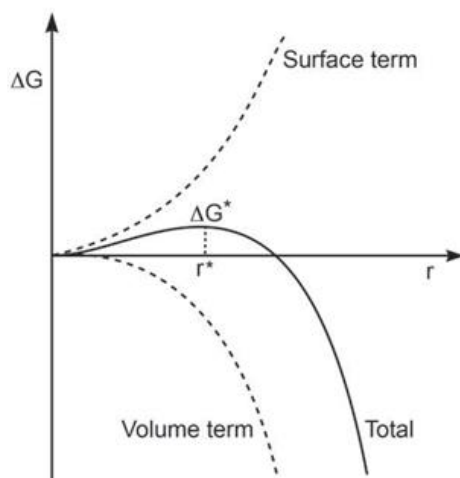


Figure 1.6 Change in the Gibbs free energy as a function of the nucleus radius (r) as a sum of the volume and surface free energies (Camargo et al. 2015).

1.2.1.1 Particle growth by theoretical approach

According to Lamer model the mono-dispersed particles can be synthesized by separating nucleation and growth. Therefore, some theoretical models are required to predict the actual and final particle size distribution. Reiss (Reiss 1951) has developed a model called “growth by diffusion” soon after Mer. According to this, the monomer flux supplied to the particles decides the spherical particles growth rate. If diffusion growth mechanism is only dependent on the monomer fluxes, then the smaller particles will grow predominantly with respect to larger particles leading to a narrow size distribution. This mechanism does not include other effects such as aggregation, coalescence or dissolution (Ostwald ripening). The broadening of particles size distribution by considering nanoparticle dissolution was explained by Sugimoto (Sugimoto 1987) by considering the Gibbs–Thomson equation. There are several approaches that have been used to characterize the particle growth such as single particle growth laws or rate equations and CNT. The limited availability of experimental time resolved *in situ* data for the rates of nanoparticles formation and growth enables to verify theoretical models.

1.2.1.2 Stabilization of nanoparticles / colloidal stability of nanoparticles

The nanoparticles tend to agglomerate due to electrostatic, magnetic and van der Waals forces. These arise because of small size, large surface area and short inter-particle distance. Thus, it is important to study the nanoparticle stabilization in a dispersed medium. These nanoparticles tend to agglomerate in the absence of any counteractive repulsive forces. The electrostatic and steric stabilization provides the repulsive forces to the nanoparticles. Electrostatic stabilized nanoparticles possess at least one electrical double layer due to surface charge, this causes electrostatic repulsion between the particles. If this electrostatic repulsion is sufficiently high, then coagulation between the particles can be prevented. As an example, in the synthesis of gold nanoparticles using sodium citrate, the gold nanoparticles are stabilized by electrical double layer formed by adsorbed citrate and chloride ions from gold precursor and sodium salts.

The two major interaction forces between the nanoparticles are:

- (i) van der Waals force, and (ii) Electrostatic interaction.

Van der Waals interaction

The intermolecular attraction force $W(D)$ between the two molecules of distance r , by Lennard-Jones potential is

$$W(D) = -\frac{C}{r^6} + \frac{B}{r^{12}}$$

The above equation shows that the extent of van der Waals force varies inversely as the sixth power of the distance between the surfaces of two adjacent particles. Constant C is van der Waals

attractive force and B is Born repulsion force, this term can be neglected. Then the van der Waals interaction between two molecules of radius R_1 and R_2 can be simplified as

$$W_a(D) = -\frac{\pi^2 \rho_1 \rho_2}{6} C \left[\frac{2R_1 R_2}{C^2 - (R_1 + R_2)^2} + \frac{2R_1 R_2}{C^2 - (R_1 - R_2)^2} + \ln \left(\frac{C^2 - (R_1 + R_2)^2}{C^2 - (R_1 - R_2)^2} \right) \right]$$

Here ρ is electron density, c is distance between center to center of two particles and D is distance between two particle surfaces ($D = c - (R_1 + R_2)$), for two identical particles $R = R_1 = R_2$ and $D \ll R$ that means particles in close proximity, then the equation is modified as

$$W_a(D) = -\frac{\pi^2 \rho_1 \rho_2 CR}{12D} = -\frac{AR}{12D}$$

A is Hamaker constant, the above equation shows that the surface interaction potential (thus the surface forces) decays less with distance D than the interaction potential between two molecules ($1/D$ compared to $1/r^6$) and that potential is proportional to the particle size ($W_a(D) \sim R$).

Electrostatic interaction

As discussed above, the van der Waals interaction is the attractive force between the molecules which promotes reversible/ irreversible agglomeration of suspended particles. In order to control the size and stability of the nanoparticles, the opposite force to van der Waals interaction is needed. Surface charge on the metal nanoparticles often provides the repulsive inter-particle forces. The surface charges on the nanoparticles are shielded by the solvated ions in the solution. The surface charge decreases within two layers, which is called as electrical double layer (EDL) (according to Stern–Gouy–Chapman theory). This double layer is measured in terms of Debye length λ (κ^{-1}) and by using simple electrostatics it can be quantified. The compact inner layer is called stern layer and the second layer is diffuse layer; see Figure 1.7. The boundary in the diffusion layer is called slipping plane. The interaction between at least two EDLs is important to describe the colloidal

stability. The particles agglomeration is prevented when this repulsive interaction overcomes the van der Waals attractive forces.

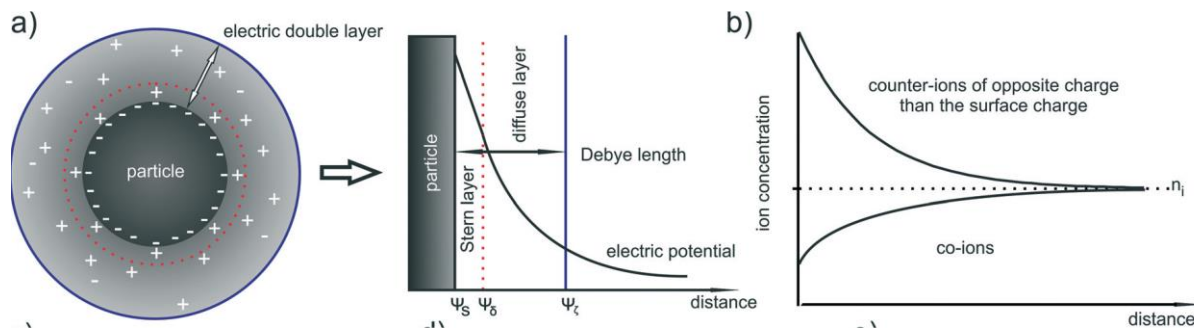


Figure 1.7 The Schematic representation of electric double layer (EDL) formed around a nanoparticle (according to Gouy-Chapman model) which consists of inner Stern layer and the outer diffusive layer, and (b) corresponding decrease of the counter and co-ion concentration with respect to the distance from the particle surface (Polte 2015).

DLVO theory

The DLVO theory (theory is named after the scientists Derjaguin, Landau, Verwey and Overbeek) has been developed to explain colloidal stability more than 70 years ago and is still considered as ground breaking characterization models in the physics and chemistry of colloids (Verwey and Overbeek 1948). According to this theory, the potential interaction between the two particles is the sum of van der Waals (attractive force) and electro static interaction (repulsive) forces.

$$W_{\text{total}}(D) = W_a(D) + W_r(D)$$

With thin EDL and constant surface potential assumption, the above equation says that in a close proximity the particle size is proportional to both attractive and repulsive terms. Therefore, for charge stabilized particles colloidal stability increases because the aggregation barrier increases with increasing size.

Steric stabilization

The stabilization caused by the adsorption of larger molecules like polymers or surfactants on the particle surface is termed as steric stabilization. The polymer/surfactant coating on the particle prevents the aggregation. The density of the adsorbed molecules coating depends on the inter-particle distance. As the inter-particle distance decreases, the adsorbed molecule density between the inter-particle spaces would increase resulting in a decrease in entropy, this is less energetically favourable because of increase in Gibbs free energy. Because of increase in density and higher solubility of the stabilizing molecule counteracts agglomeration (Pomogailo and Kestelman 2006). Hence, interaction potential extended by further term to the DLVO theory describing about steric stabilization (W_{steric}) as:

$$W_{total}(D) = W_a(D) + W_r(D) + W_{steric}$$

The stability of the particles mainly depends on the concentration of the polymer, temperature, average chain length and solubility of the polymer but not on the particle size (Hunter 2001; Napper 1983; Verwey and Overbeek 1948; Simo et al. 2012). As an example, when silver nanoparticles formed by reducing the silver nitrate with sodium borohydride, the negative charge formed on the nanoparticles surface by BH_4^- ions repel each other so that these particles are electrostatically stabilized. When these nanoparticles are capped with cetyltrimethyl ammonium bromide (CTAB), the positive charge on the ammonium in the CTAB molecules react with negative centre on the particle's surface. Therefore, the Ag nanoparticles are stabilized sterically by the long cetyl chains which prevent the particles from getting close in the range of attractive forces; see Figure 1.8.

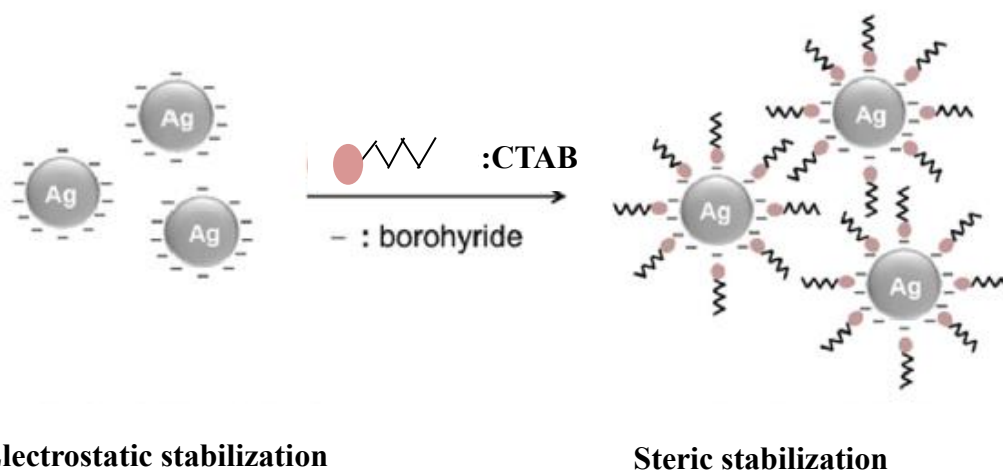


Figure 1.8 Schematic representation of electrostatic and steric stabilization of the Ag nanoparticles (Tüzüner and Demir 2015).

1.2.2 Top down approach

This approach involves in breaking up larger particles into smaller by using of physical processes like crushing, milling or grinding. The major disadvantage using top-down approach is the imperfection of the surface structure. These surface imperfections have a significant impact on the physical properties and surface chemistry of nanomaterials. This technique is similar to the approach used by the semiconductor industry in forming devices out of an electronic substrate (silicon), utilizing pattern formation (such as electron beam lithography) and pattern transfer processes.

1.3 Metal nanoparticles as catalyst

Noble metal nanoparticles are often used as the nanocatalysts (NCs) in organic and inorganic transformations. Decrease in size and increase in surface area of the nanoparticles not only change their physical and electronic properties but also change their chemical behaviour as the catalysts.

In nanoscale region both quantum chemistry and classical laws of physics hold. In catalysis the ability to accept or donate charge plays a key role. The electrons are delocalized extensively and the extent of delocalization varies with the size in nanoscale region. Similarly, the surface energies and surface morphologies are also size dependent. There are always the questions arise how the catalytic activity is related to size of catalyst? how the catalytic activity is maximized, there exist an ideal size? The relationship between size and activity depends on the choice of catalyst and reaction. Based on these relationships, the reactions are divided into three types of reactions: positive size-sensitivity reactions, negative size-sensitivity reactions, and size-insensitive reactions.

In positive size-sensitivity reactions the turnover frequency (TOF) (which is defined as the total number of moles transformed into the desired product by one mole of active site per hour) increases with decrease in a particle size. Methane activation is example for this, in which dissociative bond cleavage is the rate limiting step. In negative size-sensitive reactions, the turnover frequency decreases with the particle size. Example is dissociation of CO and N₂ molecules i.e. in which formation and dissociation of a π -bond is rate limiting step. These require step-edge sites and contact with multiple atoms but, these sites do not always exist in very small nanoparticles. But sometimes, the certain particle sizes geometrically favour the formation of these sorts of sites. In this case, a local maximum in turnover frequency versus particle size exists. In size-insensitive reactions, there is no dependence of turnover frequency on nanoparticle diameter. Example is hydrocarbon hydrogenation on transition metal catalysts. Here, the rate-limiting step is complimentary associative σ -bond formation. In addition to size-sensitivity effects, reactions are structure-sensitive also. Arrangement of atoms on a surface has a significant effect on the catalytic behaviour. Nanoparticles predominantly form (111) oriented surface which is the lowest

energy crystal face. Different shapes of nanoparticles show the different stability, activity and selectivity. In nanomaterials, the under coordinated surface atoms provide an additional freedom to the reactants in catalysis compare to its bulk counterpart. The impact of under-coordination is tremendous because of deviation from bond length, order and angle.

Catalysis is the driving force behind some chemical industries and also is foundation for a large-scale production of the chemical and petroleum industry. In recent years, the significant achievements have been made in the area of metal nanoparticles as heterogeneous catalysts. With the help of molecular orbital (MO) theory, the interaction between an adsorbate and a metal catalyst can be explained. Noble metal nanoparticles show superior catalytic activity because these nanocatalysts are involve in the formation of bonds between reactant molecules and the surface atoms of the nanoparticles, which causes weakening of the bonds in the reacting molecules. This eventually results in the lowering of activation barrier. Electronic structure and the geometry is an important consideration in the metal nanoparticles catalysis. From Bronsted-Evans-Polanyi (BEP) relation, the strong adsorption energies result in the faster reaction rates for first order surface reactions. The BEP relation shows that the strong binding will lead to small energy barriers, and thus the catalytic performance is limited by desorption of the products. However, in the case of weak binding, the reaction rate is limited by the large activation energies as predicted by BEP. Therefore, an optimum binding energy is needed for better performance of a catalyst. The reduction of *p*-nitrophenol (PNP) using mono and bi-metallic nanoparticles has been studied by Pozun et al. 2013. Using BEP relation, they have shown that the rate of PNP reduction can be predicted from the binding energy of adsorption. The PNP reduction in an excess of sodium borohydrate (NaBH_4) follows pseudo-first-order kinetics in the presence of metal nanoparticles catalysts and depends only on the concentration of PNP in solution. Here, the PNP molecule binds

to the metal nanoparticles through two oxygen atoms of the nitro group and creates a pentagonal cyclic intermediate (M-O-N-O-M). Hence, the rate constant for the catalytic reaction can be correlated easily to the initial adsorption of the PNP molecule to the nanoparticles surface. Therefore, the rate of the reaction is controlled by the PNP adsorption onto the metal nanoparticles in the presence of excess of NaBH_4 as reductant.

The Hammer-Nørskov (Hammer and Nørskov 1995) model suggests that the primary controlling factor in chemisorption is d-band of the metal surface. After interaction of the adsorbate with metal d-band, the adsorbate state overlaps with the metal states and is split off into bonding and antibonding interactions. The antibonding states are increasingly populated, as the d-band becomes farther below the Fermi energy and the overall chemisorption strength weakens. Figure 1.9 shows a scatter plot of the d-band centre against the adsorption energy. As can be seen from Figure 1.9, the adsorption strength increases as d-band centre gets closer to Fermi energy. The adsorption energy decreases as we move down the columns of the periodic table. This trend has been observed by Hammer for oxygen adsorption on noble metals. The d-band is nearly filled and many antibonding states are populated for coinage metals. The population of bonding and anti-bonding levels cause repulsive forces which increase with the orbital size down the periodic table. This causes eventually weaker adsorption on to Pd and Pt rather than Cu, despite differences in d-band centres.

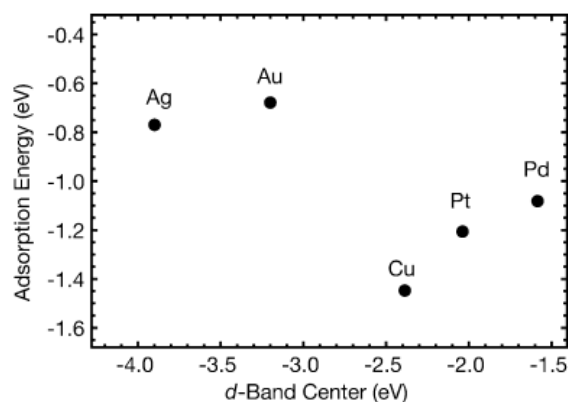
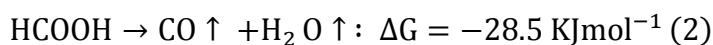
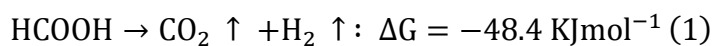


Figure 1.9 A scatter plot of the d-band centre of the metal surface versus the adsorption strength of *p*-nitrophenol (Pozun et al. 2013).

Similarly, the effect of d-band centre of noble metals for the formic acid decomposition has been studied. Formic acid is an *in situ* source of hydrogen which has been studied in the fuel cell applications. Formic acid is non-toxic, offers high energy density (contains 4.4 wt% of hydrogen), safely handled in aqueous solutions, and more importantly it is one of the major products formed during biomass processing. As reported in literature, formic acid decomposes in two path ways on the Pd surface and some of other metal complexes at suitable temperatures (Akiya and Savage 1998; Ruthven and Upadhye 1971; Hill and Winterbottom 1988; Puddephatt and Yap 1998; Coffey 1967; Hyde and Poliakoff 2014; Abdur-Rashid et al. 2002).



From the above equations, dehydrogenation (eq 1) is a promising decomposition process for hydrogen gas production compare to dehydration (eq 2). CO gas produced during dehydration of formic acid contaminates the catalytic surface which leads to reduction in the activity of catalyst. There are two ways reported in the literature to overcome this problem. The first one is by using the core-shell nanoparticles of noble metals. The CO adsorption on metal surfaces follows the

trend: Pd > Cu > Ag > Au (Abild-Pedersen and Andersson 2007). This shows that Ag and Au do not form stable complexes with CO (Judai et al. 2003). When the Pd is alloyed with Cu, Ag, and Au, the resultant core-shell particles inhibit the adsorption of CO on Pd surface (Johanek et al. 2001; Karski et al. 2005). Hence, the occupied active sites are released due to desorption of CO from the Pd surface and consequently reaction (1) is not inhibited. The second one is by basic groups containing platform for hydrogen production, in which a cooperative action between active Pd NPs and weakly basic groups ($-NR_2$) on the supported platform plays an important role in achieving efficient catalytic performance. The basic groups containing matrices eliminate the requirement for the additives to suppress the concomitant CO formation. The decomposition of formic acid on the Pd⁰ surface is shown in Figure 1. 10.

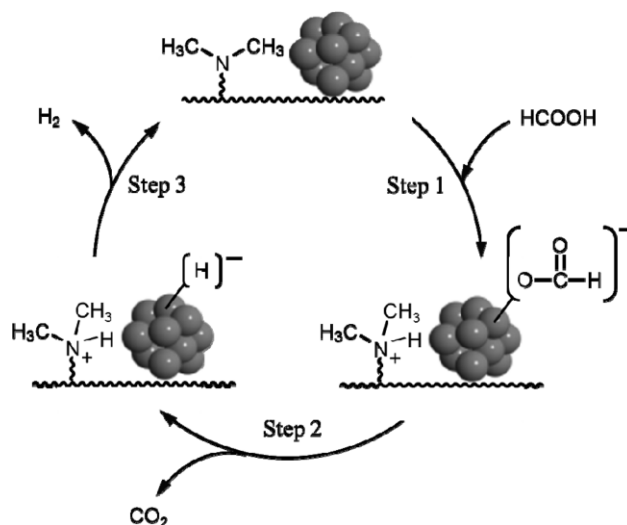


Figure 1.10 The possible reaction pathway of formic acid decomposition by Pd on basic groups containing membrane/resin (Mori et al. 2013).

As shown in Figure 1.10, first $-O-H$ bond cleavage of formic acid is facilitated by the weakly basic group ($-NR_2$). This acts as a proton scavenger and forms a Pd-formate complex/species. The Pd-formate species undergoes β -hydride elimination to produce CO_2 and palladium hydride

species. The reaction of hydride species with $-\text{HN}(\text{R}_2)$ produce molecular hydrogen along with regeneration of the Pd^0 species.

To understand the trends in the reactivity of metal surfaces, Ruban et al. have proposed a model for the chemisorption systems. This model involves the density functional theory (DFT), summarized by the d-band centre model (Ruban et al. 1997). The closer d-band centre is to the Fermi level of a metal, the higher the adsorption energy it exerts on an adsorbate until reaching optimum at Pd. The adsorption trend of formic acid on noble metal follows: $\text{Pd} > \text{Rh} > \text{Pt} \approx \text{Ru} > \text{Au} > \text{Ag}$. Thus, the activity of formic acid decomposition depends on intrinsic electronic properties of the metallic NPs. In Figure 1.11, the decomposition of formic acid versus d-band centre is depicted. Among transition metals, Pd is the most active monometallic element that had been reported in the literature for formic acid decomposition in aqueous phase.

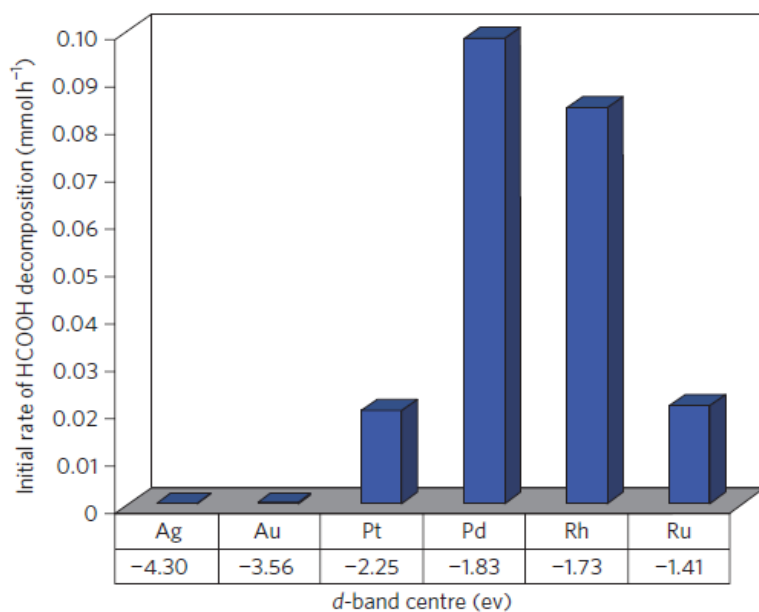


Figure 1.11 Plot of rates of formic acid decomposition versus d-band centre (Tedsree et al. 2011).

1.4 Immobilization of nanocatalyst on solid supports

Among the metal nanocatalysts, noble metal nanoparticle catalysis has emerged as one of the forefront subjects in scientific community due to their spectacular properties such as tuneable surface plasmon and photo-thermal effects, excellent resistant to corrosion and air oxidation, and lesser cytotoxicity as well as their easy experimental realization. These properties make them excellent candidates for the biological, opto-electronic and environmental related applications. However, because of their small size and high surface area, they tend to agglomerate causing the physical instability. Moreover, they are difficult to withdraw from the system because of their size. This problem limits their recyclability and reusability. Therefore, a support matrix is prerequisite to stabilize effectively and prevent the nanocatalysts from agglomeration. In recent years the solid supports such as carbon nanomaterials (Yang et al. 2014, Su et al. 2013), superparamagnetic Fe₃O₄ nanoparticles (Gawande et al. 2013), inorganic particles (silica and titania) (Boudjahem et al. 2010), porous inorganic supports, synthetic/natural polymers (film, membranes, resins and beads) (Mori et al. 2013; Trzeciak et al. 2008) have been examined. Among all these solid supports, nanocatalysts immobilized on the magnetic nanoparticles and polymer films /membranes are easily retrievable from the process in which they act as nanocatalysts.

1.4.1 Synthetic polymer membranes as host matrix

Synthetic polymer membranes have been extensively used as a host matrix for numerous applications as shown in Figure 1.12. These membrane hosts provide an inter phase that separates two phases and controls the transport of various components from one phase into the other in a specific manner. The membrane systems are compact and low energy consuming. A membrane can have defined pores in the range of 1 nm to 1000 nm. Membrane may be liquid or solid and

may consist of organic, inorganic, or metallic materials. It may be neutral or it may carry positive or negative charges, or functional groups having specific binding abilities. The thickness of the membrane can be less than 100 nm or more than several millimetres. Driving forces in membranes processes are gradients in the activity, hydrostatic pressure, electrical potential, and temperature that can lead to a diffusive and/or convective transport of the individual molecules through membrane. Membranes can be porous or homogeneous dense membranes. These dense membranes can be carrying electrical charges or selective functional groups. Structure of the membrane may be isotropic or symmetric, that is the structure is identical over the cross-section of the membrane. Anisotropic or asymmetric, that is the structure varies over the cross section of the membrane.

Membrane supported transition/noble metal nanoparticles have the potential applications in catalysis. Nanocomposites containing metal nanoparticles embedded in the polymer matrix are used in optics, sensors and catalysis applications see Figure 1.12. The control over size and distribution of nanoparticles in the polymer matrix are the main issues in the polymer nanocomposites. The immobilization of nanoparticles in solid and dense matrix may cause a diffusion resistance during the catalytic reaction as reactants need to diffuse to the nanoparticle surface. The diffusion resistance can be minimized by immobilizing the nanoparticles in an open matrix like microfiltration membrane. The porous structure of the membrane is essential for attaining the efficient utilization of available sites and easy accessibility to the nanoparticles embedded at the interior membrane matrix. Nanoparticles immobilized in the membrane have great advantage for the catalytic reactions because diffusion limitation can be minimized under convective flow.

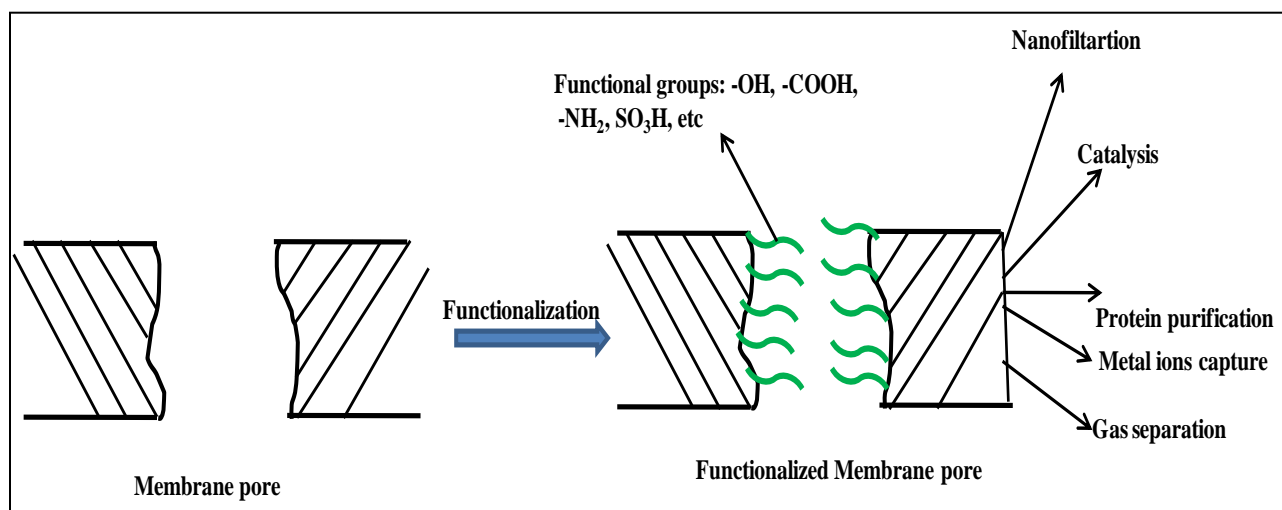


Figure 1.12 Various applications of the functionalized polymer membranes.

1.4.2 Bio-polymers as host matrix

Even though nanocatalyst colloid suspensions are having high catalytic activities, these face serious issues such as irreversible agglomeration and difficulty in product separation and recycling. Therefore, the effective way of maintaining these nanocatalysts is immobilizing them on a solid support. Among many solid supports, biopolymer supports provide a green to the nanoparticles synthesis. Bio-polymers including eggshell membrane, plant tissue, and mushrooms have been used as solid supports. Because eggshell membrane is rich in functional groups like -NH₂, -OH, and -CHO on the surface, it has been explored as a bio-sensing material, high performance electrode material, heavy metal ions adsorber and as a catalyst support material. The eggshell membranes are very good supports for the nanoparticles synthesis because the functional groups on the fiber surfaces act as stabilizing as well as reducing agents, which removes the need of external reducing agent and capping agents for NPs synthesis. As reported in the literature (Nakano et al. 2003; Zheng et al. 2010; Mallampati and Valiyaveetil 2014), the main constituents of chicken eggshell membranes are amino acids (glycine and alanine) and uronic acid. The aldehyde

moiety of uronic acid and saccharides in eggshell play significant role in reducing the surface-adsorbed metal ions to NPs. In addition to the eggshell membrane, the bio polymer chitosan has also been used as a catalyst support. The amine and hydroxyl groups on the chitosan polymer stabilize the nanoparticles formed on it and also prevent them from oxidation (Baig et al. 2014).

1.4.3 Electrospun fibres mat

Nanostructured materials such as nanoparticles, nanotubes, nanofibers (NFs), and nanowires are the most studied nanomaterials (Safari et al. 2014; Khajeh and Dastafkan 2014; Zohoori et al. 2014; Meng et al. 2014; Choi 2014.). Among these materials, NFs are the most efficient and promising nanomaterials due to their distinctive characteristics like flexibility of their surface functionalities and high surface to volume ratio. Therefore, NFs are extensively used as the building blocks of nanodevices, and nanomembranes (Wu et al. 2007; Suren et al. 2014). The NFs have also got applications in the fields of catalysis (Panthi et al. 2013; Chun and Jo 2014; Zhang et al. 2010), antibacterial (Liu et al. 2014), biomedical (Du et al. 2012; Shao et al. 2011), and sensing (Zheng et al. 2014; Yoon et al. 2012) applications. Electrospinning was first reported in 1934 (Anton 1934). Since then it has been widely used technique for making NFs. It is low cost, handy, and high-speed technique to fabricate NFs with diameter ranging from nanometer to micrometer. Different applications of NFs are given in Figure 1.13.

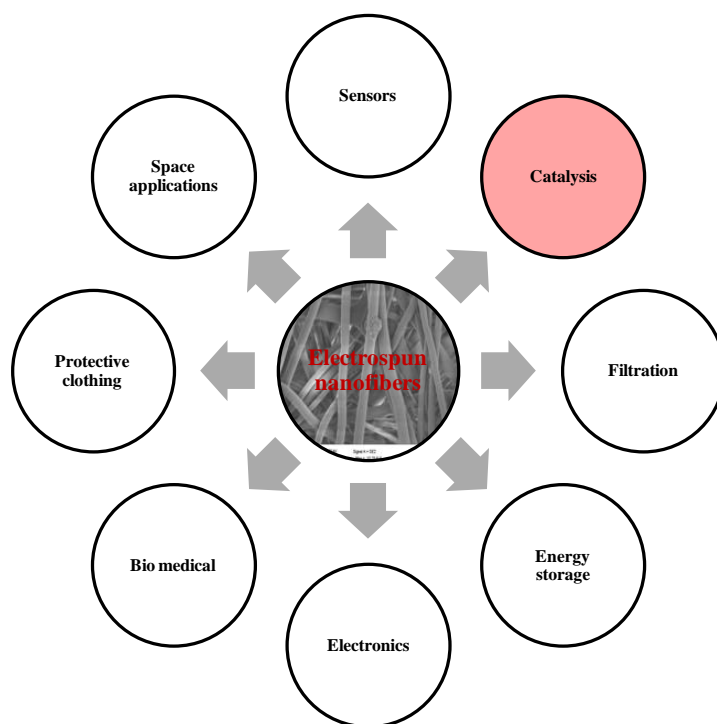


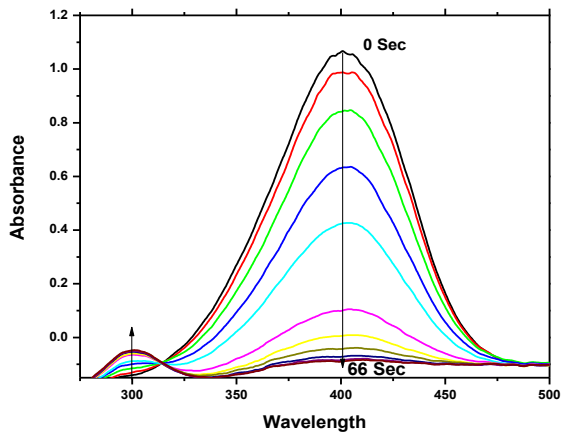
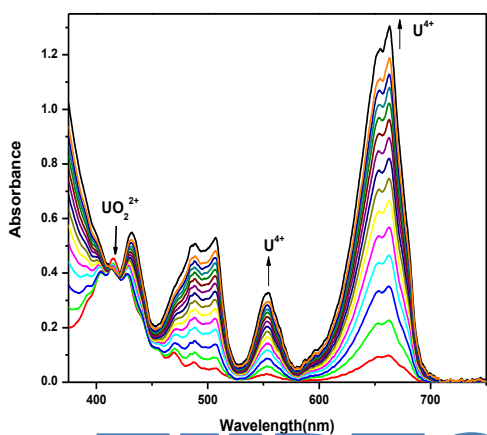
Figure 1.13 Various applications of electrospun fibres.

Synthetic and natural polymers are being used for the fabrication of NFs. Synthetic polymers such as poly(vinyl alcohol) (PVA) (Yang et al. 2007), poly (vinyl acetate) (PVAc) (Park et al. 2008), poly(ethylene glycol) (PEG) (Wang et al. 2012), poly(acrylonitrile) (PAN) (Liao et al. 2011), polyamide (PA) (Im et al. 2008), polyurethane (PU) (Ge et al. 2013), and poly(ether sulfone) (PES) (Tang et al. 2009) and natural polymers like chitosan (Geng et al. 2005), chitin (Noh et al. 2006), collagen (Ding et al. 2003), cellulose (Memarian et al. 2014) etc are the most studied polymers. Catalysis is the most explored application among the various applications of NFs. Encapsulating nanomaterials within the polymeric NFs in the form composite is an effective technique. By synthesizing composite NFs, the aggregation, leaching and size distribution can be controlled. Another way of controlling the size distribution is metallization on the surface of the NFs by introducing functional groups on to NFs.

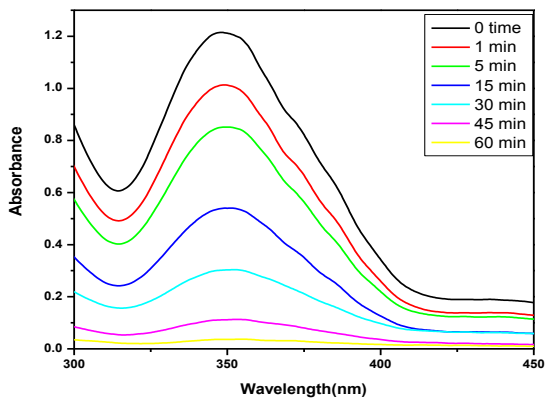
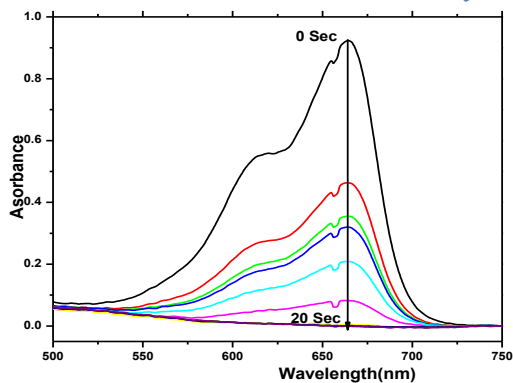
1.5 Scope of the thesis

As discussed above, the noble metal nanoparticles exhibit exceptional catalytic activity originating from their size reduction and shape variation. However, their recyclability and stability are major issues in large scale viable applications. To address these problems, the present thesis is mainly focused on the functionalization of microporous membranes and electrospun microfibers mat by UV-initiator induced grafting/anchoring with subsequent chemical modifications to host the noble metal nanoparticles such as Ag, Au, Pd, Ru and Rh. These noble metals are well known for their catalytic activity in the organic/inorganic transformations. The choice of membrane as host has been based on the egg shell membrane which self-reduces noble metal ions and stabilizes thus formed nanoparticles. The nanoparticles hosted on the egg shell membrane exhibit very high catalytic activity due to its fibrous structure and uncapped nanoparticles. Therefore, the polymer membranes mimicking egg shell membrane in terms of physical and chemical architectures have been synthesized and evaluated for their catalytic activity in the representative inorganic reductions, degradation of organic dyes and Mizoroki-Heck coupling reactions. The reductions of oxyions such as Cr(VI) and U(VI) have been studied not only due to their remediation point of view but also their many technological applications, especially for reduction of U(VI) ions. The functionalized polymeric host materials developed in this work can be divided into three parts i.e. (i) self-reducing membranes/electrospun microfibers, (ii) cation-exchange membranes, and (iii) amine/phosphate-functionalized membranes. The oxy-ions reductions have been carried out by *in situ* hydrogen produced by formic acid decomposition. The decomposition of formic acid in the presence of Pd is being studied extensively for the hydrogen production. Therefore, it is interesting to use formic acid decomposition for the reduction of the oxy-ions.

CHAPTER 2. EXPERIMENTAL



EXPERIMENTAL



2.1 Nanoparticles synthesis

Size and shape of the nanomaterials have a strong influence on their physicochemical properties, which affect the particular applications like catalysis, optical sensing, antibacterial activity, biomedical field, and as molecular markers etc. Therefore, control over morphology, size and distribution of nanoparticles (NPs) is very important. These can be controlled by different synthetic routes, different reducing agents, stabilizers/ligands, and varying experimental conditions. The appropriate advanced techniques would be needed to get the information regarding structural, morphological, optical and chemical properties of these materials. The bottom up chemical approach was adopted in the present work for the synthesis of noble metal nanoparticles in the polymer membranes and on electrospun microfibers mats. In this chapter, therefore, the general introduction related to principle, working, instrumentation and applications of different characterization techniques used in the present work has been discussed. The methodologies adopted for the synthesis of noble metal nanoparticles in the polymer membrane and on electrospun microfibers mats have been described briefly from the experimental point of view. The methods/methodology involved in the studies of the applications of these matrices supported noble metals NPs in the reduction/transformation of organic, inorganic molecules/ions and monitoring the progression of these reductions/transformations etc have also been described in this chapter.

2.1.1 Experimental methods used for syntheses of noble metal NPs

2.1.1.1 *Materials and reagents*

Glycidyl methacrylate (GMA), ethylene glycol dimethacrylate (EGDM), α,α' -dimethoxy- α -phenyl-acetophenone (DMPA), *N*-methyl-*D*-glutamine (NMDG), 2-acrylamido-2-methyl-1-propane sulfonic acid (AMPS), spacer (3-acryloxypropyl)trimethoxysilane (APTMS), Pd/C (10

w/w%), ethylene glycol methacrylate phosphate (EGMP), and polyethylenimine (PEI) (branched polymer, $M_n = 10,000$) were purchased from Sigma-Aldrich. The noble metal salts AgNO_3 , PdCl_2 , RuCl_3 , RhCl_3 and $\text{H}_2\text{PtCl}_6 \cdot x\text{H}_2\text{O}$, Hydrazine hydrate (99%), methanol, dimethyl acetamide (DMAc), formic acid and HNO_3 (69-70%) were obtained from S.D. Fine Chem. Ltd. India and HAuCl_4 from Pravat Chemicals, India. Acetone was procured from Sisco Research laboratories Pvt. Ltd, India. Formic acid (98-100%) was obtained from BDH-Chemicals Ltd, Poole England. PES (granules having 3 mm nominal size) were purchased from Good Fellow Cambridge Ltd. (England). The microporous poly(propylene) (PP) membranes (Accurel^R PP 1E) having 0.1 μm pore-size and 90 μm thickness were obtained from Membrana GmbH, Germany and also poly(propylene) (PP) host membranes having 0.1 μm pore-sizes, thickness 50 μm and nominal porosity 78% was obtained from Sterlitech corporation. The grafting was done in a multilamps photo-reactor obtained from Heber Scientific, Chennai, India (model no. HML-SWMWLW-888). All the reagents used in the present work were A.R. Grade.

2.1.1.2 General procedure for synthesis of pore-filled host membranes

The UV-initiator induced graft/homopolymerization method has been used for developing the polymer grafted/anchored precursor membranes and sheets, followed by chemical modifications to generate required functional groups in the polymeric host materials. Depending upon the functionality required for hosting the noble metal nanoparticles, various functional groups were grafted/anchored in the commercially available poly(propylene) (PP) membranes and on the home-made poly(ether sulfone) (PES) fiber mats as described below:

To synthesize the various functionalized membranes/fiber mats, the commercially available microporous PP sheets and microfibers mats were soaked in methanol for 3h before immersing in the polymerizing solution. To saturate the pores of the host membranes/fibers with polymerizing

solution, the substrates were immersed for overnight under ambient conditions. The excess of polymerizing solution adhering on the surface was removed gently with Teflon rod. Then, the resultant solution filled substrates were sandwiched between two glassware sheets and removed trapped air bubbles in the sheets and substrate (membrane) and exposed to 365 nm UV light in a multi-lamps photo-reactor for a period of optimized 20 min. After exposure in the photo-reactor, the polymeric materials were removed and washed subsequently with the solvent to remove the un-polymerized components.

The photo-reactor consisted of eighteen lamps (8 watt each) arranged in a circular geometry as shown in Figure 2.1. These eighteen lamps were separated into six sets emitting a fixed wavelength (λ) (254, 312 and 365 nm). After sandwiching the polymer membranes in polyester sheets, these were fixed on to a glass plate and followed by UV-irradiation with desirable wavelength in the photo-reactor. The irradiation time was optimized depending on the percentage grafting required, and wavelength of the irradiation was chosen depending on the photo-initiator used in the polymerizing solution. In the present work, 365 nm wavelength was used for all the irradiation experiments. In the presence of UV-light, the initiator forms free radical which initiates the graft/homo-polymerization in the membrane. The mechanism of formation of free radicals produced from the photolysis of the initiator “ α' - α -dimethoxy- α -phenyl acetophenone (DMPA)” in presence of UV-light ($\lambda=365$ nm) is shown in Scheme 2.1, similarly the free radicals production from the poly(ether sulfone) (PES) upon exposure to UV irradiation is given in Scheme 2.2. The general procedure for the synthesis of pore-filled membranes is given in Figure 2.1. and the possibility of synthesizing various types of membranes by changing the monomer concentration, exposure time and the way of exposure of the membrane to UV-light are shown in Figure 2.2,

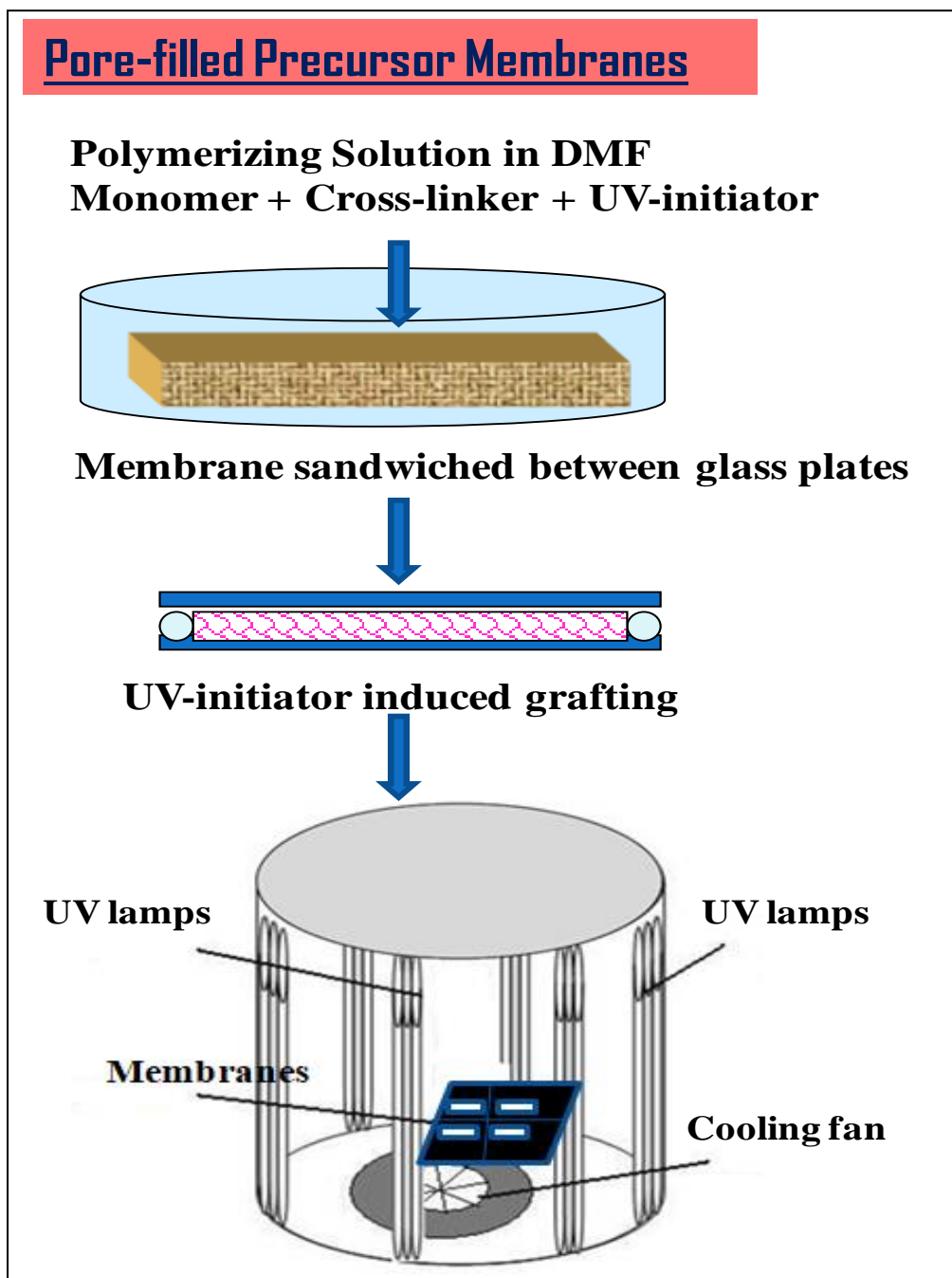
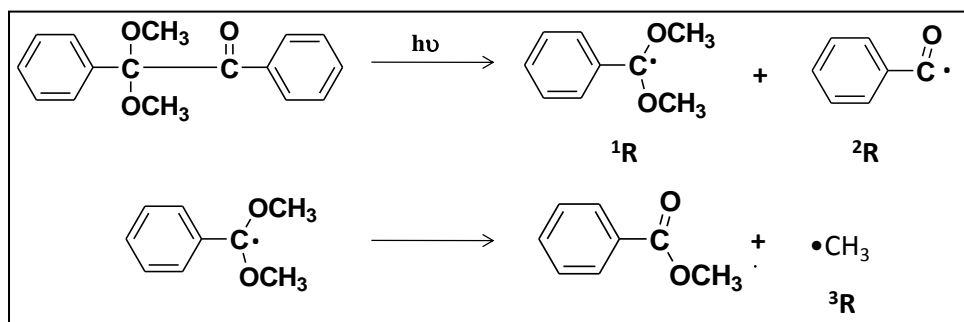


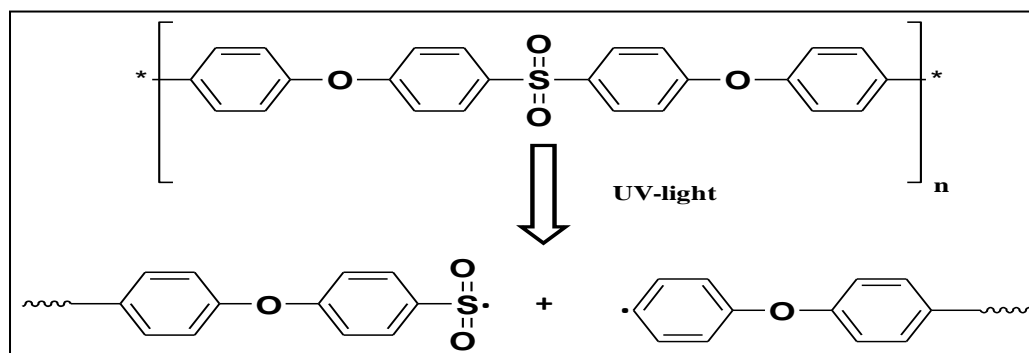
Figure 2.1 Schematic representation of the steps involved in synthesis of pore-filled precursor membranes.

Photolysis of α' - α -dimethoxy- α -phenyl acetophenone (DMPA)



Scheme 2.1 Formation of free radicals (1R , 2R , 3R) from photolysis of α' - α -dimethoxy- α -phenyl acetophenone (DMPA).

Photolysis of Photolysis of poly(ether sulfone) (PES)



Scheme 2.2 Mechanism of formation of free radicals from photolysis of poly (ether sulfone).

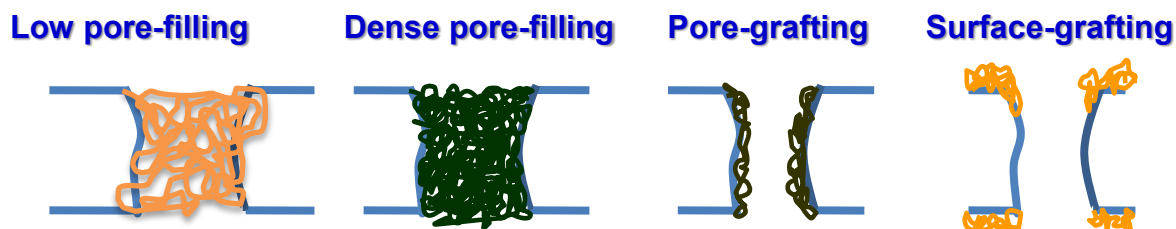


Figure 2.2 The different types of pore-filling membranes prepared by controlling the amount of polymer anchored/grafted on the pore walls of the membrane.

2.1.1.3 Self-reducing membranes as host matrix

The inspiration and motivation of synthesizing noble metal nanoparticles without using any external reducing agents was attributed from the self-reducing biomaterials. Biomaterials like egg shell membranes, sugars, vitamins, and agricultural extracts can be used for the reduction as well as capping of the nanoparticles and these biomaterials are low cost, non-toxic, and may provide control over shape and size distributions of NPs.

In the present work, a synthetic self-reducing polymer membrane was developed by anchoring glycidyl methacrylate along with a cross linker in the pores of a poly(propylene) (PP) membrane by UV-initiator induced polymerization. To this membrane, the self-reducing moieties *N*-methyl-*D*-glucamine (NMDG) /or hydrazine were attached covalently by epoxy ring opening of glycidyl units of grafted/anchored poly(glycidyl methacrylate) (GMA). The NMDG anchored PP membrane was found to reduce and form Ag, Au, Pd, Rh and Ru nanoparticles by simply dipping the membrane samples in the 0.1 mol L⁻¹ solutions of AgNO₃, HAuCl₄, PdCl₂, RhCl₃ and RuCl₃ solutions (Chapter 3). Similarly, the hydrazine anchored membrane was found to form Pd NPs from PdCl₂ salt solution without using any external reducing agent (Chapter 5).

2.1.1.4 Self-reducing PES microfibers mat as host matrix

Porous poly(ether sulfone) (PES) microfibers mat has been prepared by electrospinning technique. This microfibers mat was functionalized with poly(glycidyl methacrylate) (poly(GMA)) by UV-induced graft-polymerization. The reducing moiety hydrazine was anchored via epoxy ring opening of poly(GMA). The grafted poly(GMA) shell around porous microfiber was found to perform the reduction of precursor ions by anchored hydrazine leading to the nucleation and growth of Pd NPs on the host matrix (Chapter 4).

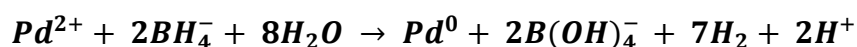
2.1.1.5 Ion-exchange membrane as host matrix

The cation-exchange membrane was prepared on the PP membrane by polymerizing 1:1mol proportions of monomers acrylamido-2-methyl-1-propanesulfonic acid (AMPS) and (3-acryloxypropyl) trimethoxysilane (APTMS) along with cross-linker ethylene glycol dimethacrylate (EGDM) and UV-initiator 2,2'-dimethoxy-2-phenylacetophenone (DMPA) in pores of PP membrane. After anchoring, the membrane was conditioned in 0.1 mol L⁻¹ NaCl solution for 24 h, and then equilibrated with 0.01 mol L⁻¹ PdCl₂ solution to load Pd²⁺ ions by ion-exchange. Then these Pd²⁺ loaded membrane samples were reduced to Pd⁰ by immersing in 10% v/v aqueous hydrazine solution.

2.1.1.6 PEI functionalized membrane as host matrix

The host PP membrane was functionalized with poly(GMA) by UV-initiator induced polymerization of GMA monomer. To this, high molecular weight (M_n=10,000) polyethylenimine (PEI) was attached. The Pd²⁺ ions were loaded in to this PEI functionalized membrane followed by reducing with 0.05 mol L⁻¹ sodium borohydride (NaBH₄). The loading capacity towards Pd⁰ of these membranes were varied by varying the amount of PEI and was estimated using ICP-AES.

Similarly, another type of phosphate functionalized membrane was prepared by anchoring the monomer ethylene glycol methacrylate phosphate (EGMP) in the host PP membrane using similar methodology. The Pd²⁺ ions were loaded on to this membrane followed by reducing with 0.05 mol L⁻¹ sodium borohydride (NaBH₄). The equation involving formation Pd NPs from borohydride reduction is given below. The loading capacity towards Pd⁰ of this membrane was estimated using ICP-AES. (Chapter 6)



2.2 Analytical techniques for characterization of nanoparticles

Surface and cross-sections of the nanoparticles containing host membranes were characterized using the JSM-7600F field emission scanning electron microscopy (FE-SEM). Energy dispersive spectrometer (EDS) (equipped with FE-SEM) was also used to obtain information about elemental distributions across the host matrix. Inductively coupled plasma atomic emission spectroscopy (ICP-AES) analysis was done using high resolution simultaneous atomic emission spectrometer (Spectro Arcos, Germany) coupled with ICP. DC arc as the excitation source and charge coupled device (CCD) as the detector were used to quantify the amount of nanoparticles formed on the host matrices. Radiotracer technique was used to determine the ion-exchange capacity. To monitor the catalytic redox reactions, UV-Visible spectrometer (USB4000-UV-VIS-ES, Ocean Optics) was used. These experimental methods/techniques, instrumentations and principles involved are discussed below.

2.2.1 Electron microscopy

Unlike optical microscope in which visible light (400-700nm) is used as light source, the electron microscope uses a beam of accelerated electrons as a source in electron microscopy. Much lower de Broglie wavelength of electrons makes electron microscope possible to get a spatial resolution thousand times better than light microscope. Electron microscope has resolution of the order of a few angstroms whereas, optical microscope is limited to about 200nm. The difference in the resolution is mainly due to light diffraction limit. The optical resolution can be estimated as $\lambda/2NA$ (λ = wavelength) (NA is the numerical aperture of a lens. For an average white light wavelength of 500nm, the best resolution is of few hundred nm. Thus decreasing the wavelength is only the way to get better resolution. The wavelength of electron beam produced from a 20kV electron gun is 0.06nm corresponds to resolution limit of $\lambda/2=0.3 \text{ \AA}$ (theoretically). The comparisons of

schematic of optical/light microscope (LM), scanning electron microscope (SEM) along with transmission electron microscope (TEM) are shown in Figure 2.3.

In electron microscopy, electrons are generated by thermionic emission i.e. electrons are generated by heating of a tungsten filament by means of current and temperature for about 2800°C. In FE-SEM, there is no heating involved but so called “cold” source is used. For cold source, an extremely thin and sharp tungsten filament is used as electron source which functions as a cathode in front of primary and secondary anode. The voltage between cathode and anode is kept in the order of 0.5 to 30kV so that the electron beam produced in FE source is about 1000 times smaller than the standard electron microscopes. If the vacuum is maintained stable, the filament tip last theoretically for a life-time comparable to conventional tungsten filament. Two types of electron microscopes are commonly used to probe the objects in nanoscale. They are (i) scanning electron microscopes (SEM), and (ii) Transmission electron microscope (TEM).

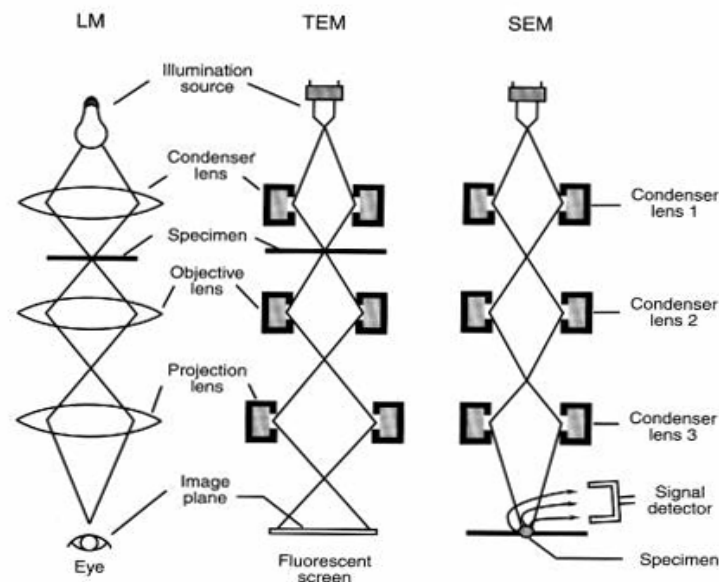


Figure 2.3 Schematic comparison of optical/light microscope (LM), transmission electron microscope (TEM) and scanning electron microscope (SEM).

2.2.1.1 Field-emission scanning electron microscopy (FE-SEM)

In field-emission microscope electrons are used as light source and these electrons are produced by field emission source. This technique is used to visualise very small topographic details on the surface of an object. The electron beam diameter produced by FE source is about 1000 times smaller compared to thermionic source used in SEM. To resolve a feature on the specimen surface, the beam diameter must be smaller than the feature. The electron beam can lose energy after interaction with matter. This loss of energy converts into many forms such as heat, emission of low energy secondary electrons, high energy back scattered electrons, and X-rays emission, and all of this carry information about surface structure of the object. There is no true image exists in this kind of microscopes rather synthesized electronically.

The samples have to be prepared for SEM in such a way that it should withstand high vacuum conditions and high energy beam of electrons. Nonconductive samples such as polymers are made conductive because these specimens collect charge when scanned by an electron beam, resulting to faults and other image artefacts. To minimize accumulation of electric charge, these specimens are made conductive and electrically grounded. This is done by coating the samples by an extremely thin layer (0.5-3nm) of gold or gold-palladium. Polymers, ceramics and crystals are usually less problematic and retain their structures under SEM conditions as compared to biological materials that require the pre-fixation. A typical FE-SEM image of porous poly(propylene) membrane which was used in the present work is shown in Figure 2.4.

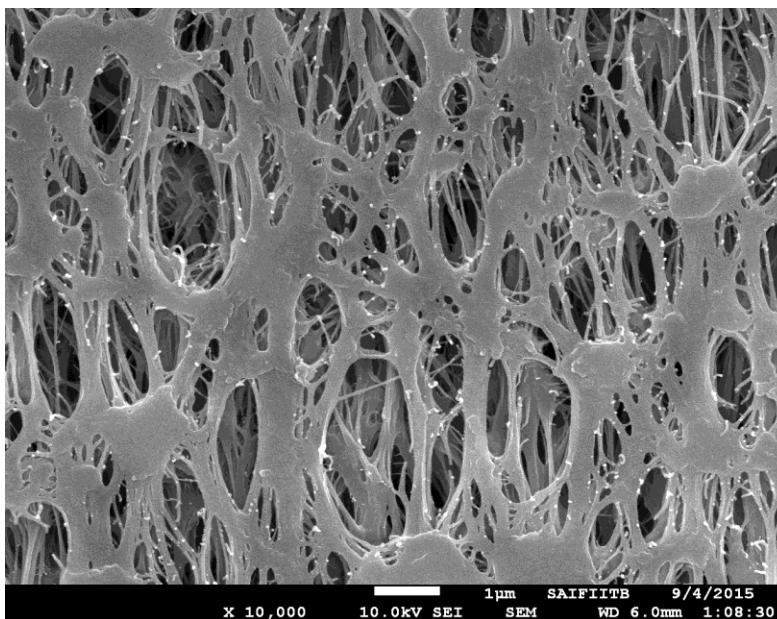


Figure 2.4 A representative FE-SEM image of poly(propylene) membrane.

2.2.2 Inductively coupled plasma-atomic emission spectroscopy (ICP-AES)

Atomic emission spectroscopy coupled with ICP is used to determine the metal ions concentration in solution phase. In this the liquid sample is introduced into the system via a nebulizer. The injected liquid was made into plasma by torch, in which the temperature ranges from 6000 to 10000K. Argon gas was used as a carrier. The plasma is created when argon atoms are ionized with a Tesla coil, while the RF induction coil produces a magnetic field. The atoms in the sample are excited when the torch breaks up the molecules and ionizes them. When the ions are de-excited, the photons of characteristic wavelength are emitted. The intensity of this emitted light is proportional to the concentration of the elements in the sample. Diffraction grating is used to separate the emitted light spectrum into individual wavelengths. The schematic representation of the ICP-AES instrument was shown in Figure 2.5.

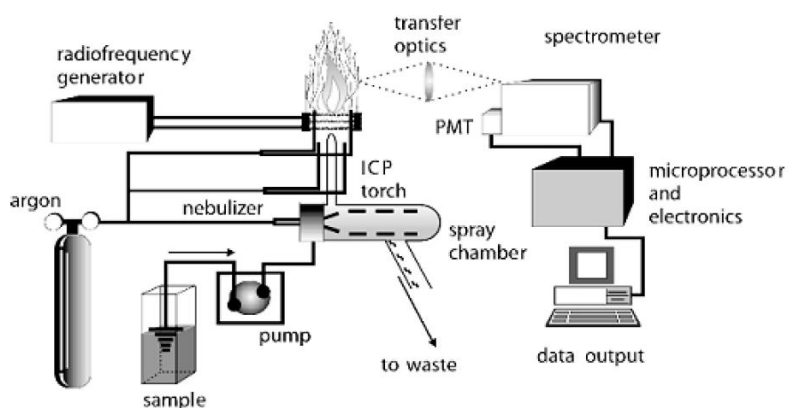


Figure 2.5 The schematic representation of ICP-AES instrument.

2.2.3 Ultraviolet-Visible spectroscopy

This spectroscopic technique studies interaction of electromagnetic radiation with matter. Ultraviolet-visible spectroscopy refers to absorption or reflectance in the ultraviolet-visible region. When the energy from ultraviolet or visible light was absorbed by a molecule, one of its electrons jumps from a lower energy to higher energy molecular orbital. This absorption of light utilized for transfer of electron from the ground state to the excited state is measured by using this technique (shown in Figure 2.6). This analytical technique is complimentary to the fluorescence spectroscopy. In fluorescence spectroscopy the electronic transitions from excited states to the ground states were measured.

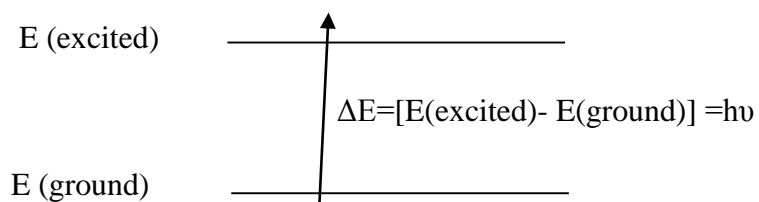


Figure 2.6 The excitation process.

In most of the molecules, the lowest energy occupied molecular orbitals are the σ orbitals (corresponds to σ bonds). The higher energy molecular orbitals than σ orbitals are π orbitals above these the unshared pairs or nonbonding orbitals (n). The unoccupied or antibonding orbitals (π^* and σ^*) are the orbitals of having highest energy. Figure 2.7 gives the possible electronic transitions and energy levels in a molecule.

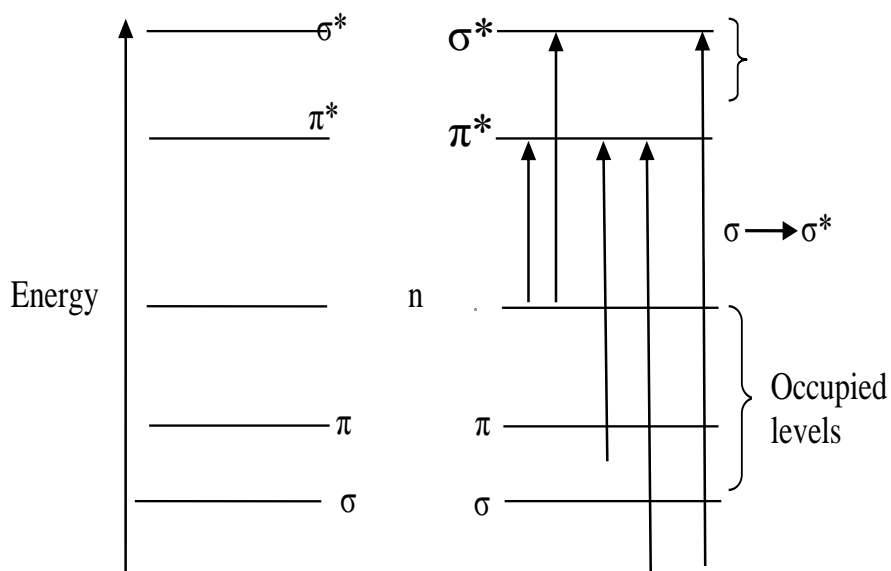


Figure 2.7 Electronic energy level and transitions.

The probable electron transfer in most of the molecules is from highest occupied molecular orbital (HOMO) to the lowest unoccupied molecular orbital (LUMO). Clearly, the energy required for the transfer of electron from HOMO to LUMO is less than the energy required to that required from a lower occupied energy level. However, not all the transitions are observed in a molecule as these transitions follow some selection rules. If transition involves a change in the spin quantum number of an electron, this transition is not allowed and termed as “spin-forbidden” transitions. The forbidden transitions are not often observed, but these transitions are observed in certain cases

though the intensity of the absorption is normally much lower than the allowed transitions. The $n \rightarrow \pi^*$ transition is the most common type of forbidden transition.

An atom having absorption in the UV-Vis region gives the absorption spectrum consisting of very sharp lines. In case of molecules, the UV-Vis absorption spectra appear as bands due to the fact that electronic transition is accompanied by rotational and vibrational transitions (shown in Figure 2.8.). Therefore, the electronic transition consists of a vast number of closely spaced lines and the spectrometer cannot resolve them. Hence, the observed spectrum is envelope over the entire pattern. The wavelength at which maximum absorption occurs is called λ_{max} and the intensity of absorption is determined by molar extinction co-efficient which is property of absorbing molecule.

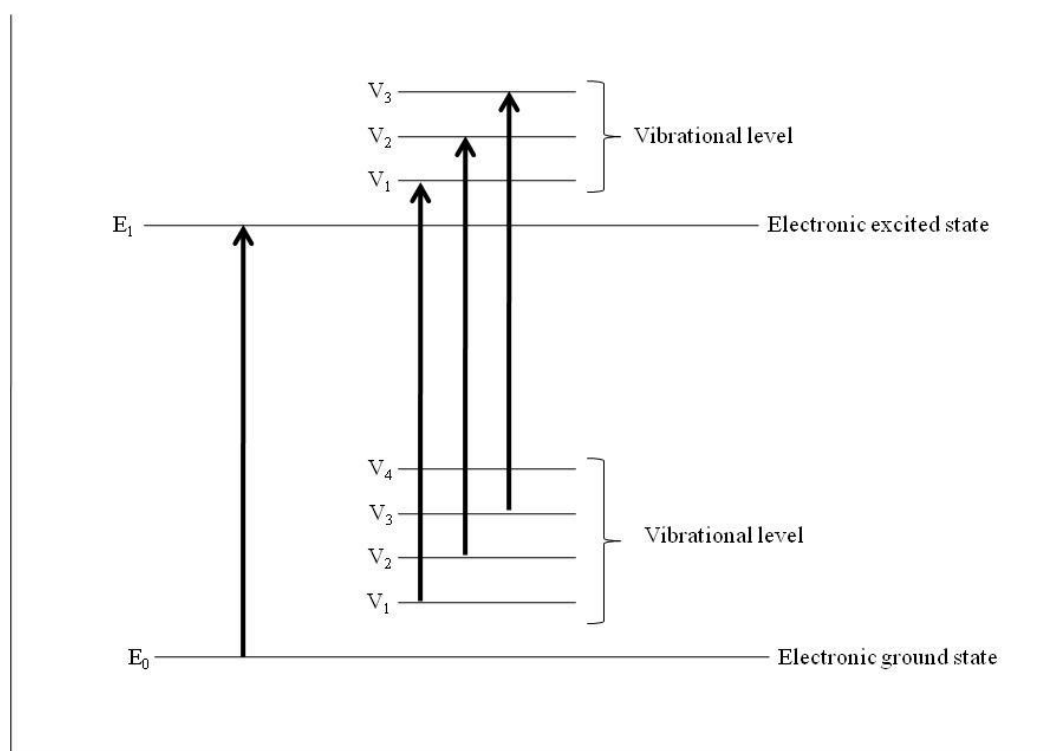


Figure 2.8 Electronic transitions with vibrational transitions superimposed. (Rotational levels, which are very closely spaced within the vibrational levels, are omitted for clarity.)

Principles and instrumentation of absorption spectroscopy

Greater extent of light absorption is observed if a greater number of molecules are capable of absorbing light of a given wavelength. The absorption phenomenon follows Beer-Lambert law. According to Beer's law the absorption is proportional to the concentration of the absorbing molecules. According to Lambert's law, the fraction of radiation absorbed is independent of the intensity of the incident radiation. The empirical expression of the Beer-Lambert law formulated as (eq 1)

$$A = \log_{10} \left(\frac{I_0}{I} \right) \epsilon c l \quad (1)$$

A = Absorbance

I_0 = Intensity of the incident light

I = Intensity of the transmitted light

ϵ = molar absorptivity ($\text{mol}^{-1} \text{dm}^3 \text{cm}^{-1}$)

c = molar concentration of solute (mol dm^{-3})

l = length of sample cell (cm)

The term $\log(I_0/I)$ is known as absorbance (or the optical density). The molar absorptivity (or molar extinction coefficient) is a property of the molecule undergoing electronic transition. The molar absorptivity ranges from 0 to 10^6 . Values above 10^4 are termed as high-intensity absorptions, while values below 10^3 are low-intensity absorptions. Forbidden transitions have absorptivities in the range from 0 to 1000. Beer-Lambert law is obeyed when a single species gives rise to the observed absorption. However, Beer-Lambert law is not obeyed when different forms of the absorbing molecule are in equilibrium, solute and solvent form complexes through some sort of association, thermal equilibrium exists between ground and low-lying excited electronic states or when fluorescent compounds or compounds changed by irradiation of light are present.

There are three general arrangements in single beam UV-Visible spectroscopy instrument (Figure 2.9). First, the incident beam passes through the monochromator/grating which segregates the wavelengths. Then, the desegregated light goes through the sample and finally photo-detector and amplifier. In single beam geometry, the reference spectrum is measured first, and then the sample spectrum corrected by reference spectrum.

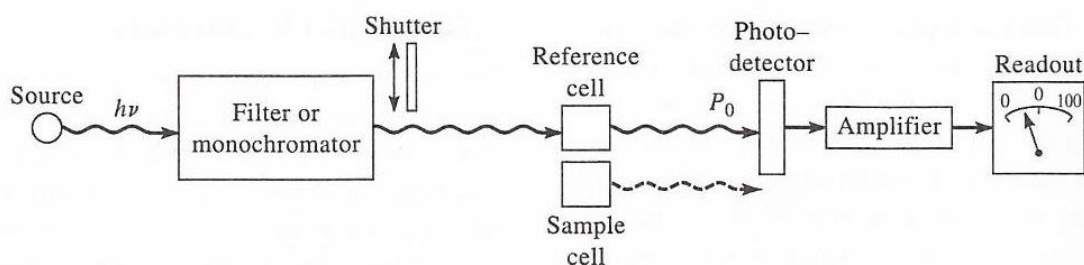


Figure 2.9 Schematic representation of a typical UV-Visible spectrophotometer.

2.2.4 X-ray diffraction (XRD)

XRD is a non-destructive technique. This is used to identify the crystalline phase, orientation, lattice parameter, phase composition, strain, grain size, atomic arrangement, space group symmetry, translational symmetry etc of an unknown sample. In this, a collimated beam of X-rays interacts with the crystal and the angles at which the beam is diffracted are measured. Each diffracted X-ray signal corresponds to a coherent reflection, which is known as Bragg reflection, from successive planes of the crystal. The Bragg's law is defined as (eq 2):

$$2d \sin \theta = n\lambda \quad (2)$$

Samples are scanned through a range of 2θ angles. For a powdered material, all diffraction directions are possible due to random orientations. These diffraction peaks give d-spacing which allows identification of sample by comparing with standard reference pattern because each has unique set of d-spacing. A perfect crystal would extend in all directions to infinity but no crystal

is perfect because of its finite size. Broadening in the diffraction peaks was observed because of deviation from the perfect crystallinity. This broadening occurs from several sources like, finite crystalline size, strain, extended defects and instrumental effects. However, this type of broadening is negligible above 100-500 nm size of the crystal. XRD measures crystallite size which may not be same as particle size. Techniques like dynamic light scattering, electron microscopy and atomic force microscopy measures the particle size rather than crystallite size.

The XRD instrument consists of three basic elements: an x-ray tube, sample holder, and an X-ray detector (Shown in Figure 2.10). When high energy electrons dislodge inner shell electrons of the target material, the characteristic X-ray spectra is produced. This spectrum consists of several lines but the most common are K_{α} and K_{β} . The specific wavelengths are characteristic of the target material. Copper is the most common used material for single crystal diffraction technique which has K_{α} radiation of 1.5418\AA . During interaction with the sample, when these X-rays satisfy the Bragg equation, constructive interference occurs and peak in intensity is observed. A detector records, processes and converts the signal to count rate.

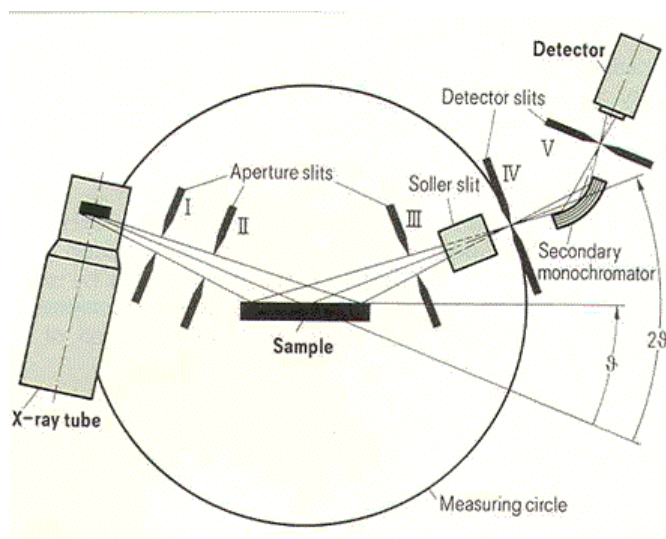


Figure 2.10 A typical XRD instrumental setup.

2.2.5 Energy dispersive X-ray fluorescence (EDXRF)

EDXRF is similar as EDS or EDAX. Only difference is electrons beam causes excitation instead of X-rays beam. This spectroscopic technique uses fluorescence to obtain elemental composition of the material. It is based on the principle of measurement of the energies or wavelengths of the X-ray spectral lines emitted from the sample, which are the characteristic or signature of the elements present in the sample. H.G.J. Mosley in 1913 discovered the relationship of photon energy and element, and laid down the basis of XRF. The characteristic X-rays are independent of chemical state of the element, because X-ray spectra originate from the inner orbitals. Therefore, Mosley deduced a relation which states the reciprocal of wavelength ($1/\lambda$) or frequencies (ν) of characteristic X-rays are proportional to the atomic number (Z) of the element emitting the characteristic X-rays. The sample interacts with the primary X-rays (from source) causing emissions of the secondary X-ray spectral lines having their characteristic energies or wavelength. The intensities of these emitted characteristic X-rays are proportional to the corresponding elemental concentrations. Unlike WDXRF (Wavelength Dispersive X-Ray Fluorescence), the fluorescent photons from the sample are not dispersed spatially prior to detection. These are detected by multi-channel analyser which acts as the energy dispersive device, though no real dispersion takes place. The detector receives the un-dispersed beam of different energies on the basis of their average pulse heights. EDXRF consists of three basic units. Excitation source (X-ray tube), sample holder, and semiconductor detector Si (Li). The optimum target thickness, current, and voltage are needed to get the best data from EDXRF system.

In addition to this, a primary beam filters (Table 2.1) the secondary targets are also equally important to get the best results. Because, the primary excitation source leads to both continuum and characteristic peaks fall on the sample. The beam filters are thin metal foil placed between

source and sample. These primary filters eliminate the scattered background and these are used based on the fact that an element absorbs wavelength shorter than its absorption edge. As primary X-ray source gives broad spectrum of bremsstrahlung along with characteristic line of the target material and to eliminate this background and bremsstrahlung radiation, a secondary target is used where the primary beam is allowed to strike it. EDXRF directly measures energies of X-rays using semiconductor detector and multichannel analyser (MCA) with no physical discrimination of the secondary radiation that leaves the sample and enters the detector.

Table 2.1 The primary beam filters used in EDXRF.

Primary beam filter element	Suitable for analysis of elements
Fe	Ni, Cu, Zn, Ga, Ge, As, Pb
Cu	Ge, Ar, Se, Pd
Ti	Cr, Mn, Fe, Co, Ni, Cu, Zn
Mo	Pb, Ag, In, Cd

2.2.6 Nuclear magnetic resonance spectroscopy (NMR)

NMR spectroscopy is a supplementary technique to IR spectroscopy. IR spectroscopy gives information about functional groups of a compound while NMR gives the exact nature of the proton, carbon and its environment. This spectroscopy is based on the measurement of absorption of electromagnetic radiation in the radio-frequency region of roughly 4 to 900 MHz. Nuclei of atoms rather than outer electrons are involved in the absorption process. It is necessary to place

the analyte in an intense magnetic field to induce nuclei for developing the energy states required for absorption to occur.

NMR is a non-destructive technique and it needs less than one milligram of the sample to get the spectral information. Proton NMR technique is mostly used to characterize the organic compounds. It gives information about different kinds of environments of the hydrogen atoms in the molecule and also gives information about number of protons of each type and the ratio of different types of protons in the molecule. The nuclei behave like a tiny magnet. The spinning nucleus of a hydrogen atom (^1H or proton) is the simplest and is commonly encountered in the organic compounds. The hydrogen nucleus has a magnetic moment, $\mu = 1/2$. Hence, in an applied external magnetic field, its magnetic moment may have two possible orientations. One is in alignment with the external magnetic field called as α -spin state which is more stable (lower energy) and the other is in opposite alignment called β -spin state, the difference in energy (ΔE) between the two states is equal to $h\nu$ ($\Delta E = h\nu$) as shown in Figure 2.11(a) and (b). In NMR spectroscopy, the radiation frequency is kept constant, and the strength of magnetic field is varied. At some value of the field strength, the energy required for flipping the proton matches with the energy of the radiation. In this condition, absorption of radiation occurs and a signal is obtained. Such a spectrum is called a nuclear magnetic resonance (NMR) spectrum. Tetramethylsilane (TMS) is generally employed as internal standard for measuring the position of ^1H , ^{13}C , and ^{29}Si in the NMR spectrum because it gives a signal sharp peak, is chemically inert and miscible with a large range of solvents.

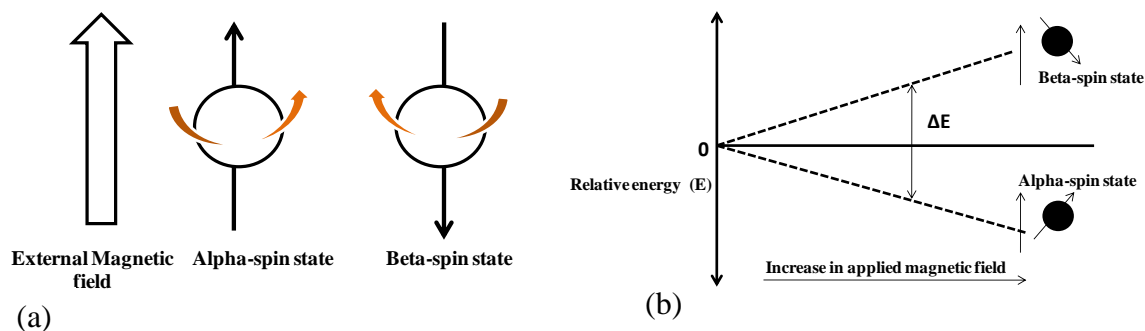


Figure 2.11 The direction of magnetic moment due to spinning of proton (a) and the difference in energy of the two spin states (b).

2.2.7 X-ray photoelectron spectroscopy (XPS)

XPS is a surface sensitive technique, which measures the elemental composition up to parts per thousand. This is also known as electron spectroscopy of chemical analysis (ESCA). This technique was developed in the 1960s by the Swedish Kai Siegbahn for which he received the Nobel Prize in 1981. XPS provides the information about the chemical composition, chemical structure, electronic and valance state of the atoms in the material. Except hydrogen and helium, it detects almost all the elements in the periodic table. XPS is a non-destructive technique, which is routinely used to analyze organic material, bio-material, metal/metal oxide nanomaterial, polymers, glasses, ceramics, paints, bones, viscous oils and many others materials.

Principle

The XPS spectra are obtained by irradiating the sample with beam of X-rays and measuring the number of electrons that escape from the surface thickness about 0 to 10 nm of the materials and their kinetic energies. The Mg K_{α} and Al K_{α} X-rays are generally used because of their limiting penetrating power in a solid. XPS requires high vacuum (10^{-8} milli bar) conditions. The energy of the ejected electrons without energy loss was measured in the range of 20 to 2000 eV. The

interaction between X-rays and surface atom is explained on the basis of photoelectric effect. Thus, kinetic energy (KE) of the escaped electron can be obtained from the below equation (eq 3).

$$BE = h\nu - KE - \phi_s \quad (3)$$

Where, $h\nu$ is the energy of the incident photon, BE is the binding energy of the orbital from which the electron originates and ϕ_s is the work function of spectrometer. From above equation, all three quantities are measurable by XPS. Therefore, information about elements can be obtained by the binding energy of the electron.

In practice, the measurements of binding/kinetic energy is done by the control electronics or data system accompanying with the spectrometer, and the analyst only choose the range of binding energy whichever is considered the more possible. The determined binding energy is used to produce the XPS spectrum which is a plot of number of electrons captured (intensity) vs. their binding energy. The chemical environment of the elements results in shifting of the binding energy of core level electron, which is known as chemical shift. This shift is generally observed in the order of 1-10 eV.

Instrumentation

The main components in XPS instrument are source of X-rays, an ultra-high vacuum chamber with pumps, an electron collection lens and an electron energy analyzer in addition to the vacuum chamber, sample mounts and a data collection system. The Figure 2.12 represents the main components of an XPS system.

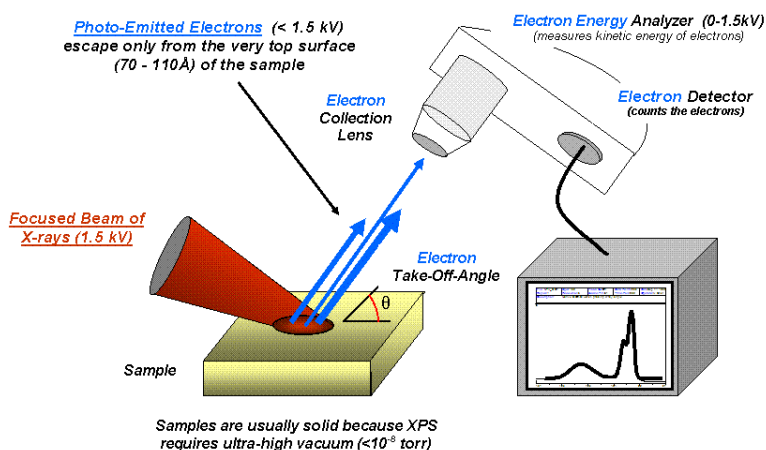


Figure 2.12 The schematic diagram of XPS.

In the present work, XPS measurements were carried out using $\text{Mg-K}\alpha$ (1253.6 eV) source and DESA-150 electron analyser (Staib Instruments, Germany). A typical XPS survey analysis spectra taken for Pd NPs immobilized on to the PEI functionalized PP host membrane is given in Figure 2.13. The survey spectrum is the starting point in XPS analysis as it gives information about all the elements present on the sample surface.

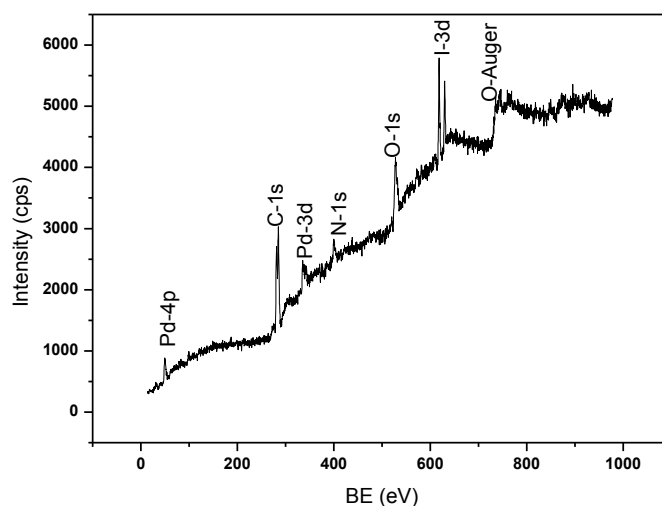


Figure 2.13 A representative survey spectrum of Pd NPs embedded in PEI functionalized PP host membrane.

2.2.8 Small angle X-ray scattering (SAXS)

Small angle X-ray scattering (SAXS) is non-destructive and provides information about size and shape of nanostructured materials (particles, fractals, etc.), pore sizes, distance between scatters in partially ordered materials etc. by measuring elastically scattered X-rays ($\lambda = 0.1\text{-}0.2\text{ nm}$) at very small angles (typically $0.1\text{-}10^0$) (Glatter and Kratky 1982; Porod 1982; Guinier et al. 1955). It can be broadly used for the characterization of metals, polymers, oil, plastics, cements, proteins, food and pharmaceuticals in fundamental research as well as in quality control. This experiment can be performed using a laboratory X-ray source or synchrotron light source.

Principle of SAXS

When a collimated beam of monochromatic radiation is incident on an object, part of it undergoes elastic scattering, which changes the direction of incident radiation. This scattering intensity is a function of scattering angle (2θ) or a scattering vector (q). The difference between the incident (K_i) and scattered (K_s) wave vector is called scattering vector. K_i and K_s are proportional to the linear momentum of the scattered and incident photon respectively ($p = hK$). The scattering vector $p = K_s - K_i$ denotes the momentum transfer vector. The schematic representation of SAXS experimental setup is shown in Figure 2.14. the scattering vector described as $q = |q| = 4\pi \sin(\theta)/\lambda$, 2θ is scattering angle.

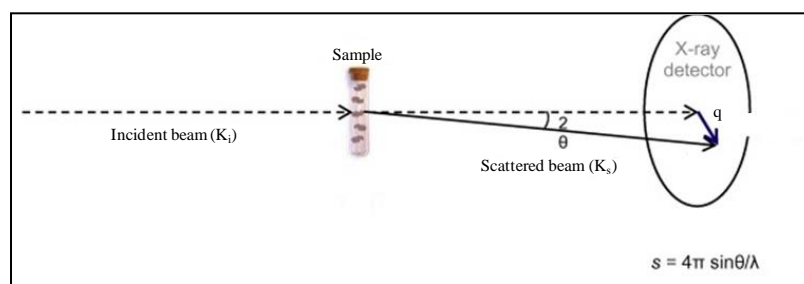


Figure 2.14 Schematic representation of the experimental setup for a SAXS experiment and representation of the scattering vector (q) on the detector surface (Kikhney and Svergun 2015).

A typical laboratory based SAXS experimental setup consists of X-ray source, monochromator, collimator, and detector. Since 2θ is small, a large sample to detector distance is maintained to improve angular resolution. In SAXS, the non-scattered beam that merely travels through the sample must be blocked without obstructing the closely adjacent scattered radiation. This problem can be overcome by making beam parallel by a multilayer parabolic mirror in conjunction with slit collimation.

2.2.9 Capillary flow porometry (CFP)

Capillary flow porometer measures the most constricted part of through pores. In this the the pressure necessary to blow the gas through a liquid filled porous membrane was measured. As the applied gas pressure increases, at certain point the pressure overcomes the surface tension of the liquid and pushes the liquid out of the pore. Based on this, the pressure can be correlated with the pore diameter of the membrane using Washburn equation. The schematic representation of this method is shown in Figure 2.15.

$$\Delta P = 4\gamma \cos \theta / D \quad (4)$$

ΔP = applied pressure

D = diameter of the most constricted part of pore

γ = air-liquid interface surface tension

θ = wetting angle with solid matrix of the membrane

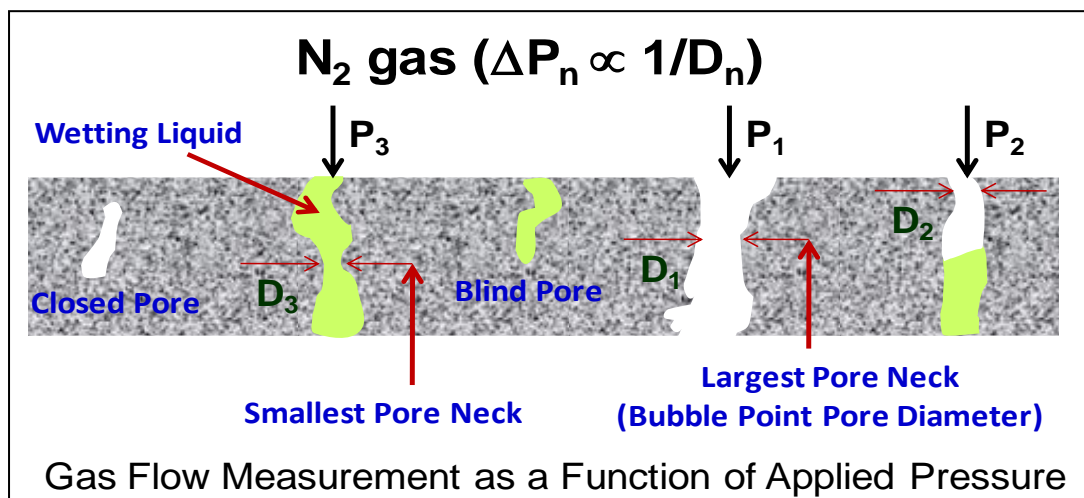


Figure 2.15 The schematic representation of principles of CFP of a membrane.

For membrane-based catalysis, the information regarding pore diameter distribution in a membrane is necessary. To get the information on characteristics of pores in a membrane, the methods such as microscopy, Brunauer-Emmentt-Teller (BET) gas adsorption method, bubble pressure method (capillary flow porometry, liquid extrusion porosimetry, mercury intrusion porosimetry), permeation methods (Gas/liquid flux variation with pressure) are used generally. If the membrane pores are cylindrical and straight, then the microscopic methods such as scanning electron microscopy (SEM), atomic force microscopy (AFM) are useful. However, the surface views of the pores are not useful if the membrane pores are not perfectly cylindrical or well defined. In BET surface area measurement, the nitrogen adsorption-desorption detects very small pores, but it cannot distinguish dead-end pores. In mercury intrusion porosimetry, mercury is used as a non-wetting liquid but mercury in the pores may distort the soft matrix. The molecular weight cut-off method depends on solute type (proteins, polyethylene glycols, polystyrenes, dextrans etc.) and test conditions like pressure, temperature, concentration, feed velocity, pH etc. In addition to these, the concentration polarization makes the data obtained by this technique difficult to interpret and compare. Capillary flow porometer (CFP) has several advantages compare to other techniques

as CFP is a non-destructive technique, easy to handle and, capable of providing pore diameter distribution in a single operation.

The porometer model POROLUX™1000 was used for the measurements. The standard operating pressure range is 0-35 bar with flow rates up to 200 L per minute for this instrument, and sample holder diameter was 25mm. The data acquisition and analysis was carried out using LabView software which was supplied by the manufacturer. The wetting liquid used for the CFP measurements was “porefil” liquid of $\gamma = 0.016 \text{ Nm}^{-1}$ supplied by Benelux scientific, Belgium. The membrane sample was wetted in pore-filled liquid for 1h at room temperature and then mounted on the sample holder after wiping out the excess liquid on the surface of the membrane. To determine the pore size (diameter) distribution by CFP, the plots of N_2 gas flow rates as a function of applied pressure across the membrane with wetting liquid “Porefil” (wet run) and without wetting liquid (dry run) were analysed. The curves of flow rates as a function of applied pressure are shown in Figure 2.16. The portion of the wet run from a point where first flow of gas was observed up to a point where it meets the dry run plot was used for determining the pore-neck diameter distribution. By using the Washburn equation, the applied pressure was converted to diameter using the experimentally measured surface tension of pore-filled liquid. The maximum and minimum pore-diameters were determined by bubble point (pressure at which the first flow of gas across wet membrane was observed) and from the pressure where wet and dry runs converged, respectively. Mean flow pore diameter was calculated from the pressure at which wet flow is half of dry flow (see Figure. 2.16). The measurements of mean flow pore-neck diameters by CFP were found to be reproducible within 7-5% as obtained in the triplicate measurements. The measured ratio (f) of flow rates through wet (F_w) and dry sample (F_d) can be used for obtaining the flow-based pore-neck diameter distribution $f_F(D)$ as given in eq 5.

$$\phi = \frac{F_w}{F_d} = \int_{D_{\min}}^{\infty} f_F(D) dD \quad (5)$$

D_{\min} is a diameter of the smallest constriction of pores that has been opened by maximum applied pressure. $f_F(D)$ has the property that it integrates to 1.0, and its unit is inverse of distance (m^{-1}).

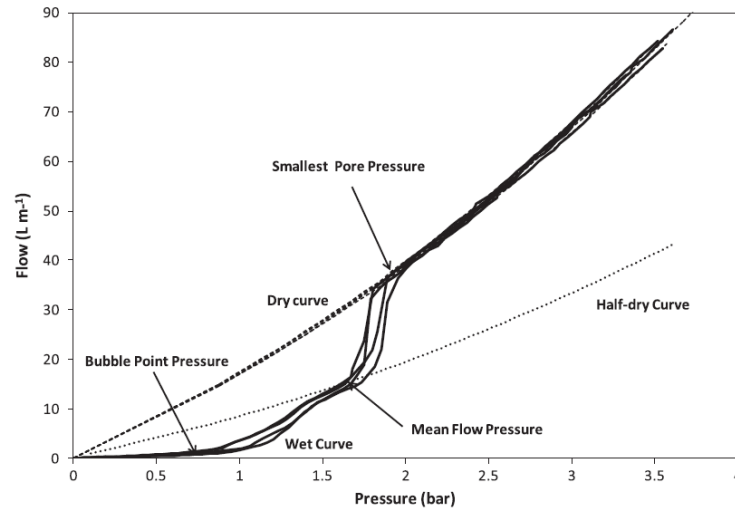


Figure 2.16 The plots showing flow rates as a function of applied pressure across dry and wet poly(propylene) membrane.

The measurements by CFP are not expected to be affected either by tortuosity (ratio of pore length to thickness) or thickness of the membrane. However, the membrane requires longer time period for achieving constant gas flow rates with increasing tortuosity or thickness. The porometer used in the present work was designed to record stabilized flow rates at every increment of applied pressure.

2.2.10 Electrospinning technique

Electrospinning is an electrostatic fabrication technique. Because of its versatility and potential applications in diverse fields, electrospinning has been given more attention in recent years. Some of the most important applications include the preparation of NFS mat for filtration, nanocatalysis,

wound dressing, biosensors, tissue engineering, drug delivery, defence and security, and environmental engineering applications etc. The nano/micro fibers are generated by the application of strong electric field on polymer solution or polymer melt. The fibers produced by this technique have high surface to volume ratio, tuneable porosity, and properties the polymer composition can be manipulated to get desired functionality and. This technique shares characteristics of both electro spraying and conventional solution dry spinning of fibers.

Process

Electrospinning technique uses electrostatic force to produce fine fibers using polymers solution or melt. A DC voltage used in this technique range from kV to several tens of kV. When a sufficiently high voltage is applied to a liquid droplet, the body of liquid droplet becomes charged and electrostatic repulsion counteracts the surface tension and the droplet is stretched. At a certain point, the liquid droplet erupts from the surface and reaches the collector (grounded collector usually a metal screen, plate, or a rotating cylinder). The point of eruption is known as Taylor cone. When a charged liquid jet was ejected from tip of the Taylor cone, an unstable and rapid whipping of the jet occurs in the space between the capillary tip and the collector. This leads to evaporation of solvent and leaving the polymer behind. The uniform and nano/micro meter scale diameter fibers are formed because of bending instability of polymer jet.

Apparatus

Electrospinning experiment was carried out at room temperature and at normal atmospheric conditions. A typical electrospinning system consists of three major components: a high voltage power supply, a spinneret (e.g, syringe needle tip), and a grounded collector. The experimental setup is shown in Figure 2.17 and a SEM image of typical poly (ether sulfone) fiber mat produced using electrospinning is given in Figure 2.18.

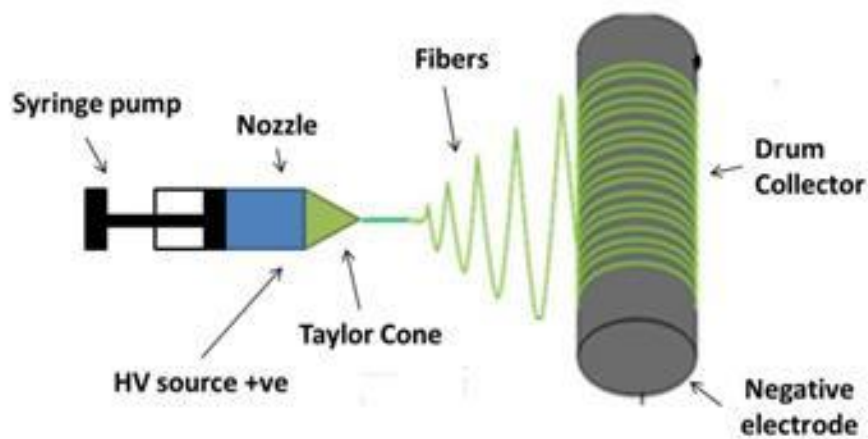


Figure 2.17 A schematic representing the electrospinning apparatus.

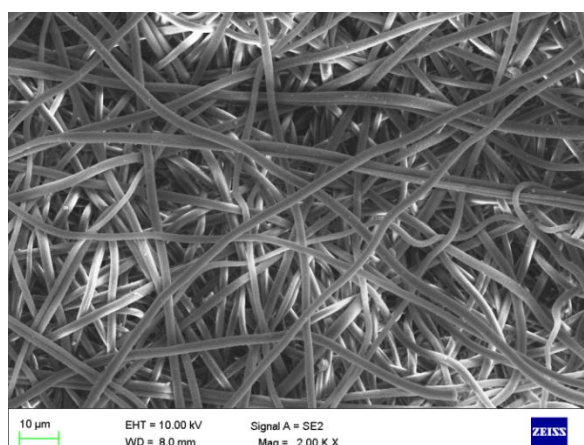


Figure 2.18 A typical electrospun fiber mat produced by electrospinning technique.

2.3 Application of nanoparticles for catalysis

It is well known that catalytic activities of metal nanoparticles (MNPs) are dependent not only on the size but also on the shape and surface of the nanoparticle as well. To evaluate the catalytic activity and efficiency of MNPs, it is very important to find/choose a model reaction. The chosen model reaction should have a universal appeal and studied with certainty using simple experimental setup. The preferred model reaction should proceed only in the presence of catalyst

and is easy to monitor. In the present work, the reductions of *p*-nitrophenol and methylene blue were studied as the model reactions. The prepared catalysts have also been explored for the reductions of U(VI) to U(IV) and Cr(VI) to Cr(III). The catalytic conversions of these reactions were monitored by UV-Vis spectroscopy.

2.3.1 Reduction of *p*-nitrophenol (PNP)

The aqueous phase reduction of *p*-nitrophenol by sodium borohydride to *p*-aminophenol (PAP) has been widely studied in different laboratories. Any metal nanoparticles can be used as a catalyst for this reaction. The pioneering work carried out by Pradhan et al. 2002 and Esumi et al. 2002, has made this reaction as a benchmark for studying the activity of metal nanoparticles. The PNP reduction involves six electron transfer process (this is facilitated by the metal NPs) in the presence of sodium borohydride (NaBH₄) and produce only *p*-aminophenol (PAP) without any side product. PNP has absorption at 317nm which shifts to 400 nm when the solution is made alkaline, while the product PAP shows a weak absorption peak at 300 nm. Thus, the PNP reduction can be easily monitored by UV-Vis spectroscopy. A pseudo first order reaction is assumed to follow in the presence of excess of reducing agent (borohydride) (Ghosh et al . 2004; Hayakawa et al. 2003). It was also observed that, the reduction doesn't proceed in the absence of a catalyst (Shine and Mallory 1962). The reduction is not only a model reaction to evaluate the catalyst but also helps in easy depletion of hazardous nitro phenol from environment. The reduced product PAP and its derivatives have got applications in pharmaceuticals, herbicides, polymers etc. Figure 2.19 gives reduction reaction scheme of PNP to PAP, the mechanism is shown in Figure 2.20 and the spectral changes involved in the reduction are shown in Figure 2.21.

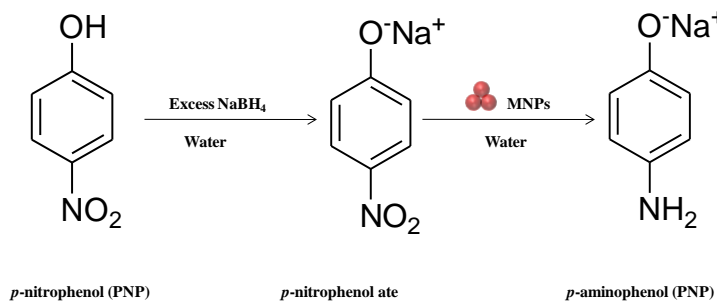
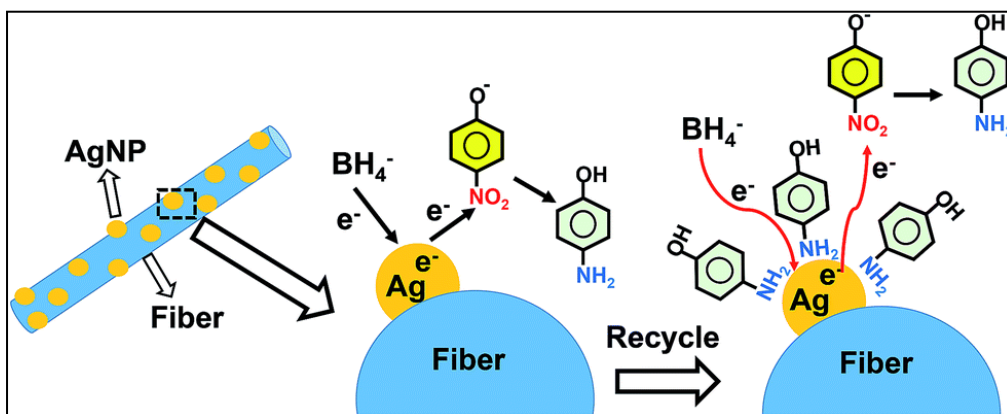
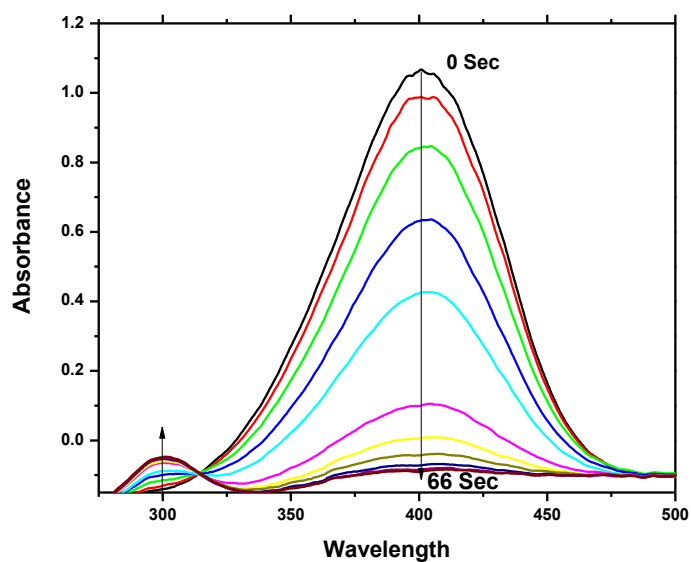
Figure 2.19 Reduction scheme of *p*-nitrophenol to *p*-aminophenol.

Figure 2.20 The mechanism involved in PNP reduction with borohydride in presence of Ag NPs (Baruah 2016).

Figure 2.21 The UV-Vis spectra of *p*-nitrophenol to *p*-aminophenol conversion.

2.3.2 Reduction of methylene blue (MB)

Methylene blue is one of the most studied model reaction after PNP to test the catalytic activity of metal nanoparticles. MB is a pollutant produced from textile, paper, food and pharmaceutical industries. These kinds of synthetic dyes are harmful to the human health as well as to the environment. To test the catalytic activity of the Ag NPs formed on the polymer membrane substrates, the reduction of MB was used as a model reaction in the presence of excess NaBH_4 . MB exists in two different forms (given in Figure 2.22), the oxidised form of MB is blue in colour and the reduced form is colourless. As shown in Figure 2.23, the absorption peak intensity of methylene blue at 665 nm decreases with time due to reduction.

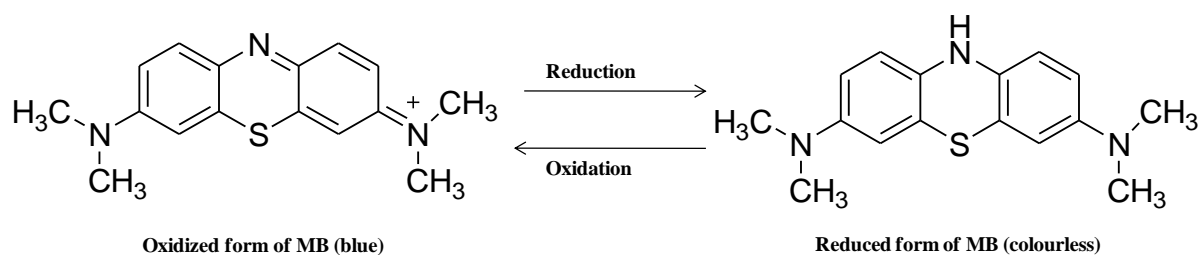


Figure 2.22 Chemical structure of methylene blue in its oxidized and reduced forms.

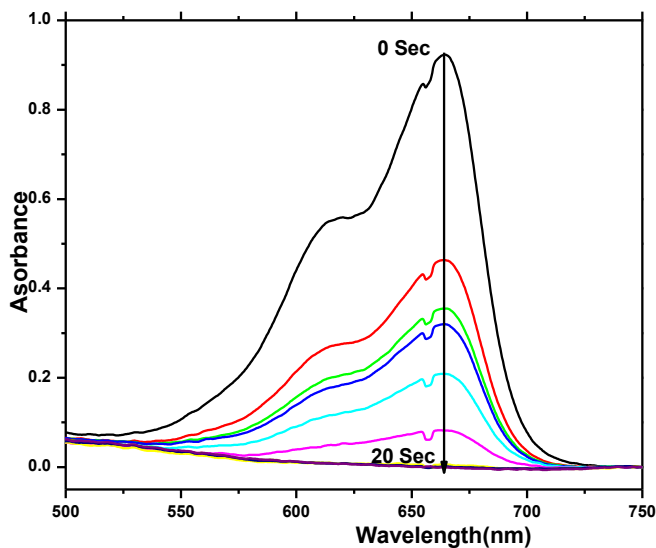


Figure 2.23 The UV-Vis spectra of methylene blue degradation.

2.3.3 Hexavalent chromium reduction

Heavy metals are harmful to the environment and chromium is one of the most toxic inorganic pollutants among them. Cr (VI) is hazardous to the human health which has carcinogenic properties by inducing oxidative stress, DNA damage and altered gene expression. Cr (VI) has high mobility in ground water since it is not absorbed by the soils, while Cr (III) is relatively nontoxic and it is an essential nutrient for humans in small quantities (Costa and Klein 2006; Kotas´ and Stasicka 2000; Bagchi et al. 2002). Cr (III) usually precipitates as hydroxides, oxides, or oxyhydroxides (Bagchi et al. 2002) and, therefore, it does not migrate in ground water. Hence, the chemical reduction of Cr (VI) to Cr (III) is the efficient method to eliminate the Cr (VI) pollutants. In this work, the developed Pd NPs embedded membranes have been studied for the efficient reduction of hexavalent chromium. The formic acid decomposition on Pd surface was used to produce hydrogen gas which *in situ* reduces the hexavalent chromium. The progress of the reduction was monitored by measuring the absorbance at 348nm by UV-Vis spectrophotometer shown in Figure 2.24.

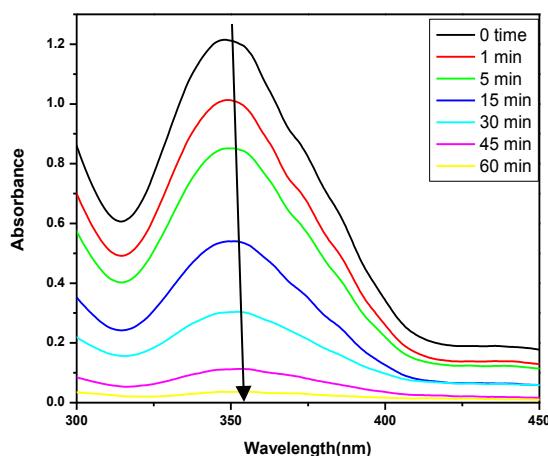


Figure 2.24 UV-Vis spectra showing reduction of Cr(VI) to Cr(III) with formic acid at 45 °C as a function of time in the presence of Pd NPs loaded membrane.

2.3.4 Reduction of uranium (VI to IV)

U (IV) is the best used reductant universally for plutonium partitioning by plutonium uranium reduction extraction (PUREX) process. This process is most followed internationally to recover U and Pu from spent nuclear fuels. Indian reprocessing plants mostly use electrochemical reduction for the uranous (U(IV)) production from uranyl nitrate having 50-60% conversion rate. This method increases the load on the uranium purification cycle. Therefore, an alternative method is needed for the higher conversion of U (VI) to U (IV). In the present thesis, the developed Pd catalyst embedded polymer membrane was studied to reduce uranyl ion in the presence of formic acid (acts as hydrogen source), and nearly 97-100% conversion rate was obtained. The reaction was monitored by UV-Vis spectrophotometer. The successive UV-Vis spectra of uranyl ion reduction recorded for every 5 minutes are shown in Figure 2.25.

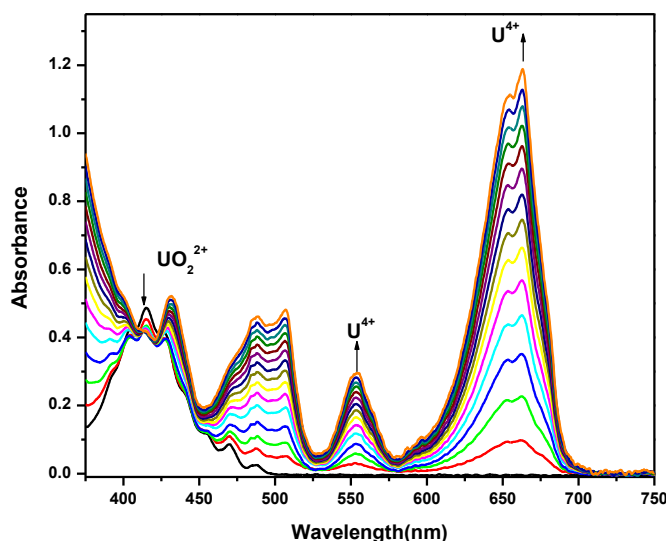
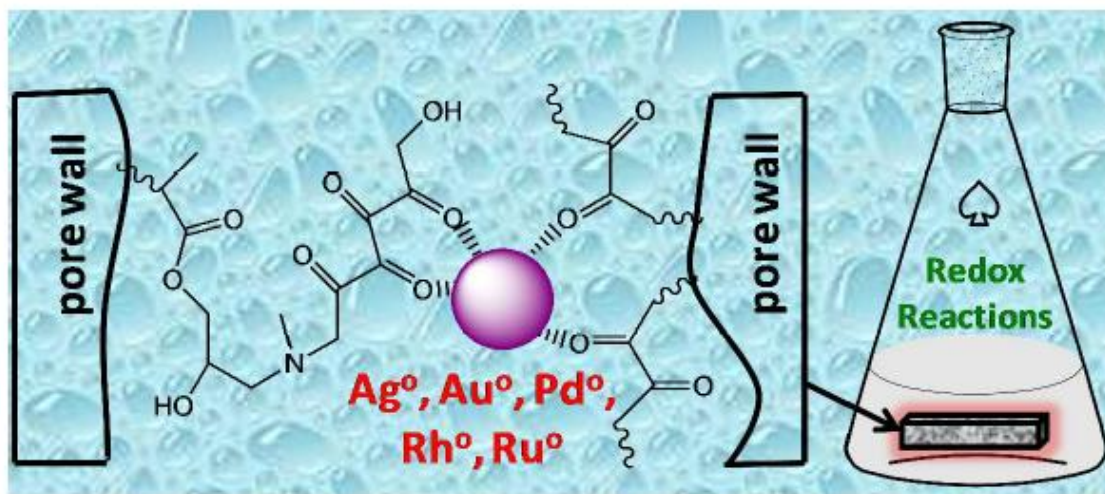


Figure 2.25 UV-Vis spectra showing reduction of U (VI) to U(IV).

CHAPTER3. SELF-REDUCING ASYMMETRIC POLYMER MEMBRANE FOR IN SITU FORMATION AND CONTAINMENT OF NOBLE METAL NANOCATALYSTS



3.1 Introduction

A synthetic polymer membrane mimicking eggshell membrane in terms of reduction and stabilization of noble metal nanocatalysts (NCs) has been developed. The synthetic polymer membrane developed in the present work not only provides a green route for synthesis of NCs in a solid matrix by simply dipping it in the precursor ion solution for fixed period of time, but also enhances the catalytic activity of thus formed NPs in the organic and inorganic redox reactions. Thus, the self-reducing membrane developed in the present work offer a numerous possibilities as a host for the single/bimetallic/core-shell noble metal catalysts for the organic and inorganic reactions.

Technological and commercially important redox reactions can be advanced significantly by employing the noble metal NCs. Despite of their advantageous such as high surface to volume ratio, under-coordinated surface sites at the surface, high dispersion, desired shapes for exposing reactive facets, and quantum confinement effects (Nguyen et al. 2015; Li and Shen 2014; Yan et al. 2013; Zhang et al. 2013; Mahmoud et al. 2013), they have some key issues for utilizing as heterogeneous catalysts. The major issues as their physical instability (agglomeration), chemical instability (chemical corrosion), and difficulty in withdrawing them from the systems causing problems in recyclability and product contamination. To address these problems, the NCs are immobilized on solid supports like carbon nanomaterials (Yang et al. 2014; Su et al. 2013), superparamagnetic Fe_3O_4 particles (Gawande et al. 2013), synthetic polymer membranes (Troppmann et al. 2014; Soukup et al. 2014; Faria et al. 2014; Ruiz and Muñoz 2011), inorganic particles (Corma and Garcia 2008; Hu et al. 2013), biopolymer matrices (Baig et al. 2014), porous inorganic supports (Liu et al. 2013; Lin et al. 2015), and resins/polymers (Lei et al. 2015; Alonso et al. 2012; Kao et al. 2013; Doménech et al. 2014]. Among these solid supports, NCs immobilized

on the films/membranes and magnetic particles are easy to retrieve from the process in which these material acts as catalyst.

Biomaterials are inexpensive, non-toxic, and may provide control over shape and size distributions. Biomaterials like sugars, vitamins, agricultural extracts and residues etc can be used for the reduction as well as capping of the nanoparticles (Nadagouda and varma 2008; Eising et al. 2014; Jung et al. 2014). Chicken eggshell membrane (ESM) contains amino acids (glycine and alanine) and uronic acid. The saccharides and aldehyde group of uronic acid reduces the surface adsorbed metal ions to NPs. The other functional groups like $-OH$, $-NH_2$ on the ESM stabilises the NPs, which obviates the need for additional reagents like reducing and capping agents for NPs synthesis. The NPs stabilized in ESM exhibit good catalytic activity due to the fibrous structure which provides high accessibility to the NPs (Mallampati and Valiyaveetil 2014; Liang et al. 2014). Bacterial cells can also be utilized for the intracellular synthesis of NPs. These NPs are then released due to rupture of the cell wall (Gaidhani et al. 2014). In most of the biomaterials, the phenolic derivatives are responsible for the precursor ions reduction and sugars provide effective capping for NP formation (Santos et al. 2014; Pestov et al. 2015). The polysaccharides are the most studied class of natural polymers due to their multi-functionality. Among all the polysaccharides, chitosan is the most studied polymer because of its polycation nature. The β -(1-4)-linked *D*-glucosamine and *N*-acetyl-*D*-glucosamine group of chitosan can effectively bind $[AuCl_4]^-$ ions which helps in control the growth and nucleation of NPs (Pestov et al. 2015).

In the present work, a synthetic polymer membrane has been prepared by anchoring glycidyl methacrylate (GMA) along with cross-linker in pores of a commercially available poly(propylene) membrane by UV-initiator induced *in situ* polymerization in pores of the membrane. The

poly(GMA) anchored membrane has a highly porous interior and dense at the surfaces which was quite different from the homogenous micro-porous membrane.

3.2 Experimental

Details of materials and reagents used are given in chapter 2.

3.2.1 Synthesis of self-reducing membrane

The details of synthesis of pore-filled membranes are given in chapter 2. Briefly, the polymerizing solution for anchoring GMA on to the host poly(propylene) membrane was prepared by dissolving the monomer GMA 1.5g in a 2 mL of DMF (solvent), to this 2 wt% of UV-initiator (DMPA) and 5 mol% of cross-linker (EGDM) was added. To homogenize, the polymerizing solution was sonicated for 20 min. The host PP membranes having 5×5 cm² dimensions were soaked in methanol for 4-5h prior to immersing in the polymerizing solution for overnight. Before exposing the polymer solution filled PP membrane to UV light, the excess of solution adhering to surface of the host substrates were removed gently and were sandwiched between two Garware polyester sheets. These sandwiched membranes were exposed to 365nm UV light in a multi lamps photo-reactor for a period of 20 min. To remove the un-polymerized components after exposing to UV light, the poly(GMA) anchored membranes were washed with DMF and with water till the constant weights were obtained. The anchoring yield obtained from the increase in weight of the membrane with respect to pristine membrane was found to be 100 wt%. NMDG group was attached to the poly(GMA)-anchored membrane samples by treating with 1 w/v% solution of NMDG in DMF at 60°C, maintained by a water bath for 4 h. The anchoring of NMDG occurred through opening epoxy ring of GMA. After chemical treatment, the membrane samples were washed with methanol and water, and dried at 45°C under vacuum condition.

3.2.2 Formation of noble metal NPs in self-reducing membrane

All the noble metal salts were dissolved in de-ionised water. The concentrations of these metal salt solutions were 0.1 mol L^{-1} , and pH of these solutions was adjusted to 2. The NMDG anchored membrane samples ($2 \times 2 \text{ cm}^2$) were equilibrated with 10 mL of each noble metal salt solution for 12 h at room temperature. To know the loading capacity of these membranes towards Ag^0 and Pd^0 , the known weighed samples of NMDG-anchored membrane ($2 \times 1 \text{ cm}^2$) were equilibrated in the 0.05 mol L^{-1} AgNO_3 and PdCl_2 solutions separately for a predetermined time with constant stirring at room temperature. After each time interval, the membrane samples were taken out and washed thoroughly with de-ionized water. To leach out the Ag and Pd NPs loaded in the membrane, the membrane samples were immersed in the 10 mL of 3 mol L^{-1} HNO_3 solutions. The nearly complete leaching of Ag and Pd was confirmed by EDXRF analysis and then the leach solutions were subjected to ICP-AES analyses for determining the Ag and Pd content.

3.2.3 Reduction of *p*-nitrophenol (PNP) and methylene blue (MB)

The Ag^0 -loaded membrane was used to study the reductions of *p*-nitrophenol and methylene blue (MB) with sodium borohydrate (NaBH_4) as a reducing agent. To monitor reduction online, the reductions were carried out in a standard quartz cell with path length of 1 cm. The reaction solution having 0.1 mL of 2 mmol L^{-1} PNP, 0.1 mL of 200 mmol L^{-1} freshly prepared NaBH_4 and 2.8 mL of de-ionised water were taken in a quartz cell. The Ag^0 loaded membrane having $1 \times 2 \text{ cm}^2$ dimension was placed at opaque side of the quartz cell to avoid the light beam path. The solution was stirred gently using micro-bar magnetic stirrer. The cuvette was placed in a portable UV-Vis spectrophotometer (K-MAC Technology, South Korea) kept on a magnetic stirrer, and the successive UV-Vis absorption spectra were recorded to monitor the reaction kinetics. The

reduction of *p*-nitrophenolate anions was monitored by measuring the absorbance at 400 nm as a function of reduction time.

The similar experiments were carried out for reduction of MB using BH_4^- as reducing agent. The reaction solution contained 0.5 mL of 0.2 mmol L^{-1} MB, 0.5 mL of 20 mmol L^{-1} of freshly prepared NaBH_4 solution, and 2 mL of de-ionised water. The progress of reduction was monitored by measuring the absorbance at 665 nm (λ_{max}). The absorbance values at 665 nm (MB) and 400 nm (PNP) were used to obtain the apparent reduction rate constant (*k*) using following equation.

$$\ln \left[\frac{A_t}{A_0} \right] = -kt$$

Where, A_0 and A_t are the absorbance at time 0 and *t*, respectively.

3.2.4 Reduction of Cr(VI) ions

For the reductions of Cr(VI) ions, formic acid was used as the reducing agent and Pd NPs embedded membrane used as the catalyst. The reduction process was studied by recording UV-Vis spectra as a function of time at regular time interval. The absorbance was monitored by UV-Vis spectrophotometer model V 53 from JASCO (Tokyo, Japan). The reaction solution consisted of 5 mL of 7 mmol L^{-1} Cr(VI) solution and 5 mL of 70 mmol L^{-1} formic acid. The temperature for reduction of Cr(VI) to Cr(III) solution maintained at 45°C by using constant temperature water bath and Pd loaded membrane ($1 \times 2 \text{ cm}^2$) was immersed in this solution. The solution was stirred with magnetic stirrer with constant 300 rpm. The decrease in absorbance at 350 nm corresponding to Cr(VI) was monitored by taking out 0.5 mL of aliquot in a cuvette and diluted it to 3 mL for measuring the absorbance.

3.3 Results and discussion

The host poly(propylene) membrane provides a mechanical framework with soft microgel anchored in its pores. The hydrogel-filled membranes were used for the separations, catalysis, biomedical technologies, sensing and analytical applications etc (Yang et al. 2011; Pandey et al. 2001). These hydrogel-filled membranes were similar to the pore-filled membrane synthesized in the present work. The microgel anchored in the pores of the membrane provided interlinked porous structure leading to high accessibility of the functional groups. The physical architecture of the pore-filled membrane synthesized in the present work is different from the homogenous pore-filled membrane reported in the literature (Yang et al. 2011; Pandey et al. 2001). This may due to the 100% weight gain of the poly(GMA)-anchored pore-filled membrane tend to reorganize during drying that would shrink the polymer chains to form dense surface and a fibrous interior (see Figure 3.1).

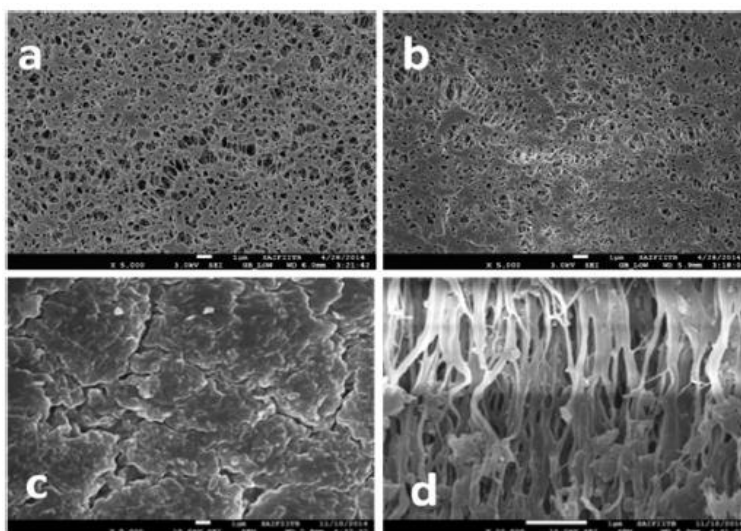
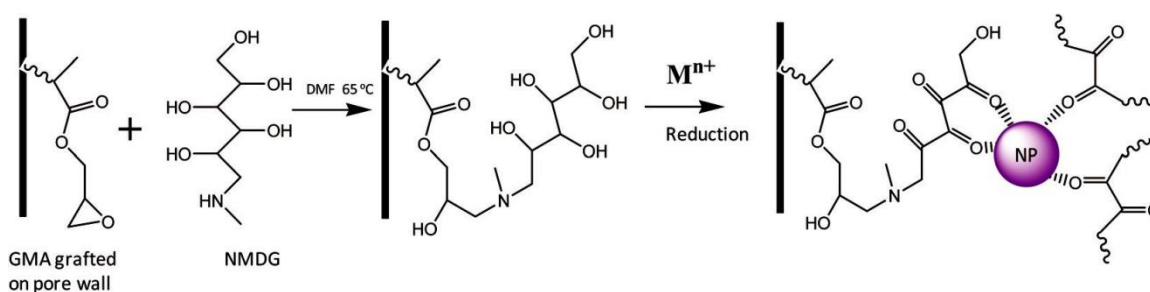


Figure 3.1 FE-SEM images showing surface (a) and cross-section (b) of the host poly(propylene) membrane, and surface (c) cross-section (d) of the same host membrane after anchoring with poly(GMA) and subsequent treatment with NMDG.

As discussed in the experimental section, the poly(GMA) anchored membranes were reacted with NMDG to introduce the self-reducing groups in the membrane. This chemical treatment method was similar to the that described for the synthesis of the As(V) selective membrane [Shinde et al. 2014]. However, the reducing properties of the NMDG were not known and, therefore, the self-reducing properties of the NMDG was explored first time in this work. The overall process involved in the covalent attachment of NMDG groups in the poly(GMA) anchored membrane and its role in the reduction and stabilization of noble metal NPs are shown in scheme 3.1.

As given in experimental section, the Ag, Au, Rh, Ru, and Pd NPs were formed by simply dipping the membranes in the 0.1 mol L^{-1} solutions of the respective precursor salts for 12 h at room temperature. As shown in scheme 3.1, the loading of noble metals in the membrane occurred only by reduction and deposition in the form of NPs. Thus, this process was similar to the electroless deposition of the metal.



Scheme 3.1 The chemical reaction involved in the anchoring of NMDG on to the poly(GMA) anchored membrane that reduces noble metal precursor ions and stabilizes the thus formed NPs.

The field emission scanning electron microscopy (FE-SEM) images and elemental mappings by energy dispersive spectroscopy (EDS) of NPs embedded membranes are shown in Figure 3.2. As can be seen from this Figure 3.2, the nitrogen, which represents the self-reducing group NMDG,

and Rh NPs are uniformly distributed on the surface of the membrane. It is also seen from the FE-SEM images given in Figure 3.3, the different shapes and sizes of NPs formed at the surface of the membrane depending on the precursor metal ions and their concentrations.

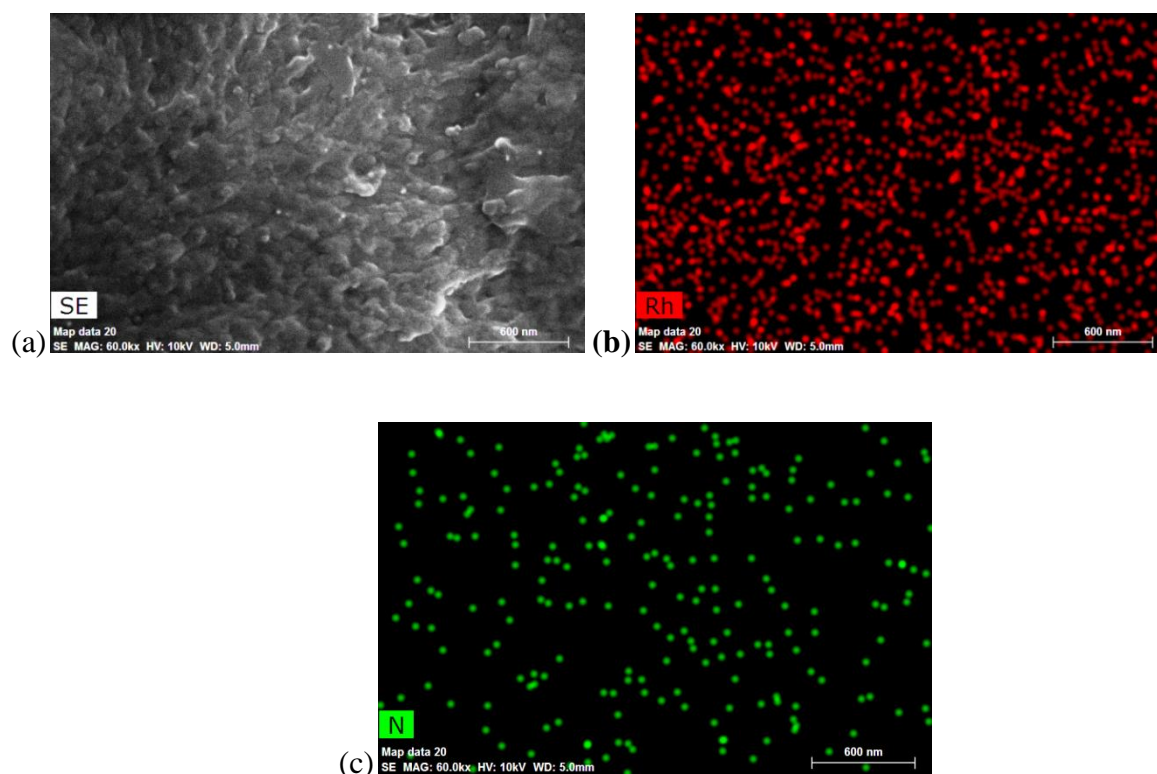
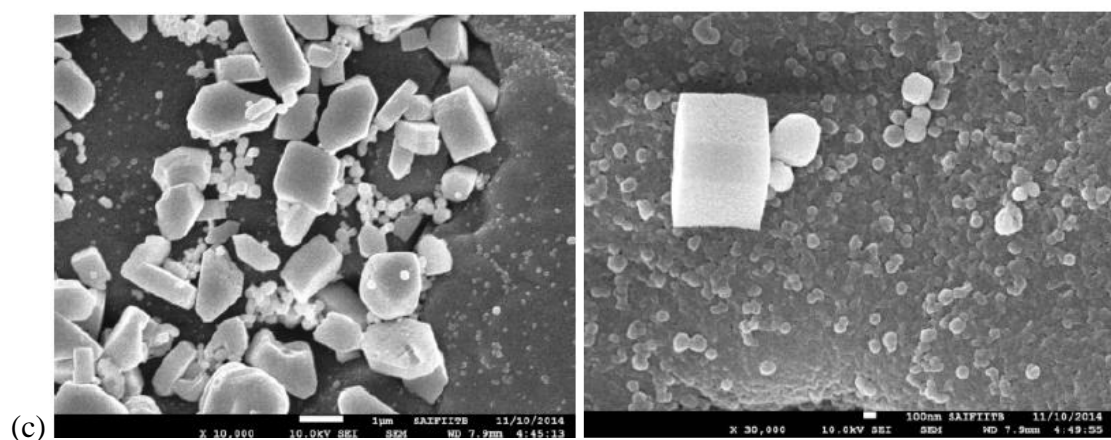
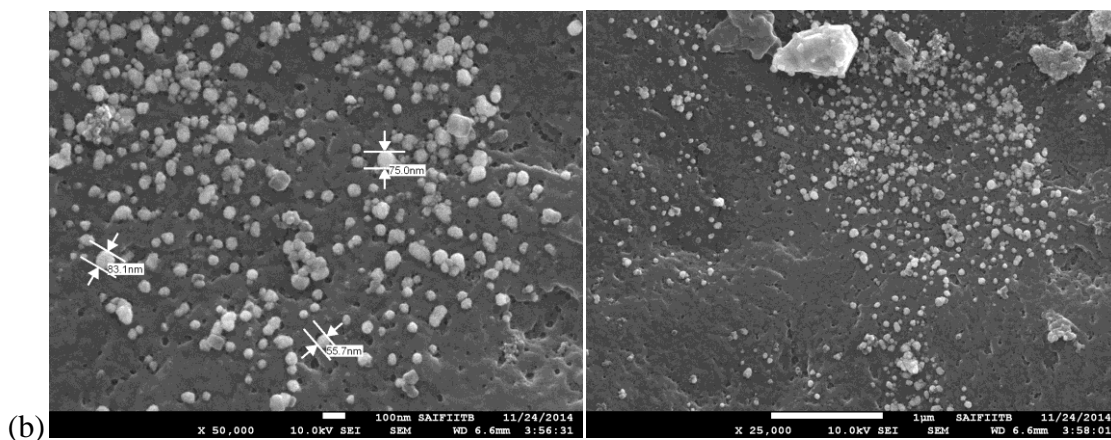
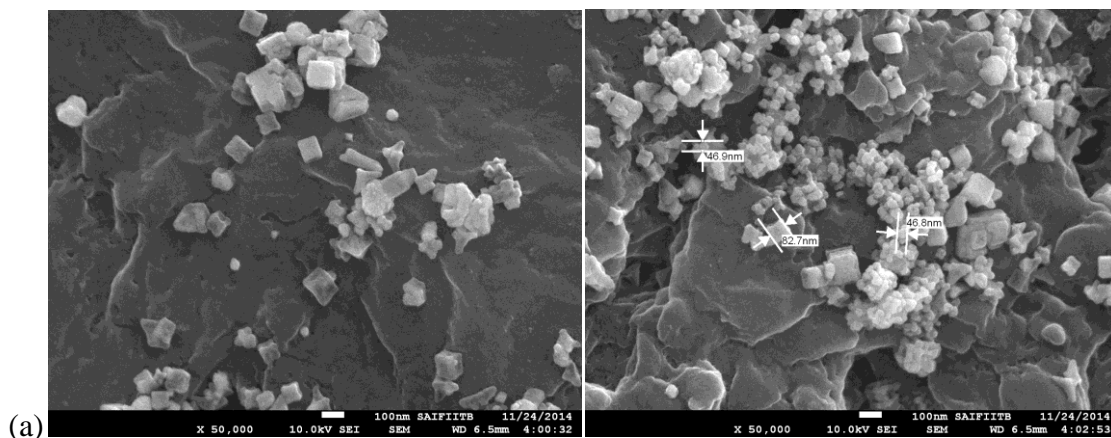


Figure 3.2 The representative FE-SEM image of the surface of Rh NPs loaded membrane (a), and corresponding elemental mappings of nitrogen (b) and Rh (c) by EDS.

The self-reducing membrane developed in this work is capable of reducing all the noble metal ions which are having redox potential of $E^0 \geq 0.68\text{V}$. However, Pt NPs could not be formed using PtCl_6^{2-} precursor at room temperature. From the literature, it is known that the formation of Pt NPs using reducing agents like ethylene glycol or BH_4^- requires high temperature and pressure from its precursor salt H_2PtCl_6 (Stepanov et al. 2014). As shown in Figure 3.3, the Au cubes and prisms were formed at the surfaces and spherical Au NPs were formed at porous surfaces.



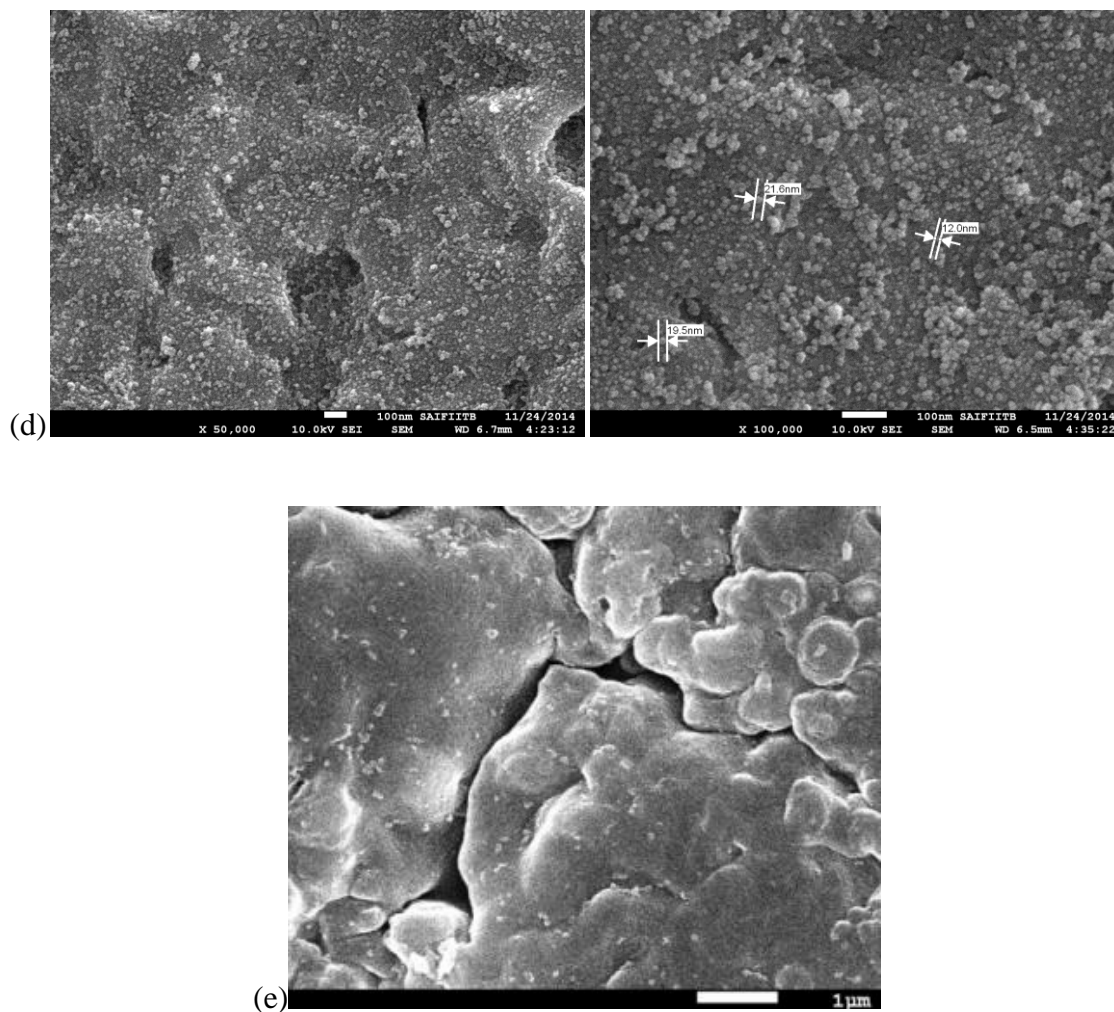


Figure 3.3 FE-SEM images showing Au NPs having geometries of cubes and prisms at the surface (a), spherical at the porous surface (b), Silver NPs (c), Palladium NPs (d) and Ru NPs (e) formed at the surfaces of membrane samples equilibrated with $0.1 \text{ mol L}^{-1} \text{ HAuCl}_4/\text{AgNO}_3/\text{PdCl}_2/\text{RuCl}_3$ solutions for overnight.

The formation of Ru and Rh NPs were also confirmed by the energy dispersive X-ray fluorescence (EDXRF) analyses of the membrane samples as given in Figure 3.4.

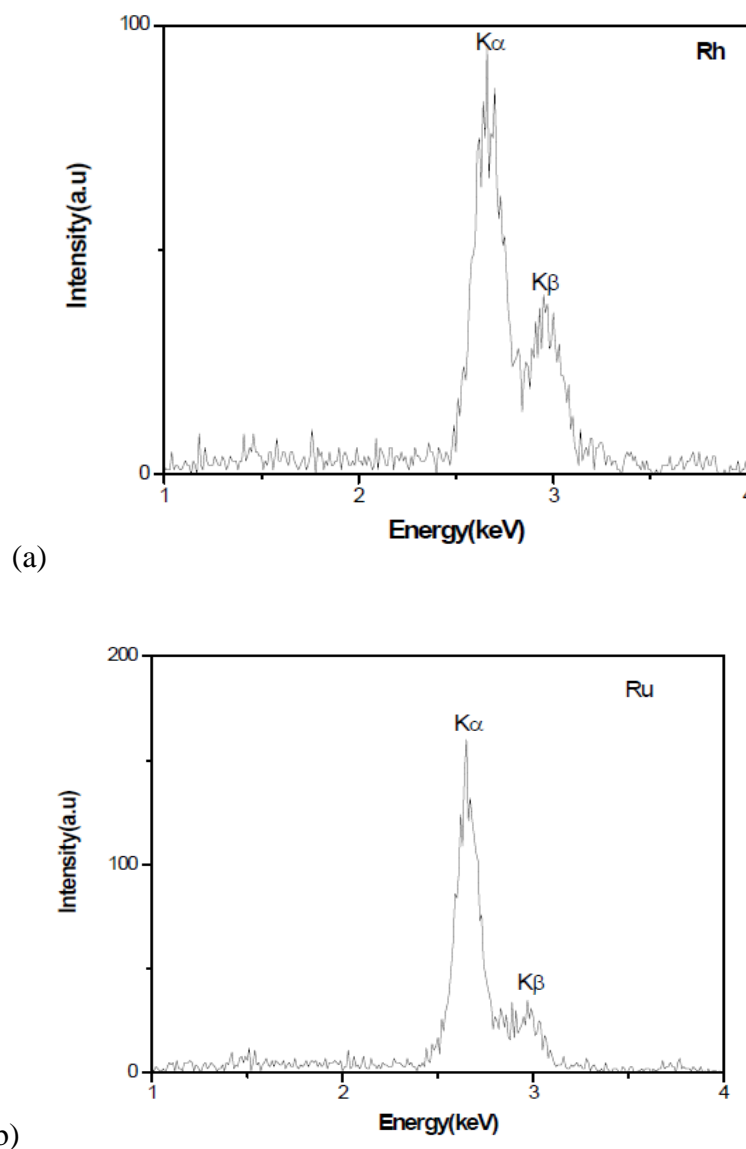


Figure 3.4 EDXRF spectra of Rh (a) and Ru NPs (b) loaded membrane.

From cross-sectional FE-SEM images of the Ag NPs loaded membrane given in Figure 3.5, it was observed that a negligible number of NPs were formed at the fibrous interior matrix. However, it is clear from the FE-SEM image and elemental mapping that Ag^0 was coated on the fibers at the interior matrix of the membrane. The nitrogen mapping across the thickness of the membrane indicated that NMDG was uniformly distributed at the interior matrix of the membrane.

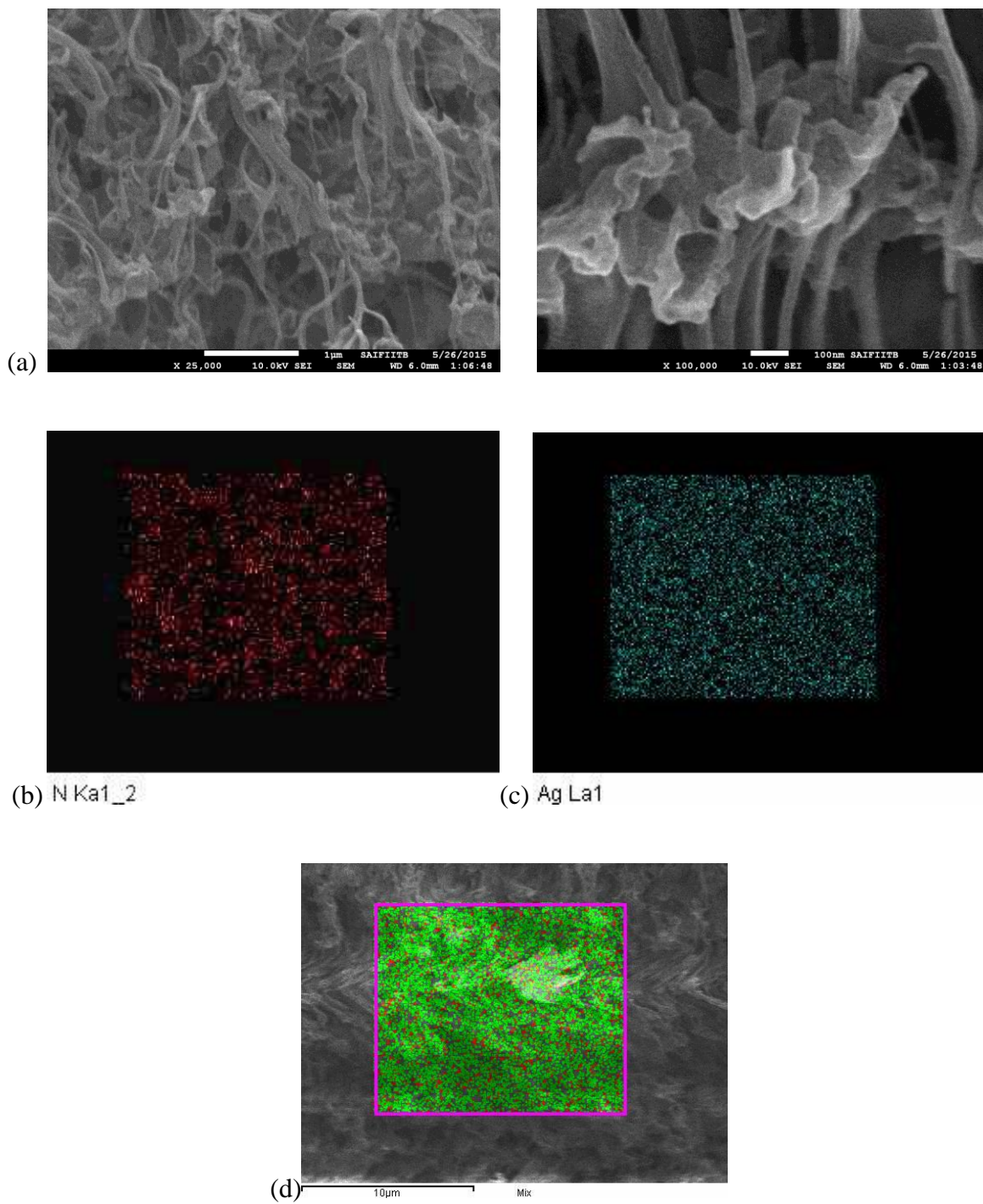


Figure 3.5 FE-SEM images of cross-section of the Ag^0 loaded membrane samples (a), elemental mappings of nitrogen (b), Silver (c), and mixed elemental mapping image of nitrogen and silver (d).

To explore the possibility of controlled loading of noble metal NPs, the membrane samples were equilibrated with 0.05 mol L^{-1} AgNO_3 and PdCl_2 solutions as a function of time. The loadings of Ag^0 and Pd^0 as a function of equilibration time of the membrane samples are shown in Figure 3.6.

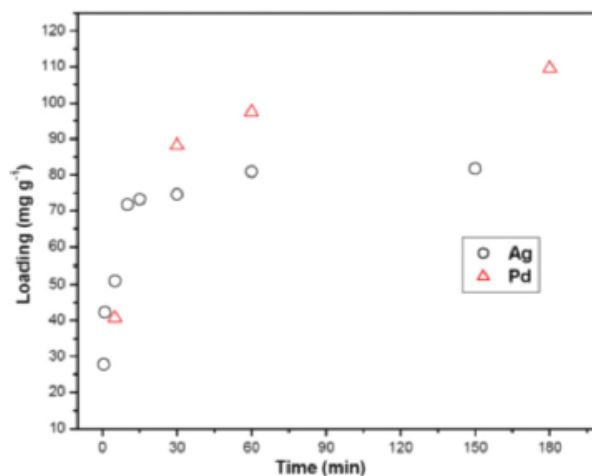


Figure 3.6 Variations in loading of Ag^0 and Pd^0 in the membrane as a function of equilibration time at room temperature in 0.05 mol L^{-1} solutions of AgNO_3 and PdCl_2 .

The amount of Ag and Pd NPs loaded in the membrane as a function of equilibration time was determined by leaching the Ag and Pd NPs in 5 mL of 2 mol L^{-1} HNO_3 solutions, which was further diluted to 10 mL by adding 5 mL of deionised water and subjecting these leach solutions to ICP-AES analyses. From Figure 3.6, it could be seen that the Ag loading reached 70 mg g^{-1} within 10 min, and then slowly approached a saturation loading capacity of 80 mg g^{-1} . It is also evident from Figure 3.6, the rate of Pd^0 deposition was comparable to that of Ag^0 though the reduction of Pd^{2+} ions needed two electrons. And the saturation loading towards Pd^0 in the membrane was higher (120 mg g^{-1}) than the Ag^0 saturation loading in the same membrane. Thus, the reduction efficiency of NMDG anchored membrane increased with an increase in a redox potential of the precursor ions.

These preliminary results suggest that the M^0 content and particle size can be controlled by equilibrating a membrane sample in the precursor salt solution for a predetermined time. The FE-SEM images given in Figure 3.7 show that the size of Ag NPs decreased from ≈ 75 nm at saturation loading to ≈ 15 nm in the membrane which was equilibrated for 1 min in AgNO_3 0.05 mol L^{-1} solution. It was also observed that some clusters of Ag NPs also been formed at some places in the membrane equilibrated for 1 min in AgNO_3 solution. The loading of the metal content in the membrane could also be controlled by controlling the amount of reducing moiety NMDG in the membrane which is correlated to poly(GMA) anchoring. This is based on a fact that the poly(GMA) anchoring yield was dependent upon the concentration of GMA monomer in the solution used for in situ polymerization in pores of the host micro porous PP membrane (Shinde et al. 2014).

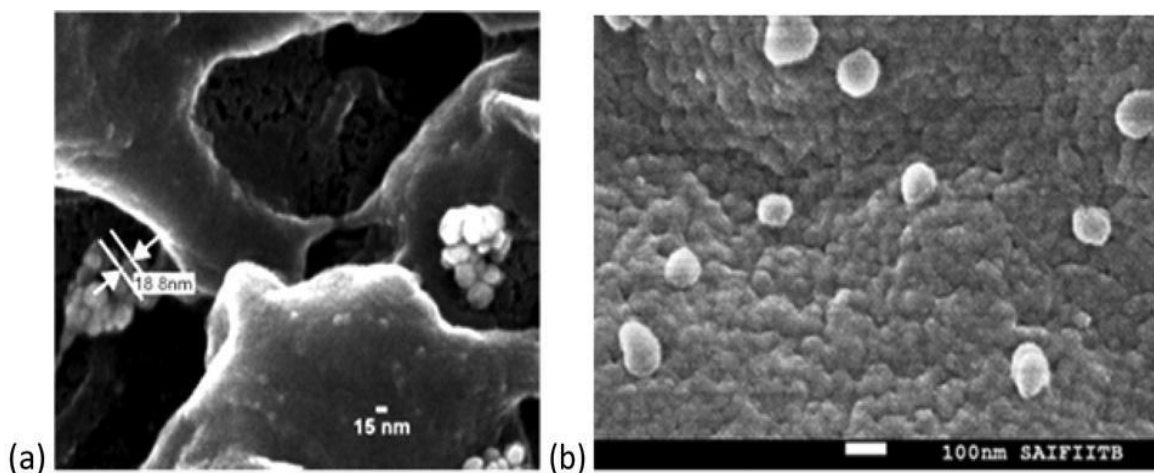


Figure 3.7 FE-SEM images showing Ag NPs formed on the surfaces of the membrane after 1 min (a) and 60 min (b) equilibration in 0.05 mol L^{-1} AgNO_3 solution.

The unchanged physical appearance, catalytic activity and XRD pattern (see Figure 3.8) of the Ag NPs loaded membrane sample stored under ambient conditions for a time period of three months seems to suggest that the Ag NPs have long shelf life in the membrane.

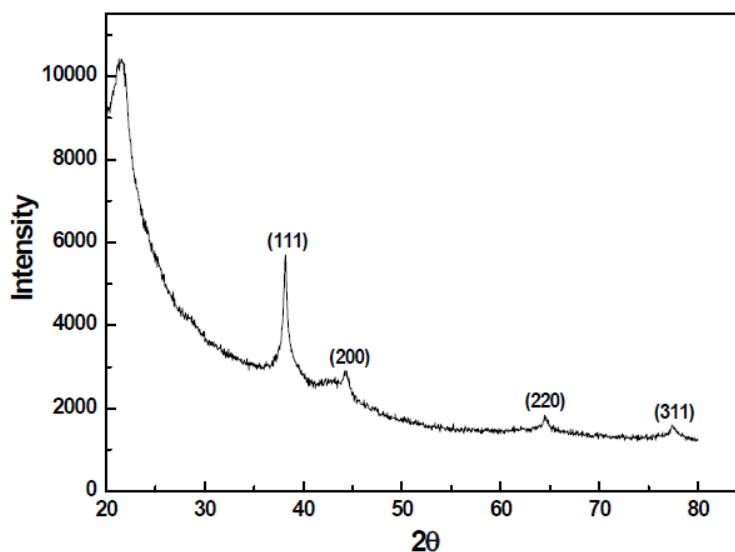


Figure 3.8 XRD pattern of Ag NPs loaded membrane stored for three months under ambient conditions.

The catalytic properties of a Pd loaded membrane was studied in the Cr(VI) reductions using formic acid at 45°C. The Cr(VI) reduction is important for its remediation (Yadav and Xu 2013). Since, Cr (VI) is more toxic and labile than that of Cr (III) so, the reduction has got importance in remediation (Zhu et al. 2013; Baruah et al. 2013). The choice of using formic acid as reducing agent is because it is an excellent source for hydrogen (4.4 wt%) and it is one of the major products formed during biomass processing. Also, formic acid is inexpensive and nontoxic. As discussed in chapter 1, the d-band centre for Pd NPs towards decomposing formic acid is higher compared to other noble metal NPs. As can be seen from Figure 3.9, in the presence of Pd NPs the reduction of Cr(VI) had progressed efficiently.

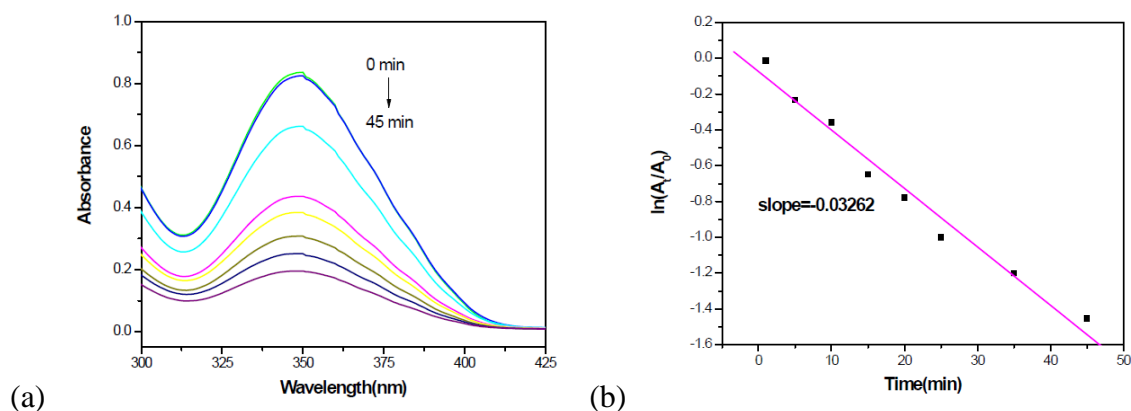


Figure 3.9 Successive UV-Vis spectra showing reduction of Cr(VI) to Cr(III) at 45°C using formic acid as a function of time in the presence of a Pd NPs loaded membrane (a), and corresponding variation of logarithm of A_t/A_0 as a function of reduction time (b). A_t and A_0 represent absorbance at 350 nm corresponding to concentration of Cr(VI) at time t and initial respectively.

It was observed that the reductions did not proceed under similar experimental conditions using the blank NMDG-membrane (without Pd NPs) as shown in UV-Vis spectra given in Figure 3.10.

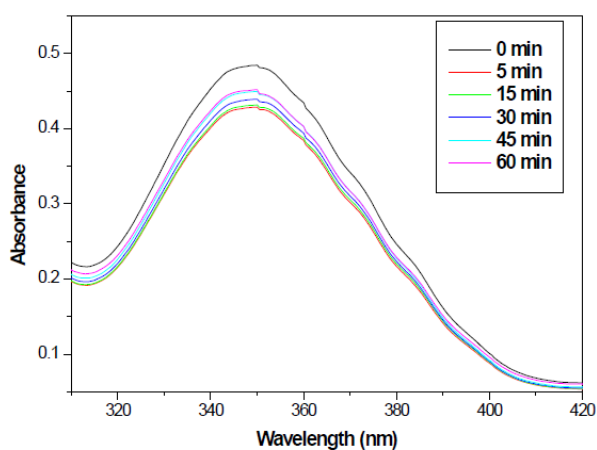


Figure 3.10 UV-Vis spectra showing the absence of significant reductions of Cr(VI) with formic acid at 45°C as a function of time in the presence of NMDG-membrane sample without Pd NPs.

In the literature, *p*-nitrophenol (PNP) and methylene blue (MB) reductions by sodium borohydride have been studied as a model reaction to evaluate the catalytic efficiencies of coinage metal NPs (Corma and Garcia 2008; Hu et al. 2013; Lei et al. 2015; Alonso et al. 2012; Kao et al. 2013; Domenech et al. 2014; Pradhan et al. 2002; Esumi et al. 2002). These organic redox reactions follow generally a pseudo-first-order kinetics in the presence of an excess of NaBH_4 . In the present work, Ag NPs loaded membrane was used for PNP and MB reduction in the presence excess of BH_4^- ions. The membrane developed in the present work is neutral and hence, both anionic (*p*-nitrophenol) and cationic (methylene blue) species would easily enter into the membrane matrix.

As shown in the UV-Vis spectra, the decrease in absorbance at 665 nm indicated degradation of methyl blue dye with the time (Figure 3.11), and the growth of a product peak at 300 nm was observed for *p*-nitrophenol reduction (see Figure 3.12). These suggested that the reduced products were not retained in the membrane matrix. As expected, both the reductions followed pseudo-first-order kinetics in the presence of excess BH_4^- ions. Both the reductions were completed within a minute, and the apparent reduction rate constants ($K_{\text{PNP}} = 0.1 \text{ s}^{-1}$, $K_{\text{MB}} = 1.5 \text{ s}^{-1}$) thus obtained were significantly higher as compared to those reported in the literature (Patra et al. 2014). There are several reasons that may be responsible for the higher redox catalytic activity of the Ag NPs loaded membrane in the present work. These are: (i) higher accessibility of NPs to the reactants, (ii) absence of capping agents that retards the catalytic activity (Niu and Li 2014), and (iii) nanoconfinement effects. In nanoconfined environment molecules/complexes behaves differently than they are in the bulk. It has been shown that silver citrate complexes readily undergo redox decomposition in the nanoscale confinement to form the Ag NPs (Patra et al. 2014). It has also been reported that the catalytic behaviour of nanoporous materials is strongly influenced by the confinement effects (Goettmann and sanchez 2007). These are related to geometrical constraints,

reduced mixing of reactants and products, sorption of reacting species on the pore-wall etc. that may accelerate the redox kinetics.

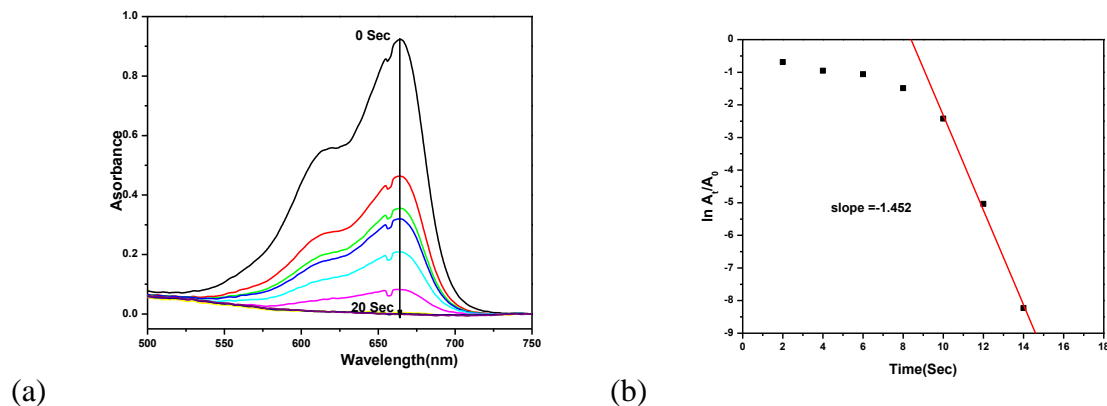


Figure 3.11 Successive UV-Vis spectra showing the reduction of methyl blue with BH_4^- ions at room temperature as a function of time in the presence of Ag NPs loaded membrane (a), and corresponding variation of logarithm of A_t/A_0 as a function of reduction time (b).

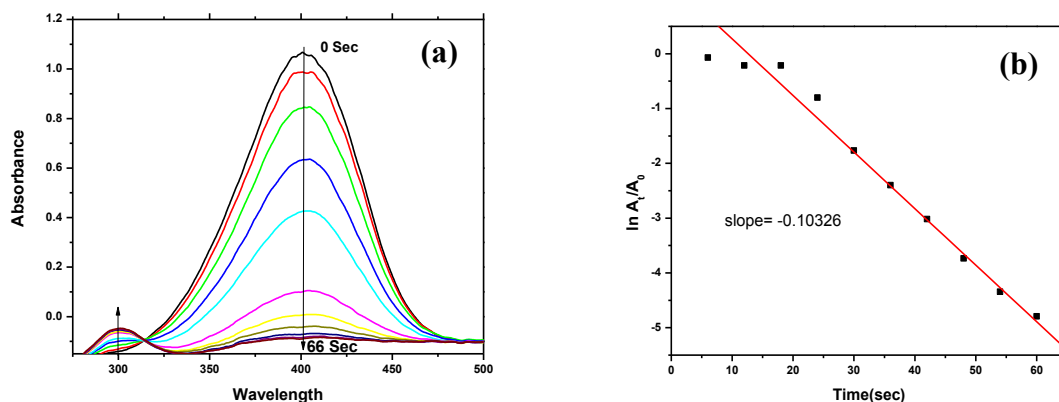


Figure 3.12 Successive UV-Vis spectra showing the reduction of *p*-nitrophenol to *p*-aminophenol reduction with BH_4^- ions at room temperature as a function of time in the presence of Ag NPs loaded membrane (a), and corresponding variation of logarithm of A_t/A_0 as a function of reduction time (b).

3.4 Conclusions

The synthetic polymer membrane developed in the present work not only provides a green route for the synthesis of noble metal NPs in a solid matrix by simply dipping in the precursor salt solution for a fixed period of time, but also shown enhanced catalytic activity in both the organic and inorganic redox reactions. This membrane acts as a robust container of almost bare NPs without affecting their accessibility to the reactants, and also these NPs have a long shelf-life. The same synthetic route can also be applied for the synthesis of self-reducing materials such as graphene oxide, silica particles and Fe₃O₄ particles etc.

CHAPTER 4. PALLADIUM NANOPARTICLES HOSTED IN HYDRAZINE/SULFONATE ANCHORED MEMBRANES FOR CATALYZING REDUCTION OF URANYL(VI) IONS



4.1 Introduction

As discussed in chapter 1, the matrix supported nanocatalysts (NC) have potential applications as the heterogeneous catalysts. These matrix supports prevent the nanoparticles from agglomeration and also makes them easy to withdraw from the system. Solid supports like carbon nanomaterials, inorganic particles, superparamagnetic Fe_3O_4 particles, synthetic polymer membranes, and resins/polymers are used. Among these supports, magnetic particles and films/membrane immobilized NCs are retrievable easily from the process. The nanoparticles immobilized on appropriate host matrices find potential applications in water treatment, remediation of toxic oxidation state of ions, process chemistry, synthetic chemistry of metal complexes having desirable oxidation state, sensor and for many other applications (Sharma et al. 2015; Omole et al. 2011; Moakhar et al. 2017; Liu et al. 2017; McCleskey et al. 2001). The nanocatalysts immobilized on inorganic or polymer supports could be used to address the aromatic pollutants generated by chemical industries, which causes serious environmental problem (Hu et al. 2015; Liu et al. 2016). It is important to note that the redox reactions of oxyions are not feasible under ambient conditions. One of such example is the reduction of UO_2^{2+} ions to U^{4+} ions. The U^{4+} ions has applications in nuclear industry such as reduction and stripping of Pu^{4+} ions in PUREX process and also used in the preparation of UO_2 and UF_4 (McCleskey et al 2001; Liu et al. 2016). In PUREX process, the U^{4+} ions are preferred as the reductant to avoid contamination of the feed. The UO_2 can be easily precipitated at basic pH for its removal and remediation purposes (Lu et al. 2017). The catalytic properties of U^{4+} complexes have not been explored but these complexes may catalyze the reactions that are normally impossible with the widely used transition metal based catalysts due to availability of f orbitals electrons (Lu et al. 2017; Fox et al. 2008).

The reduction of UO_2^{2+} ions to U^{4+} ions has been explored by different methods such as electrochemical reduction (Nogami et al. 2008), photocatalytic reductions (Hu et al. 2015; Salomone et al. 2015), chemical reduction (Boltoeva et al. 2008; Tyumentsev et al. 2014), and sonolysis reduction (Toraishi et al. 2007). An interesting approach has been reported by Sheng et al. for the remediation objective of U(VI) ions. This approach involves the adsorption and reduction of UO_2^{2+} to U^{4+} , formation of UO_2 particles and finally retention of the particles using hosts such as haematite, titanate nanotubes, and nanoscale zero-valent iron immobilized on diatomite or Na-Bentonite (Zhao et al. 2012.; Sheng et al. 2014, 2015, 2016). As discussed in chapter 1&3, formic acid is not only good source for the hydrogen production but also generating *in situ* hydrogen for carrying out the reductions. Formic acid is liquid at room temperature and can be decomposed on NPs surface at amenable temperatures. The *in situ* generated hydrogen has been used for catalyze reductions of $\text{Cr}_2\text{O}_7^{2-}/\text{CrO}_4^{4-}$ anions to Cr^{3+} ions (Yadav and Xu 2013; Huang et al. 2013; Omole et al. 2007; Gong et al. 2015], destruction of nitrate ions in the aqueous discharges (Ren et al. 2015; Soares et al. 2014; Mohamed et al. 2014), and nitrite reduction in water (Dodouche and Epron 2007).

The Pd NPs are efficient catalyst for the decomposition of formic acid to produce hydrogen. However, Pd NPs have tendency to agglomerate because of high surface area and under coordinated sites, and also difficult to withdraw for recycle. Therefore, the Pd NPs need to be immobilized on the solid supports such as Al_2O_3 , SiO_2 , TiO_2 , Fe_3O_4 (Dodouche and Epron 2007; Gawande et al. 2013; Pan and Xu 2014; Li et al. 2013), carbon nanomaterials (carbon nanotubes, grapheme oxide, carbon spheres) (Su et al. 2013; Chang and Wu 2013; Ren et al. 2014), hydrogels (Hapiot et al. 2013), resin beads (Mori et al. 2013; Trzeciak et al. 2008), electrospun fibers mats (Huang et al. 2008; Demir et al. 2004), ploy(HIPE) (Desforages et al. 2005), and membranes

(Alonso et al. 2012; Bonggotgetsakul et al. 2015; Zeng et al. 2014; Soukup et al. 2014). The Pd NPs immobilized on to the poly(vinyl alcohol) and cellulose acetate films have been used as the “dip catalysts” for the organic reactions (Hariprasad and Radhakrishnan 2012; Faria et al. 2014). The hallmarks of supported Pd NPs not only include chemical and physical stabilities but also the simplicity of fabrication, easy retrieval, recyclability and amenability for scale up. The porous supports like membranes, poly(HIPE) and electrospun fibers mat provide high accessibility to the heterogeneous nanocatalysts that enhances the catalytic activity (Sheng et al. 2016; Desforges et al. 2005). Because of three dimensional fibrous structure and various functionalities of the eggshell membrane, it holds and reduces the precursor metal ions, and also protect the metal nanoparticles without affecting their catalytic activity (Nasrollahzadeh et al. 2016; Liang et al. 2014). As discussed in chapter 3, we have synthesized an asymmetric poly(glycidyl methacrylate) poly(GMA) anchored polymeric membrane, and introduced subsequently *N*-methyl-*D*-glucamine groups to reduce variety of precursor ions such as Ag^+ , Pd^{2+} , Rh^{3+} , Ru^{3+} and AuCl_4^- ions and stabilizes thus formed NPs in the membrane.

In the present work, the Pd NCs have been formed in the hydrazine-grafted neutral polymer membrane to mimic eggshell membrane with a better mechanical properties and highly microporous architecture. This synthesized membrane reduces Pd^{2+} ions itself and provides stability to Pd NCs. Thus, the reducing and capping agents could be avoided. This eggshell mimicking membrane has been prepared by anchoring (poly(GMA)) by *in situ* UV-initiator induced polymerization in the pores of PP membrane similar to that described in chapter 3. Instead of *N*-methyl-*D*-glucamine groups, the poly(GMA)-anchored membranes have been reacted with hydrazine to incorporate the reducing moiety. The Pd NCs are formed in these hydrazine grafted membranes by equilibrating them in solutions containing Pd^{2+} precursor ions for a fixed period of

time. The loading of Pd⁰ content in these host materials has been found to be dependent upon equilibration time till saturation loading. These Pd NCs embedded materials have been tested for the UO₂²⁺ ions reduction with formic acid under different conditions including high intensity ultrasonication. The UO₂²⁺ ions reduction has been studied as an example of inorganic reduction based on the fact that its reduction is difficult than Cr(VI) and nitrate reduction, and its reduction product is not very stable at ambient conditions. In general, hydrazine is used for the catalytic reduction of UO₂²⁺ ions. However, formic acid has been selected in the present work due to its wide range of applications like nitrate and Cr(VI) reduction apart from hydrogen production as discussed above. The cation-exchange membrane embedded with Pd NCs has also been studied for UO₂²⁺ ions reduction under similar conditions. The UO₂²⁺ ions reduction to U(IV) have been analyzed for pseudo-first-order, pseudo-second-order, and diffusion-controlled kinetics.

4.2 Experimental

The UV-initiator induced anchoring of precursor polymer in the poly(propylene) membranes were carried out by using the procedure discussed in chapter 2&3. The FE-SEM imaging of the pristine and the Pd NPs embedded membranes were done using FE-SEM (Model No. JSM-7600F) at SAIF, IIT-Bombay, Mumbai, India. UV-Vis spectrophotometer model V 53 from JASCO (Tokyo, Japan) was used to record successive UV-Vis absorption spectra during reduction of UO₂²⁺ to U⁴⁺ ions. On-line monitoring of UO₂²⁺ ions reduction was carried out by pumping reaction solution to 10 mm path length Z-cell (FIA-1000-Z, Ocean Optics) using peristaltic pump. The Z cell was connected to light source (AvaLight-DH-S-BAL) and spectrometer (USB4000-UV-VIS-ES, Ocean optics) at opposite sides with 400 μm optical fibers. The photograph of this setup is shown in Figure. 4.1.

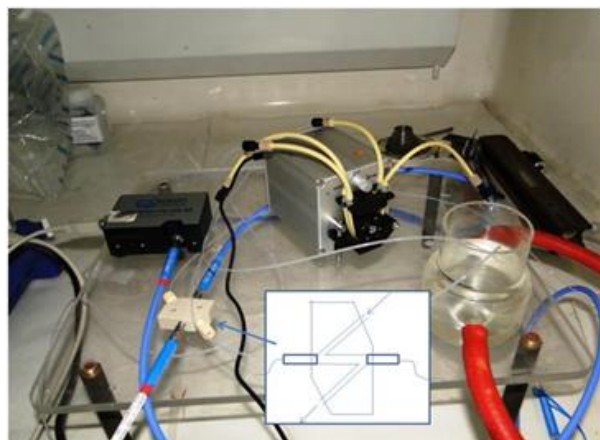


Figure 4.1 The experimental setup of Z-flow cell spectrophotometry used for on-line monitoring of UV-Vis absorption spectra during U(VI) to U(IV) ions reduction.

4.2.1 Formation of Pd NPs embedded neutral membrane

The precursor pore-filled polymer membranes were prepared by UV-initiator (DMPA) induced in situ polymerization of monomer (GMA) along with cross-linker (EGDM) in pores of the microporous host membranes. The polymerizing solution was prepared by dissolving 1.5 g of GMA in 2 mL of DMF solvent along with 5 mol % of cross-linker (EGDM) and 2 mol % of UV-initiator (DMPA). Before pore-filling, the polymerizing solution was sonicated for 15 min for homogenization. The poly(propylene) membrane having dimensions of 5X5 cm² area were soaked first in methanol for a period of 3h and then immersed in the polymerizing solutions for overnight. After pore-filling, solution adhering to surfaces of the host substrates was removed gently with Teflon roller. The polymerizing solution filled membranes were sandwiched between two Garware polyester sheets and irradiated with 365 nm light in a photo-reactor for a period of 20 min. After polymerization (anchoring), to remove the un-polymerized components (monomers), the membranes samples were washed thoroughly with DMF and water mixture at 40-50⁰C till constant weights were obtained.

The poly(GMA)-anchored membranes were reacted with hydrazine hydrate (99 %) for 12 h with constant stirring at room temperature. After treatment with hydrazine, the polymer membranes were thoroughly washed with de-ionized water several times to remove un-reacted hydrazine, and vacuum dried for further use. The hydrazine attachment with the glycidyl units anchored in the PP membrane was monitored by nitrogen analysis. These hydrazine attached membranes were equilibrated with the solutions containing $0.01 \text{ mol L}^{-1} \text{ PdCl}_2$ at pH=1 for the predetermined time period to form controlled amount of Pd NPs in the membrane.

4.2.2 Formation of Pd NPs embedded cation-exchange membrane

The cation-exchange membrane was prepared using similar procedure described in chapter 2, and as previously reported by Agarwal et al. (Agarwal et al. 2013). Briefly, the sulfonic acid monomer AMPS and silane based monomer APTMS were taken in 1:1 mol proportion and were dissolved in DMF solvent along with 2 wt % UV-initiator (DMPA) and 5 mol% of cross-linker (EGDM). The silane monomer APTMS was used as filler to minimize dimensional changes and brittleness in the dry state as observed in the cation-exchange membrane prepared without using APTMS. The membranes were soaked in the polymerizing solution similar to the procedure described for poly(GMA) anchoring, and exposed to 365 nm UV light for 30 min, un-polymerized monomers were removed by washing with DMF and water. After anchoring, the membrane was conditioned in $0.1 \text{ mol L}^{-1} \text{ NaCl}$ solution for 24 h, and then equilibrated with $0.01 \text{ mol L}^{-1} \text{ PdCl}_2$ solution overnight to load Pd^{2+} ions by the ion-exchange mechanism. The Pd^{2+} ions loaded membrane samples were immersed in 10% v/v hydrazine aqueous solution to reduce Pd^{2+} ions held at the ion-exchange sites to Pd^0 .

4.2.3 Determination of Pd⁰ content loaded in membranes

To know the amounts of Pd⁰ loaded in the membrane, the membrane samples having known dimension (2x1 cm²) and weights were leached in aqua-regia solution for 12 h at room temperature. The leach liquor was evaporated to dryness under IR heating and re-dissolved in 10 mL of 0.1 mol L⁻¹ HNO₃. The complete leaching of Pd⁰ was confirmed by EDXRF analyses of the membrane sample before and after leaching. These solutions were subjected to ICP-AES analyses for the determination of concentration of Pd, which was used to calculate the amount of Pd-loaded in the membrane sample. The ICP-AES analyses were done using high resolution simultaneous atomic emission spectrometer (Spectro Arcos, Germany) with ICP and DC arc as the excitation sources and a charge-coupled device (CCD) as the detector. It has continuous wavelength coverage of 130-800 nm with resolution of 0.01 nm from 130-450 nm and 0.02 nm from 450-800nm (Adya et al. 2016). The experimental details are described in Chapter 2.

4.2.4 Characterizations of membranes

The void volumes (vol %) of the pristine, hydrazine grafted, and Pd NPs embedded membranes were measured by using wetting liquid “porefil” liquid ($\gamma = 0.016\text{Nm}^{-1}$) supplied by Benelux scientific, Belgium by using the following equation.

$$\text{Void Volume} = \frac{(w_1 - w_d)}{\rho_l V_m} \times 100 \quad (1)$$

Where w_1 , w_d , ρ_l and V_m were weight of porefil liquid wetted sample, weight of the dry membrane, density of porefil liquid, and volume of the membrane sample, respectively. The membrane samples were immersed in porefil liquid of having known dimensions (V_m) and weight (w_d) for the period of 4-5h. After that the excess liquid clinging on the surface of the membrane removed and weighed to obtain the weight of wetted membrane (w_1). The dimensions of the membrane did

not change after wetting in porefill liquid. The pore size distributions were measured by capillary flow porometry (CFP) using porefill liquid as described in chapter 2. by using the equation 4, Chapter 2

The surface morphologies of pristine and Pd NPs embedded membranes were obtained by FE-SEM. The samples were coated with gold prior to microscopy to make them conducting. The elemental mappings of Pd across the cross-section and surface were carried out by energy dispersive spectroscopy (EDS). The acidity/basicity of the membrane samples were measured by HCl-NaOH titrations and ^{137}Cs radio tracer was used to measure the the ion-exchange capacity of the cation-exchange membrane.

4.2.5 Reduction of U(VI) ions

The reduction of U(VI) ions was carried out in a double jacketed glass vessel kept at constant temperature using thermostat bath as shown in Figure 4.1. The reaction solution contains equal volumes (8mL each) of $0.1 \text{ mol L}^{-1} \text{UO}_2(\text{NO}_3)_2$ solution at $\text{pH} = 2$ and 1 mol L^{-1} formic acid. This solution was poured in the reaction vessel kept at a fixed temp. (25, 40, 50, and 60°C). The fixed dimensions ($1 \times 2 \text{ cm}^2$) or known weights having Pd NPs loaded membranes were immersed in to the reaction vessel after attaining desired temperatures. The immersion time was taken as start time. The UV-Vis spectra given in Figure 4.2, showing no characteristic absorption peaks of U^{4+} ions, indicates no reduction of U(VI) ions was observed without catalyst and with catalyst at room temp. The progress of U(VI) ions reduction was monitored by taking 1 mL aliquot from the reaction solution at a fixed time interval, and UV-Vis spectra of these samples were recorded after diluting this to 3 mL by adding $\text{pH} = 2$ solution. Similar experiment was carried out using high intensity ultrasonication by immersing SS horn in the reaction solution. This instrument was obtained from, (Ultrasonic Laboratory Processor, model SONAPROS PR-500MP, SS Horn having

12 mm dia., 20 ± 3 KHz) Oscar Ultrasonics Pvt. Ltd., India. The reaction solution temp. at 150 W power sonication was increased to 60°C . The Pd NPs embedded membrane was introduced after achieving the required temperature.

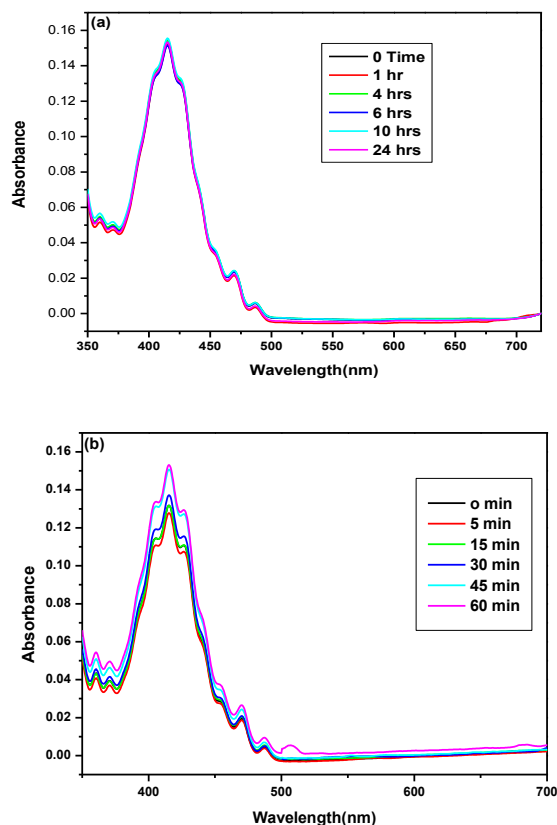


Figure 4.2 Successive UV–Vis spectra showing reduction of UO_2^{2+} to U^{4+} ions using formic acid: (a) in the presence of Pd NPs embedded hydrazine-grafted PP membrane at room temperature and (b) in the presence of hydrazine-grafted membrane without Pd NPs at 50°C as a function of time.

The reaction solution was circulated to Z flow cell with peristaltic pump with constant speed (2 mL min^{-1}) to monitor the reaction online and successive UV–Vis absorption spectra were recorded at 5 min time intervals. The most intense peak of U(IV) ion at 665 nm was used for kinetic experiments and was calibrated by measuring the U(IV) ions concentration by electro analysis. To prevent back oxidation of U(IV) ions to U(VI) ions during long storage, the solution

was kept in a freezer and UV-Vis spectra was monitored again to ensure the extent of oxidation of U^{4+} ions.

The quantification of formation of U(IV) ions was carried out by controlled potential coulometric method using CHI 760D electrochemical work station. The working electrode was hollow cylindrical platinum wire gauze of 0.07 m height and 0.032 m diameter. A thin platinum wire was used as counter electrode. The reported potentials were with respect to the saturated Ag/AgCl. All the experiments were carried out at room temperature. The concentration of U^{4+} ions was determined employing controlled potential coulometry. The electrode was submerged in 1 mol L⁻¹ H₂SO₄ and was anodized at 1.4 V for 15 min to activate platinum electrode. This was immediately followed by cathodization in the same electrolyte at 0.150 V vs. Ag/AgCl until the current reached the background level of 25 μ A. The aqueous samples (25 mL of solution of U^{4+} ions in formic acid) were subjected to the oxidation of U(IV) to U(VI) ions at potential of +1.4V. Electrolysis was terminated at the background current level. The total charge obtained for the oxidation was noted and the amount of U(IV) oxidized to U(VI) ions was calculated using Faraday's first law of electrolysis.

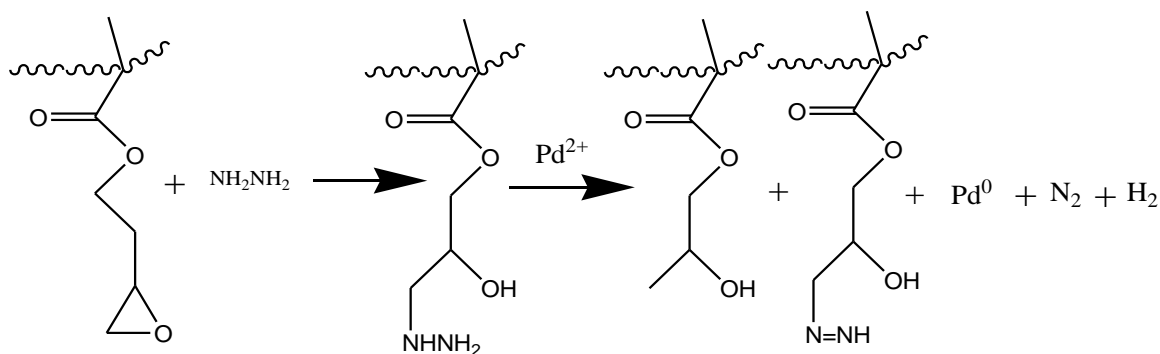
$$m = \frac{M \times Q}{n \times f} \quad (2)$$

Where, 'm' is the mass of the analyte, 'M' is the molar mass of the analyte, 'F' (= 96487 C) is the Faraday constant, 'n' is the number of electron changed in the redox process, 'Q' is the amount of electrical charge consumed/produced.

4.3 Results and discussion

4.3.1 Characterizations of Pd NPs embedded membranes

The self-reducing neutral membrane and cation-exchange membranes were the two membranes prepared in the present work. This class of pore-filled membranes had two components *i.e.* microporous base membrane that provided support to the cross-linked microgel (poly(GMA)) holding Pd NPs in pores of the host PP membrane and hydrazine which was anchored to the poly(GMA) to induce self-reducing property. The mass-gains (anchoring yields) obtained from the increase in weight of the pore-filled membrane with respect to pristine membrane was found to be 85 ± 5 wt % ($n = 3$, where n is no. of exp). In pores of the PP membrane, the anchoring occurred through hydrogen abstraction from base poly(propylene) chains and also cross-linked homopolymer poly(GMA) chains interpenetrating network structure was formed in pores of the membrane. The hydrazine units were anchored via epoxy ring opening of poly(GMA). The Pd NPs were formed by just dipping the hydrazine-grafted membrane in a PdCl_2 solution. The nitrogen contents of the hydrazine grafted PP based membrane samples were found to be 4.2 and 2.1 wt % before and after saturation loading of Pd^0 content, respectively. This seems to suggest that all hydrazine units were not utilized for the reduction of Pd^{2+} ions. The possible reactions during different chemical treatments involved in the formation of Pd NPs in the membrane are shown in Scheme 4.1.



Scheme 4.1 Chemical modifications involved in the formation of Pd NPs in the neutral PP membrane.

The void volume of the pristine membrane was 86 v/v%, hydrazine grafted membrane was found to be 35 v/v% which is significantly lower than the pristine PP membrane. However, there was no significant change in the void volume of membrane sample after the formation of Pd NPs (34 v/v%). This suggested that the catalytic membrane had a porous interior. To study the change in distribution of through-pore sizes, the pristine, hydrazine-grafted, and Pd NPs embedded membrane samples were subjected to capillary flow porometry. The pore size distributions are shown in Figure 4.3 in which flow (%) given in y-axis is a measure of number density. Using the pore size distributions, three important observations were made (i) Pd NPs membrane had through pores, (ii) pore-size reduced after hydrazine grafting to 0.18 μm but did not further reduce after formation of Pd NPs, and (iii) pore-size distribution became narrower after hydrazine grafting which was further improved after formation of Pd NPs.

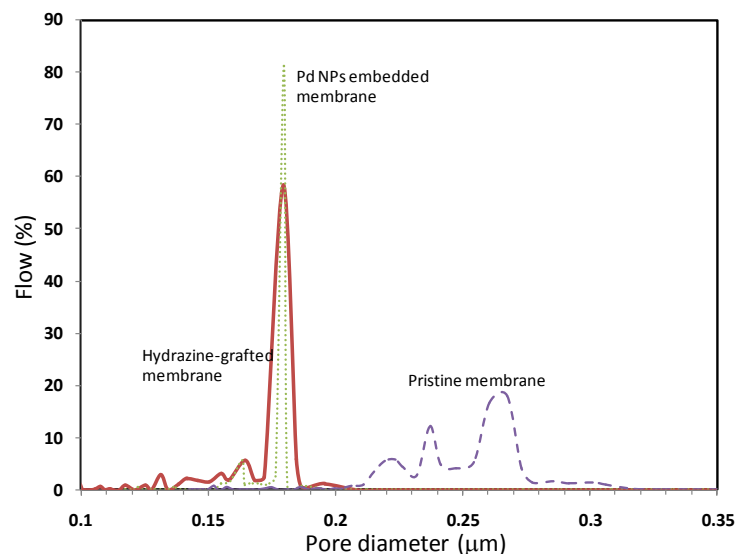


Figure 4.3 Comparison of pore-size distributions obtained by capillary flow porometry in the pristine poly(propylene) membrane, hydrazine-grafted poly(propylene)membrane, and Pd NPs embedded membrane samples.

As shown in Figure 4.4, the saturation Pd⁰ loading in the hydrazine grafted membrane was found to be $124 \pm 1 \text{ mg g}^{-1}$ after equilibration with 0.01 mol L^{-1} PdCl₂ solution at pH = 3 for 15h. From the nitrogen analysis, the left-over nitrogen even after saturation loading suggests that all hydrazine units were not utilized for the reduction of Pd²⁺ ions. This was also confirmed by the basicity of the hydrazine-grafted membrane which was found to $1.55 \pm 0.05 \text{ meq g}^{-1}$ and was reduced to $0.5 \pm 1 \text{ meq g}^{-1}$ after the formation of Pd NPs. The statistical uncertainty quoted is for duplicate experiments ($n = 2$). The residual hydrazine could facilitate the formic acid decomposition (Li et al. 2013). To explore the possibility of increasing saturation Pd⁰ loading capacity of the membrane. The anchoring yield of poly(GMA) was increased by increasing its conc. in the polymerizing solution, the mass gain was increased from $85 \pm 5 \text{ wt\%}$ to $155 \pm 5 \text{ wt\%}$, similarly the Pd saturation loading capacity was also increased from $124 \pm 1 \text{ mg g}^{-1}$ to $200 \pm 5 \text{ mg g}^{-1}$. However,

the Pd NPs loaded membrane with 85 wt% mass-gain was used for further studies as the porosity would be reduced and pores may be blocked in the membrane sample having higher mass gain.

As shown in Figure 4.4, the Pd⁰ loading was fast within 30 min equilibration (82 mg g⁻¹) and became very slow thereafter. This suggested that the Pd⁰ content in the membrane could be controlled by its equilibration time in Pd²⁺ salt solution. The saturation Pd⁰ loading of hydrazine grafted membrane was 124 ± 1 mg g⁻¹. It is evident from the Figure 4.4 that the desirable amount of Pd⁰ could be loaded as a function of equilibration time but could be loaded only up to the saturation loading. The expected Pd⁰ saturation loading in the hydrazine grafted membrane was 152 mg g⁻¹ based on 50% reduction of nitrogen content, which was comparable to the experimental saturation loading 124 ± 1 mg g⁻¹. Thus, the most of the Pd⁰ content (80%) was retained in the membrane in the form of Pd NPs.

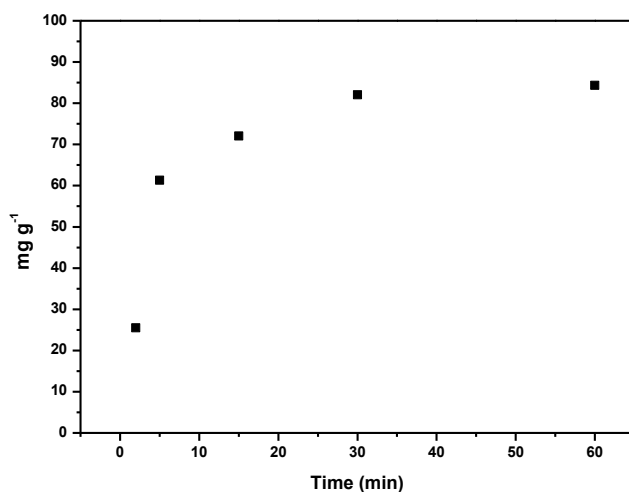
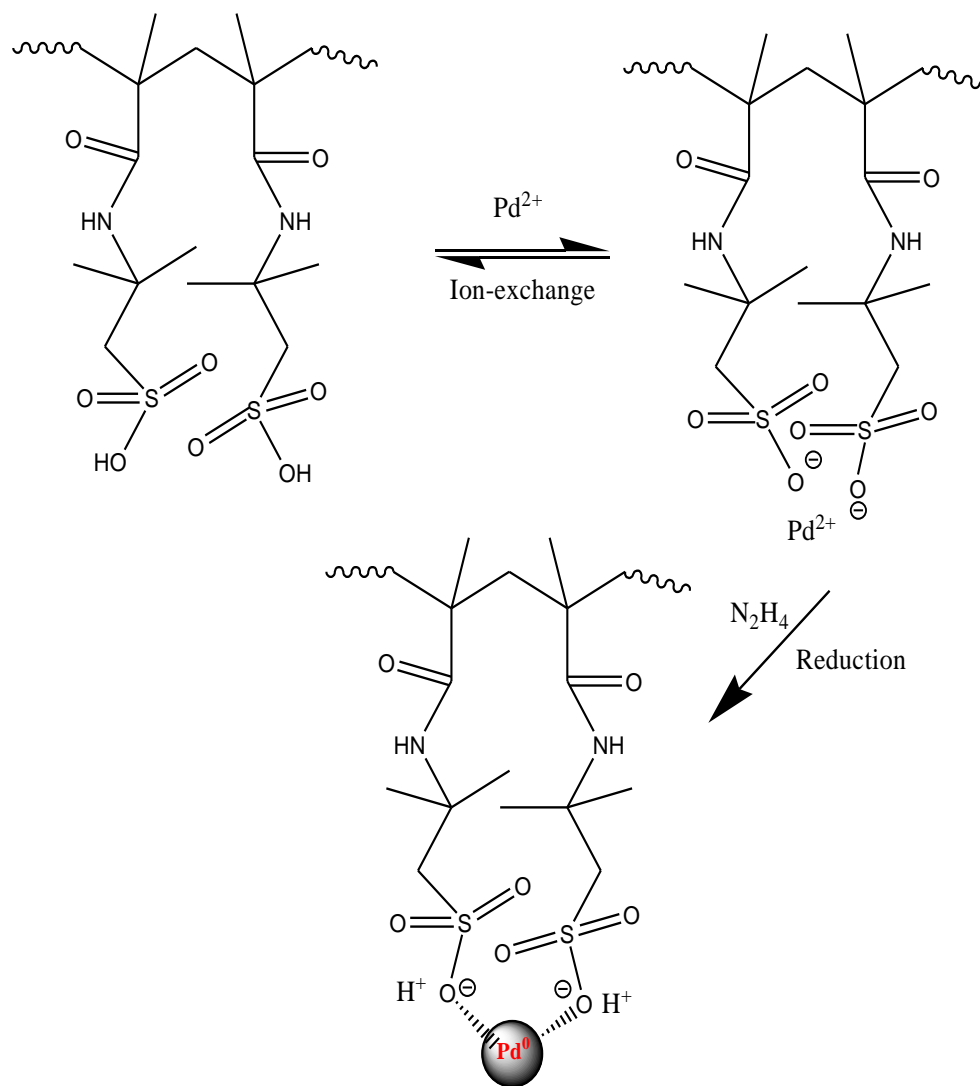


Figure 4.4 Variation of Pd⁰ content in the hydrazine-grafted membrane sample as a function of equilibration times in the aqueous solution containing 0.01 mol L⁻¹ PdCl₂ at pH = 2.

The mass-gain of cation-exchange membrane was found to 170 ± 5 wt% in the same host PP microporous membrane and the ion-exchange capacity (acidity) was found to be 1.6 ± 0.2 meq

g^{-1} . The Pd NPs formation in this membrane followed two steps process as shown in Scheme 4.2. First, the precursor Pd^{2+} ions were loaded in the membrane by the ion-exchange mechanism and then reduced subsequently with hydrazine.

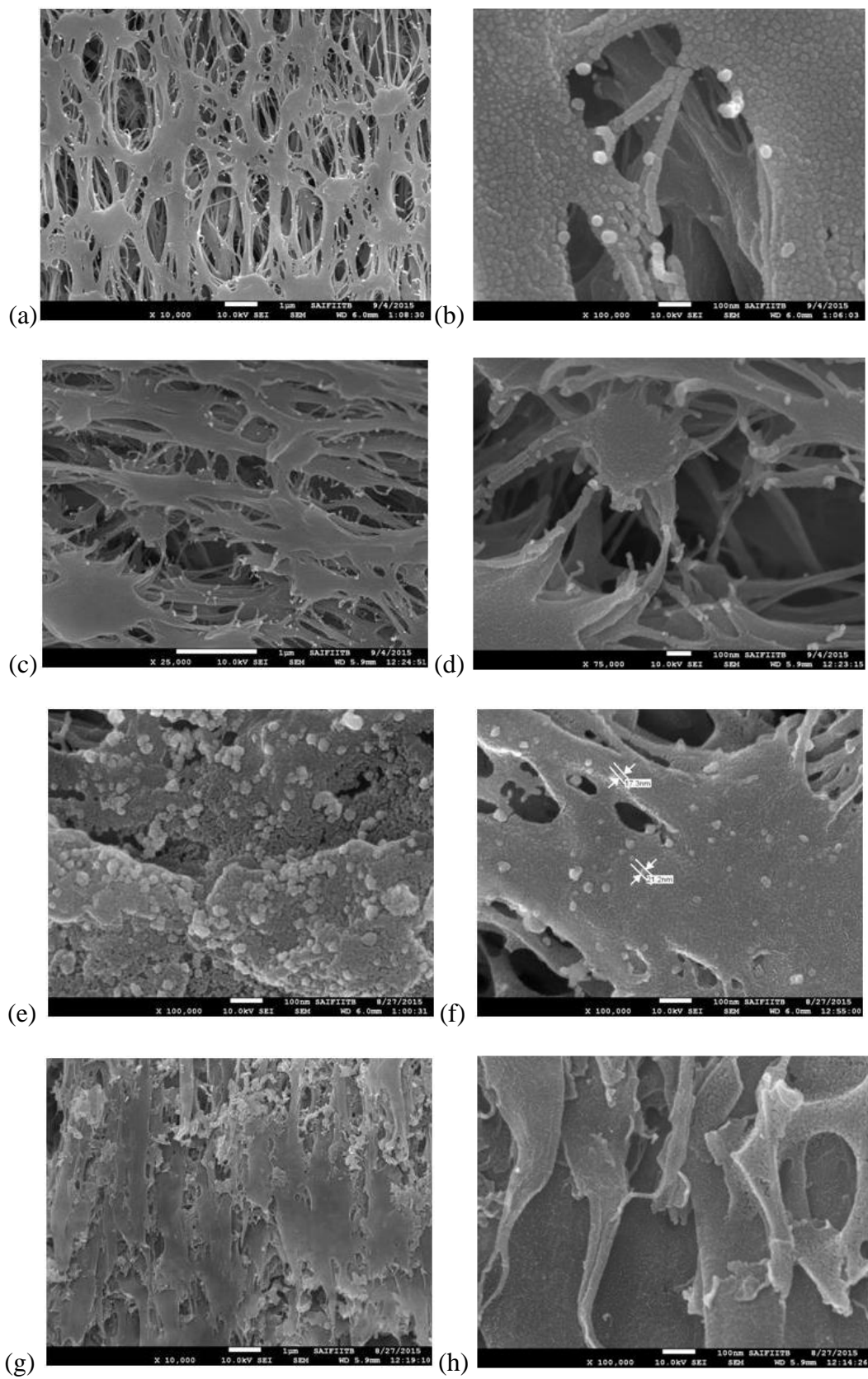


Scheme 4.2 Representative steps involved in the formation of Pd NPs in the cation-exchange membrane.

The Pd^0 saturation loading in the cation-exchange membrane sample was $13 \pm 2 \text{ mg g}^{-1}$, which was considerably lower than that in the hydrazine-grafted membrane sample. The loading capacity 6-

7 times lower than expected saturation loading. This may be due to either inefficient reduction of Pd^{2+} ions in the acidic environment or slow reduction process leading to a substantial loss of Pd^0 seeds before locking as NPs in the membrane (Goia and Matijević 1998). The reduction of Pd^{2+} ions in hydrazine grafted membrane would be fast and dependent only on the diffusion of Pd^{2+} ions in the pores of membrane leading to a high Pd NPs content. However, in the case of cation-exchange membranes the Pd^0 loading could be improved by repeating cycle of loading of Pd^{2+} ions and subsequent reduction with hydrazine to form Pd^0 and regenerating ion-exchange sites as shown in Scheme 4.2.

FE-SEM imaging and elemental mapping of N and Pd by EDS were used to characterize the Pd NPs formed on the surface as well as in the cross-section of the hydrazine grafted membrane. The EDS images given in Figure 4.5 (i, j & k) suggest a uniform grafting of hydrazine and uniform formation of Pd NPs throughout the membrane matrix. As shown in Figure 4.5 (a-h), the comparison of the FE-SEM images of Pd NPs loaded hydrazine grafted PP membrane with that of the pristine PP membrane indicated high porosity of the Pd NPs embedded neutral membrane as expected from the experimentally measured void volume. The high porosity having Pd NPs embedded membrane helps in improving the catalytic activity by easy accessible. From Figure.4.5 (e & f), it is seen that 17 ± 4 nm size Pd NPs were formed on the surfaces of PP membrane after saturation loading. However, the size of Pd NPs were much smaller (<5 nm) at the interior matrix and could be distinguished from the polymer matrix only by EDS mappings, see Figure. 4.5 (i, j & k). The sizes of Pd NPs were much smaller than pore size ≈ 180 nm that ensured possibility for the reactants and catalyst to come in a contact.



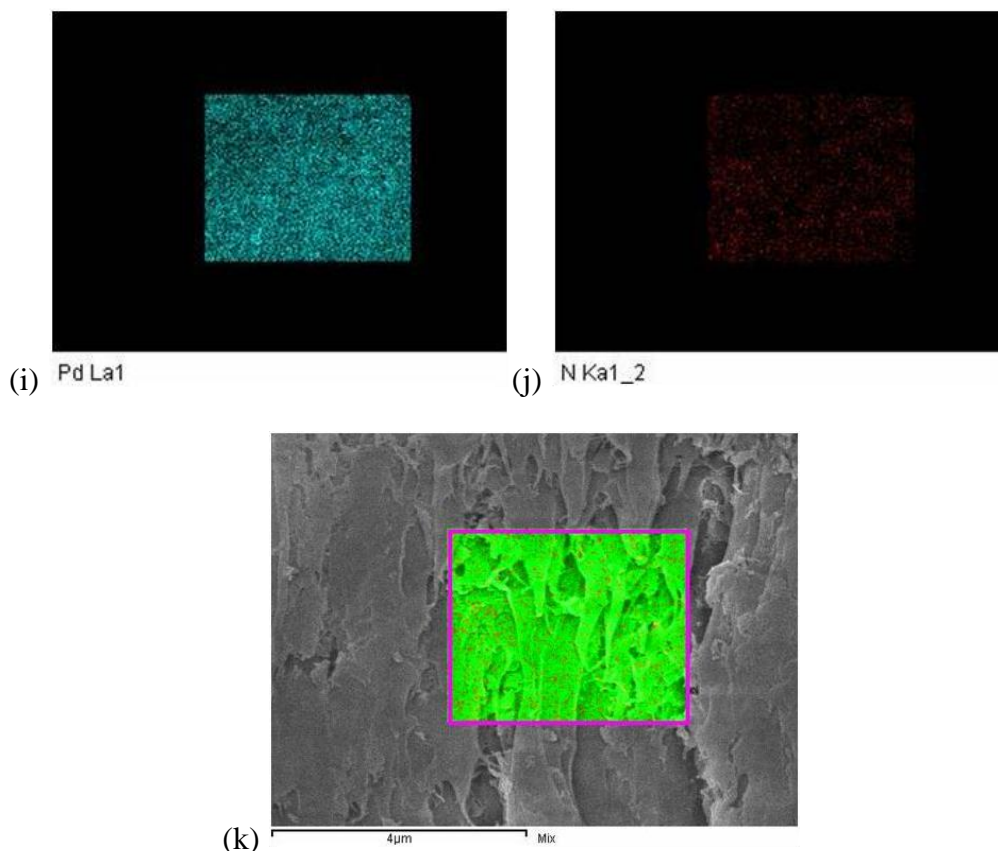


Figure 4.5 The representative FE-SEM images of surface of pristine PP membrane (a & b), cross-section of pristine PP membrane (c & d), surfaces of Pd NPs embedded hydrazine grafted membrane (e & f), cross-section of Pd NPs embedded hydrazine-grafted membrane (g & h), and EDS elemental mappings of nitrogen (i), Pd (j) and mixture of N and Pd at cross-sections ($4 \times 4 \mu\text{m}$) of the same Pd NPs embedded hydrazine-grafted membrane (k).

The physical structure of the membrane and distribution of Pd NPs in the cation-exchange membrane was also studied using FE-SEM/EDS. It is seen from the FE-SEM images of surface and cross-section of the PP based cation-exchange membrane shown in Figure 4.6 that this membrane had a porous physical structure similar to hydrazine grafted PP membrane and Pd NPs were uniformly distributed throughout the matrix as indicated by the Pd elemental mapping. Thus, Pd NPs in both the membrane could be compared for their catalytic activity.

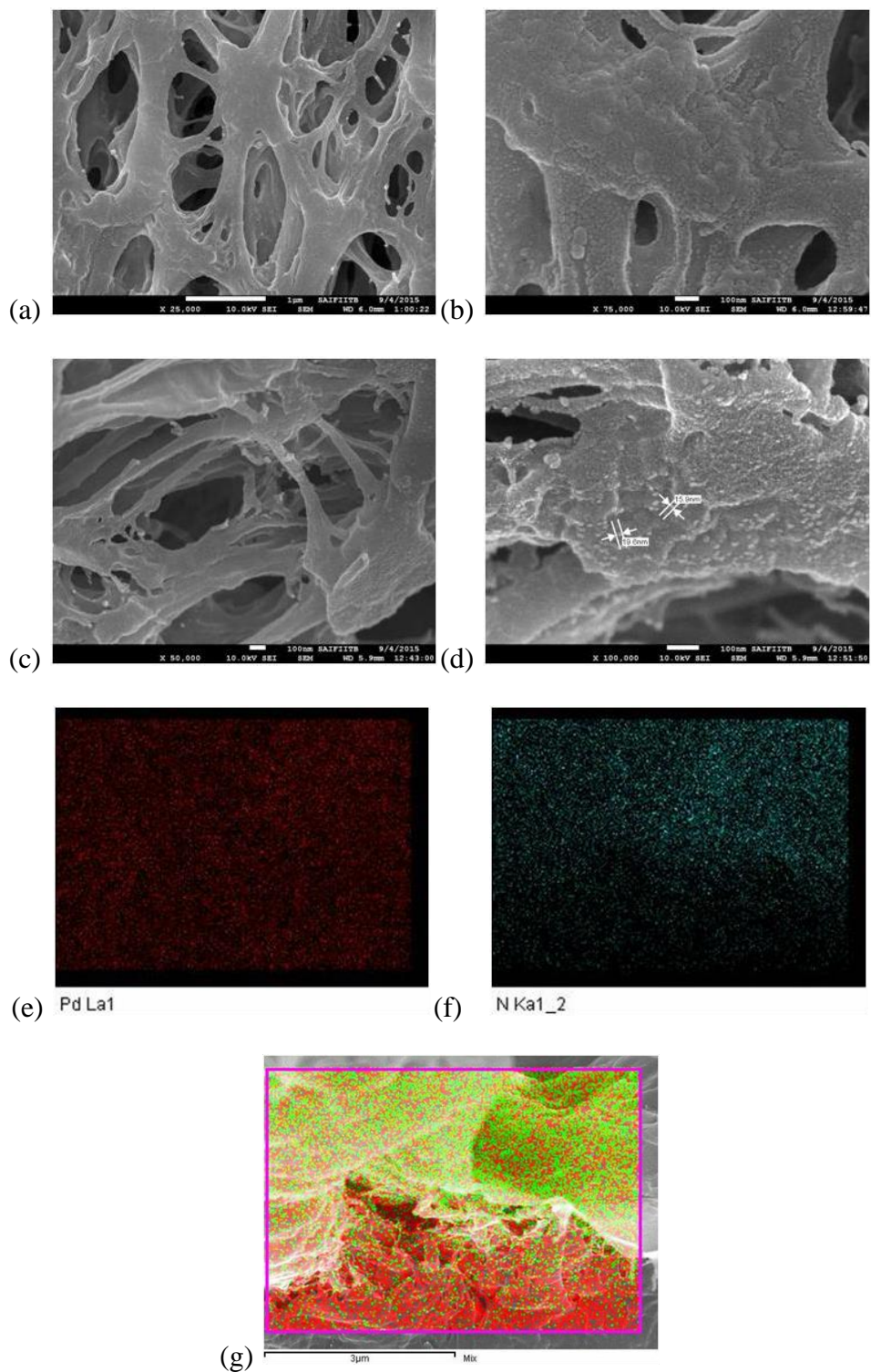
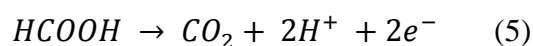
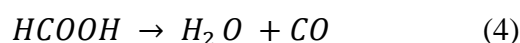
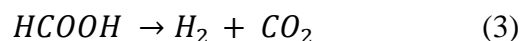


Figure 4.6 Representative FE-SEM images of surface (a & b), cross-section (c & d) of PP based cation-exchange membrane, and elemental mappings of Pd (e), N (f), and mixture of Pd and N along the cross-sections of the same PP membrane (g).

4.3.2 Comparison of catalytic activities of Pd NPs embedded membrane.

Formic acid is used as a reducing agent for the UO_2^{2+} ions reduction on Pd NPs surface. Formic acid is a two electron transfer reductant with a potential -0.199 V for $\text{HCOOH}/\text{CO}_2, 2\text{H}^+$ couple. And the reduction potential for $\text{UO}_2^{2+} + 2\text{e}^- \rightarrow \text{U}^{4+}$ couple is 0.41 V vs. standard hydrogen electrode (Toraishi et al. 2007). Therefore, the reduction should be feasible but it was observed that in absence of Pd catalyst the reaction did not occur at room temperature, as shown in Figure 4.2(a). This seems to suggest a high activation barrier in the UO_2^{2+} ions reduction. It was known from the literature that, Pd NPs catalyze the decomposition of formic acid (Mori et al. 2013; Gralec and Lewera 2016). As given below, the Pd NPs decomposes formic acid in two modes (Eq 3 & 4); the carbon monoxide produced during dehydration of formic acid can deactivate the Pd surface. Therefore, dehydrogenation is very important for improving the life time of the catalyst.



To understand the effect of temperature on reduction of UO_2^{2+} ions by Pd NPs, the reaction was carried out at three different temperatures (40°C , 50°C , and 60°C) and analysed the conc. of UO_2^{2+} ions as a function of reduction time with formic acid by pseudo-first-order kinetic equation that is normally applicable in the presence of excess of reducing agent as discussed in chapter 3. As shown in Figure.4.7 that the variations of $\ln[\text{U(VI)}]_t/[\text{U(VI)}]_0$ as a function of reduction time with formic acid in the presence of Pd NPs embedded PP membrane at different temperatures is reasonably linear as expected from first-order kinetic equation given below and could be used for a qualitative comparison, though correlation coefficients ($R^2 = \approx 0.98$) indicated not the best fits.

$$\ln \frac{[U(VI)]_t}{[U(VI)]_0} = -kt \quad (6)$$

Where $[U(VI)]_t$ and $[U(VI)]_0$ represent conc. of UO_2^{2+} ions at time t and initial, respectively, t is reduction time, and k is apparent first-order reduction rate constant. As k is dependent on the amount of Pd catalyst, the values of k were normalized with the amount of Pd^0 to obtain catalytic activity ($s^{-1}g^{-1}$) for studying the effect of variables involved in the reduction of UO_2^{2+} ions with formic acid.

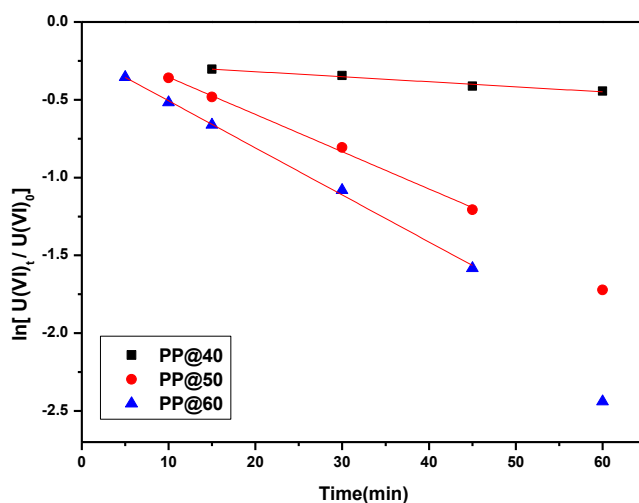


Figure 4.7 Variation of logarithm of $[U(VI)]_t/[U(VI)]_0$ as a function of reduction time with formic acid in the presence of Pd embedded PP membrane at 40, 50, 60°C temp. $[U(VI)]_t$ and $[U(VI)]_0$ represent conc. of UO_2^{2+} ions at time t and initial, respectively.

The values of catalytic activities towards UO_2^{2+} ions reduction of Pd NPs embedded on hydrazine grafted membrane at three different temperatures 40, 50, and 60°C were found to be 0.11, 0.39, and $0.46 s^{-1}g^{-1}$, respectively. The catalytic activities suggest that, there was a significant jump of the catalytic activity at 50°C and slowly increased thereafter. And it was also found from the experiments that the critical amount of Pd (20 mg) needed for the reduction to take place at 50°C.

As shown in Figure.4.8, the catalytic activity of Pd NPs in UO_2^{2+} reduction increased with increase in amount of Pd NPs to attain optimum value $0.39 \text{ s}^{-1}\text{g}^{-1}$, but decreased subsequently on further increase of the Pd NPs content. This could be indicative of the onset of formic acid decomposition via unfavourable reactions 5&6 in the presence of high amount of Pd NPs catalyst. Thus, an optimum amount of Pd NPs is required for the efficient reduction. For comparison, the catalytic activity of Pd/C (5 wt%) was measured and found to be $0.13 \text{ s}^{-1}\text{g}^{-1}$ under similar conditions, which was significantly lower than the $0.39 \text{ s}^{-1}\text{g}^{-1}$ obtained using the Pd NPs embedded hydrazine grafted membrane.

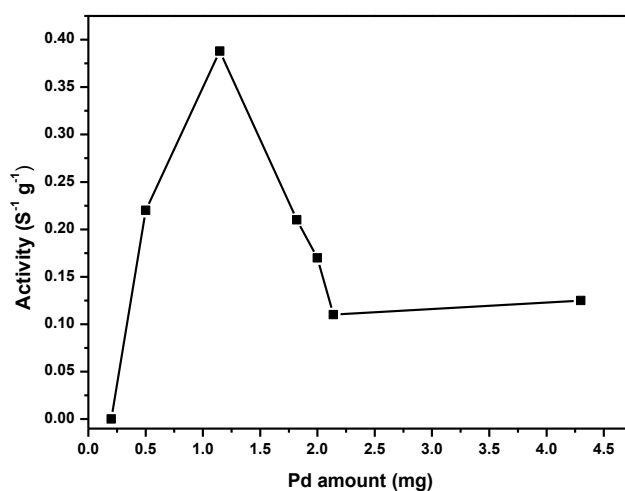


Figure 4.8 Variation of catalytic activity of the Pd NPs embedded in hydrazine-grafted membrane as a function of Pd^0 content in the reduction of U(VI) ions by formic acid to U(IV) ions at 50°C .

Contrary to Pd NPs in the hydrazine grafted membrane, the Pd NPs in the cation exchange membrane did not show any catalytic activity towards UO_2^{2+} ions reduction at any given temperature with formic acid (Figure 4.9(a)). To ensure that the UO_2^{2+} ions reduction is not affected by the conc. of Pd NPs in the cation-exchange membrane, the Pd content was boosted to approximately four times by repeating a cycle of Pd^{2+} ions loading and reduction in the cation-

exchange matrix four times. Even using this Pd NPs loaded membrane, the extent of UO_2^{2+} reduction was not very significant (less than 5% in 60 min) as shown in Figure 4.9(b).

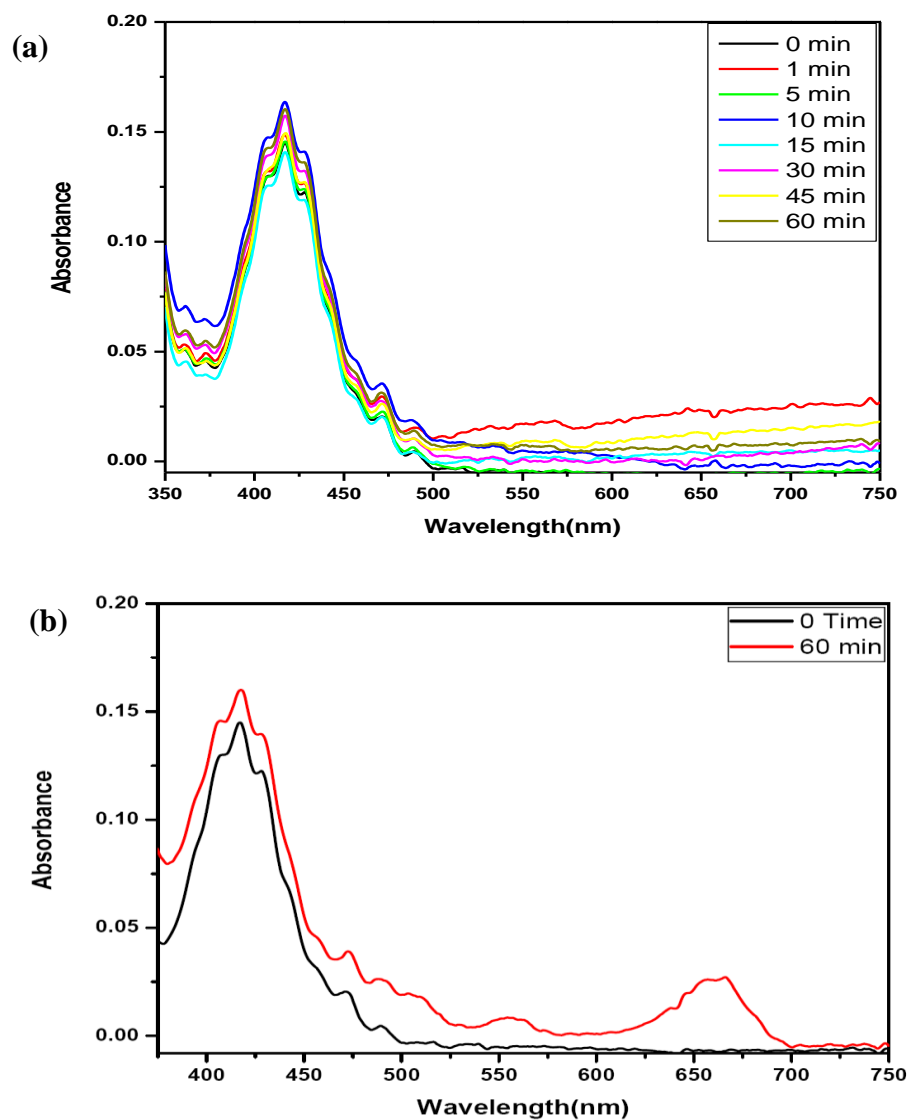
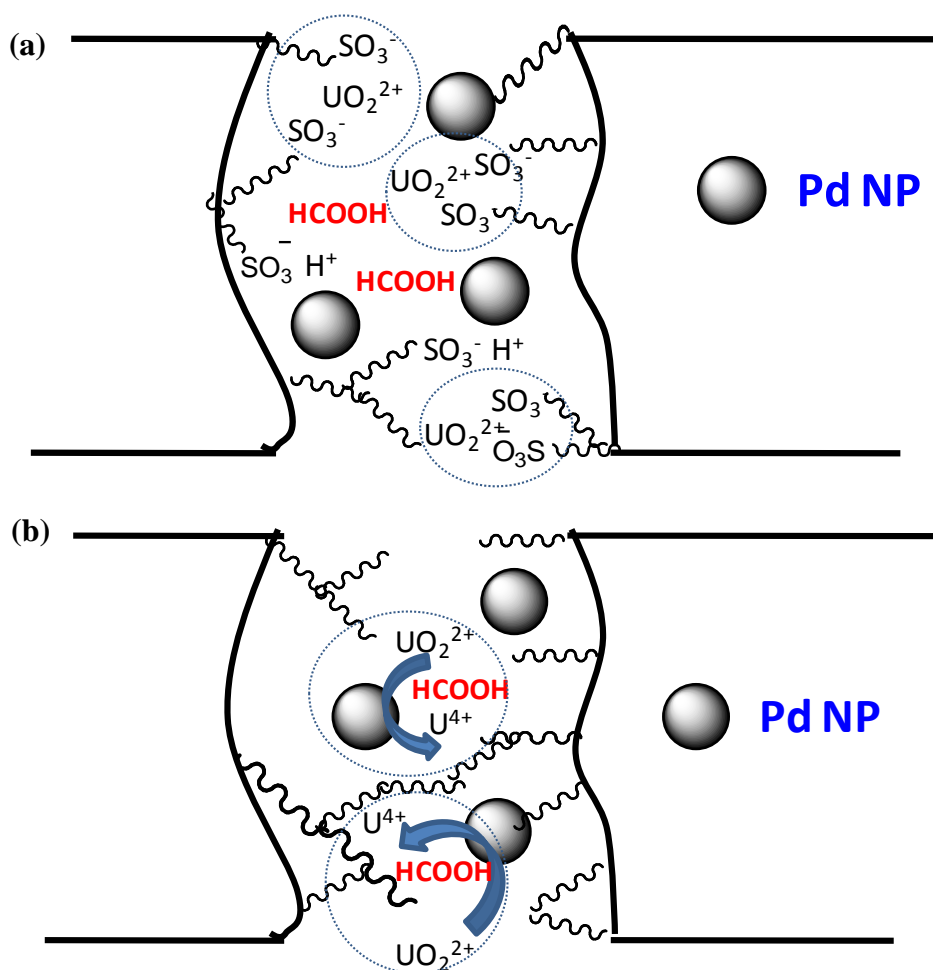


Figure 4.9 UV-Vis spectra showing no reduction of U(VI) with formic acid in the presence of Pd NPs immobilized in the cation-exchange membrane at 50°C. Figures. a & b present the experiments carried out using the cation-exchange membrane loaded with Pd NPs in one cycle and four cycles, respectively.

The absence of catalytic activity of Pd NPs in the cation-exchange membrane may be due to strong interaction of uranyl ions (UO_2^{2+}) with the fixed negative charge sites ($-\text{SO}_3^-$) in cation-exchange matrix which would hinder UO_2^{2+} ions interactions with Pd NPs required for the reduction with formic acid as shown in Scheme 4.3. It is also important to note that, the uranyl ions reduction in the presence of hydrazine grafted membrane would be enhanced due to basic local environment (caused by residual hydrazine), which helps in the formic acid decomposition and efficient reduction of UO_2^{2+} ions.



Scheme 4.3 Preferential UO_2^{2+} ions interactions with sulfonic acid groups in a pore of Pd NPs embedded cation-exchange membrane (a), and with Pd NPs in hydrazine-grafted membrane (b).

4.3.3 Quantification of U(VI) ions reduction with formic acid

The catalytic conversion of UO_2^{2+} ions to U^{4+} ions by formic acid in presence of Pd NPs embedded hydrazine grafted PP membrane at 50°C was monitored by online spectrophotometry using the setup shown in Figure 4.1. The spectra recorded at each 5 min interval time was given in Figure 4.10. It is obvious from Figure 4.10 that the absorbance peaks of U^{4+} ions increased continuously as a function of reduction time and saturated at 70 min. It was observed that $>99\%$ UO_2^{2+} ions were reduced to U^{4+} ions during 70 min reduction time under the conditions stated in the experimental section.

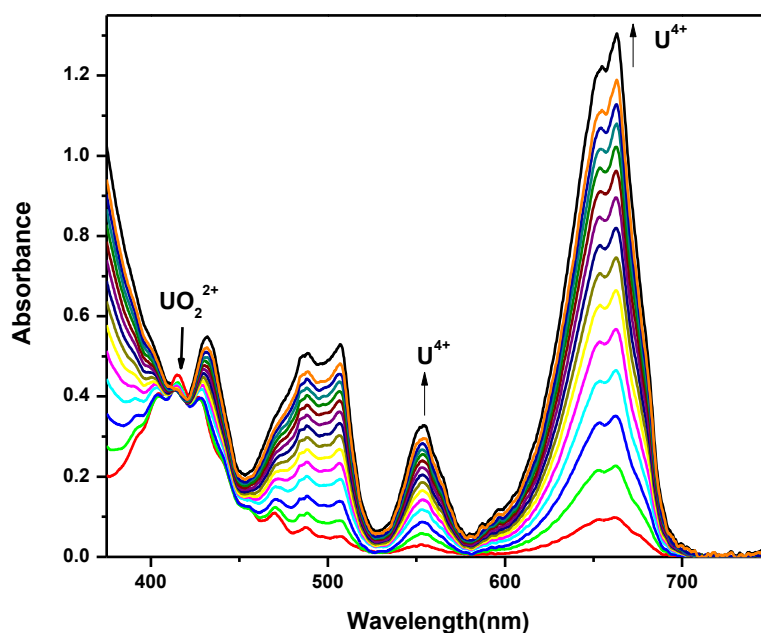


Figure 4.10 The successive UV–Vis spectra obtained online after every 5 min intervals during 70 min reduction of U(VI) ions with formic acid in the presence of Pd NPs embedded hydrazine-grafted PP membrane at 50°C .

The comparison of absorption peaks of U^{4+} ions given in Table 4.1, the red shift in absorption peaks observed in solution with respect to that of expected in a solution having no complexing ions

(Misbah and Iftikhar 2013). This could be due to the formation of complex between un-used formate ions with U^{4+} ions leading to red shifting of the absorption peaks corresponding to f-f transitions in the UV-Vis spectrum. The formation of formate complex would provide stability to U^{4+} ions against oxidation during storage under ambient conditions.

Table 4.1 Comparison of absorption energy levels for U(IV) ion in solution (Misbah and Iftikhar 2013) and observed in the present work due to its complex formation with formate.

Transition	Expected λ (nm)	Observed λ (nm)
$^3H_4-^1G_4$	644	665
$^3H_4-^1D_2$	631	654.3
$^3H_4-^3P_1$	546	555
$^3H_4-^1I_6$	471	489.4
$^3H_4-^3P_2$	427	434.6

The oxidation of U^{4+} ions occurs readily at ambient conditions in solution. Therefore, the storage of solution is difficult and U^{4+} ions have to be precipitated as UO_2 by adjusting pH to 9 with NaOH.

In the present work, the reaction solution was stored at $-4\ ^\circ\text{C}$ for a month. The UV-Vis spectra of

freeze-stored solution indicated that U^{4+} ions did not oxidize back to UO_2^{2+} ions during one month storage (see Figure 4.11(a)). However, the same reaction solution, U^{4+} ions were oxidized back completely to UO_2^{2+} ions kept at room temperature (25°C) for 7 days (see Figure 4.11(b)).

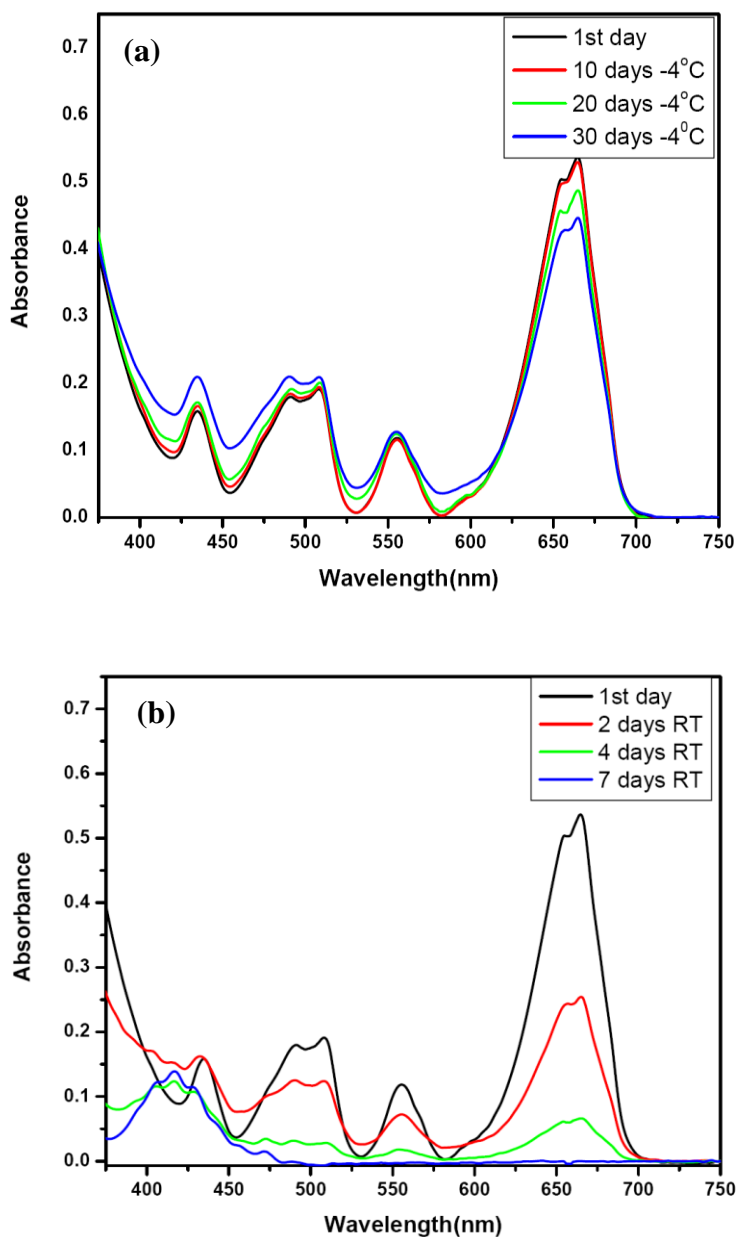


Figure 4.11 UV-Vis spectra showing the stability of absorbance peaks of U(IV) ions stored at -4°C (a) and at room temperature (25°C) (b).

The reusability and reproducibility are very important factors for synthesizing the catalyst. The reusability of the Pd immobilized catalyst synthesized in this work was tested by repeating cycle of UO_2^{2+} ions reductions at 50°C under identical conditions for 1 h. UV–Vis spectra obtained after the end of each cycle are compared in Figure. 4.12. It was seen from this comparison that the catalytic activity of the Pd NPs embedded PP membrane did not deteriorate even after five cycles. The Pd NPs embedded in the PP membrane was stored for three months under ambient conditions. The experiments showed that the catalytic activity of this sample did not change significantly after storing for three months.

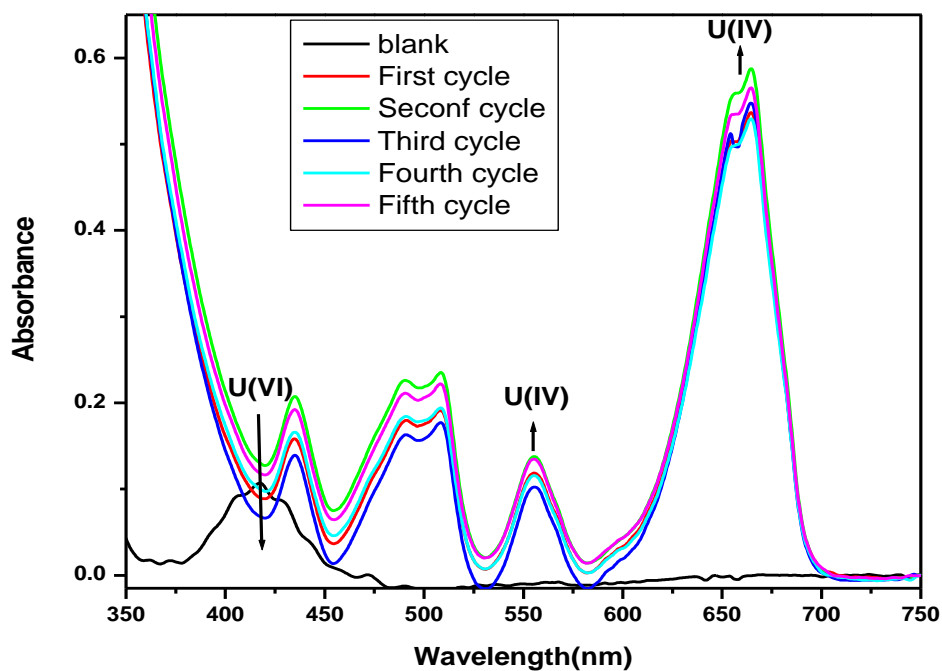


Figure 4.12 UV–Vis spectra showing the absorbance peaks corresponding to U(IV) ions after 1 h successive cycles of the reduction of U(VI) ions with formic acid in the presence of Pd embedded PP membrane.

4.3.4 Kinetics of reduction

Pseudo-first-order kinetic model is used to analyze the kinetic of reduction processes in general, using Eq. (7). However, it is known that the reaction/sorption kinetics obeys pseudo-first-order kinetics at high initial conc. of solute and pseudo-second-order kinetics at lower initial concentration of reactant/solute (Azizian 2004; Das et al. 2009). Also, the reduction would proceed in the host polymer matrix having interconnecting tortuous pores. This may lead to a diffusion-controlled reduction process. To understand the controlling mechanism operating in the reduction process, the reduction profiles of the UO_2^{2+} ions were analyzed in terms of pseudo-first-order, pseudo-second-order, and inter-particle diffusion kinetics models using linearized Eqs. (7)-(8), respectively (Das et al. 2009).

$$\frac{t}{[\text{U(VI)}]_t} = \frac{1}{k_2[\text{U(VI)}]_e^2} + \frac{t}{[\text{U(VI)}]_e} \quad (7)$$

$$[\text{U(VI)}]_t = k_d t^{1/2} \quad (8)$$

Where $[\text{U(VI)}]_t$ and $[\text{U(VI)}]_e$ represent concentration of UO_2^{2+} ions at time t and at equilibrium, respectively. k_2 and k_d are the apparent pseudo-second-order rate constant and apparent diffusion rate constant, respectively, and t is the reduction time. The analyses of reduction kinetic using these three kinetic models under identical conditions in the presence of Pd NPs in different hosts are given in Table 4.2. The reduction of UO_2^{2+} ions with formic acid in the presence of Pd NPs embedded membrane was fast and expected to follow the pseudo-first-order kinetics. Contrary to this, the reduction profile followed a pseudo-second-order kinetics. The switching of UO_2^{2+} ions reduction kinetic to diffusion-controlled process was observed depending upon temperature of the reacting solution and amount of Pd NPs loaded in the PP membrane. As can be seen from Table 4.2, the reduction followed the pseudo-second-order at lower temperature (40°C) and switched to

diffusion controlled kinetic with increase in temperature to 50 °C, which was again switched to pseudo-first-order on increasing the content of Pd NPs from 1.82 mg to 4.30 mg. However, high amount of Pd NPs is not desirable as it would promote decomposition reactions shown in Eqs.(3) & (4).

Table 4.2 Analyses of the kinetics of U(VI) ions reduction with formic acid in the presence of Pd NPs hosted in the hydrazine-grafted PP membrane. The chemical conditions were kept constant and varied either temperature or catalyst.

Temp. (Pd amount)	Plot	Correlation coefficient (R ²)	Kinetics of sorption
40 °C (1.15 mg)	$\ln [(U(VI))_t/[U(VI)]_0]$ vs. t	0.971	Pseudo-first-order
	$t/[U(VI)]_t$ vs. t	0.998	Pseudo-second-order
	$[U(VI)]_t$ vs. $t_{1/2}$	0.968	Diffusion controlled
50 °C (1.15 mg)	$\ln [(U(VI))_t/[U(VI)]_0]$ vs. t	0.988	Pseudo-first-order
	$t/[U(VI)]_t$ vs. t	0.869	Pseudo-second-order
	$[U(VI)]_t$ vs. $t_{1/2}$	0.999	Diffusion controlled
60 °C (1.15 mg)	$\ln [(U(VI))_t/[U(VI)]_0]$ vs. t	0.972	Pseudo-first-order
	$t/[U(VI)]_t$ vs. t	0.759	Pseudo-second-order
	$[U(VI)]_t$ vs. $t_{1/2}$	0.999	Diffusion controlled
50 °C (0.51 mg)	$\ln [(U(VI))_t/[U(VI)]_0]$ vs. t	0.993	Pseudo-first-order
	$t/[U(VI)]_t$ vs. t	0.993	Pseudo-second-order
	$[U(VI)]_t$ vs. $t_{1/2}$	0.999	Diffusion controlled
50 °C (1.82 mg)	$\ln [(U(VI))_t/[U(VI)]_0]$ vs. t	0.991	Pseudo-first-order
	$t/[U(VI)]_t$ vs. t	0.948	Pseudo-second-order
	$[U(VI)]_t$ vs. $t_{1/2}$	0.992	Diffusion controlled
50 °C (4.30 mg)	$\ln [(U(VI))_t/[U(VI)]_0]$ vs. t	0.994	Pseudo-first-order
	$t/[U(VI)]_t$ vs. t	0.877	Pseudo-second-order
	$[U(VI)]_t$ vs. $t_{1/2}$	0.977	Diffusion controlled

4.3.5 Enhancement of kinetics of reduction using sonication

High intensity ultrasound in water produces cavitation, heat and agitation, which are extremely useful in a heterogeneous chemical system for improving mass transfer and reaction kinetics (Xu

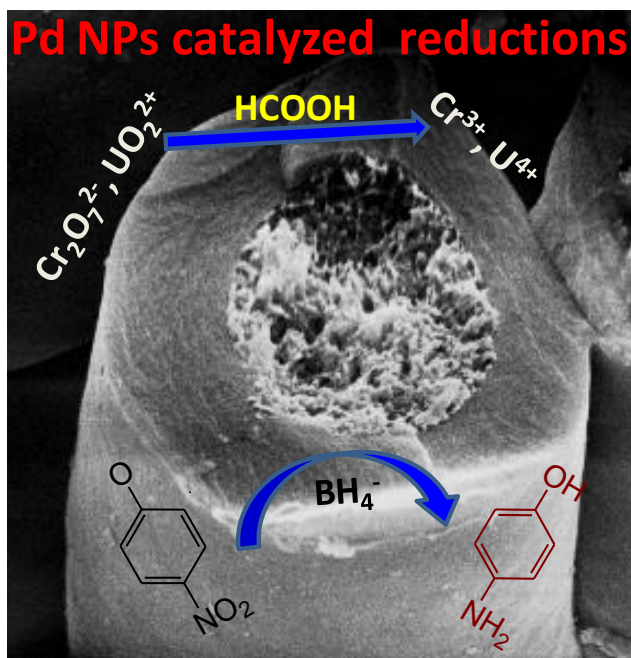
et al. 2013.; Adewuyi 2001). As reported in the literature (Nikitenko et al. 2010) that, high intensity ultrasound accelerates the reduction of UO_2^{2+} ions with hydrazine catalyzed by Pt and in the presence of 2-propanol as an inhibitor for H_2O_2 formation. Therefore, the effects of high intensity ultrasonication on the UO_2^{2+} ions reduction was studied in this work by using Pd NPs embedded hydrazine grafted membrane with formic acid. It was interesting to note that the kinetic of reduction at same temperature was switched from the diffusion controlled kinetics to pseudo-first-order kinetics. And also it was observed that, the catalytic activity of the Pd NPs was enhanced two times during ultrasonication ($0.93 \text{ s}^{-1}\text{g}^{-1}$ from $0.46 \text{ s}^{-1}\text{g}^{-1}$) obtained at corresponding $60 \text{ }^\circ\text{C}$ temp. This phenomenal enhancement in the catalytic activity of the Pd NPs by ultrasonication could be due to improved mass transfer of the reactants to membrane matrix which is important in such a heterogeneous system. Thus, the reduction process was no longer controlled by the diffusion process in the host PP matrix.

4.4 Conclusions

In this work, a new method was developed to host Pd nanocatalysts in the through pores hydrazine-grafted synthetic polymer membrane for the UO_2^{2+} ions reduction to U^{4+} ions with formic acid. It was not possible to load high amount of precursor Pd^{2+} ions in the membrane in the absence of ion-exchange and complexing groups. Therefore, the reducing agent hydrazine itself was grafted in pores of the membrane that facilitated high amount of Pd^0 loading, depending upon hydrazine grafting and reduction solution pH, in the form of Pd NPs in membrane under ambient conditions. The residual hydrazine in the membrane after formation of Pd NPs was found to be facilitate the decomposition of formic acid there by increasing the reduction process of UO_2^{2+} ions to U^{4+} ions. The Pd NPs embedded in the highly porous hydrazine grafted PP membrane exhibited a good catalytic activity in the reduction of UO_2^{2+} ions with formic acid that could be further enhanced

using high intensity sonication. The reusability of the catalyst has been tested and it was found that, the catalytic activity of this Pd NPs embedded membrane did not deteriorate during successive recycling. The analyses of reduction rate under different experimental conditions indicated that the reductions of UO_2^{2+} with formic acid follow pseudo-second-order kinetics but switched to diffusion controlled kinetics on increasing the amount of Pd NPs due to matrix effects. However, the enhancement of the reduction of UO_2^{2+} with formic acid under ultrasonication switched the kinetics from diffusion controlled to pseudo-first-order in the presence of lower amount of Pd NPs due to improved mass transfer of reactants to the host membrane matrix. Thus, the hydrazine-grafted membrane developed in the present work mimics egg-shell membrane in terms of formation and stabilization of Pd NPs. In addition to this, it is robust, efficient, recyclable and having a long shelf-life.

CHAPTER 5. GRAFTED-ELECTROSPUN POLYMER MICROFIBER SCAFFOLD HOSTED PALLADIUM NANOPARTICLES FOR CATALYZING REDOX REACTIONS



5.1 Introduction

The electrospinning technique is a simple and versatile method for synthesizing the microfibers of various polymers, composites, and ceramics, and also this technique offers a simple route to prepare the polymer fibers mimicking structures of biomaterials (Ke et al. 2014). The diameter of the polymer fibers can be varied by the concentration of the polymer in solution or composition used for electrospinning. In addition to these, the electrospinning conditions such as applied electric field, tip to collector distance, flow rate, collector spinning rate, temperature and humidity etc are also affect the elctrospinning process. To impart porosity to the fibers, the co-solvent having low boiling point can be added (Sun et al. 2014; Bharadwaj and Kundu 2010; Li and Xia 2004). These polymer fibers possess several desirable features such as high porosity, large surface area, easy separation and superior mechanical properties (Greiner and Wendorff 2007; Huang et al. 2003). These features make the polymer fibers excellent host substrates for the applications such as catalysis (Demir et al 2004; Panthi et al 2013; Chun and Jo 2014; Zhang et al 2010), antibacterial (Liu et al. 2014), biomedical (Du et al. 2012; Shao et al. 2011), and sensing (Zheng and Liu 2014; Yoon et al. 2012). Therefore, the electrospun nanofibres (NFs) are extensively used as a building blocks of nanoscience, nanodevices, and nanomembranes (Wu et al. 2007; Kim et al. 2015; Suren et al. 2014).

Catalysis is the most explored application among the various applications of NFs. Fabrication of composite NFs consisting of inorganic nanostructured materials anchored in the polymer matrix have been studied intensively in the field of catalysis because these host materials form easily retrievable and recyclable heterogeneous catalysts without affecting catalytic activity of the nanocatalysts (Greiner and Wendorff 2007; Zhang and Yu 2014; Lu et al. 2009; Dai et al. 2016; Patra et al. 2016; Neyertz et al. 2010; Lu et al. 2007). There are two possibilities to anchor

nanoparticles (NPs) or NCs in the electrospun polymer fibers; one during electrospinning, and second post processing of the fibers (Dai et al. 2016; Patra et al. 2016; Neyertz et al. 2010; Lu et al. 2007; Higaki et al. 2015). In first case, the nanomaterials aggregation and leaching can be controlled. The post processing of electrospun polymer fibers has advantage that the NPs can be positioned on the surface to provide higher accessibility. In general, the methods used for the incorporation of NPs on the electrospun polymer fibers are: (i) direct attachment of noble metal NPs via electrostatic force, hydrogen bonding or binding through functional groups on NPs, (ii) loading of precursor noble ions through ion-exchange/complexation with binding sites on the fibers and subsequent in situ chemical reduction, and (iii) hydrothermal assisted methods mostly used for the metal oxide NPs (Zhang and Yu 2014). The different electrospun fibers made up of chitosan/poly(methacrylic acid) (Shao and Ren 2015), poly(ϵ -caprolactone) surface functionalized with poly(dopamine) (Kim and Son 2015), porous carbon nanofibers formed by precursor fibers of poly(styrene)/ poly(acrylonitrile) (PAN) (Guo and Bai 2015), polyacrylic acid (PAA)/polyvinyl alcohol (PVA) (Hu and Huang 2014), polyethyleneimine (PEI)/PVA (Hu and Huang 2014; Huang et al. 2012), poly(L-lactic acid)/ amino-functionalized silsesquioxane (Gardella et al. 2013), nanoporous PVA mat (Shao et al. 2012), carbon nanofibers prepared from electrospun PVA mat (Barakat et al. 2016) etc. have been used to host metal NCs for the organic transformations and inorganic reductions. The sulfonic groups functionalized PAN fibers have been found to be efficient heterogeneous catalysts for the acetalization and esterification organic reactions (Shao et al. 2012). It is interesting to note that poly(vinyl pyrrolidone) (PVP) fibers act as both reducing agent as well as capping agent (Jiang et al. 2016). It is also possible to graft the reducing moiety on polymer matrix for the direct formation and deposition of noble metal NPs as described in Chapter 3&4.

The catalyzed inorganic and organic redox reactions are becoming increasingly important for the objectives of environmental remediation and industrial importance such as: (i) reduction of Cr(VI) to Cr(III) (Huang et al. 2012; Yadav and Xu 2013; Omole et al. 2007; Liang et al. 2014; Wang et al. 2016; Dandapat et al. 2011), (ii) reduction of U(VI) to U(IV) (McCleskey et al. 2001; Salomone et al. 2015; Shand and Anderson 2013), (iii) decompositions of nitrate and nitrites (Neyertz et al. 2010; Shand and Anderson 2013; Mishra et al. 2011; Ren et al. 2015; Dodouche and Epron 2007; Wehbe et al. 2009), and (iv) reduction of organic pollutants (Niu et al. 2016; Zhang et al. 2012). For developing a sustainable environmental remediation technology, it is important to have a benign reductant along with a highly efficient and recyclable noble metal catalyst. The formic acid decomposition catalyzed by the noble metal NPs immobilized on the support is being explored for hydrogen production (Gao et al. 2016; Zhou et al. 2008; Wang et al. 2014). It is interesting to note that thus *in situ* produced hydrogen can also be used for the inorganic and organic reductions having technological and environmental importance.

In the present work, a porous poly(ether sulfone) (PES) microfibers mat has been prepared by electrospinning technique using the optimized conditions. The reducing moiety has been attached covalently to the PES microfibers mat by UV-graft polymerization of glycidylmethacrylate, and reacting subsequently with hydrazine via epoxy ring opening. PES is UV-active and thus free radicals can be generated directly on PES fibres under UV irradiation. The grafted polymer shell around porous microfiber has been found to perform the reduction of precursor ions by grafted hydrazine which leads to the nucleation and growth of Pd nanoparticles (NPs) on the host matrix itself. The as formed Pd Nps had been used to study the reductions of U(VI)/Cr(VI) with formic acid, and *p*-nitrophenol with borohydride/hydrazine. The controlled loading Pd NPs and catalyst reusability have also been examined.

5.2 Experimental

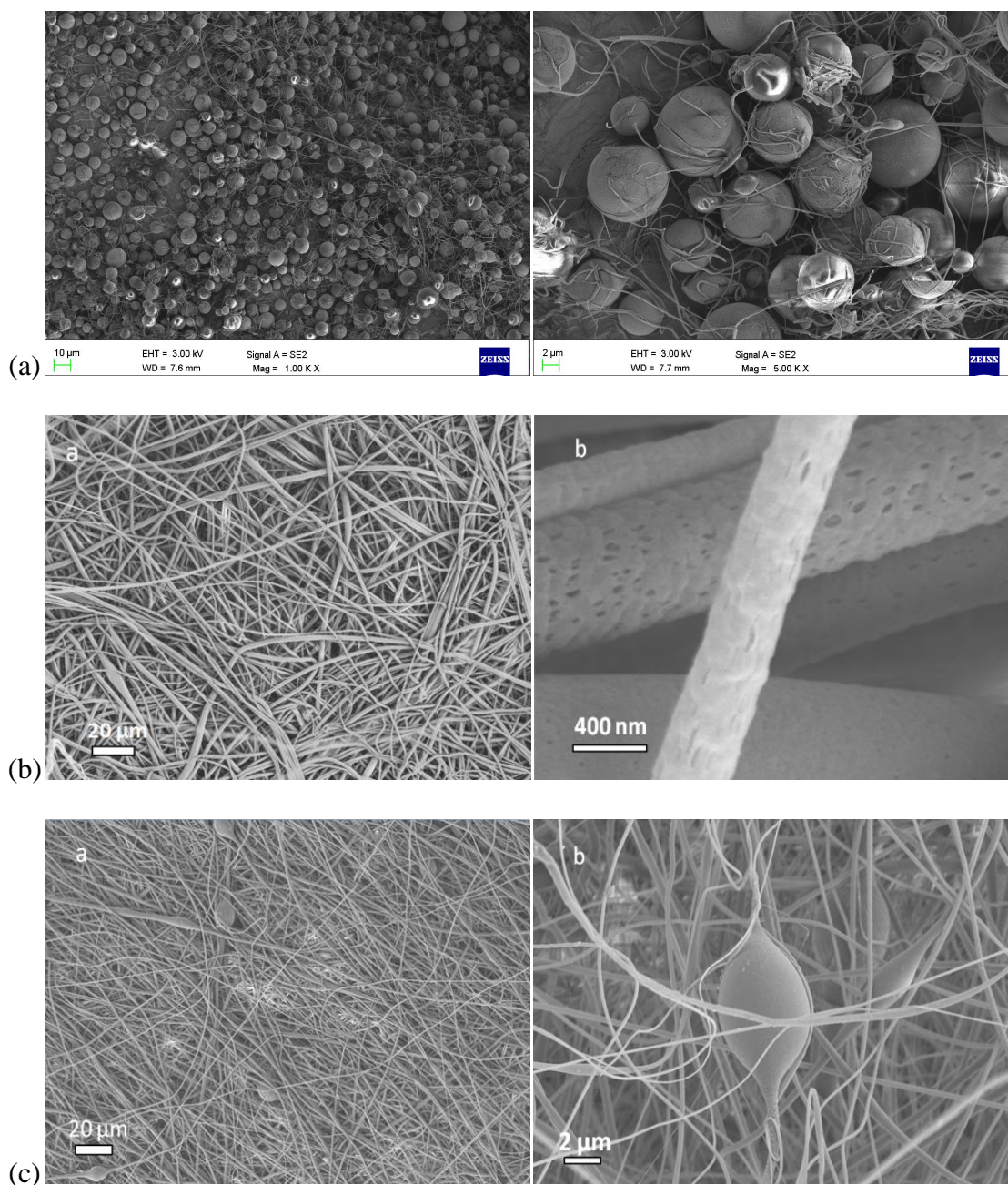
Details of materials and reagents used are given in chapter 2.

5.2.1 Preparation of electrospun PES microfibers mat

The detailed experimental setup of electrospinning was given in Chapter 2. The experimental setup contains syringe pump, high voltage source and a grounded collector. In this experiment an 11-Elite syringe pump was used, which was procured from Harvard Apparatus Holliston, MA, USA. High voltage DC source (Model MK30P02.5) from a Glassman High voltage (NJ, USA) was used for applying a high voltage. The fibers were collected on a rotating drum wrapped with aluminum foil. The Al foil was grounded to a negative -350 V using a high voltage DC source purchased from Aplab high voltage DC source Pvt. Ltd, India. The working distance between needle and collector was of 12 to 16 cm and operating voltage of 12-14kV were optimized after a series of trial runs. The effects of different solvents and solvent to PES polymer ratio on the formation of PES microfibers were studied and the solvents such as DMF, DMAc and NMP were used. After a series of trials, DMF was selected as the suitable solvent. To form the uniform, beads free fibers, the polymer to solvent ratio was optimized using different amount of PES granules dissolved in DMAc. It was observed that 20 wt. % of PES in DMAc resulted in the formation of beads rather than fibers as shown in FE-SEM images given in Figure. 5.1(a), that was attributed to lower viscosity of the solution. On increasing PES concentration to 28 wt % in DMAc, the uniform bead free fibers were formed (Figure.5.1(b)). On further increasing amount of PES, formations of non-spherical beads and non-homogenous fibers were observed; see Figure.5.1(c).

To induce porosity in the microfibers, the lower boiling solvent was used generally as a co-solvent. Here, in this experiment acetone was used along with DMAc with known v/v ratio. Acetone evaporates faster than DMAc during Rayleigh instability region of electrospinning, leaving behind

voids on the surface of the fibers. The optimized proportion of solvent to form porous fibers was DMAc: acetone as 80 : 20 v/v as shown in Figure. 5.1(d).



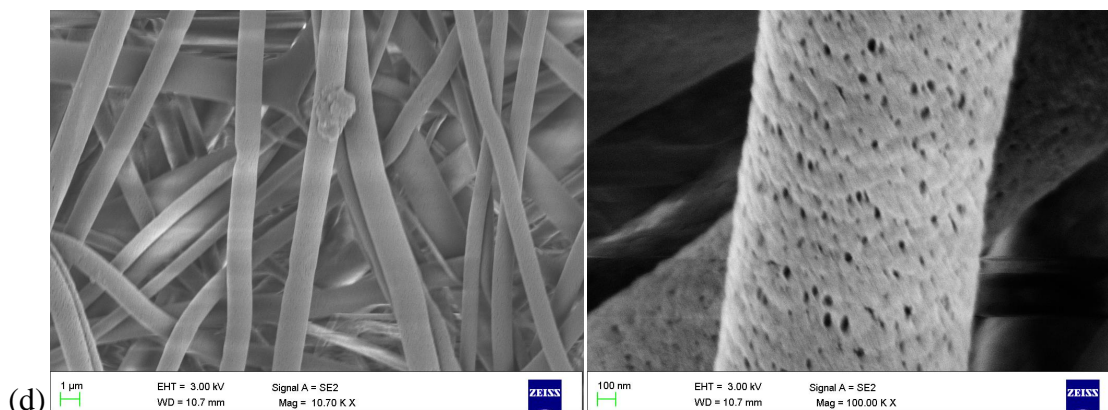


Figure 5.1 FE-SEM images of electrospun nanofiber mats formed by using the solutions having: (a) 20 wt. % of PES in DMAc, (b) 28 wt. % of PES in DMAc, (c) 30 wt. % of PES in DMAc, and (d) 28 wt. % of PES in DMAc: acetone in 80:20 ratio under lower and higher magnifications.

5.2.2 Chemical treatments

For anchoring poly(GMA) on PES microfibers mat, the monomer solution containing GMA was prepared by dissolving 1.5 g of GMA in 2 mL of ethanol solvent and adding 2mol % of cross-linker (EGDM) along with 1 wt. % of UV-initiator (DMPA). The PES polymer is UV-active and GMA could be anchored without UV-initiator. However, UV-initiator and cross-linker were used to obtain higher poly(GMA) grafting yield. The microfibers mat was soaked in the polymerizing solution for about 3h prior to irradiate with 365 nm light in photo-reactor for a period of 20 min. After polymerization, the microfibers mat samples were washed with ethanol and water mixture to remove un-polymerized components. The choice of solution composition and UV-irradiation time was based on the optimization of in situ grafting/polymerization methods in terms of optimum yield [Chapter3 & 4]. The poly(GMA) anchored electrospun PES fibers mats were reacted with hydrazine hydrate (99 %) for 12 h with a constant stirring at room temp. The hydrazine reacted mats were thoroughly washed with deionized water several times to remove un-reacted hydrazine,

and vacuum dried for the further use. These hydrazine attached microfibers mats were equilibrated with the solutions containing $0.01 \text{ mol L}^{-1} \text{ PdCl}_2$ at pH=2 for 15 h to form Pd NPs.

5.2.3 Reductions of U(VI), Cr(VI) and *p*-nitrophenol

The reduction of UO_2^{2+} ions was carried out in a double jacketed glass vessel kept at constant temperature using thermostat bath. For UO_2^{2+} ions reduction, equal volumes of (8 mL each) $0.1 \text{ mol L}^{-1} \text{ UO}_2(\text{NO}_3)_2$ solution at pH=2 and 1 mol L^{-1} formic acid were taken and for $\text{Cr}_2\text{O}_7^{2-}$ reduction, 5 mL of $10 \text{ mM Cr}^{\text{VI}}$ and 5 mL of 0.1 M formic acid were taken in a reaction vessel kept at a constant 50°C temp. The known weights of Pd NPs loaded PES microfibers mat samples were used to calculate the catalytic activity. There was no reduction of UO_2^{2+} or $\text{Cr}_2\text{O}_7^{2-}$ ions observed without catalyst and with catalyst at room temperature. The progress of UO_2^{2+} ions reduction was monitored by taking 1 mL aliquot from the reaction solution at a fixed time interval, and UV-Vis spectra of these samples were recorded after diluting this to 3 mL by adding pH=2 solution. Similarly, $\text{Cr}_2\text{O}_7^{2-}$ ions reduction was monitored by taking 0.5 mL of solution at regular time interval and diluted to 3 mL for recording the UV-Vis spectrum. For kinetic experiments, the most intense peak at 665 nm of U^{4+} ion was calibrated by measuring the U^{4+} concentration by electroanalysis. To prevent oxidation of U^{4+} ions to UO_2^{2+} during long storage, the solution was kept in a freezer and UV-Vis spectrum was recorded again to ensure the extent of oxidation of U^{4+} .

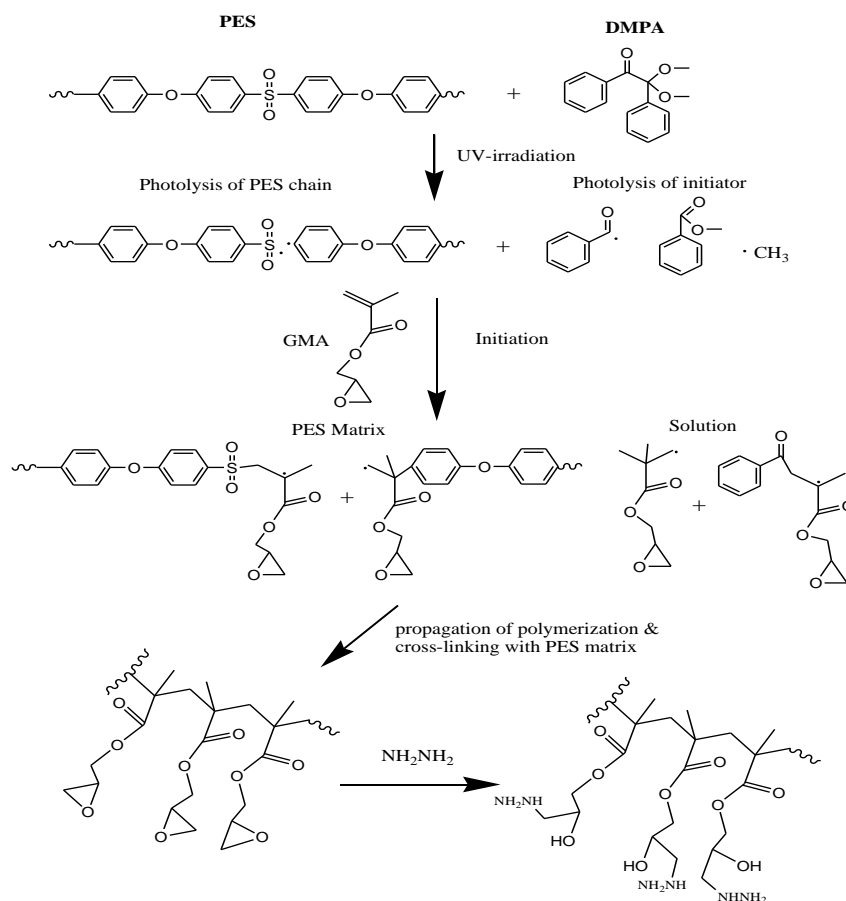
Borohydride and hydrazine were used as reducing agents for the reduction of *p*-nitrophenol (PNP) to *p*-aminophenol (PAP) in the presence of known weight of Pd NPs loaded PES microfibers mat. For continuous monitoring, the reaction was carried in a cuvette kept in miniature spectrophotometer and UV-Vis spectra were recorded with one min time interval. The reaction solution was stirred with magnetic bar. The reaction solution contained 2 mM of 0.1 mL PNP and 0.1 mL of 200 mM of NaBH_4 and 2.8 mL of deionized water was added to make 3 mL volume in

cuvette. Similar conditions (2mM of 0.1 mL PNP , 0.1 mL of 200 mM N₂H₄ and 2.8 mL of deionized water) were used for the hydrazine as a reducing agent for PNP.

5.3 Results and discussion

5.3.1 Formation of Pd NPs embedded PES fibers mat

The PES fiber mat produced in this work did not contain any functional groups to hold the precursor Pd²⁺ ions and subsequently to reduce them to form the Pd NPs. The covalent attachment of hydrazine onto the poly(GMA) anchored PES fibers mat made it dual-functional as shown in Scheme 5.1.



Scheme 5.1 Chemical modifications involved in the covalent attachment of reducing hydrazine groups on the electrospun PES microfibers mat.

PES used in the fiber mat formed free radicals on photolysis under UV-light irradiation, and initiated graft-polymerization of GMA as shown in Scheme 5.1 (Paul et al. 2015; Susanto and Ulbricht 2007). However, the poly(GMA) anchored (2-5 wt%) on to the electrospun PES fibers mat did not give higher extent of the hydrazine-grafting required for higher reduction of Pd²⁺ ions.

To improve loading of Pd on fibers mat, UV-initiator DMPA and cross-linker EGDM were used to increase the poly(GMA) anchoring on the PES fibers mat. During UV-irradiation, the photolysis of DMPA in polymerizing solution also occurred to form free radicals (Tehfe et al. 2013; Szablan et al. 2007), which could initiate homo-polymerization of GMA. The poly(GMA) chains in solution were linked with poly(GMA) anchored on PES fibers either by terminating chain reaction or cross-linking of the poly(GMA). This resulted in the anchoring of poly(GMA) on the PES fibers to 300 wt.%. The reducing moiety hydrazine was attached to poly(GMA) anchored PES fibers covalently. The hydrazine modified PES fibers mat found to reduce Pd²⁺ ions readily at ambient conditions to Pd⁰ atoms that nucleated on the PES microfiber itself to form Pd NPs. The saturation loading of Pd⁰ on the electrospun fibers mat was found to be 22±3 mg g⁻¹.

The morphology change after chemical modification of the microfibers mat was studied by FE-SEM. As shown in Figure. 5.2, the PES fibers lengths were shortened after the attachment of hydrazine via anchored poly(GMA) and the porous surface became smoother. The stiffening of the PES microfibers and increase in the diameter of fibers from ≈2 μm in the pristine PES microfibers to ≈4 μm were because of the higher grafting and cross-linking (300 wt.%). It was also clear from the Figure. 5.2 that there was no cross-linking between the fibers or retention of the homo-poly(GMA) gel that might had formed by UV-initiator. The Pd NPs were embedded in the grafted layer on PES microfibers that could be seen as white spots in the FE-SEM image given in Figure. 5.2(d). The uniform distribution of Pd NPs in the fibers mat was shown by EDS mapping

(Figure 5.3). The left-over nitrogen shown in EDS mapping after saturation loading of Pd⁰ suggest that hydrazine was not utilized fully for the reduction of Pd²⁺ ions. Thus, the Pd NPs embedded microfibrers mat also had basic groups that would enhance the formic acid oxidation as reported in the literature (Mori et al.2013).

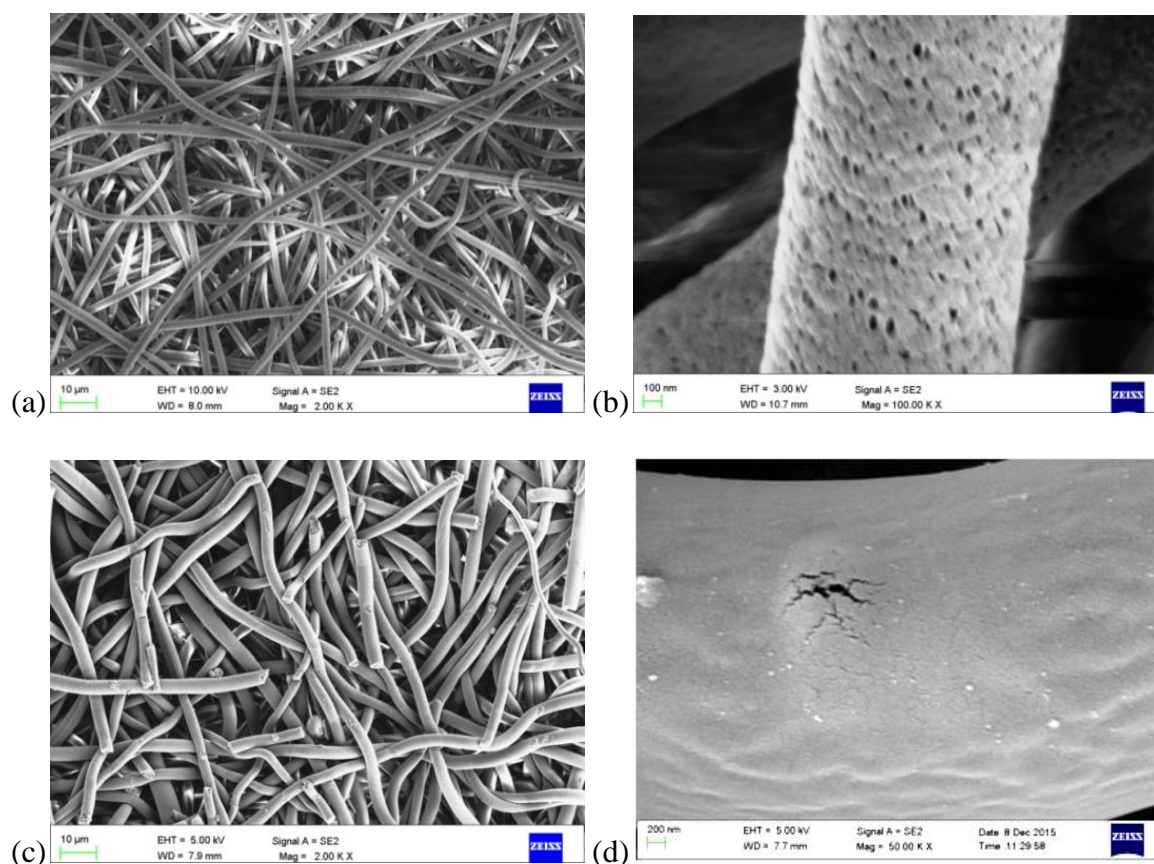


Figure 5.2 FE-SEM images of the pristine PES nanofibers mat (a,b), and same nanofibers mat after the chemical modifications shown in Scheme 1 (c,d) under higher and lower magnifications.

The morphology changes after grafting with poly(GMA) on the pristine micro fibers mat along the cross-section was studied using FE-SEM. As given in Figure 5.4 that, the grafted polymer shell of thickness $0.68 \pm 0.20 \mu\text{m}$ was formed on porous core having $1.57 \pm 0.30 \mu\text{m}$ diameter. This core diameter is similar to the diameter of the pristine electrospun microfibers ($1.47 \pm 0.60 \mu\text{m}$)

indicating the growth of grafted polymer on their outer surface. The cross-section of bunch of microfibers showed uniform distributions of these elements Figure 5.5.

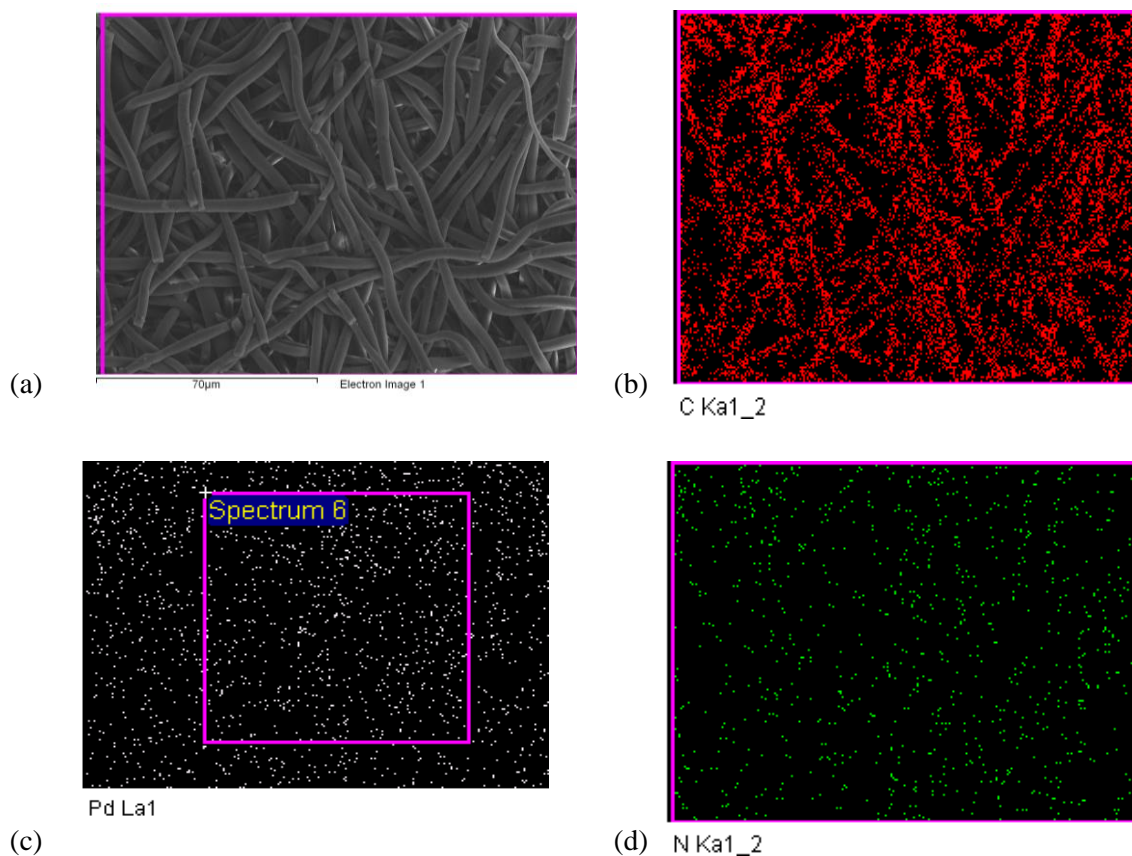


Figure 5.3 The C, N, Pd elemental mappings of Pd NPs loaded PES microfibers mat (70x70 µm)

by EDS showing the presence of nitrogen from residual hydrazine and Pd NPs.

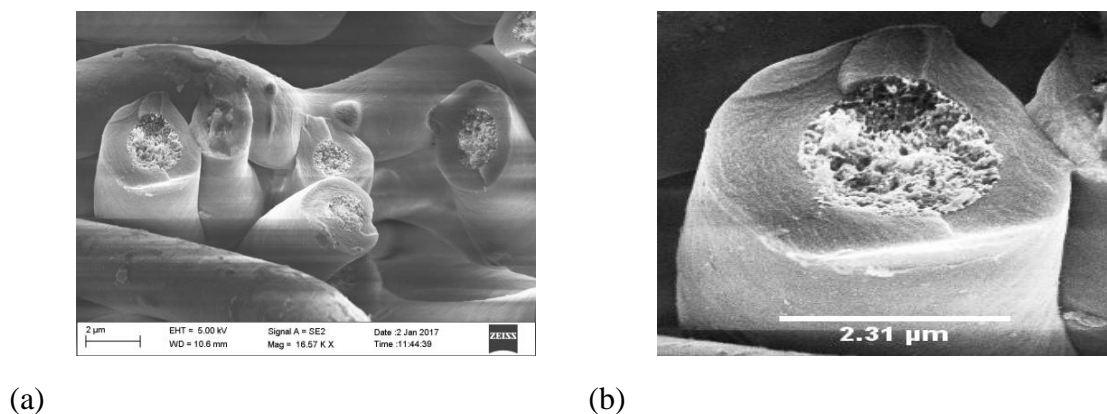


Figure 5.4 Cross-sectional FE-SEM image of Pd NPs loaded microfiber.

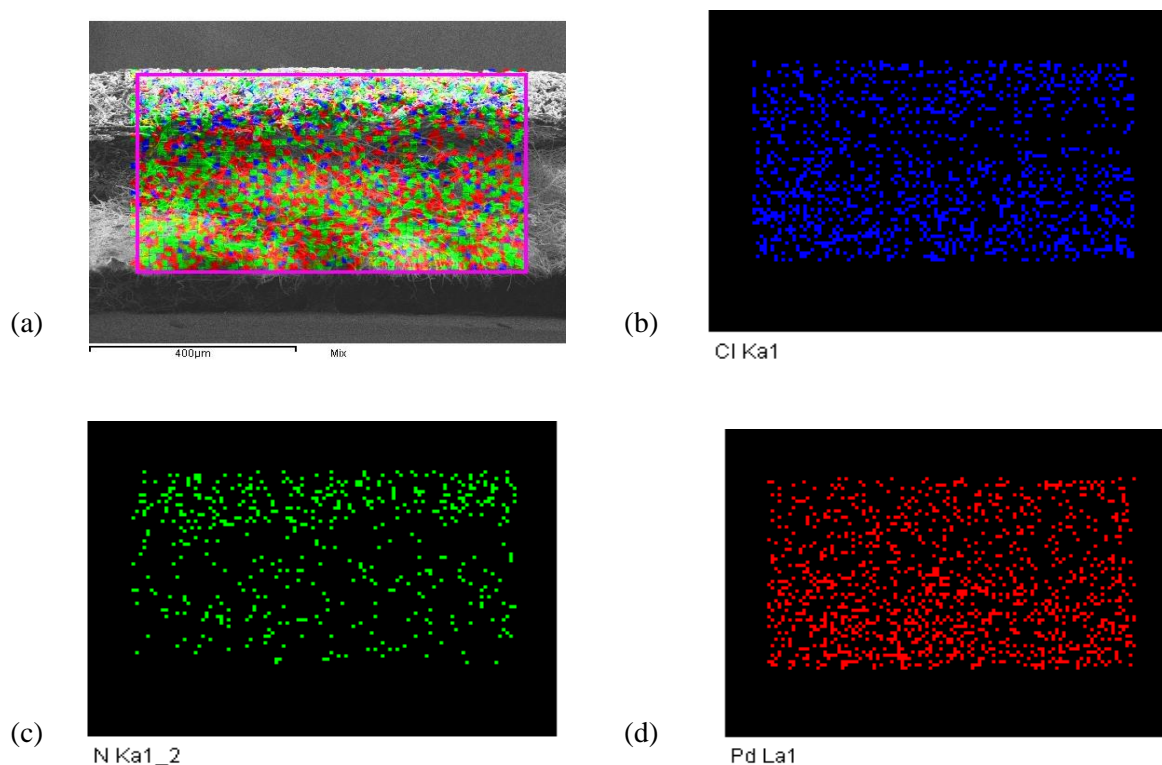


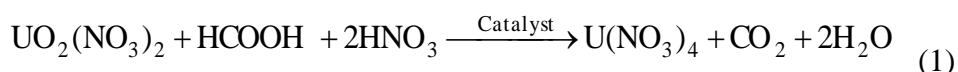
Figure 5.5 Elemental mappings of Pd and N on the cross-section of Pd NPs loaded PES microfibers Fiber@Pd using FE-SEM/EDS.

Nitrogen analysis was carried out to know that extent of reaction of anchored poly(GMA) with hydrazine. The nitrogen content of hydrazine reacted fibers was found to be 11.14 wt.% which corresponded to 70 % reaction of glycidyl units with hydrazine. The amount of glycidyl units was obtained by gravimetrically (mass-gain after anchoring). The nitrogen content of the microfibers after Pd NPs loading was found to be 6.98 wt.% indicating 50% utilization of grafted hydrazine for the reduction of Pd^{2+} ions. Assuming one hydrazine was required for the reduction of one Pd^{2+} ion, the comparison of nitrogen amount consumed (4.16 wt.%) and Pd content loaded (22 mg g^{-1}) seems to suggest that only 20 wt.% of Pd^0 was locked as Pd NPs in the microfibers; and rest of the Pd^0 content might had been lost to the solution used for providing precursor Pd^{2+} ions. However, the ICP-AES analysis of solution after 3 cycles of reductions did not show any loss of

Pd content from the fibers. Thus, the Pd⁰ locked as Pd NPs had high stability and adherence in the microfibers.

5.3.2 Catalytic reduction of U(VI) ions

The UO₂²⁺ ions reduction with formic acid in presence of Pd NPs formed on fibres mat was tested. The reduction of UO₂²⁺ ions with formic acid involves two electron transfer and this reaction in presence of catalyst was represented as (eq(1))



To evaluate catalytic activity of Pd NPs embedded PES microfibers (Fiber@Pd), the linear variation of $\ln [U(VI)]_t/[U(VI)]_0$ vs. t during UO₂²⁺-reduction with formic acid at 50°C was analyzed using pseudo-first-order kinetic equation given below:

$$\ln \frac{[U^{VI}]_t}{[U^{VI}]_0} = -kt \quad (2)$$

Where $[U^{VI}]_t$ and $[U^{VI}]_0$ represent concentrations of UO₂²⁺ ions at time t and initial, respectively, t is reduction time, and K is apparent reduction rate constant. The pseudo-first-order kinetic equation was used here because formic acid was used in excess. The concentration of U⁴⁺ ions was monitored from absorbance at 665 nm which was calibrated by electro-analysis. The choice of 665 nm for monitoring was based on the fact that it is the most intense peak of f-f transitions in U⁴⁺ as can be seen from the successive UV-Vis spectra recorded during reduction, see Figure.5.6.

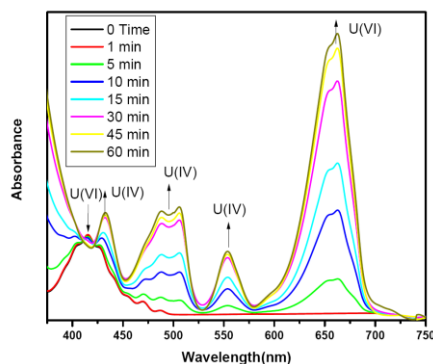


Figure 5.6 The increase in the concentration of U(IV) ions as a function of reduction time of U(VI) ions with formic acid at 50°C was monitored from the f-f transition peaks in successive UV-Vis spectra recorded from the samples taken from reaction solution.

The UO_2^{2+} ions conc. at time t was obtained from the mass-balance. Commercially available Pd/C (10 wt%) was also used for the reduction of UO_2^{2+} ions with formic acid, to compare the catalytic activity with Pd NPs immobilized fibers mat. The kinetic data analysis given in Table 5.1 seems to indicate that the catalytic activity of Fiber@Pd ($0.22 \text{ s}^{-1}\text{g}^{-1}$) is considerably higher than that of Pd/C ($0.16 \text{ s}^{-1}\text{g}^{-1}$) under the identical conditions of reduction of UO_2^{2+} ions with formic acid at 50°C.

Table 5.1 Comparison of the catalytic activities of Fiber@Pd with Pd/C during the reduction of UO_2^{2+} ions with formic acid at 50°C temp. The conditions were kept same in all the experiments as $0.1 \text{ mol L}^{-1} \text{UO}_2(\text{NO}_3)_2$ at pH=2 and 1 mol L^{-1} formic acid.

Host	Catalyst wt. (mg)	Pd wt. (mg)	k ($\times 10^{-3} \text{ s}^{-1}$)	Catalytic activity ($\text{s}^{-1} \text{g}^{-1}$)
Fiber@Pd	53.0	1.16	0.25	0.22 ± 0.02
Pd/C (10 wt.%)	6.0	0.60	0.10	0.16 ± 0.02

5.3.3 Catalytic reduction of Cr(VI) anions

The $\text{Cr}_2\text{O}_7^{2-}$ ions reduction with formic acid in the presence of Pd NPs formed on microfibers mat was studied at 25°C and 50°C and was analyzed by monitoring the absorbance at 348 nm corresponding to conc. of Cr(VI). Since absorbance (A) at 348 nm represents conc. of Cr(VI) ions, the conc. in equation 2 was replaced by absorbance for analyzing the kinetics of reduction. The successive UV-Vis spectra is given in Figure. 5.7. As shown in Fig. 5.7(a), the complete disappearance of absorption peak at 348 nm was observed during 60 min reduction time indicating complete reduction of Cr(VI) with formic acid at 50°C in the presence of Fiber@Pd. It is also seen from Figure. 5.7(b) that the Cr(VI)-reduction also occurred at 25°C with a slower rate under the similar conditions; but did not occur in the absence of the catalyst (Figure. 5.7(c)). The successive UV-Vis spectra obtained as a function of reduction time and the corresponding variations of $[A]_t / [A]_0$ versus t were also given Figure 5.7.

The apparent pseudo-first-order reduction rate constants and catalytic activities obtained at 25°C and 50 °C were compared with that reported in the literature in Table 5.2. It is seen from Table 5.2 that the catalytic activity towards Cr(VI) ions in the presence of fiber@Pd found to be higher than the Pd NPs supported on other host materials reported in the literature. The higher catalytic activity of fiber@Pd may due to accessibility of Pd NPs, the presence of basic groups left after reduction of Pd^{2+} ions (Mori et al. 2013), and uncapped surface of the Pd NPs. The catalytic activity of fiber@Pd in the reduction of Cr(VI) with formic acid ($0.79 \text{ s}^{-1}\text{g}^{-1}$) was higher than that in the reduction of U(VI) ($0.22 \text{ s}^{-1}\text{g}^{-1}$) under similar conditions. This was attributed to higher redox potential for Cr(VI)/Cr(III) (1.33 V) than that for $\text{U}^{\text{VI}}/\text{U}^{\text{IV}}$ couple (0.41V). Although both these couple potentials are convenient for the reduction with formic acid ($\text{HCOOH}/\text{CO}_2, 2\text{H}^+$ couple is -0.199 V), the lower redox potential of U(VI)/U(IV) couple and high activation barrier, due to

strongly bound oxygen in UO_2^{2+} ions, lowered the catalytic activity of Fiber@Pd with respect to Cr(VI)/Cr(III) couple under similar conditions. The lower activation barrier also resulted in the reduction of Cr(VI) in the presence of Fiber@Pd at room temp.

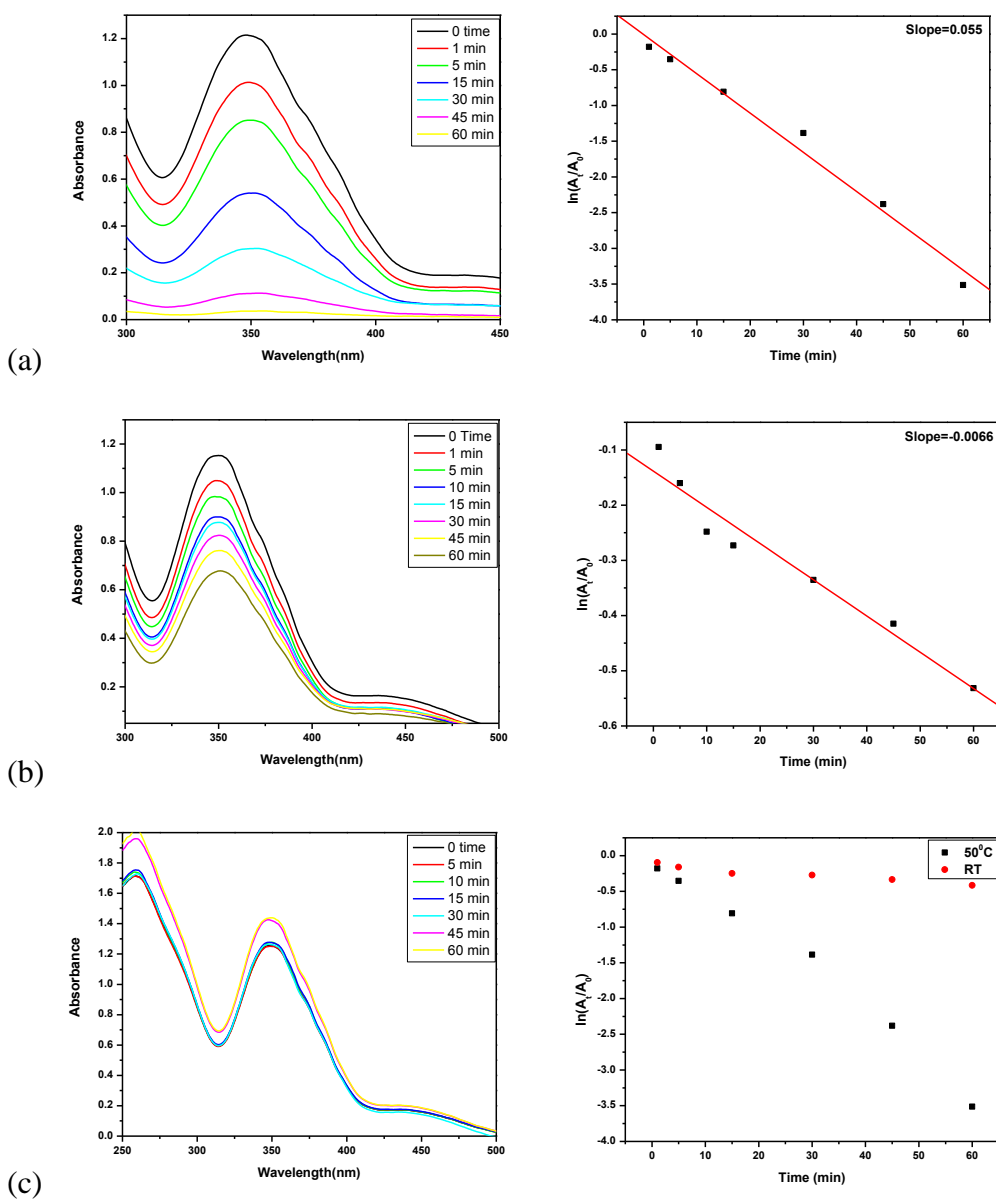


Figure 5.7 Successive UV-Vis spectra obtained during reductions of Cr(VI) with formic acid at 50°C (a) and 25°C (b) and corresponding variation of $\ln [A]_t/[A]_0$ vs reduction time (t) in the presence of Fiber@Pd. The UV-Vis spectra shown in (c) indicate no reduction of Cr(VI) under

similar conditions (50°C) in absence of the catalyst along with comparisons of reduction rate profiles at room temperature and at 50°C.

Table 5.2 Comparison of catalytic activity of Pd NPs hosted in different matrices for the reduction of Cr(VI) anions with formic acid.

Catalyst	Chemical conditions	Catalytic Activity (s⁻¹ g⁻¹)	Ref.
Poly(vinylpyrrolidone)-stabilized NPs	Formic acid, 45°C	0.37	Tu et al. 2013
Pd NPs on Fe ₃ O ₄	Formic acid, 45°C	0.124	Tu et al. 2013
Viral-templated Pd NP	Formic acid, 25°C	0.46x10 ⁻³	Yang et al. 2014
Pd NPs in polym. grafted Fe ₃ O ₄	Formic acid, 50°C	0.517	Shrivastava et al. 2016
Pd NPs in polym. grafted SiO ₂	Formic acid, 50°C	0.138	Shrivastava et al. 2016
Fiber@Pd	Formic acid, 50°C	0.79	Present work
Fiber@Pd	Formic acid, 25°C	0.095	Present work

5.3.4 Catalytic reduction of *p*-nitrophenol

The reduction of *p*-nitrophenol (PNP) to *p*-aminophenol (PAP) with borohydride at room temperature in the presence of coinage metal nanocatalysts (Aditya et al. 2015; Patra et al. 2014), including the Pd NPs (Komathi et al. 2010) was used as a model reaction to evaluate the catalytic

activity. Therefore, the catalytic performance of the Fiber@Pd in this redox system was also studied. The successive UV-Vis spectra taken during reduction of PNP with borohydride in the presence of Fiber@Pd showed that PNP was quantitatively reduced to PAP, see Figure. 5.8. Hydrazine was also used in the presence of borohydride for PNP reduction. It was observed that the PNP reduction with borohydride and hydrazine did not occur significantly in the absence of the catalyst as can be seen from UV-Vis spectra given in Figure. 5.9. Figure 5.8(b) showed, there were two slopes suggesting that the initial reduction process was slower and accelerated as reaction proceeded. The similar observation was reported earlier with borohydride in the presence of Ag NPs embedded poly(styrene) beads at room temp, and was attributed to nanoconfinement effect (Patra et al. 2014). However, the lag time in onset of reduction was not observed in the present case.

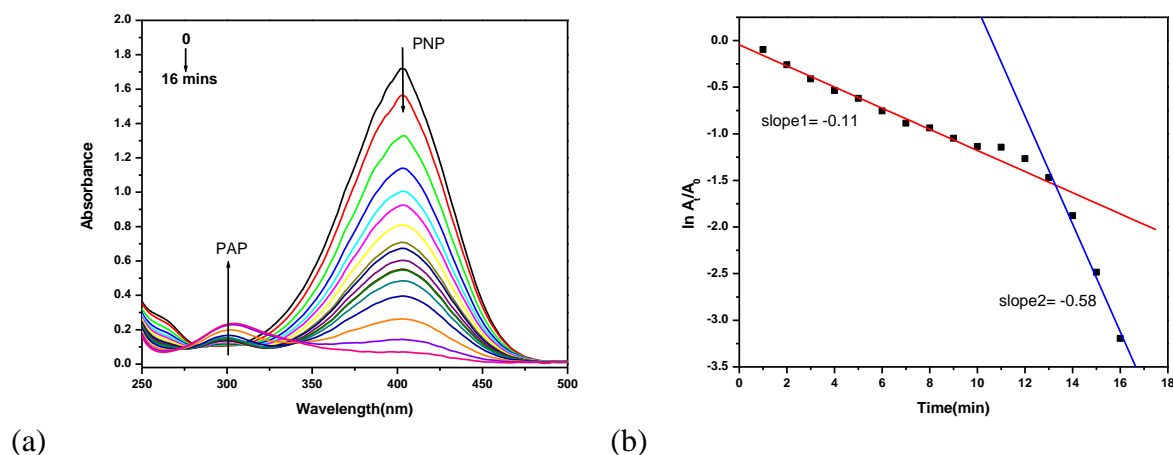


Figure 5.8 The successive UV-Vis spectra showing quantitative conversion of PNP to PAP with borohydride in the presence of Fiber@Pd (a) and corresponding variation of $\ln [A]_t/[A]_0$ vs. reduction time (b).

From the kinetic plot given Figure. 5.8(b), it was observed that the Pd NPs on the surface had lower catalytic activity compared to Pd NPs embedded in the hydrazine-grafted PES microfibers.

The higher grafting (300 wt%) yield increased the probability of formation of Pd NPs at the interior of the fiber matrix. The lag time was not observed in this case because the Pd NPs at the surface provided immediate access to the reactants as reported in the literature (Aditya et al. 2015; Patra et al. 2014). The reactants diffused to the Pd NPs embedded in grafted polymer shell on the PES microfibers during progress of the reaction resulted in acceleration of the reduction in the later stage.

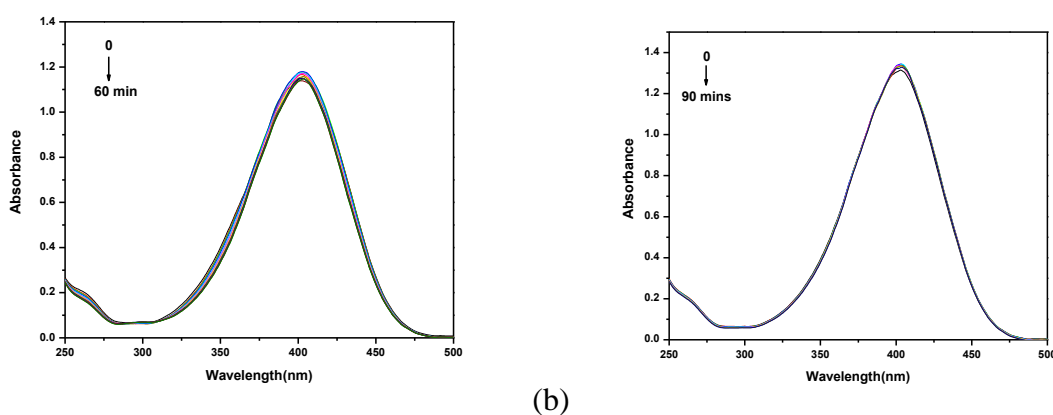


Figure 5.9 The successive UV-Vis spectra showing no reduction of *p*-nitrophenol to *p*-aminophenol with borohydride (a) and hydrazine (b) in the absence of catalyst Fiber@Pd.

PNP reduction with hydrazine was found to be slower than the borohydride. The reduction was completed approximately after 90 min. However, the kinetics profile was similar to borohydride reduction. The initial catalytic activity of the Fiber@Pd in the hydrazine reduction of PNP was found to be $0.24 \text{ s}^{-1}\text{g}^{-1}$ which was increased substantially to $0.80 \text{ s}^{-1}\text{g}^{-1}$ at the later stage as shown in Figure, 5.10. This phenomenal increase in the catalytic activity shown in second slope of the PNP reduction kinetic profiles of both with the borohydride and hydrazine could be attributed to: (i) embedded Pd NPs were protected from the corrosion, (ii) nanoconfinement effects, (iii) and more defects/active centers on the Pd NPs due to a restriction of growth in the confined space.

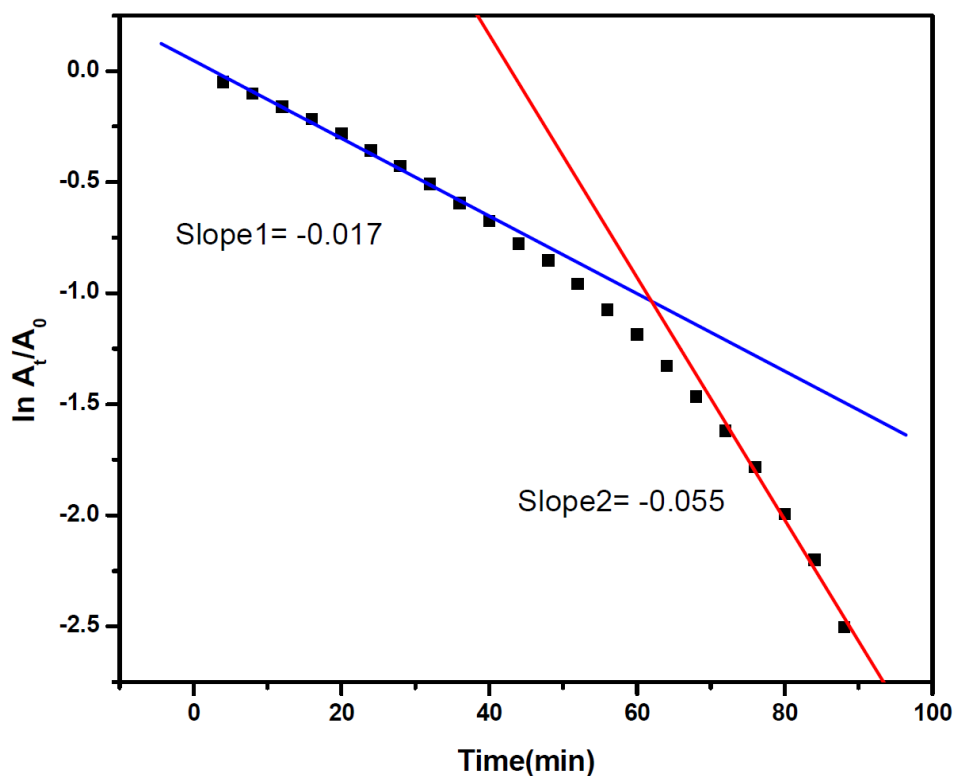


Figure 5.10 The kinetic rate profile showing variation of $\ln [A]_t/[A]_0$ vs. time in the reduction of *p*-nitrophenol to *p*-aminophenol with hydrazine at room temp.

The catalytic activities of Pd NPs synthesized in this work were compared with Ag and Au NPs reported in the literature towards the PNP reduction. From Table 5.3, it is seen that catalytic activity (k_i) of Fiber@Pd is in comparable with the values reported in the literature in the reduction of PNP with borohydride. However, the catalytic activity in the later stage (k_1) was considerably higher than those listed in Table 5.3. It was reported based on the theoretical modeling of binding of nitrophenolate with surfaces of the coinage metal NPs that Au and Ag NPs would have better catalytic activity than other coinage metal such as Cu, Pt and Pd (Pozun et al. 2013).

Table 5.3 Comparison of the catalytic activity of Fiber@Pd in the reduction of *p*-nitrophenol with borohydride at room temp. with the catalytic activities of Pd, Au and Ag NPs reported in literature under similar conditions.

Catalyst	k ($\times 10^{-3} \text{ s}^{-1}$)	Catalytic activity ($\text{s}^{-1}\text{g}^{-1}$)	Ref.
Biogenic Ag	4.06	-	Gangula et al. 2011
Biogenic Au	9.19	-	Gangula et al. 2011
Ag/C	1.69	1.69	Tang et al. 2010
Ag NPs aggregate	2.10	2.00	Liu et al. 2013
Ag NPs coral like dendrite	5.19	1.30	Rashid and Mandal. 2007
Ag NPs banana leaf like dendrite	1.65	0.41	Rashid and Mandal. 2007
Capped Ag NPs	0.36	0.09	Rashid and Mandal. 2007
Au NPs in Amyloid - Carbon hybrid membrane	0.03	-	Bolisetty and Mezzenga. 2016
Pd NPs in grafted membrane	-	3.6	Emin et al. 2014
Fiber@Pd	$k_i=1.83$ $k_f=9.67$	1.54 8.41	This work

To check the shelf-life of the Pd NPs on the fibers mat, the Fiber@Pd stored for 3-4 months and then tested its catalytic activity, it was observed no deterioration in the catalytic activity. However,

the catalytic activity of Fiber@Pd decreased on successive reuses in the reduction of PNP with borohydride as well as hydrazine as shown in Figure. 5.11. As no Pd losses from the microfibers were observed, the reduction of catalytic activity of Pd NPs was attributed to the poisoning of their surfaces by hydrogen sorption produced during reduction process.

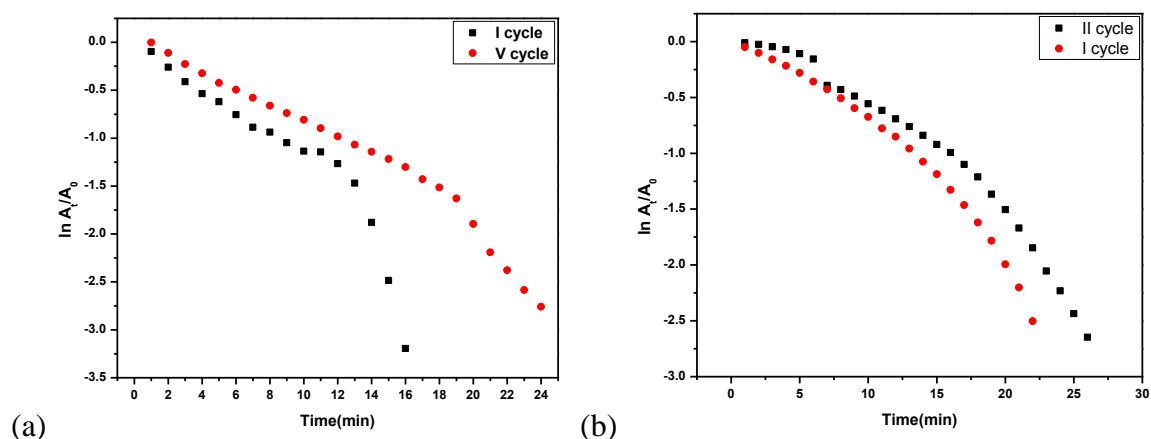


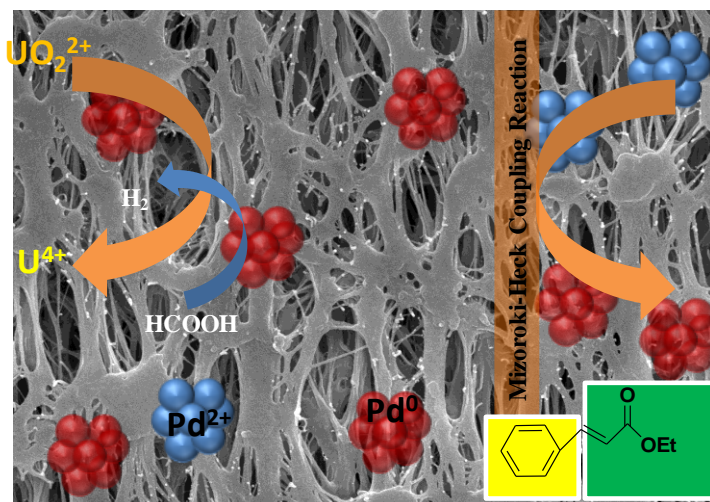
Figure 5.11 The kinetic rate profiles showing variations of $\ln [A]/[A]_0$ vs. time in the reductions of *p*-nitrophenol to *p*-aminophenol with borohydride (a) and hydrazine (b) at room temperature in recycles of catalyst Fiber@Pd.

5.4 Conclusions

A new method has been developed in the present work to form the dual functional high surface area polymer scaffold on the porous electrospun PES fibers for hosting Pd nanocatalysts, which may find extensive applications as the heterogeneous catalysts. This is similar to that reported in chapter 4. The synthesis of this polymer scaffold involves grafting of reducing agent hydrazine on the porous surface of electrospun PES microfibers mat. Thus formed polymer scaffold reduces Pd^{2+} ions readily and provide support for nucleation and growth of Pd NPs. The Pd NPs on electrospun PES microfibers mat exhibit higher catalytic activity in the inorganic ion reductions (U^{VI} and Cr^{VI} with formic acid) and organic reduction (PNP with borohydride and hydrazine). The

reduction rate profiles of PNP with borohydride and hydrazine revealed two reduction kinetics i.e. initially slower reduction which was accelerated significantly during later stage of the reduction. This was attributed to remarkable higher catalytic activity of the Pd NPs embedded at interior matrix of the grafted electrospun microfiber. The studies carried out in the present work seems to suggest that the heterogeneous nanocatalyst based on the Pd NPs embedded electrospun PES microfibers mat is recyclable and efficient in catalyzing the inorganic and organic redox reactions. However, the catalytic activity of Pd NPs loaded membrane described in chapter 4 was better than that obtained with the Pd NPs embedded microfibers mat. This could be related to dense grafting on microfibers that retarded the accessibility to Pd NPs embedded in the interior matrix.

CHAPTER 6. PALLADIUM NANOPARTICLES HOSTED IN POLY(ETHYLENIMINE) AND POLY(ETHYLENE GLYCOL METHACRYLATE PHOSPHATE) ANCHORED MEMBRANES FOR CATALYZING U(VI) IONS REDUCTION AND MIZOROKI-HECK COUPLING REACTION



6.1 Introduction

In general, the physical instability of NPs could be avoided by using appropriate surfactants during NPs syntheses (Drinkel et al. 2014; Xu et al. 2017; Mirzaei et al. 2017; Tejamaya et al. 2012). However, these NPs suspended in colloidal solutions are difficult to handle/withdraw, and also surfactants coatings on NPs may block the catalytic sites. This would lead to slower reaction kinetics by hindering the interaction of reactants with the catalyst surface. These problems can be addressed by immobilizing the NPs on insoluble solid supports such as synthetic polymer membrane as given in Chapter 3, 4 and 5, silica (SiO_2) (Boudjahem et al. 2010; Tyumentsev et al. 2014; Boltoeva et al. 2008), alumina (Al_2O_3) (Li et al. 2013), carbon nanomaterials (carbon nanotubes, grapheme oxide) (Krittayavathananon et al. 2014; Huang et al. 2014), superparamagnetic materials (Fe_3O_4) (Gawande et al. 2013; Sobhani and Pakdin-Parizi 2014) etc. Among the solid supports, the porous polymeric membrane provides not only better physical and chemical stability but also high accessibility of the NPs to reactants. It is also possible to tune the size and shape of the NPs and have added advantage of ease of handling/withdrawing for recycling. However, the major issue is uniform distribution of NPs across the thickness of the pristine polymeric membrane. Therefore, these polymer supports need to be functionalized for uniform formation of NPs at interior matrix and loading high amount of NPs without compromising physical and chemical stability. The charge (cationic/anionic) on the membrane is also important for mass transfer of reactants to the membrane phase embedded with NPs, and some cases adversely affect the interactions of reactants with the surface of NPs. It has been reported that the neutral weak basic (no ion-exchange sites) membrane not only provides the optimum interactions with the nanocatalyst but also holds high amount of the metal NPs (Chapter 4&5).

Among the noble metals, palladium (Pd) NPs has been studied extensively as a prime catalyst for the applications in industrial and biological important coupling reactions involving carbon-carbon and carbon-heteroatom coupling reactions (Narayanan 2010; Cheong et al. 2010), remediation of toxic ions including nitrite reduction (Dodouche and Epron 2007), reduction of $\text{Cr}_2\text{O}_7^{2-}/\text{CrO}_4^{2-}$ anions to Cr^{3+} ions (Yadav and Xu 2013), and reduction of UO_2^{2+} to U^{4+} ions (Chapter 4 & 5) having applications in nuclear industries. Palladium and Pd NPs supported on solid matrices (heterogeneous) have been extensively used in many organic coupling reactions (Nabid et al. 2011; Sobhani and Pakdin-Parizi 2014) and inorganic transformations, and exhibit better catalytic activity compare to their traditional homogeneous analogues such as $\text{Pd}(\text{OAc})_2$ and PdCl_2 . The palladium catalyzed Mizoroki–Heck reaction was most explored C-C bond coupling reaction industrially, provides efficient route for the vinylation of aryl/vinyl halides or triflates. The most studied soluble phosphine complexes are difficult to separate and also these are expensive, sensitive to air and moisture, and toxic in nature (Cho and Shaughnessy 2011).

In the present work, the microporous poly(propylene) (PP) membrane functionalized with poly(ethylenimine) (PEI) and poly(ethylene glycol methacrylate phosphate) (poly(EGMP)) have been synthesized to host the Pd NPs. The membranes have been formed by *in situ* UV-initiator induced polymerization in the pores of host PP membranes. Thus formed membranes have been characterized for size distribution of Pd NPs, loading capacity toward Pd^0 , physical structures, and Pd elemental mapping across the membrane. These characterized membranes have been studied for their catalytic activities in the representative inorganic reduction (UO_2^{2+} to U^{4+}) and Mizoroki-Heck coupling reaction between iodobenzene and ethy acrylate. This reaction has been studied in the presence of Pd^0 (Pd NPs) or Pd^{2+} (palladium salt) loaded PEI/poly(EGMP)-membranes with

and without triethylamine at 100 °C. The change in oxidation state of Pd²⁺ to Pd⁰ during reaction has been monitored by X-ray photoelectron spectroscopy (XPS).

6.2 Experimental

Details of materials and reagents used are given in chapter 2.

6.2.1 Synthesis of Pd NPs on polyethylenimine (PEI) anchored membrane

The PEI functionalized membrane was prepared by UV-light induced in situ polymerization of monomers in pores of the host PP membrane matrix under the optimized conditions based on our previous work. UV-polymerization was carried out in a photoreactor described in the experimental section. The pore-filling polymerizing solution was prepared by dissolving different amounts of monomer GMA (1.5, 0.75, 0.5, and 0.2g) in a 3 mL DMF solvent along with 5 mol% cross-linker (EGDM) and 2 wt% UV-initiator (DMPA). To homogenize, the polymerizing solution was sonicated for 15 min. The PP membranes having dimensions of 5×5 cm² area were first soaked in methanol and then immersed for 6 h in polymerizing solution. After pore-filling, the excess solution adhering on host PP membrane was removed gently and the pore-filled membranes were sandwiched between two Garware polyester sheets and irradiated with 365 nm light in a photoreactor for a period of 20 min. After UV irradiation, the membrane samples were washed thoroughly with DMF to remove the un-polymerized components. This washing was continued till constant weights were obtained.

The poly(GMA)-anchored membrane samples were reacted with a 10 (w/v %) solution of PEI in DMF at 60°C for a period of 4h to anchor PEI (M_n=10,000, branched polymer) by opening epoxy ring of GMA units. The constant temperature was maintained by using water bath. The membrane samples were washed extensively with water after chemical treatment and dried at 45°C under

vacuum condition. Then these PEI anchored membranes were equilibrated with the solutions containing $0.01 \text{ mol L}^{-1} \text{ PdCl}_2$ at $\text{pH} = 2$ for 12 h. After loading with Pd^{2+} ions, the membranes were washed several times with de-ionized water and reduced with $0.05 \text{ mol L}^{-1} \text{ NaBH}_4$ solution, washed and dried for further use.

6.2.2 Synthesis of Pd NPs in poly(ethylene glycol methacrylate phosphate) (EGMP) anchored membrane

Similar to the PEI functionalized membrane, a phosphate-anchored membrane was prepared by polymerizing monomer ethylene glycol methacrylate phosphate (EGMP) dissolved in DMF solvent along with 5 mol% cross-linker (EGDM) and 2 wt% UV-initiator (DMPA) in pores of the host PP membrane using similar conditions. After anchoring cross-linked poly(EGMP), the membrane was conditioned in $0.1 \text{ mol L}^{-1} \text{ NaCl}$ solution for 24 h, and then equilibrated with $0.01 \text{ mol L}^{-1} \text{ PdCl}_2$ solution to load Pd^{2+} ions by ion-exchange. These Pd^{2+} loaded poly(EGMP)-membrane samples were reduced to Pd^0 with 0.05 mol L^{-1} sodium borohydride (NaBH_4) as described above for the PEI-membrane.

6.2.3 Characterizations of membranes

The loading capacities of these functionalized membranes toward Pd^0 were determined by ICP-AES. For this, the known dimension ($2 \times 1 \text{ cm}^2$) and weight of the Pd^0 -loaded membranes were leached completely in aqua-regia solution for overnight. To confirm the complete leaching, the membrane samples were analyzed by EDXRF for residual Pd content, if any. After complete leaching, the liquor was evaporated and re-dissolved in 10 mL of $0.1 \text{ mol L}^{-1} \text{ HNO}_3$. These re-dissolved solutions were subjected to ICP-AES analyses to determine Pd concentration and were used to calculate the amount of Pd content loaded in the membrane sample. The ICP-AES analyses

were done using high resolution simultaneous atomic emission spectrometer (Spectro Arcos, Germany). The details of the instrument and procedures were discussed in Chapter 2.

The porosity of the PEI functionalized membranes along with pristine PP membranes were measured by using wetting “porefil” liquid. The void volume/porosity was measured by using the following equation.

$$\text{Void Volume} = \frac{(w_l - w_d)}{\rho_l v_m} \times 100 \quad (1)$$

Where w_l , w_d , ρ_l and v_m were weight of porefil liquid wetted membrane sample, weight of the dry membrane, density of porefil liquid, and volume of the membrane sample, respectively. The procedures for obtaining these values were described in Chapter 4 in detail. The pore size distributions of the PEI and EGMP functionalized PP membranes were also measured by capillary flow porometry (CFP) using porefil liquid as described in chapter 2.

The ionic state of palladium was measured by using X-ray Photoelectron Spectroscopy (XPS). The XPS analysis was carried out using Mg K_{α} (1253.6 eV) X-ray source and a DESA-150 electron analyzer (M/s. Staib Instruments, Germany). The binding energy scale was calibrated to Au-4f_{7/2} line of 83.95 eV. The XPS spectra are fitted using XPSPEAK41 software and elements chemical states were obtained by the binding energies from the literature. FE-SEM image analysis was done to know the surface morphology of the pristine, PEI functionalized and EGMP functionalized PP membranes. The elemental mappings of Pd across the cross-section and surface were carried out by energy dispersive spectroscopy (EDS). The size distribution of Pd NPs formed in the PEI-functionalized membrane was analyzed using Small-Angle X-ray Scattering (SAXS). SAXS experiments were performed using a laboratory-based SAXS instrument with Cu K_{α} as probing radiation. Radial averaged scattering intensity ($I(q)$) was obtained within a wave vector transfer

$q = 4\pi \sin(\theta)/\lambda$, where λ is the wavelength and 2θ is the scattering angle) range from ~ 0.1 to 2.5 nm^{-1} . The sample to detector distance was nearly 1 m. One dimensional scattering profiles were obtained through radial averaging of the scattering data. The details of SAXS data analysis are given in chapter 2.

6.2.4 Mizoroki-Heck coupling reaction

The Pd^{2+}/Pd NPs immobilized on PEI and EGMP functionalized membranes were studied for their catalytic activities in Mizoroki-Heck coupling reaction. In a typical experiment, 1 mmol of iodobenzene, 1.1 mmol of ethyl acrylate and 3 mmol of triethylamine were added to double jacketed glass vessel. To this reaction mixture, known weight of the membrane having palladium catalyst was added and then heated to $100 \text{ }^{\circ}\text{C}$ without any solvent for 1h. Due to volatile nature, the ethyl acrylate was taken in slightly excess to that of iodobenzene in this reaction. The reaction was tested in the presence of the PEI/poly(EGMP)-membrane containing Pd^0 or Pd^{2+} , with and without external base (triethylamine). The progress of the reaction was monitored by thin-layer chromatography (TLC). After completion of the reaction, the mixture was cooled to room temperature and the catalytic membrane was removed, and then the mixture was washed with ethyl acetate and dried using rotavapor. In the next step, the product and excess (un-reacted) iodobenzene were separated by column chromatography using 1-10% (v/v %) of ethyl acetate to hexane mixture. Finally, the product was concentrated by evaporating the solvent and dried for further characterizations. The final product was characterized by nuclear magnetic resonance (NMR) spectroscopy and liquid chromatography attached to mass spectrometry (LC-MS). The recovered catalyst was washed with water and ethanol several times and dried for further use. The purity and identification of the compounds were carried out using ^1H , ^{13}C NMR and HRMS. Based on NMR the minimum purity of the compound is $\sim 95\%$. The NMR spectrum was recorded by

using Varian, 500MHz, Inc, USA and the sample was prepared by dissolving 5 mg of product sample in CDCl_3 and transferred into NMR tube. The LC-MS spectrometry was carried out by using model number 410 Prostar Binary LC with 500 MS IT PDA Detectors supplied by Varian, Inc. USA.

6.2.5 Reduction of U(VI) ions

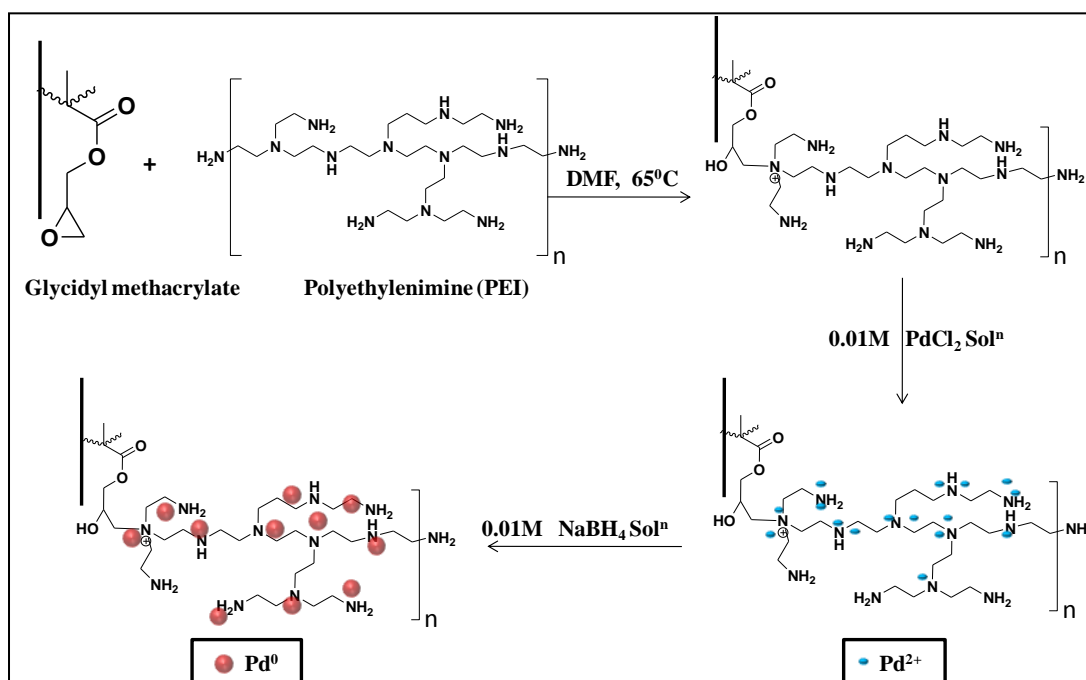
The UO_2^{2+} ions reduction was carried out in a double jacketed glass vessel which was kept at constant temperature using thermostat bath. The experimental setup is shown in chapter 4. The reduction was carried out 50°C by mixing 8 mL of $0.1 \text{ mol L}^{-1} \text{UO}_2(\text{NO}_3)_2$ solution at $\text{pH} = 2$ and 8 mL of 1 mol L^{-1} formic acid in a beaker. The known weights of Pd NPs loaded membranes were immersed in to the reaction vessel after attaining desired temperatures. The immersion time was taken as start time. The UV–Vis spectra showed no reduction of UO_2^{2+} ions without catalyst and also with catalyst at room temp. The reduction of UO_2^{2+} ions was monitored time to time by taking 1 mL aliquot from the reaction solution at a fixed time interval, and UV–Vis spectra of these samples were recorded after diluting this to 3 mL by adding $\text{pH} = 2$ solution.

To study the reduction kinetics, the most intense peak of U^{4+} ion at 665 nm was used and calibrated by measuring the U^{4+} ions concentration by electro-analysis. To prevent back oxidation of U^{4+} ions to UO_2^{2+} ions during long storage, the solution was kept in a freezer and UV-Vis spectra was monitored again to ensure the extent of oxidation of U^{4+} ions. The detailed electro-analysis is discussed in chapter 4.

6.3 Results and discussion

The PEI-functionalized membrane is a neutral membrane with weak basic amine groups. It is known that weak basic amine groups play an important role in many catalyzed reactions such

Mizoroki-Heck coupling reactions. Apart from chemical composition, the physical architecture of host substrate is also important for providing accessibility to Pd nanocatalysts embedded at interior matrix. Therefore, the microporous membrane was selected to host the Pd NPs in weak basic local environment. Also, the amine groups in PEI have strong coordination towards Pd^{2+} ions, which would result to high amount of Pd^{2+} ions loading. The Pd NPs have been formed by reducing the Pd^{2+} ions loaded PEI membrane with sodium borohydride aqueous solution. The detailed mechanism involved in the formation of Pd NPs on the membrane is given in Scheme 6.1.



Scheme 6.1 Chemical modifications involved in formation of Pd NPs on the PEI anchored PP membrane.

The anchoring of PEI was likely to affect the porous network of the membrane. To control the porosity, the anchoring of the precursor poly(GMA) was controlled by varying its concentration in the polymerizing solution filled in the pores of the membranes. Thus formed membranes were characterized for their porosity and pore-size distributions by using capillary flow porometry

(CFP). The variation of % mass-gain, porosity and percentage of water uptake of thus formed membranes are given in Table 6.1. To compare the catalytic activity in acidic complexing environment, the acidic phosphate bearing membrane was also prepared by anchoring poly(EGMP) in the same host PP membrane.

Table 6.1 The comparisons of the amount of polymer anchored, percentage of water uptake (hydrophilicity) and amount of Pd⁰ loading in PEI and poly(EGMP) anchored PP membranes.

Membrane Type	Amount of Monomer	Pore-filling (wt%)	Water Uptake (wt%)	Pd Loading Capacity (mg g ⁻¹)	Porosity (%)
PP1	1.5g (GMA)	240±10	40±2	350±5	< 6
PP2	0.75g (GMA)	91±5	114±5	162±5	45
PP3	0.5g (GMA)	23±3	168±5	64±2	72
PP4	0.2g (GMA)	12±3	214±5	31±2	78
Poly(EGMP)	1.5g (EGMP)	200±10	35±2	14±2	< 6

It is seen from Table 6.1 that the amount of Pd NPs loading on to the PEI functionalized membrane was higher than self-reducing membranes given in the previous chapters. As shown in Table 6.1, the Pd⁰ saturation loading capacity of the membrane increased with the increasing the monomer GMA concentration in the polymerizing solution, which provide precursor epoxy groups to link PEI. Depending on the mass gain of the membranes by GMA and PEI, membranes are denoted as PP1, PP2, PP3, and PP4 as given in Table 1 (PP1 to PP4 decreasing in mass gain). The void volume of the membrane decreased with the increase in percentage of polymer anchored in the membrane. Pristine PP membrane was having void volume of 83 (v/v%). While, the higher percentage of polymer fillings in both PP1 and poly(EGMP) membranes resulted to almost non-porous physical architecture having void volume of <6 (v/v%), see Table 6.1. Similarly, the water uptakes of the membranes were decreased with the increasing in the pore-filling percentage. The change in

through pore-size distributions of these functionalized membranes along with pristine membrane were studied by capillary flow porometry (CFP). The membranes denoted as EGMP and PP1 were not subjected to CFP as these were non-porous. The pore-size distributions are shown in Figure. 6.1 were obtained from CFP data analyses as described elsewhere (Agarwal et al. 2012). The percentage gas flow given in y-axis could be taken as an equivalent to pore number density for the interpretation. It is seen from Figure. 6.1 that, the pristine membrane was having a uniform pore-size distribution, which was around 0.150 to 0.190 μm with majority of pores having 0.185 μm pore-size. After functionalization with PEI, the porous nature of the membrane has been changed significantly. The pore-size distributions of PP3 and PP4 were reduced with respect to pristine membrane and spread over longer range 0.125-0.190 μm . In case of PP2 membrane, the pore diameters reduced significantly (less than 100nm) due to higher extent of pore-filling.

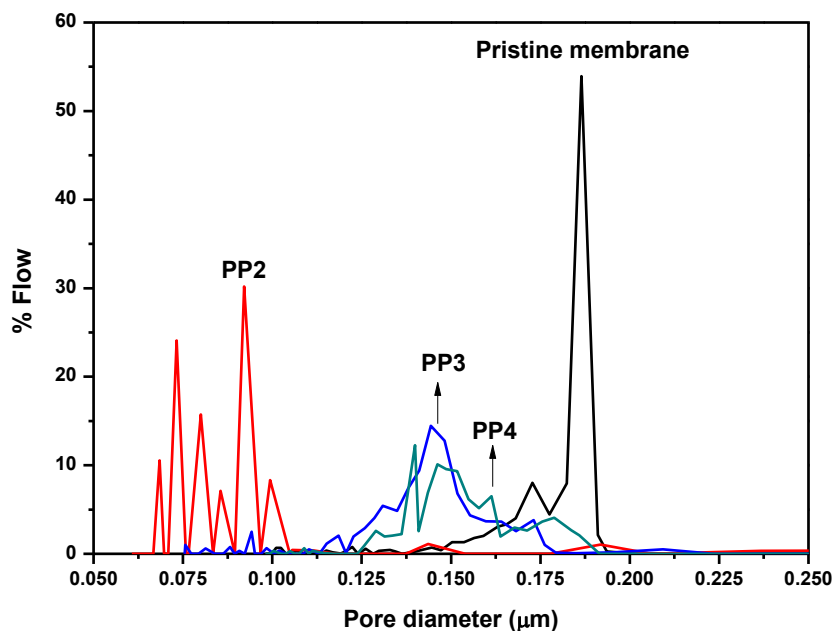


Figure 6.1 The comparison of obtained pore-size distributions of pristine membrane and PEI functionalized membrane (PP2, PP3 and PP4) by capillary flow porometry.

The physical architectures of the membranes formed by varying the amount of polymer on the membrane are shown in Figure 6.2.

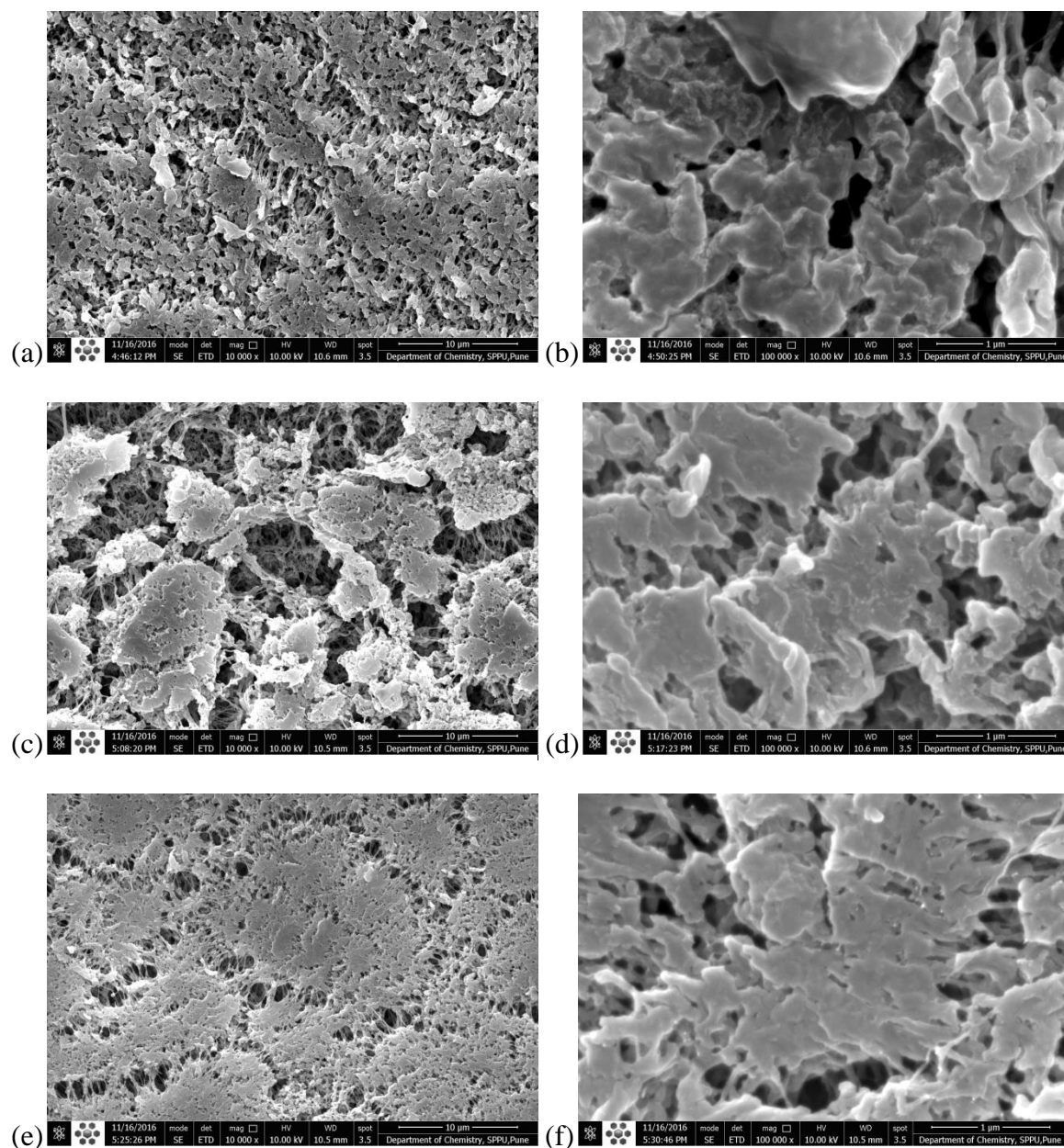


Figure 6.2 A representative SEM images of the PP membranes anchored with different amounts of polymer PP2 (a & b), PP3 (c & d) and PP4 (e & f), respectively, under two different magnifications.

As the amount of polymer pore-filling in the membrane increased, the porosity decreased accordingly. It is clear from Figure. 6.2 that the SEM images for PP2 (a & b) are denser than that for PP3 (c & d), whereas the images for PP4 (e & f) seems to have the similar physical architecture. These results are in agreement with the void volume data given in Table 6.1 and through pore size distribution shown in Figure 6.1. The uniform distribution of Pd NPs formed on the membrane PP2 by EDS elemental mapping given in Figure 6.3.

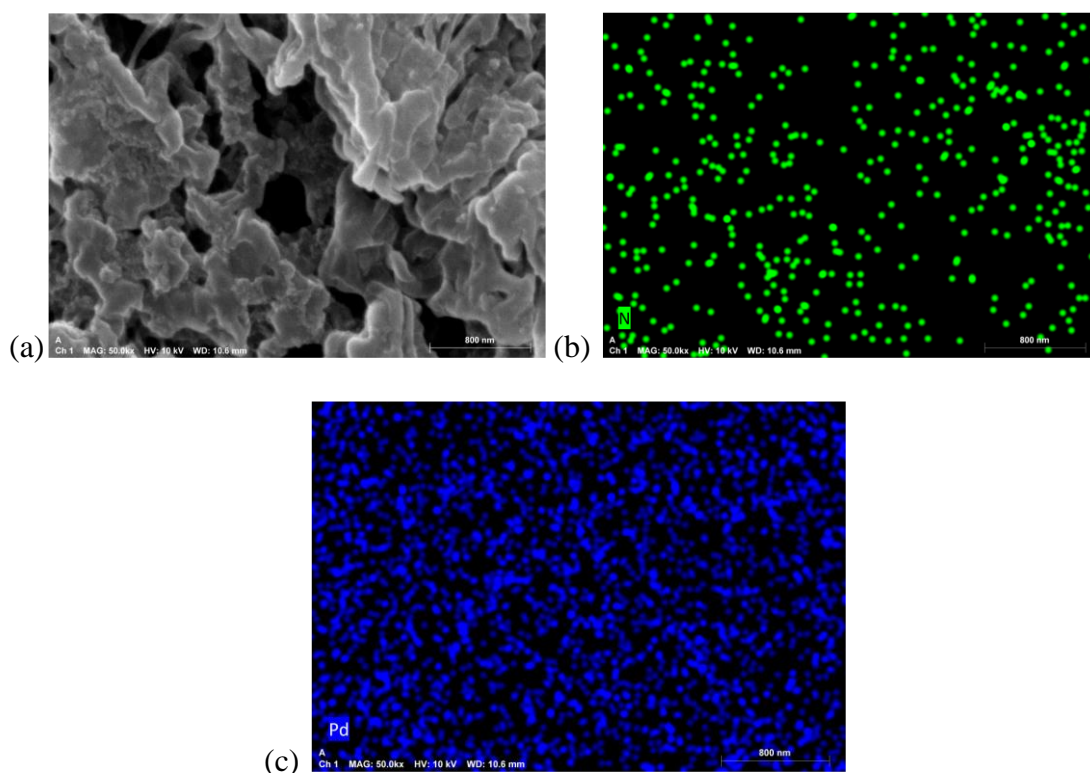


Figure 6.3 The representative SEM image of the Pd NPs formed on the PP2 membrane (a), and corresponding elemental mappings of nitrogen (b) and Pd (c) by EDS.

The surface morphology of Pd NPs embedded densely filled PP1 membrane was also analyzed by FE-SEM imaging. As shown in Figure 6.4, the membrane having fibrous interior and dense at the surface is because of the change in physical structure during drying that resulted to formation of dense surface and fibrous interior. From the SEM images shown in Figure. 6.4, the Pd NPs formed

in the membrane were not visible indicating very small size. However, the resolution of FE-SEM images could not be improved further due to charging of non-conductive polymer matrix.

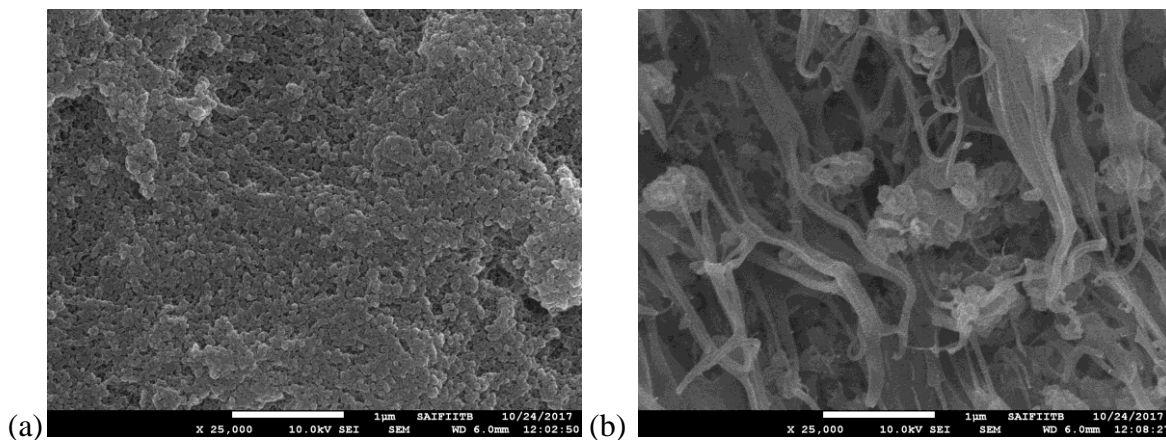


Figure 6.4 The surface morphology of Pd NPs embedded membrane (PP1) (a) and cross-sectional image of the same membrane (b) under same magnification.

The small angle X-ray scattering (SAXS) experiments and EDS elemental mappings of the membrane samples were carried out. The scattering contribution of the PEI anchored (denoted as PP1 blank), Pd²⁺ ions loaded, and Pd NPs loaded membranes were plotted and the scattering contributions from blank membrane was subtracted from Pd NPs embedded membrane as shown in Figure 6.5 (a)&(b). Poly-disperse spherical particle model, assuming a standard lognormal size distribution of the particles, was fitted to the data using non-linear least square. A Porod type (q^{-4}) of scattering contribution, arising from larger length scale (probably the agglomerates), was also considered to explain the increasing trend of intensity in low q regime. The size distributions of the Pd NPs formed in the membrane is shown in Figure 6.6. It is evident from size distribution of Pd NPs shown in Figure 6.6, that the very small diameter Pd NPs (2 nm) were formed with slight right side tailing in Pd NPs' size distribution extending up to 6 nm and also from Figure 6.5(a) it was observed that, there is a small scattering contribution from the Pd²⁺ ions loaded membrane

this may be due to a small amount of Pd^{2+} ions getting reduced by PEI, and size of it was similar to PP3 membrane but number of particles are less. The reduction of Pd^{2+} ions with PEI without reducing agent was also confirmed by XPS. Similarly, the size distributions of Pd NPs on PP3 and PP4 were analyzed by SAXS. Unlike the Pd NPs on PP1 membrane, the size distributions were found to be two types of distributions. For PP3 membrane, the average radius distribution was 1.18 and 7.58nm (shown Figure 6.6(b)) and for PP4 membrane 1.36 and 12.03nm (shown Figure 6.6(c)) with standard deviation of 0.05nm. It was observed size of the NPs decreased with the increase in the amount of PEI. This may be due to more number of nuclei formed in a short period of time (due to high amount of PEI) followed by growth without additional nucleation. In addition to smaller NPs bigger NPs also formed but number is less comparatively.

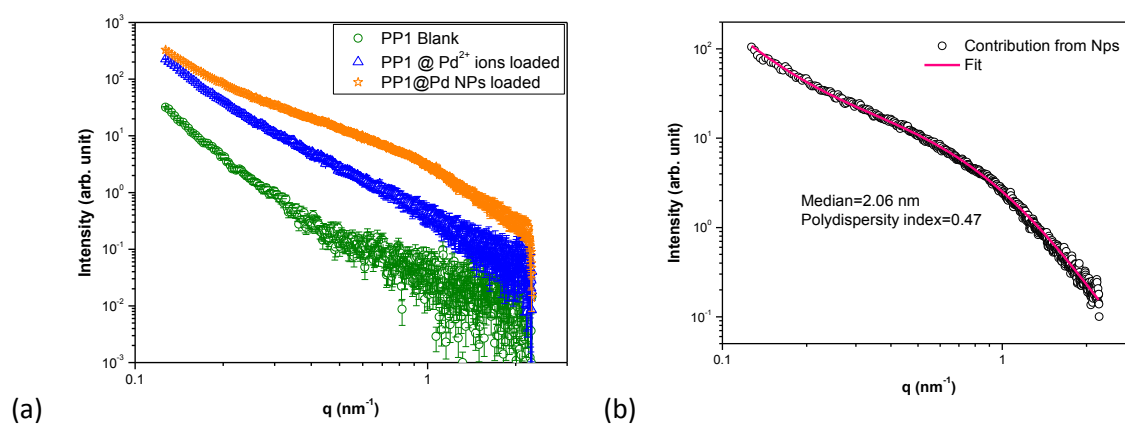


Figure 6.5 (a) Scattering profile from blank membrane, Pd^{2+} ions loaded and Pd NPs loaded membrane, (b) Scattering contribution solely from the nanoparticles as obtained from the subtraction of scattering profile of blank and Pd^{2+} ions loaded membrane.

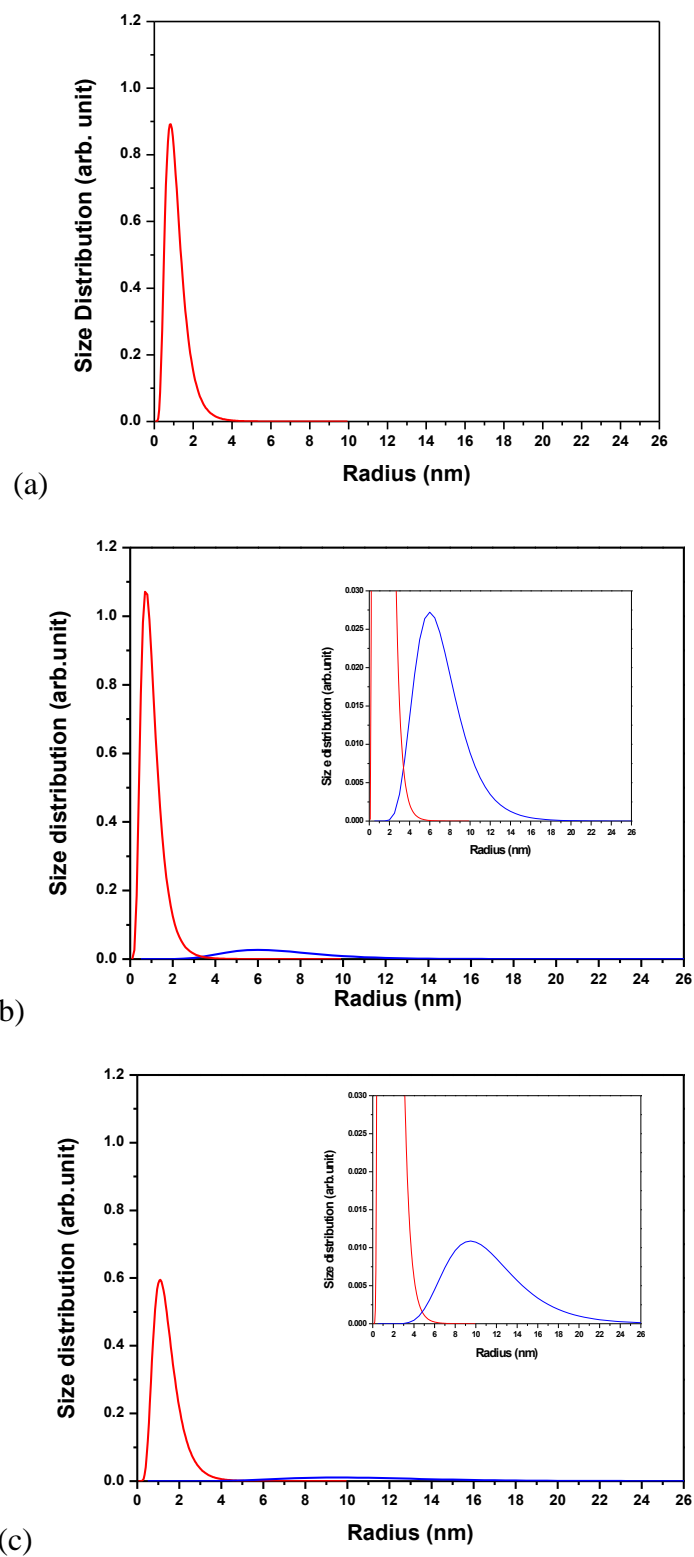


Figure 6.6. Size distribution of the Pd NPs in the PEI-membrane PP1 (a), PP3 (b), and PP4 (c) as obtained from the SAXS data analysis.

From EDS analysis, the N and Pd elemental mappings across PP1 membrane sample given in Figure 6.7. The uniform N and Pd distribution along cross-section of the elemental mapping suggested a uniform anchoring of PEI across the membrane.

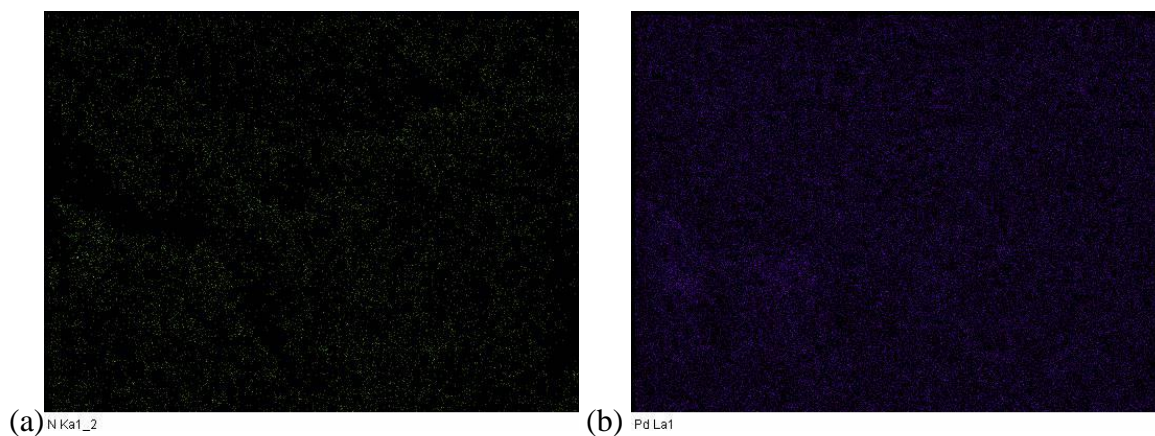
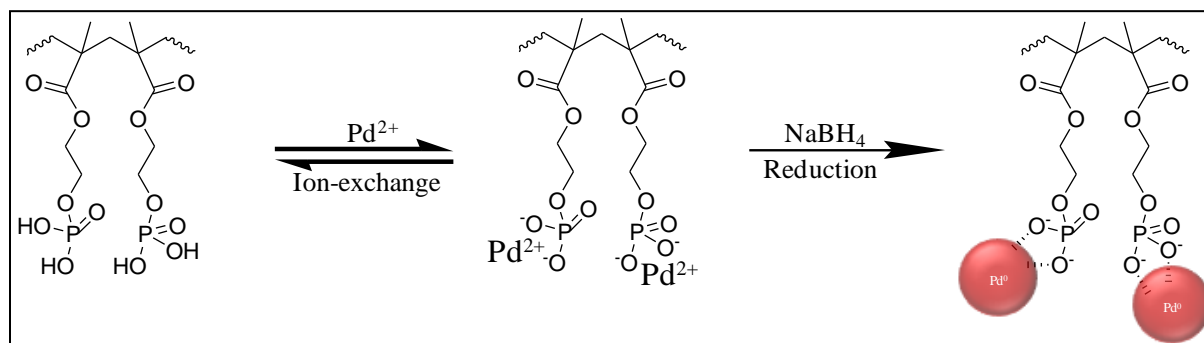


Figure 6.7 The EDS elemental mappings of nitrogen (a), palladium (b) across the cross-section of the PP1 membrane.

In addition to the PEI anchored membrane, acidic phosphate bearing cation-exchange membrane was also prepared by anchoring poly(EGMP) in the same PP host matrix as described in the experimental section. As shown in Table 6.1, the saturation loading capacity of this cation-exchange membrane towards Pd^0 was found to be $14 \pm 2 \text{ mg g}^{-1}$, which was much lesser than the Pd^0 loading capacity of the PEI-functionalized membrane. During reduction of Pd^{2+} ions to Pd^0 , there might be substantial loss of palladium before locking as NPs in the poly(EGMP) membrane matrix. The formation of Pd NPs in the poly(EGMP) membrane is shown in Scheme 6.2.



Scheme 6.2 Formation of Pd NPs in the poly(EGMP)-membrane.

The physical architecture of the poly(EGMP) membrane was dense due to high amount of polymer content. The elemental distribution of this membrane was found to be uniform by EDS mapping.

The surface morphology and EDS elemental mapping was shown in Figure 6.8.

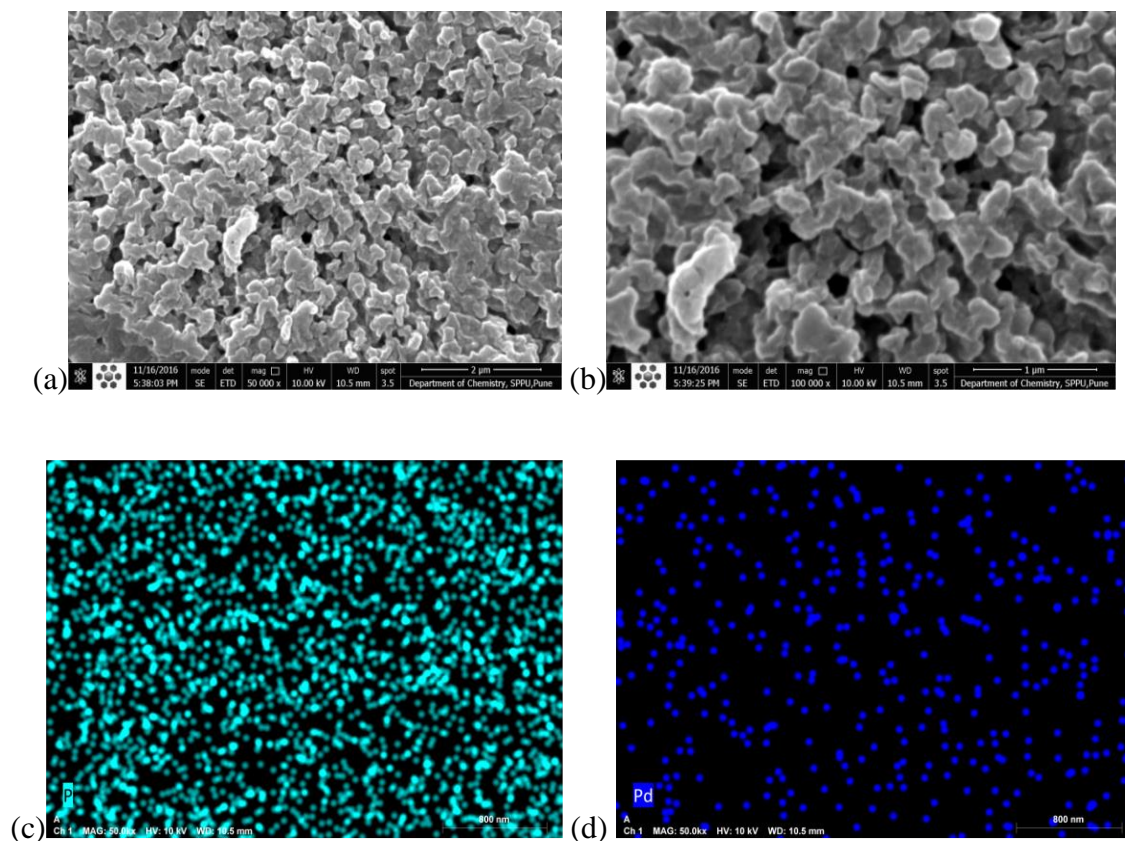


Figure 6.8 Representative FE-SEM images of surface (a & b) and corresponding elemental mappings of phosphorus (c) and palladium (d) by EDS of poly(EGMP)- membrane.

6.3.1 Catalytic activities of Pd NPs embedded PEI and poly(EGMP) in U(VI) ions reduction

The conversion of UO_2^{2+} to U^{4+} was used to test the catalytic activities of the Pd NPs embedded in PEI and EGMP anchored membranes. The reaction was carried out in the presence of Pd NPs at 50°C using formic acid as a source of reducing agent as described in the previous chapter. The *in situ* generated H_2 gas during decomposition of formic acid on the Pd NPs surface used as electron source for reducing the UO_2^{2+} ions. Because of high activation barrier the reduction of UO_2^{2+} ions (As described in Chapter 5), was found to be not successful in the absence of Pd catalyst or with catalyst at room temp.

If decomposition of formic acid on Pd NPs surface follows dehydration process, the released CO gas gets adsorbed on to Pd surface and subsequently makes the catalyst inactive. Among the noble metals Pd has strong adsorption tendency towards CO. For noble metals, the adsorption trend towards CO follows as $\text{Pd} > \text{Cu} > \text{Ag} > \text{Au}$ (Abild-Pedersen and Andersson 2007). Therefore, one way to avoid CO adsorption is to synthesize Pd core shell nanoparticles with Ag, Au and Cu. Since Ag, Cu and Au did not have strong adsorption towards CO, so the occupied active sites are released due to desorption of CO from the Pd surface. However, controlled synthesis of core shell nanoparticles is not an easy process. Another way to avoid this complicated process is formation of Pd NPs in weak basic groups containing platform for the formic acid decomposition (Mori et al. 2013). By using basic groups, the decomposition process occurs preferentially through dehydrogenation. A cooperative action between active Pd NPs and weakly basic groups ($-\text{NR}_2$) of the membrane platform could play an important role in achieving efficient catalytic performance. Firstly, the basic groups ($-\text{NR}_2$) de-protonate the formic acid (acts as a proton scavenger) and forms Pd-formate complex which subsequently undergoes β -hydride elimination to produce CO_2 and palladium hydride species. The reaction of hydride species with $-\text{HN}(\text{R}_2)$ produce molecular

hydrogen along with regeneration of the Pd⁰ species. In this work, this strategy was adapted by forming Pd NPs in the PEI-functionalized membrane. To compare the enhancement in the reduction, Pd NPs embedded in the poly(EGMP) anchored membrane was also prepared.

The UO₂²⁺ ions reduction reaction was analyzed by monitoring the conc. of U⁴⁺ ions as a function of reduction time. The reduction profiles of Pd embedded PP membranes plotted with $\ln[U(VI)_t/U(VI)_o]$ as a function of reduction time found to be linear in the presence of excess of formic acid concentration as expected from first-order kinetic equation given below and could be used for the comparison.

$$\ln \frac{[U(VI)]_t}{[U(VI)]_o} = -kt$$

Where $[U(VI)]_t$ and $[U(VI)]_o$ represent conc. of UO₂²⁺ ions at time t and initial respectively, t is reduction time, and k is apparent first-order reduction rate constant. As k is dependent on the amount of Pd catalyst, the values of k were normalized with the amount of Pd⁰ to obtain catalytic activity (s⁻¹g⁻¹) for studying the effect of variables involved in the reduction of UO₂²⁺ ions with formic acid. The successive UV-Vis spectra of UO₂²⁺ ions reduction with Pd NPs embedded PP3 membrane and its first order kinetic fitting graphs are given Figure. 6.8. In the absence of catalyst the reaction did not proceed under similar conditions for 2h, as observed from the successive UV-Vis spectra are shown in Figure 6.9(c).

The comparisons of catalytic activities towards UO₂²⁺ ions reduction of Pd NPs embedded membranes are given Table 6.2. It is clear from Table 6.2 that the catalytic activity increased with increase in the porosity of the membrane for the same amount Pd under similar experimental conditions. Even though the porosity of the PP3 and PP4 membrane were almost same, there was significant difference in the catalytic activity with same Pd amount. This was mainly due to

difference in the amount of PEI in \ membrane i.e. higher formic acid decomposition with higher PEI content in the membrane leading to higher catalytic activity. In case of PP1 membrane, even though PEI content was higher, the catalytic activity was not that higher as expected. This could be due to higher amount of polymer content on PP1 membrane caused diffusion resistance in catalytic reaction at interior matrix due to restricted accessibility of the Pd NPs embedded in dense interior matrix.

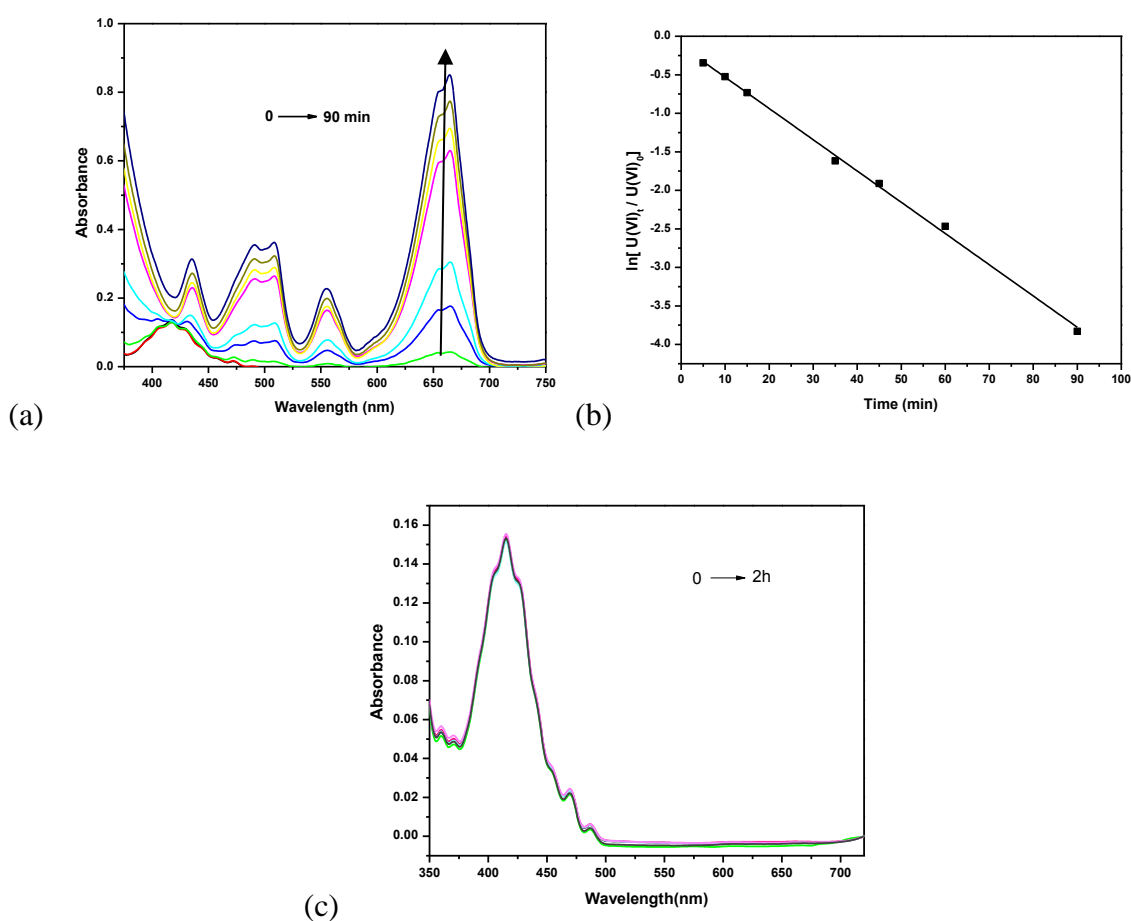


Figure 6.9. UV– Vis spectra showing growth of U(IV) ions absorption peaks (a), variation of logarithm of $[U(VI)]_t/[U(VI)]_0$ as a function of reduction time with formic acid in the presence of Pd NPs embedded PEI (PP3) membrane at 50°C , (b) and no reduction of U(VI) ions with formic acid in absence of Pd catalyst (c).

Table 6.2 The comparisons in catalytic activities of Pd NPs immobilized on PEI functionalized PP membranes.

Substrate	Temperature	Pd amount (mg)	K(min ⁻¹)	K(S ⁻¹)	Activity (K/Pd) S ⁻¹ g ⁻¹
Poly(propylene)	50 ^o C	1.19	-0.005	9.16X10 ⁻⁵	0.08
	50 ^o C	1.82	-0.012	1.95X10 ⁻⁴	0.11
	50 ^o C	1.13	-0.027	4.48X10 ⁻⁴	0.39
	50 ^o C	1.03	-0.040	6.76X10 ⁻⁴	0.65
	50 ^o C	1.04	-0.028	4.66X10 ⁻⁴	0.45

It was observed that Pd NPs immobilized in the poly(EGMP) membrane did not show significant catalytic activity towards UO_2^{2+} ions reduction. The conversion was found to be less than 20-30% even after 2 h. The less efficient reduction could be the preferential binding of UO_2^{2+} ions with phosphate group ($-\text{RPO}_3^{2-}$) on the poly(EGMP) which hindered the interaction with Pd NPs. The UV- Vis spectra of UO_2^{2+} ions reduction in the presence of Pd NPs embedded EGMP anchored membrane is given in Figure 6.10. As described in the experimental section, the percentage conversion of UO_2^{2+} to U^{4+} was obtained by measuring the concentration of U^{4+} ions in the solution by oxidizing it to UO_2^{2+} by electro-analysis.

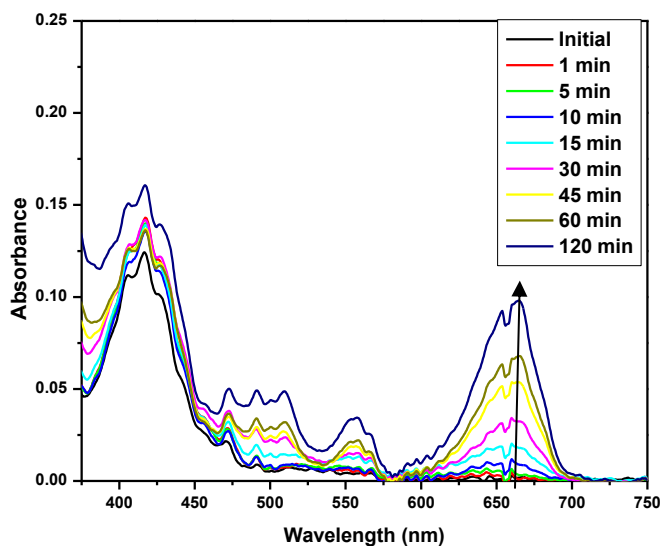
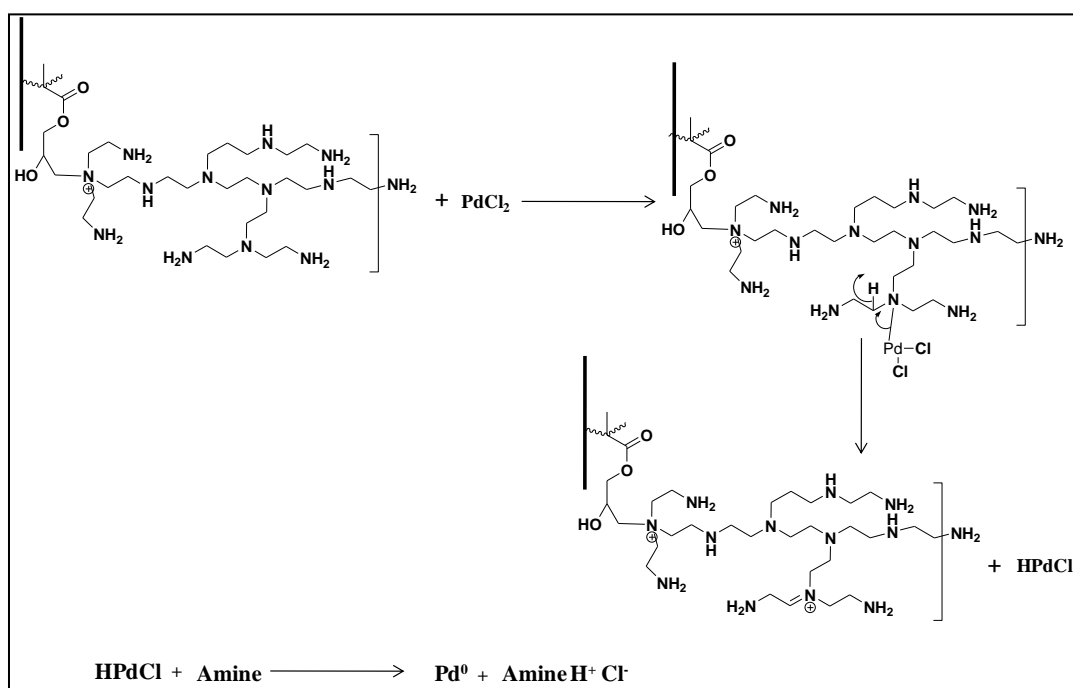


Figure 6.10 UV–Vis spectra showing less efficient growth of absorption peaks of U(IV) ions during reduction of U(VI) ions with formic acid in the presence of Pd NPs immobilized in the EGMP anchored membrane at 50°C.

6.3.2 Catalytic activities of Pd²⁺/Pd NPs loaded membranes for Mizoroki-Heck coupling reaction

Palladium is widely recognized as very important metal among noble metals for catalyzing carbon-carbon, carbon-heteroatom coupling reactions. Initially, soluble palladium salts such as PdCl₂, Pd(OAc)₂ were used in the coupling reactions as a homogeneous catalysts. In 1971, Mizoroki et al. published a preliminary result for arylation of alkenes by iodobenzene catalyzed by PdCl₂ in the presence of potassium acetate as a base. They found that the Pd⁰ particles formed in situ in the reaction acts as active catalyst. Thereafter, the extensive studies had been carried out to understand the nature of the ligand, the base and the catalyst precursor in Mizoroki-Heck reactions. To understand the effect of ligand, the reaction was carried out by using Pd(OAc)₂ as precursor without any phosphine ligand which showed the reduction of Pd(OAc)₂ to Pd⁰ *in situ* by the reagents used in this coupling reaction. Thus formed Pd⁰ initiated the catalytic cycle by an

oxidative addition to the aryl iodide because some of the alkenes proposed by Heck (Heck 1969) played a role in reducing the palladium acetate. Briefly, the alkene reacted with the acetate in $\text{Pd}(\text{OAc})_2$ by intra-molecular nucleophilic attack followed by a β -hydride elimination leading to HPdOAc and subsequent formation of Pd^0 in the presence of a base (Heck 1969.; Tsuji 1995 and 2012; Kitching et al. 1966). In addition to this, amines used as a base in Mizoroki-Heck coupling reaction have also been found to reduce $\text{Pd}(\text{II})$. Here β -hydride elimination take place in the amine coordinated to the $\text{Pd}(\text{II})$ centre, leading to HPdOAc and then to $\text{Pd}(0)$ in the presence of the amine as reported by Collman 1987. The expected mechanism of formation of Pd NPs from Pd^{2+} ions by the PEI-functionalized membrane developed in this work is shown in Scheme 6.3. These membranes were found to hold high amount of Pd^{2+} ions and can acts as *in situ* reducing agent for conversion of Pd^{2+} ions Pd^0 nanoparticles.



Scheme 6.3 Formation of Pd NPs from Pd^{2+} ions by the amine groups in the PEI functionalized membrane.

In the present work, different conditions for Mizoroki-Heck coupling used are listed in Table 6.3. As shown in Table 6.3, the reaction was found to be successful with both Pd²⁺ ions and Pd nanoparticles embedded in EGMP and PEI anchored membranes in the presence of an external base (triethylamine). However, the reaction was not found to be successful with Pd²⁺ ions loaded membrane in the absence of an external base.

Table 6.3 The outcome of Mizoroki-Heck coupling reaction examined in different experimental conditions. Triethylamine was used as external base.

Mizoroki-Heck coupling reaction			
Substrate type and nature of the catalyst	Reaction condition	% Yield	
Pd ²⁺ on PEI	Presence of base	70	
	Absence of base	Unsuccessful	
Pd ⁰ on PEI	Presence of base	76	
	Absence of base	28	
Pd ²⁺ on EGMP	Presence of base	47	
	Absence of base	Unsuccessful	
Pd ⁰ on EGMP	Presence of base	62	
	Absence of base	Unsuccessful	

The reaction was also tried with Pd nanoparticles but in the absence of an external base. In this case, the reaction was successful to some extent by Pd nanoparticles embedded in the PEI-membrane but failed with Pd nanoparticles embedded in the poly(EGMP)-membrane. This suggested that the external base can be avoided by using this amine functionalized membrane with

high concentration of amine groups in the membrane. Also, the yield of the reaction was found to be higher (76%) in case of the PEI -membranes compared to poly(EGMP)-membrane (62%). This may be due to the amine groups in the PEI-membrane that facilitate the reaction. These yields were relatively less compared with the literature reported Table 6.4 but in most of these reactions time consumed for the reaction was very high and needed a solvent. Whereas, in this work the reactions were found to be completed in 1h time without need of any solvent.

Table 6.4 Comparison of Mizoroki-Heck coupling reaction yield carried out with Pd NPs hosted in different matrices and conditions.

Catalyst	% Yield	Solvent	Time	References
Pd(II)	45-94	DMF	20h	Kantam et al. 2009
Pd Immobilized on Silica	81-95	DMF	6h	Karimi and Enders 2006
Pd/MgLaO	17-95	DMF	10h	Cwik et al. 2006
Pd Nanoparticles Supported on Polyaniline	67-90	DMF	24h	Yu et al. 2015
Pd(OAc) ₂	68-99	triethanolamine	10h	Li and Wang 2006
Pd ²⁺ on PEI	70	No solvent	1h	Present work
Pd ⁰ on PEI	76			
Pd ²⁺ on EGMP	47			
Pd ⁰ on EGMP	62			

The formation of Pd nanoparticles was studied by the X-ray photoelectron spectroscopy (XPS) after completion of the reaction. First, the PEI-membranes were loaded with Pd²⁺ ions by equilibrating in PdCl₂ solution and subjected to XPS. The deconvoluted XPS spectra reveals that there are two types of palladium species. The binding energy peaks at 336.9eV (3d_{5/2}) and at 342.3 eV (3d_{3/2}) were corresponded to Pd²⁺ ions, whereas, the binding energies at 335.9eV (3d_{5/2}) and at 340.9 eV (3d_{3/2}) see Figure 6.11(a). this indicates that a small amounts of Pd²⁺ ions gets reduced

to Pd NPs in presence of amines groups in PEI. These binding energies matches with the earlier results (Liu et al. 2015). During the Mizoroki-Heck coupling reaction, the Pd²⁺ ions were reduced to Pd NPs by the external base (triethylamine in this work) in addition to Pd NPs, the un-reduced form of palladium also present (Pd²⁺ ions) along with the oxidized Pd (PdO₂) as shown in the binding energy spectrum shown in Figure 6.11(b).

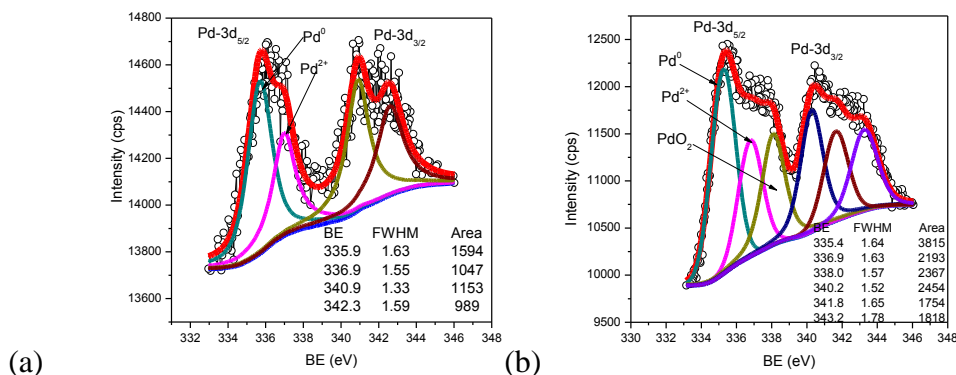
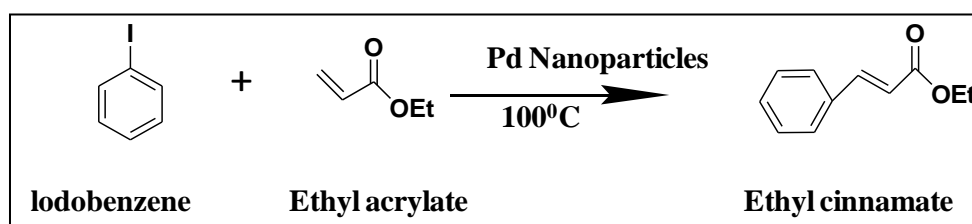


Figure 6.11 Deconvoluted XPS spectra of binding energies peaks of 3d_{5/2} and 3d_{3/2} obtained before using Pd²⁺ ions loaded PEI-membrane (a), and after coupling reaction (b).

As mentioned in the experimental section, the coupling reaction was carried out between iodobenzene and ethyl acrylate. The product ethyl cinnamate was characterized by using NMR, LC-MS and IR spectroscopy. The reaction scheme is given in Scheme 6.4.



Scheme 6.4. Mizoroki-Heck coupling reaction between iodobenzene and ethyl acrylate.

The characteristic signal peaks in ¹H and ¹³C NMR confirms the product formation (given in Figure 6.12). For ¹H NMR (500 MHz, CDCl₃) the signals observed at δ 7.71-7.68 (d, *J* = 16 Hz, 1H), 7.53-7.52 (d, 2 H), 7.39-7.38 (d, 2H), 6.46-6.43 (d, *J* = 16 Hz, 1H), 4.29-4.25 (q, *J* = 7.5 Hz,

2H), 1.36-1.33 (t, $J = 7.5$ Hz, 3H) and for ^{13}C NMR (126 MHz, CDCl_3) δ 167.0, 144.6, 134.5, 130.2, 128.9, 128.0, 118.3, 60.5, 14.3. R_F : 0.66 (10% ethyl acetate + Hexane). HR-MS: 177.0876[M+H]. The product ethyl cinnamate was also characterized by the LC-MS. The characteristic peak at 177.0876 (m/z) confirms the product. The LC-MS spectra of ethyl cinnamate given in Figure 6.13.

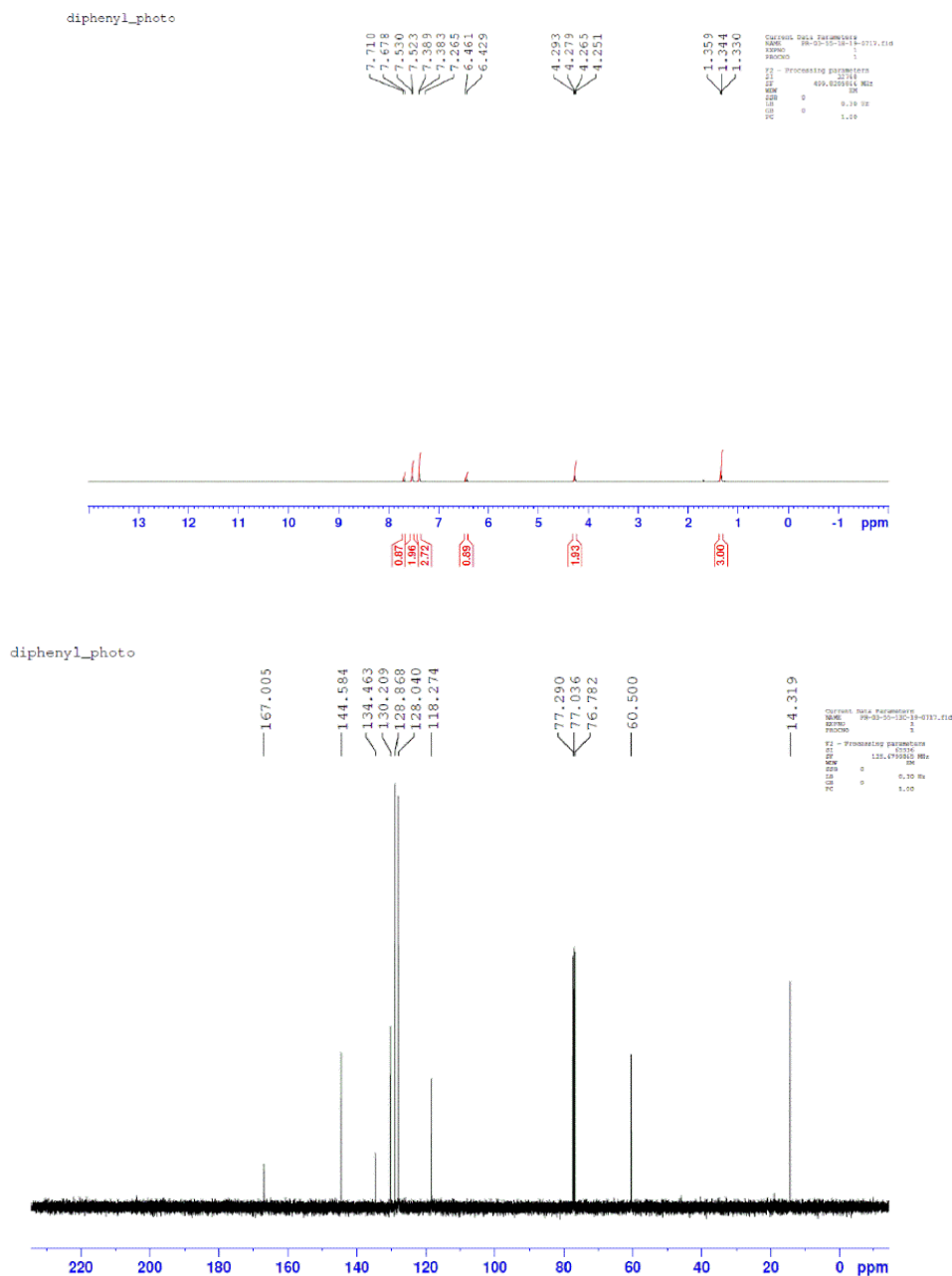


Figure 6.12 The ^1H NMR (a) and ^{13}C NMR spectra of ethyl cinnamate (b).

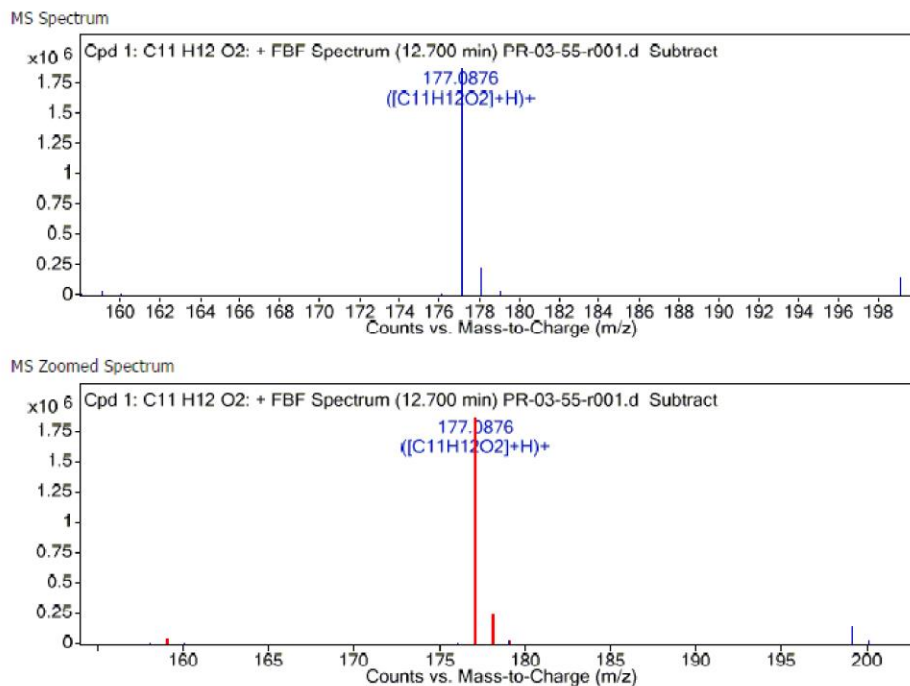


Figure 6.13 The LC-MS spectra of ethyl cinnamate

The reusability of the catalyst was tested for five consecutive cycles, see Figure 6.14, showed that there was slightly decrease in the yield. This could be formation of oxidized surface on the Pd NPs as observed from XPS of the stored Pd NPs embedded PEI membrane.

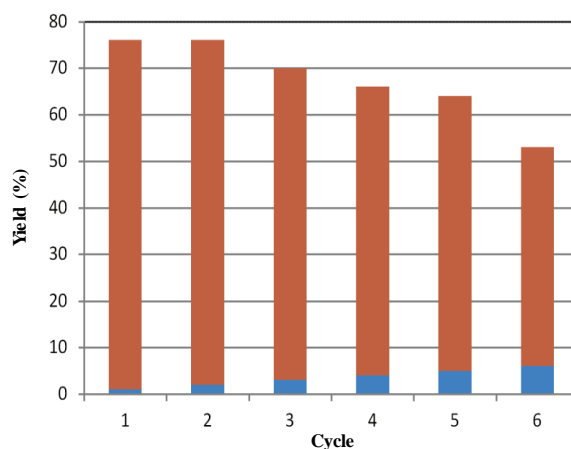


Figure 6.14 The bar diagram of catalyst (Pd NPs embedded PEI-membrane) cycle with yield (%).

6.4 Conclusions

The PEI-membrane developed in this work was found to hold higher amount of Pd NPs. The tertiary, secondary, and primary amine groups of PEI in the membrane was found to be facilitate the decomposition the formic acid on Pd surface to produce H_2 , which was used *in situ* to reduce UO_2^{2+} ions to U^{4+} ions. The success of Mizoroki-Heck coupling reaction to some extent in the absence of external base with Pd NPs embedded PEI-membrane showed the possibility of elimination need of the external base. The effect of porosity of PEI-membrane host on the catalytic activity of Pd nanoparticles studied in the UO_2^{2+} ions reduction with formic acid showed that there would be an optimum amount of porosity, amine functional groups, and Pd NPs are required for the efficient reduction of the UO_2^{2+} ions to U^{4+} ions. For comparison, the UO_2^{2+} ions reduction was also studied using the Pd NPs immobilized in the poly(EGMP) -membrane. The poly(EGMP)-membrane hosted Pd nanoparticles were found to be less efficient in reducing UO_2^{2+} ions as compared to Pd NPs hosted in the PEI-membrane. Also, the Pd nanoparticles embedded PEI-membrane gave better yield (76%) in comparison with the poly(EGMP) membrane (65%) in Mizoroki-Heck coupling reaction with the same amount of Pd NPs and under similar conditions. This could be due to the amine groups in the PEI-grafted membrane facilitating the reaction. The poly(EGMP) anchored membrane can be used as a sorbent for actinides and toxic elements like arsenic, fluoride ions etc.

CHAPTER7. SUMMARY AND FUTURE SCOPE



**Live as if you were to die
tomorrow. Learn as if you
were to live forever.**

Mahatma Gandhi

The work carried out in this thesis were aimed to explore some novel routes for the synthesis of noble metal nanoparticles in the porous polymer scaffolds and evaluate their catalytic activities in the representative inorganic and organic reductions. These porous polymer scaffolds were neutral and did not have any functional moieties to host the noble metal nanoparticles. Therefore, these polymeric materials were appropriately functionalized. These functionalized polymeric host materials developed in this work could be divided into three parts i.e. (i) self-reducing membranes/electrospun microfibers, (ii) cation-exchange membranes, and (iii) amine/phosphate-functionalized membranes. Among these functionalized membranes, the self-reducing membranes were found to reduce Ag, Au, Pd, Rh, and Ru without need of external reducing agent while, hydrazine hydrate and sodium borohydride were used as external reducing agents to form nanoparticles in the cation-exchange and amine/phosphate-functionalized membranes. The appropriate characterization techniques such as small angle X-ray scattering (SAXS), field emission electron microscopy (FE-SEM) and elemental mappings by EDAX were used to analyse the size and morphology of nanoparticles formed in these polymer platforms. The role of charge on the membrane towards the catalytic activity has been studied. The factors involved in controlling the particle size and uniform distribution across the entire polymer matrix, matrix effect on the catalytic activity and how such nanoporous polymer matrix hosted nanoparticles would act as the catalytic nanoreactor with enhanced activity were studied.

7.1 Summary of the present study and major conclusions

The study involved in the present thesis had focused on two aspects:

- (i) Chemical synthesis involved in the formation of noble metal nanoparticles in porous appropriately functionalized polymer matrices.

(ii) Catalytic applications of the metal nanoparticles hosted in the polymer matrices.

The major conclusions/findings derived from the above mentioned two parts are summarized below separately.

7.1.1 Chemical synthesis involved in synthesis of noble metal nanoparticles in polymer matrices

The supported polymer matrices used in the present thesis are poly(propylene) membranes and poly(ether sulfone) microfiber mats. Based on functionalization, these polymer matrices can be divided as self-reducing matrices, ion-exchange membranes, and amine/phosphate- functionalized membranes. The self-reducing membranes developed in this work provided an easy route to host noble metal nanocatalysts without using any external reducing agents. These membranes mimic the egg-shell membrane in terms of formation and stabilization of nanoparticles. The membranes developed in the present work had an asymmetric structure, dense at the surface and fibrous interior. The nanoparticles formed in the interior of the matrix exhibited remarkable enhancement in the catalytic activity as compared to surface immobilized nanoparticles. These functionalized membranes also provided control over nanoparticles growth/size. This could be achieved by controlling the amount of monomers anchored in the membranes or keeping the functionalized membranes in a precursor salt solution for a predetermined time.

7.1.2 Catalytic applications of the metal nanoparticles hosted on polymer matrices

The nanocatalysts synthesized on the polymer matrices were evaluated for their catalytic activities in different inorganic and organic transformations. The redox reactions were divided into two parts one is involved in organic transformations which included BH_4^- reduction of methylene blue, *p*-nitrophenol (PNP), and Mizoroki-Heck coupling reaction. The reduction of MB and PNP were

used as some model reactions using silver nanoparticles as catalysts. The second one is reduction of inorganic ions which include (i) reduction of Cr(VI) to Cr(III), and (ii) reduction of U(VI) to U(IV) using formic acid as reducing agent and palladium nanoparticles as catalyst. In these, the *in situ* generated hydrogen gas during the decomposition of formic acid on palladium surface was used as a electron source. The catalytic activities of these nanocatalysts embedded nanoporous polymer matrices were found to be significantly higher compared to earlier works reported in the literature. The higher redox catalytic activity of the nanoparticles in the membrane could be attributed to (i) high accessibility of NPs to the reactants, (ii) absence of capping that retards the catalytic activity, and (iii) nanoconfinement effects. These are also related to geometrical constraints, reduced mixing of reactants and products, sorption of reacting species on the pore-wall etc. that may accelerate the redox kinetics.

It was observed that, the reduction profile of PNP using palladium nanoparticles embedded microfibers mat showed two slopes in the kinetic of reductions. This suggested initial slower reduction process that was accelerated at later stage. The significant increase in the catalytic activity in the later stage was due to confined growth of nanoparticles leading to more defects/active centers on the Pd NPs. The palladium nanoparticles embedded on cation exchange membrane did not show any catalytic activity towards uranyl(VI) ion reduction. This was attributed to binding of UO_2^{2+} ions with the fixed negative charge sites ($-\text{SO}_3^-$) in cation-exchange matrix which would hinder UO_2^{2+} ions interactions with Pd NPs required for the reduction with formic acid.

The Pd nanoparticles embedded PEI-membrane gave better yield (76%) in comparison with the poly(EGMP) membrane (65%) in Mizoroki-Heck coupling reaction with the same amount of Pd NPs and under similar conditions. This could be due to the amine groups in the PEI-grafted

membrane facilitating the reaction. The success of Mizoroki-Heck coupling reaction to some extent in the absence of external base with Pd NPs showed the possibility of elimination need of the external base.

7.2 Future scope

Synthesis, mechanism of formation, and applications of nanoparticles as catalysts have been explored worldwide. But, there was not much literature available for the synthetic polymer membrane and electrospun polymer fibers mat hosted metal nanoparticles as the catalysts. Therefore, the exceptional catalytic activities of these metal nanoparticles in the confined nanoporous matrix remain unexplored. The present thesis aimed to explore the novel ways to synthesis metal nanoparticles on the polymer matrices which would help in the future studies to achieve best in the area of nanocatalysts. The work carried out in the present thesis is in its very early developmental stage in terms of understanding and knowledge. The future studies may include controlled synthesis of core-shell nanoparticles and study their catalytic properties under nanoconfined spaces which enables the atomic level interaction and followed by characterization with more advanced techniques. Development of flow through catalytic reactors may also be carried out in future.

REFERENCES

A

Abdur-Rashid K, Clapham SE, Hadzovic A, et al (2002) Mechanism of the hydrogenation of ketones catalyzed by trans-dihydrido (diamine) ruthenium (II) complexes. *J Am Chem Soc* 124:15104–15118.

Abild-Pedersen F, Andersson MP (2007) CO adsorption energies on metals with correction for high coordination adsorption sites—A density functional study. *Surf Sci* 601:1747–1753.

Adewuyi YG (2001) Sonochemistry: Environmental Science and Engineering Applications. *Ind Eng Chem Res* 40:4681–4715.

Aditya T, Pal A, Pal T (2015) Nitroarene reduction: a trusted model reaction to test nanoparticle catalysts. *Chem Commun* 51:9410–9431.

Adya VC, Sengupta A, Thulasidas SK, Natarajan V (2016) Direct Determination of S and P at Trace Level in Stainless Steel by CCD-based ICP-AES and EDXRF: A Comparative Study. *At Spectrosc* 37:19–24.

Agarwal C, Pandey AK, Chaudhury S, et al (2013) Ionic transport in polyelectrolyte-filled cation-exchange membranes. *J Memb Sci* 446:125–131.

Agarwal C, Pandey AK, Das S, et al (2012) Neck-size distributions of through-pores in polymer membranes. *J Memb Sci* 415:608–615.

Akiya N, Savage PE (1998) Role of water in formic acid decomposition. *AIChE J* 44:405–415.

Alonso A, Shafir A, Macanás J, et al (2012) Recyclable polymer-stabilized nanocatalysts with enhanced accessibility for reactants. *Catal today* 193:200–206.

Anton F (1934) Process and apparatus for preparing artificial threads.

Azizian S (2004) Kinetic models of sorption: a theoretical analysis. *J Colloid Interface Sci* 276:47–52.

B

Bagchi D, Stohs SJ, Downs BW, et al (2002) Cytotoxicity and oxidative mechanisms of different forms of chromium. *Toxicology* 180:5–22.

Baig RBN, Nadagouda MN, Varma RS (2014) Ruthenium on chitosan: a recyclable heterogeneous catalyst for aqueous hydration of nitriles to amides. *Green Chem* 16:2122–2127.

Barakat NAM, El-Newehy MH, Yasin AS, et al (2016) Ni&Mn nanoparticles-decorated carbon nanofibers as effective electrocatalyst for urea oxidation. *Appl Catal A Gen* 510:180–188.

Baruah B (2016) In situ and facile synthesis of silver nanoparticles on baby wipes and their applications in catalysis and SERS. *RSC Adv* 6:5016–5023.

Baruah B, Gabriel GJ, Akbashev MJ, Booher ME (2013) Facile Synthesis of Silver Nanoparticles Stabilized by Cationic Polynorbornenes and Their Catalytic Activity in 4-Nitrophenol Reduction. *Langmuir* 29:4225–4234.

Becker R, Döring W (1935) Kinetische behandlung der keimbildung in übersättigten dämpfen. *Ann Phys* 416:719–752.

Bhardwaj N, Kundu SC (2010) Electrospinning: a fascinating fiber fabrication technique. *Biotechnol Adv* 28:325–347.

Bolisetty S, Mezzenga R (2016) Amyloid–carbon hybrid membranes for universal water

purification. *Nat Nanotechnol* 11:365–371.

Boltoeva MY, Shilov VP, Anan'ev A V (2008) Catalytic reduction of U (VI) with formic acid in acid solutions on palladium catalysts. *Radiochemistry* 50:46–51.

Bonggotgetsakul YYN, Cattrall RW, Kolev SD (2015) A method for coating a polymer inclusion membrane with palladium nanoparticles. *React Funct Polym* 97:30–36.

Boudjahem A-G, Mokrane T, Redjel A, Bettahar MM (2010) Silica supported nanopalladium prepared by hydrazine reduction. *Comptes Rendus Chim* 13:1433–1439.

C

Cai Y, Xu X, Gao C, et al (2012) Structural morphology and thermal performance of composite phase change materials consisting of capric acid series fatty acid eutectics and electrospun polyamide6 nanofibers for thermal energy storage. *Mater Lett* 89:43–46.

Camargo PHC, Rodrigues TS, da Silva AGM, Wang J (2015) Controlled Synthesis: Nucleation and Growth in Solution. In: *Metallic Nanostructures*. Springer, pp 49–74.

Cao G (2004) *Nanostructures & nanomaterials: synthesis, properties & applications*. Imperial college press.

Chang H, Wu H (2013) Graphene-based nanocomposites: preparation, functionalization, and energy and environmental applications. *Energy Environ Sci* 6:3483–3507.

Cheong S, Watt JD, Tilley RD (2010) Shape control of platinum and palladium nanoparticles for catalysis. *Nanoscale* 2:2045–2053.

Cho JH, Shaughnessy KH (2011) Aqueous-phase heck coupling of 5-iodouridine and alkenes

under phosphine-free conditions. *Synlett* 2011:2963–2966.

Choi B-S (2014) Transformation of CaCO_3 to single crystalline micro/nanowires. *J Ind Eng Chem* 20:96–99.

Chun H-H, Jo W-K (2014) Polymer material-supported titania nanofibers with different polyvinylpyrrolidone to TiO_2 ratios for degradation of vaporous trichloroethylene. *J Ind Eng Chem* 20:1010–1015.

Coffey RS (1967) The decomposition of formic acid catalysed by soluble metal complexes. *Chem Commun* 923b–924.

Collman JP (1987) Principles and Applications of Organotransition Metal Chemistry.

Corma A, Garcia H (2008) Supported gold nanoparticles as catalysts for organic reactions. *Chem Soc Rev* 37:2096–2126.

Costa M, Klein CB (2006) Toxicity and carcinogenicity of chromium compounds in humans. *Crit Rev Toxicol* 36:155–163.

Cwik A, Hell Z, Figueras F (2006) Palladium/Magnesium- Lanthanum mixed oxide catalyst in the Heck reaction. *Adv Synth Catal* 348:523–530.

D

Dai Y, Formo E, Li H, et al (2016) Surface- Functionalized Electrospun Titania Nanofibers for the Scavenging and Recycling of Precious Metal Ions. *ChemSusChem* 9:2912–2916.

Dandapat A, Jana D, De G (2011) Pd nanoparticles supported mesoporous $\gamma\text{-Al}_2\text{O}_3$ film as a reusable catalyst for reduction of toxic CrVI to CrIII in aqueous solution. *Appl Catal A Gen*

396:34–39.

Das S, Pandey AK, Athawale AA, Manchanda VK (2009) Exchanges of uranium (VI) species in amidoxime-functionalized sorbents. *J Phys Chem B* 113:6328–6335.

Demir MM, Gulgun MA, Menciloglu YZ, et al (2004) Palladium Nanoparticles by Electrospinning from Poly(acrylonitrile-co-acrylic acid)–PdCl₂ Solutions. Relations between Preparation Conditions, Particle Size, and Catalytic Activity. *Macromolecules* 37:1787–1792.

Desforges A, Backov R, Deleuze H, Mondain-Monval O (2005) Generation of Palladium Nanoparticles within Macrocellular Polymeric Supports: Application to Heterogeneous Catalysis of the Suzuki–Miyaura Coupling Reaction. *Adv Funct Mater* 15:1689–1695.

Ding B, Kim H, Kim C, et al (2003) Morphology and crystalline phase study of electrospun TiO₂–SiO₂ nanofibres. *Nanotechnology* 14:532.

Dodouche I, Epron F (2007) Promoting effect of electroactive polymer supports on the catalytic performances of palladium-based catalysts for nitrite reduction in water. *Appl Catal B Environ* 76:291–299.

Domènech B, Vigués N, Mas J, et al (2014) Polymer-Metal Nanocomposites Containing Dual-Function Metal Nanoparticles: Ion-Exchange Materials Modified with Catalytically-Active and Bactericide Silver Nanoparticles. *Solvent Extr Ion Exch* 32:301–315.

Drinkel EE, Campedelli RR, Manfredi AM, et al (2014) Zwitterionic-surfactant-stabilized palladium nanoparticles as catalysts in the hydrogen transfer reductive amination of benzaldehydes. *J Org Chem* 79:2574–2579.

Du F, Wang H, Zhao W, et al (2012) Gradient nanofibrous chitosan/poly ϵ -caprolactone scaffolds as extracellular microenvironments for vascular tissue engineering. *Biomaterials* 33:762–770.

E

Edelstein AS, Cammaratra RC (1998) *Nanomaterials: synthesis, properties and applications*. CRC press.

Eising R, Elias WC, Albuquerque BL, et al (2014) Synthesis of Silver Glyconanoparticles from New Sugar-Based Amphiphiles and Their Catalytic Application. *Langmuir* 30:6011–6020.

Emin C, Remigy J-C, Lahitte J-F (2014) Influence of UV grafting conditions and gel formation on the loading and stabilization of palladium nanoparticles in photografted polyethersulfone membrane for catalytic reactions. *J Memb Sci* 455:55–63.

Esumi K, Isono R, Yoshimura T (2004) Preparation of PAMAM- and PPI- metal (silver, platinum, and palladium) nanocomposites and their catalytic activities for reduction of 4-nitrophenol. *Langmuir* 20:237–243.

Esumi K, Miyamoto K, Yoshimura T (2002) Comparison of PAMAM-Au and PPI-Au nanocomposites and their catalytic activity for reduction of 4-nitrophenol. *J Colloid Interface Sci* 254:402–405.

F

Faria VW, Oliveira DGM, Kurz MHS, et al (2014) Palladium nanoparticles supported in a polymeric membrane: an efficient phosphine-free “green” catalyst for Suzuki-Miyaura reactions in water. *RSC Adv* 4:13446–13452.

Fox AR, Bart SC, Meyer K, Cummins CC (2008) Towards uranium catalysts. *Nature* 455:341.

Freestone I, Meeks N, Sax M, Higgitt C (2007) The Lycurgus cup—a roman nanotechnology. *Gold Bull* 40:270–277.

G

Gaidhani S V, Yeshvekar RK, Shedbalkar UU, et al (2014) Bio-reduction of hexachloroplatinic acid to platinum nanoparticles employing *Acinetobacter calcoaceticus*. *Process Biochem* 49:2313–2319.

Gangula A, Podila R, Karanam L, et al (2011) Catalytic reduction of 4-nitrophenol using biogenic gold and silver nanoparticles derived from *Breynia rhamnoides*. *Langmuir* 27:15268–15274.

Gao S-T, Liu W, Feng C, et al (2016) A Ag–Pd alloy supported on an amine-functionalized UiO-66 as an efficient synergetic catalyst for the dehydrogenation of formic acid at room temperature. *Catal Sci Technol* 6:869–874.

Gardella L, Basso A, Prato M, Monticelli O (2013) PLA/POSS nanofibers: a novel system for the immobilization of metal nanoparticles. *ACS Appl Mater Interfaces* 5:7688–7692.

Gawande MB, Branco PS, Varma RS (2013) Nano-magnetite (Fe₃O₄) as a support for recyclable catalysts in the development of sustainable methodologies. *Chem Soc Rev* 42:3371–3393.

Gawande MB, Rathi AK, Nogueira ID, et al (2013) Magnetite-supported sulfonic acid: a retrievable nanocatalyst for the Ritter reaction and multicomponent reactions. *Green Chem* 15:1895–1899.

Ge J, Si Y, Fu F, et al (2013) Amphiphobic fluorinated polyurethane composite microfibrillar

membranes with robust waterproof and breathable performances. *Rsc Adv* 3:2248–2255.

Geng X, Kwon O-H, Jang J (2005) Electrospinning of chitosan dissolved in concentrated acetic acid solution. *Biomaterials* 26:5427–5432.

Ghosh SK, Mandal M, Kundu S, et al (2004) Bimetallic Pt–Ni nanoparticles can catalyze reduction of aromatic nitro compounds by sodium borohydride in aqueous solution. *Appl Catal A Gen* 268:61–66.

Goettmann F, Sanchez C (2007) How does confinement affect the catalytic activity of mesoporous materials? *J Mater Chem* 17:24–30.

Goia D V, Matijević E (1998) Preparation of monodispersed metal particles. *New J Chem* 22:1203–1215.

Gong K, Wang W, Yan J, Han Z (2015) Highly reduced molybdophosphate as a noble-metal-free catalyst for the reduction of chromium using formic acid as a reducing agent. *J Mater Chem A* 3:6019–6027.

Gralec B, Lewera A (2016) Catalytic activity of unsupported Pd-Pt nanoalloys with low Pt content towards formic acid oxidation. *Appl Catal B Environ* 192:304–310.

Greiner A, Wendorff JH (2007) Electrospinning: a fascinating method for the preparation of ultrathin fibers. *Angew Chem Int Ed Engl* 46:5670–703.

Guo L, Bai J, Wang J, et al (2015) Fabricating series of controllable-porosity carbon nanofibers-based palladium nanoparticles catalyst with enhanced performances and reusability. *J Mol Catal A Chem* 400:95–103.

H

Hammer B, Nørskov JK (1995) Why gold is the noblest of all the metals. *Nature* 376:238.

Hammer B, Nørskov JK (1995) Electronic factors determining the reactivity of metal surfaces. *Surf Sci* 343:211–220.

Hapiot F, Menuel S, Monflier E (2013) Thermoresponsive Hydrogels in Catalysis. *ACS Catal* 3:1006–1010.

Hariprasad E, Radhakrishnan TP (2012) Palladium Nanoparticle-Embedded Polymer Thin Film “Dip Catalyst” for Suzuki–Miyaura Reaction. *ACS Catal* 2:1179–1186.

Hart A, Omajali JB, Murray AJ, et al (2016) Comparison of the effects of dispersed noble metal (Pd) biomass supported catalysts with typical hydrogenation (Pd/C, Pd/Al₂O₃) and hydrotreatment catalysts (CoMo/Al₂O₃) for in-situ heavy oil upgrading with Toe-to-Heel Air Injection (THAI). *Fuel* 180:367–376.

Hayakawa K, Yoshimura T, Esumi K (2003) Preparation of gold– dendrimer nanocomposites by laser irradiation and their catalytic reduction of 4-nitrophenol. *Langmuir* 19:5517–5521.

Heck RF (1969) Mechanism of arylation and carbomethoxylation of olefins with organopalladium compounds. *J Am Chem Soc* 91:6707–6714.

Higaki Y, Kabayama H, Tao D, Takahara A (2015) Surface functionalization of electrospun poly (butylene terephthalate) fibers by surface- initiated radical polymerization. *Macromol Chem Phys* 216:1103–1108.

Hill SP, Winterbottom JM (1988) The conversion of polysaccharides to hydrogen gas. Part I: The

palladium catalysed decomposition of formic acid/sodium formate solutions. *J Chem Technol Biotechnol* 41:121–133.

Hu D, Huang Y, Liu H, et al (2014) The assembly of dendrimer-stabilized gold nanoparticles onto electrospun polymer nanofibers for catalytic applications. *J Mater Chem A* 2:2323–2332.

Hu H, Xin JH, Hu H, et al (2015) Synthesis and stabilization of metal nanocatalysts for reduction reactions - a review. *J Mater Chem A* 3:11157–11182.

Hu W, Liu B, Wang Q, et al (2013) A magnetic double-shell microsphere as a highly efficient reusable catalyst for catalytic applications. *Chem Commun* 49:7596–7598.

Huang J, Wang D, Hou H, You T (2008) Electrospun Palladium Nanoparticle-Loaded Carbon Nanofibers and Their Electrocatalytic Activities towards Hydrogen Peroxide and NADH. *Adv Funct Mater* 18:441–448.

Huang X, Yu H, Tan H, et al (2014) Carbon Nanotube- Encapsulated Noble Metal Nanoparticle Hybrid as a Cathode Material for Li- Oxygen Batteries. *Adv Funct Mater* 24:6516–6523.

Huang Y, Ma H, Wang S, et al (2012) Efficient catalytic reduction of hexavalent chromium using palladium nanoparticle-immobilized electrospun polymer nanofibers. *ACS Appl Mater Interfaces* 4:3054–3061.

Huang Z-M, Zhang Y-Z, Kotaki M, Ramakrishna S (2003) A review on polymer nanofibers by electrospinning and their applications in nanocomposites. *Compos Sci Technol* 63:2223–2253.

Hunter RJ (2001) *Foundations of colloid science*. Oxford university press

Hyde JR, Poliakoff M (2004) Supercritical hydrogenation and acid-catalysed reactions “without

gases.” *Chem Commun* 1482–1483.

I

Im JS, Park S-J, Kim TJ, et al (2008) The study of controlling pore size on electrospun carbon nanofibers for hydrogen adsorption. *J Colloid Interface Sci* 318:42–49.

J

Jiang C, Nie J, Ma G (2016) A polymer/metal core–shell nanofiber membrane by electrospinning with an electric field, and its application for catalyst support. *RSC Adv* 6:22996–23007.

Johánek V, Tsud N, Matolín V, Stará I (2001) TPD and XPS study of the CO adsorption on transition-SP metal systems: Pd and Al. *Vacuum* 63:15–22.

Judai K, Abbet S, Wörz AS, et al (2003) Interaction of Ag, Rh, and Pd atoms with MgO thin films studied by the CO probe molecule. *J Phys Chem B* 107:9377–9387.

Jung J, Park S, Hong S, et al (2014) Synthesis of gold nanoparticles with glycosides: Synthetic trends based on the structures of glycones and aglycones. *Carbohydr Res* 386:57–61.

K

Kantam ML, Srinivas P, Yadav J, et al (2009) Trifunctional N, N, O-terdentate amido/pyridyl carboxylate ligated Pd (II) complexes for Heck and Suzuki reactions. *J Org Chem* 74:4882–4885.

Kao J, Thorkelsson K, Bai P, et al (2013) Toward functional nanocomposites: taking the best of nanoparticles, polymers, and small molecules. *Chem Soc Rev* 42:2654–2678.

Karimi B, Enders D (2006) New N-heterocyclic carbene palladium complex/ionic liquid matrix

immobilized on silica: Application as recoverable catalyst for the Heck reaction. *Org Lett* 8:1237–1240.

Karski S, Witońska I, Rogowski J, Gołuchowska J (2005) Interaction between Pd and Ag on the surface of silica. *J Mol Catal A Chem* 240:155–163.

Ke P, Jiao X-N, Ge X-H, et al (2014) From macro to micro: structural biomimetic materials by electrospinning. *RSC Adv* 4:39704–39724.

Khajeh M, Dastafkan K (2014) Removal of molybdenum using silver nanoparticles from water samples: particle swarm optimization–artificial neural network. *J Ind Eng Chem* 20:3014–3018.

Kikhney AG, Svergun DI (2015) A practical guide to small angle X- ray scattering (SAXS) of flexible and intrinsically disordered proteins. *FEBS Lett* 589:2570–2577.

Kim I, Son HY, Yang MY, Nam YS (2015) Bioinspired Design of an Immobilization Interface for Highly Stable, Recyclable Nanosized Catalysts. *ACS Appl Mater Interfaces* 7:14415–14422.

Kitching W, Rappoport Z, Winstein S, Young WG (1966) Allylic Oxidation of Olefins by Palladium Acetate¹. *J Am Chem Soc* 88:2054–2055.

Komathi S, Palaniappan S, Manisankar P, et al (2010) Large Scale Preparation of Palladium Nanoparticles Loaded Polyaniline Nanostructures through Seed Induced Bulk Polymerization. *Macromol Chem Phys* 211:1330–1338.

Kotaś J, Stasicka Z (2000) Chromium occurrence in the environment and methods of its speciation. *Environ Pollut* 107:263–283.

Krittayavathananon A, Srimuk P, Luanwuthi S, Sawangphruk M (2014) Palladium nanoparticles

decorated on reduced graphene oxide rotating disk electrodes toward ultrasensitive hydrazine detection: effects of particle size and hydrodynamic diffusion. *Anal Chem* 86:12272–12278.

L

Lavrich DJ, Wetterer SM, Bernasek SL, Scoles G (1998) Physisorption and chemisorption of alkanethiols and alkyl sulfides on Au (111). *J Phys Chem B* 102:3456–3465.

Lei Y, Wu L, Zhang X, et al (2015) Palladium supported on triphenylphosphine functionalized porous organic polymer: A highly active and recyclable catalyst for alkoxy carbonylation of aryl iodides. *J Mol Catal A Chem* 398:164–169.

Li D, Xia Y (2004) Electrospinning of nanofibers: reinventing the wheel? *Adv Mater* 16:1151–1170.

Li HJ, Wang L (2006) Triethanolamine as an Efficient and Reusable Base, Ligand and Reaction Medium for Phosphane-Free Palladium-Catalyzed Heck Reactions. *European J Org Chem* 2006:5099–5102.

Li R, Zhang P, Huang Y, et al (2013) Facile Approach to Prepare Pd Nanoarray Catalysts within Porous Alumina Templates on Macroscopic Scales. *ACS Appl Mater Interfaces* 5:12695–12700.

Li Y, Shen W (2014) Morphology-dependent nanocatalysts: Rod-shaped oxides. *Chem Soc Rev* 43:1543–1574.

Liang M, Su R, Qi W, et al (2014) Reduction of Hexavalent Chromium Using Recyclable Pt/Pd Nanoparticles Immobilized on Procyanidin-Grafted Eggshell Membrane. *Ind Eng Chem Res* 53:13635–13643.

- Liao C-C, Wang C-C, Chen C-Y, Lai W-J (2011) Stretching-induced orientation of polyacrylonitrile nanofibers by an electrically rotating viscoelastic jet for improving the mechanical properties. *Polymer (Guildf)* 52:2263–2275.
- Lin H-L, Sou N-L, Huang GG (2015) Single-step preparation of recyclable silver nanoparticle immobilized porous glass filters for the catalytic reduction of nitroarenes. *RSC Adv* 5:19248–19254.
- Liu F, Yu J, Tu G, et al (2017) Carbon nitride coupled Ti-SBA15 catalyst for visible-light-driven photocatalytic reduction of Cr (VI) and the synergistic oxidation of phenol. *Appl Catal B Environ* 201:1–11.
- Liu J, Ma S, Wei Q, et al (2013) Parallel array of nanochannels grafted with polymer-brushes-stabilized Au nanoparticles for flow-through catalysis. *Nanoscale* 5:11894–11901.
- Liu K, Wang Y, Chen P, et al (2016) Noncrystalline nickel phosphide decorated poly (vinyl alcohol-co-ethylene) nanofibrous membrane for catalytic hydrogenation of p-nitrophenol. *Appl Catal B Environ* 196:223–231.
- Liu W, Wang D, Duan Y, et al (2015) Palladium supported on poly (ionic liquid) entrapped magnetic nanoparticles as a highly efficient and reusable catalyst for the solvent-free Heck reaction. *Tetrahedron Lett* 56:1784–1789.
- Liu Y, Park M, Shin HK, et al (2014) Facile preparation and characterization of poly (vinyl alcohol)/chitosan/graphene oxide biocomposite nanofibers. *J Ind Eng Chem* 20:4415–4420.
- Liu Y, Zhang Y, Ding H, et al (2013b) Self-assembly of noble metallic spherical aggregates from monodisperse nanoparticles: their synthesis and pronounced SERS and catalytic properties.

Lu C, Zhang P, Jiang S, et al (2017) Photocatalytic reduction elimination of UO_2^{2+} pollutant under visible light with metal-free sulfur doped g-C₃N₄ photocatalyst. *Appl Catal B Environ* 200:378–385.

Lu X, Wang C, Wei Y (2009) One- Dimensional Composite Nanomaterials: Synthesis by Electrospinning and Their Applications. *Small* 5:2349–2370.

Lu Y, Spyrta P, Mei Y, et al (2007) Composite hydrogels: robust carriers for catalytic nanoparticles. *Macromol Chem Phys* 208:254–261.

M

Mahmoud MA, Narayanan R, El-Sayed MA (2013) Enhancing Colloidal Metallic Nanocatalysis: Sharp Edges and Corners for Solid Nanoparticles and Cage Effect for Hollow Ones. *Acc Chem Res* 46:1795–1805.

Maier J (1987) Defect chemistry and ionic conductivity in thin films. *Solid State Ionics* 23:59–67.

Mallampati R, Valiyaveetil S (2014) Eggshell Membrane-Supported Recyclable Catalytic Noble Metal Nanoparticles for Organic Reactions. *ACS Sustain Chem Eng* 2:855–859.

Mazumder V, Sun S (2009) Oleylamine-mediated synthesis of Pd nanoparticles for catalytic formic acid oxidation. *J Am Chem Soc* 131:4588–4589.

McCleskey TM, Foreman TM, Hallman EE, et al (2001) Approaching zero discharge in uranium reprocessing: photochemical reduction of uranyl. *Environ Sci Technol* 35:547–551.

Memarian F, Latifi M, Amani-Tehran M (2014) Innovative method for electrospinning of continuous TiO₂ nanofiber yarns: Importance of auxiliary polymer and solvent selection. *J Ind*

Eng Chem 20:1886–1891.

Meng L-Y, Rhee KY, Park S-J (2014) Enhancement of superhydrophobicity and conductivity of carbon nanofibers-coated glass fabrics. *J Ind Eng Chem* 20:1672–1676.

Mer VK La (1952) Nucleation in phase transitions. *Ind Eng Chem* 44:1270–1277.

Mirzaei A, Janghorban K, Hashemi B, et al (2017) Characterization and optical studies of PVP-capped silver nanoparticles. *J Nanostructure Chem* 7:37–46.

Mishra T, Mahato M, Aman N, et al (2011) A mesoporous WN co-doped titania nanomaterial with enhanced photocatalytic aqueous nitrate removal activity under visible light. *Catal Sci Technol* 1:609–615.

Mizoroki T, Mori K, Ozaki A (1971) Arylation of olefin with aryl iodide catalyzed by palladium. *Bull Chem Soc Jpn* 44:581.

Moakhar RS, Goh GKL, Dolati A, Ghorbani M (2017) Sunlight-driven photoelectrochemical sensor for direct determination of hexavalent chromium based on Au decorated rutile TiO₂ nanorods. *Appl Catal B Environ* 201:411–418.

Mohamed RM, Baeissa ES (2014) Environmental remediation of aqueous nitrate solutions by photocatalytic reduction using Pd/NaTaO₃ nanoparticles. *J Ind Eng Chem* 20:1367–1372.

Mori K, Dojo M, Yamashita H (2013) Pd and Pd–Ag nanoparticles within a macroreticular basic resin: an efficient catalyst for hydrogen production from formic acid decomposition. *ACS Catal* 3:1114–1119.

N

Nabid MR, Bide Y, Rezaei SJT (2011) Pd nanoparticles immobilized on PAMAM-grafted MWCNTs hybrid materials as new recyclable catalyst for Mizoraki–Heck cross-coupling reactions. *Appl Catal A Gen* 406:124–132.

Nadagouda MN, Varma RS (2008) Green synthesis of silver and palladium nanoparticles at room temperature using coffee and tea extract. *Green Chem* 10:859–862.

Nakano T, Ikawa NI, Ozimek L (2003) Chemical composition of chicken eggshell and shell membranes. *Poult Sci* 82:510–514.

Napper DH (1983) *Polymeric stabilization of colloidal dispersions*. Academic Pr

Narayanan R (2010) Recent advances in noble metal nanocatalysts for Suzuki and Heck cross-coupling reactions. *Molecules* 15:2124–2138.

Nasrollahzadeh M, Sajadi SM, Hatamifard A (2016) Waste chicken eggshell as a natural valuable resource and environmentally benign support for biosynthesis of catalytically active Cu/eggshell, Fe₃O₄/eggshell and Cu/Fe₃O₄/eggshell nanocomposites. *Appl Catal B Environ* 191:209–227.

Nazir M, Naqvi II (2013) Synthesis, spectral and electrochemical studies of complex of uranium (IV) with pyridine-3-carboxylic acid. *Am J Anal Chem* 4:134.

Neyertz C, Marchesini FA, Boix A, et al (2010) Catalytic reduction of nitrate in water: promoted palladium catalysts supported in resin. *Appl Catal a Gen* 372:40–47.

Nguyen T-D, Dinh C-T, Do T-O (2015) Tailoring the assembly, interfaces, and porosity of nanostructures toward enhanced catalytic activity. *Chem Commun* 51:624–635.

Nikitenko SI, Venault L, Pflieger R, et al (2010) Potential applications of sonochemistry in spent nuclear fuel reprocessing: a short review. *Ultrason Sonochem* 17:1033–1040.

Niu J, Yin L, Dai Y, et al (2016) Design of visible light responsive photocatalysts for selective reduction of chlorinated organic compounds in water. *Appl Catal A Gen* 521:90–95.

Niu Z, Li Y (2014) Removal and Utilization of Capping Agents in Nanocatalysis. *Chem Mater* 26:72–83.

Nogami M, Hirose Y, Arai T, et al (2008) Reduction of U (VI) and some fission products in HNO₃ media by galvanostatic electrolysis. *J Alloys Compd* 451:358–360.

Noh HK, Lee SW, Kim J-M, et al (2006) Electrospinning of chitin nanofibers: degradation behavior and cellular response to normal human keratinocytes and fibroblasts. *Biomaterials* 27:3934–3944.

O

Omole MA, K'Owino IO, Sadik OA (2007) Palladium nanoparticles for catalytic reduction of Cr (VI) using formic acid. *Appl Catal B Environ* 76:158–167.

Omole MA, Okello VA, Lee V, et al (2011) Catalytic Reduction of Hexavalent Chromium Using Flexible Nanostructured Poly(amic acids). *ACS Catal* 1:139–146.

Overbeek JTG, Verwey EJW (1948) Theory of the Stability of Lyophobic Colloids: The interaction of Sol Particles Having an Electric Double Layer.

P

Pan X, Xu Y-J (2014) Efficient Thermal- and Photocatalyst of Pd Nanoparticles on TiO₂ Achieved by an Oxygen Vacancies Promoted Synthesis Strategy. *ACS Appl Mater Interfaces* 6:1879–1886.

Pandey AK, Childs RF, West M, et al (2001) Formation of pore-filled ion-exchange membranes with in situ crosslinking: Poly(vinylbenzyl ammonium salt)-filled membranes. *J Polym Sci Part A Polym Chem* 39:807–820.

Panthi G, Yousef A, Barakat NAM, et al (2013) Mn₂O₃/TiO₂ nanofibers with broad-spectrum antibiotics effect and photocatalytic activity for preliminary stage of water desalination. *Ceram Int* 39:2239–2246.

Park JY, Lee IH, Bea GN (2008) Optimization of the electrospinning conditions for preparation of nanofibers from polyvinylacetate (PVAc) in ethanol solvent. *J Ind Eng Chem* 14:707–713.

Patra S, Naik AN, Pandey AK, et al (2016) Silver nanoparticles stabilized in porous polymer support: A highly active catalytic nanoreactor. *Appl Catal A Gen* 524:214–222.

Patra S, Pandey AK, Sarkar SK, Goswami A (2014) Wonderful nanoconfinement effect on redox reaction equilibrium. *RSC Adv* 4:33366–33369.

Patra S, Pandey AK, Sen D, et al (2014) Redox Decomposition of Silver Citrate Complex in Nanoscale Confinement: An Unusual Mechanism of Formation and Growth of Silver Nanoparticles. *Langmuir* 30:2460–2469.

Patra S, Sen D, Pandey AK, et al (2013) Local Conditions Influencing In Situ Formation of Different Shaped Silver Nanostructures and Subsequent Reorganizations in Ionomer Membrane.

J Phys Chem C 117:12026–12037.

Paul S, Pandey AK, Shah R V, Aggarwal SK (2015) Chemically selective polymer substrate based direct isotope dilution alpha spectrometry of Pu. *Anal Chim Acta* 878:54–62.

Pestov A, Nazirov A, Modin E, et al (2015) Mechanism of Au (III) reduction by chitosan: Comprehensive study with ¹³C and ¹H NMR analysis of chitosan degradation products. *Carbohydr Polym* 117:70–77.

Polte J (2015) Fundamental growth principles of colloidal metal nanoparticles—a new perspective. *CrystEngComm* 17:6809–6830.

Pomogailo AD, Kestelman VN (2006) *Metallopolymer nanocomposites*. Springer Science & Business Media

Pozun ZD, Rodenbusch SE, Keller E, et al (2013) A systematic investigation of p-nitrophenol reduction by bimetallic dendrimer encapsulated nanoparticles. *J Phys Chem C* 117:7598–7604.

Pradhan N, Pal A, Pal T (2002) Silver nanoparticle catalyzed reduction of aromatic nitro compounds. *Colloids Surfaces A Physicochem Eng Asp* 196:247–257.

Puddephatt R, Yap GA (1998) An efficient binuclear catalyst for decomposition of formic acid. *Chem Commun* 2365–2366.

R

Ramakrishna W-ET and RI and S (2011) Technological advances in electrospinning of nanofibers. *Sci Technol Adv Mater* 12:13002.

Rashid MH, Mandal TK (2007) Synthesis and catalytic application of nanostructured silver

dendrites. *J Phys Chem C* 111:16750–16760.

Reiss H (1951) The growth of uniform colloidal dispersions. *J Chem Phys* 19:482–487.

Ren H-T, Jia S-Y, Zou J-J, et al (2015) A facile preparation of Ag₂O/P25 photocatalyst for selective reduction of nitrate. *Appl Catal B Environ* 176:53–61.

Ren L, Yang F, Wang C, et al (2014) Plasma synthesis of oxidized graphene foam supporting Pd nanoparticles as a new catalyst for one-pot synthesis of dibenzyls. *RSC Adv* 4:63048–63054.

Ruban A, Hammer B, Stoltze P, et al (1997) Surface electronic structure and reactivity of transition and noble metals I. *J Mol Catal A Chem* 115:421–429.

Ruiz P, Muñoz M, Macanás J, Muraviev DN (2011) Intermatrix synthesis of polymer-stabilized PGM@ Cu core-shell nanoparticles with enhanced electrocatalytic properties. *React Funct Polym* 71:916–924.

Ruthven DM, Upadhye RS (1971) The catalytic decomposition of aqueous formic acid over suspended palladium catalysts. *J Catal* 21:39–47.

S

Safari J, Zarnegar Z, Masoule SF, Najafabadi AE (2014) Aqueous dispersions of iron oxide nanoparticles with linear-dendritic copolymers. *J Ind Eng Chem* 20:2389–2393.

Salomone VN, Meichtry JM, Zampieri G, Litter MI (2015) New insights in the heterogeneous photocatalytic removal of U (VI) in aqueous solution in the presence of 2-propanol. *Chem Eng J* 261:27–35.

Santos SAO, Pinto RJB, Rocha SM, et al (2014) Unveiling the Chemistry behind the Green

Synthesis of Metal Nanoparticles. *ChemSusChem* 7:2704–2711.

Shahgaldi S, Yaakob Z, Khadem DJ, Daud WRW (2012) Characterization and the hydrogen storage capacity of titania-coated electrospun boron nitride nanofibers. *Int J Hydrogen Energy* 37:11237–11243.

Shand M, Anderson JA (2013) Aqueous phase photocatalytic nitrate destruction using titania based materials: routes to enhanced performance and prospects for visible light activation. *Catal Sci Technol* 3:879–899.

Shao L, Ji W, Dong P, et al (2012a) Coupling reactions of aromatic halides with palladium catalyst immobilized on poly (vinyl alcohol) nanofiber mats. *Appl Catal A Gen* 413:267–272.

Shao L, Ren Y, Wang Z, et al (2015) Developing chitosan-based composite nanofibers for supporting metal catalysts. *Polymer (Guildf)* 75:168–177.

Shao L, Xing G, He L, et al (2012b) Sulfonic groups functionalized preoxidated polyacrylonitrile nanofibers and its catalytic applications. *Appl Catal A Gen* 443:133–137.

Shao S, Zhou S, Li L, et al (2011) Osteoblast function on electrically conductive electrospun PLA/MWCNTs nanofibers. *Biomaterials* 32:2821–2833.

Sharma VK, Zboril R, Varma RS (2015) Ferrates: Greener Oxidants with Multimodal Action in Water Treatment Technologies. *Acc Chem Res* 48:182–191.

Sheng G, Hu J, Alsaedi A, et al (2015) Interaction of uranium (VI) with titanate nanotubes by macroscopic and spectroscopic investigation. *J Mol Liq* 212:563–568.

Sheng G, Shao X, Li Y, et al (2014) Enhanced Removal of Uranium(VI) by Nanoscale Zerovalent

Iron Supported on Na–Bentonite and an Investigation of Mechanism. *J Phys Chem A* 118:2952–2958.

Sheng G, Yang P, Tang Y, et al (2016) New insights into the primary roles of diatomite in the enhanced sequestration of UO_2^{2+} by zerovalent iron nanoparticles: an advanced approach utilizing XPS and EXAFS. *Appl Catal B Environ* 193:189–197.

Shinde RN, Chavan V, Acharya R, et al (2014) Selective removal of arsenic (V) from natural water using N-methyl-d-glucamine functionalized poly (propylene) membranes. *J Environ Chem Eng* 2:2221–2228.

Shine HJ, Mallory HE (1962) The Reduction of Aromatic Nitro Compounds by Potassium Borohydride. *J Org Chem* 27:2390–2391.

Shrivastava KC, Chappa S, Sengupta A, et al (2016) Palladium Nanoparticles Hosted on Hydrazine-Grafted Magnetite and Silica Particles to Catalyze the Reduction of Oxymetal Ions with Formic Acid. *ChemCatChem*.

Siegel RW (1993) Synthesis and properties of nanophase materials. *Mater Sci Eng A* 168:189–197.

Simo A, Polte J, Pfänder N, et al (2012) Formation mechanism of silver nanoparticles stabilized in glassy matrices. *J Am Chem Soc* 134:18824–18833.

Soares O, Pereira MFR, Órfão JJM, et al (2014) Photocatalytic nitrate reduction over Pd–Cu/TiO₂. *Chem Eng J* 251:123–130.

Sobhani S, Pakdin-Parizi Z (2014) Palladium-DABCO complex supported on γ -Fe₂O₃ magnetic

nanoparticles: A new catalyst for CC bond formation via Mizoroki- Heck cross-coupling reaction. *Appl Catal A Gen* 479:112–120.

Soukup K, Topka P, Hejtmánek V, et al (2014) Noble metal catalysts supported on nanofibrous polymeric membranes for environmental applications. *Catal Today* 236:3–11.

Stepanov AL, Golubev AN, Nikitin SI, Osin YN (2014) A review on the fabrication and properties of platinum nanoparticles. *Rev Adv Mater Sci* 38:160–175.

Su DS, Perathoner S, Centi G (2013) Nanocarbons for the Development of Advanced Catalysts. *Chem Rev* 113:5782–5816.

Sugimoto T (1987) Preparation of monodispersed colloidal particles. *Adv Colloid Interface Sci* 28:65–108.

Sun B, Long YZ, Zhang HD, et al (2014) Advances in three-dimensional nanofibrous macrostructures via electrospinning. *Prog Polym Sci* 39:862–890.

Suren S, Pancharoen U, Kheawhom S (2014) Simultaneous extraction and stripping of lead ions via a hollow fiber supported liquid membrane: Experiment and modeling. *J Ind Eng Chem* 20:2584–2593.

Susanto H, Ulbricht M (2007) Photografted Thin Polymer Hydrogel Layers on PES Ultrafiltration Membranes: Characterization, Stability, and Influence on Separation Performance. *Langmuir* 23:7818–7830.

Szablan Z, Junkers T, Koo SPS, et al (2007) Mapping Photolysis Product Radical Reactivities via Soft Ionization Mass Spectrometry in Acrylate, Methacrylate, and Itaconate Systems.

Macromolecules 40:6820–6833.

T

Tang S, Vongehr S, Meng X (2010) Controllable incorporation of Ag and Ag–Au nanoparticles in carbon spheres for tunable optical and catalytic properties. *J Mater Chem* 20:5436–5445.

Tang Z, Qiu C, McCutcheon JR, et al (2009) Design and fabrication of electrospun polyethersulfone nanofibrous scaffold for high- flux nanofiltration membranes. *J Polym Sci Part B Polym Phys* 47:2288–2300.

Tedsree K, Li T, Jones S, et al (2011) Hydrogen production from formic acid decomposition at room temperature using a Ag–Pd core–shell nanocatalyst. *Nat Nanotechnol* 6:302.

Tehfe M-A, Dumur F, Graff B, et al (2013) Design of new Type I and Type II photoinitiators possessing highly coupled pyrene-ketone moieties. *Polym Chem* 4:2313–2324.

Tejamaya M, Römer I, Merrifield RC, Lead JR (2012) Stability of citrate, PVP, and PEG coated silver nanoparticles in ecotoxicology media. *Environ Sci Technol* 46:7011–7017.

Toraishi T, Kimura T, Arisaka M (2007) A remote valency control technique: catalytic reduction of uranium(vi) to uranium(iv) by external ultrasound irradiation. *Chem Commun* 240–241.

Troppmann S, König B (2014) Functionalized Membranes for Photocatalytic Hydrogen Production. *Chem – A Eur J* 20:14570–14574.

Trzeciak AM, Mieczyska E, Ziólkowski JJ, et al (2008) Palladium (0) nanoparticles encapsulated in diamine-modified glycidyl methacrylate polymer (GMA-CHDA) applied as catalyst of Suzuki–Miyaura cross-coupling reaction. *New J Chem* 32:1124–1130.

Tsuji J (1995) *Palladium Reagents in Organic Synthesis*.

Tsuji J (2012) *Organic synthesis with palladium compounds*. Springer Science & Business Media

Tu W, Li K, Shu X, William WY (2013) Reduction of hexavalent chromium with colloidal and supported palladium nanocatalysts. *J nanoparticle Res* 15:1–9.

Tüzüner Ş, Demir MM (2015) Dispersion of organophilic Ag nanoparticles in PS-PMMA blends. *Mater Chem Phys* 162:692–699.

Tyumentsev MS, Zubavichus Y V, Shiryaev AA, Anan'ev A V (2014) Catalytic reduction of U(VI) in H₂SO₄ solutions with hydrazine and formic acid in the presence of bimetallic platinum-ruthenium catalysts. *Radiochemistry* 56:150–155.

V

V. Goia D, Matijevic E (1998) Preparation of monodispersed metal particles. *New J Chem* 22:1203–1215.

W

Wang H, Feng Y, Fang Z, et al (2012) Co-electrospun blends of PU and PEG as potential biocompatible scaffolds for small-diameter vascular tissue engineering. *Mater Sci Eng C* 32:2306–2315.

Wang X, Yang J, Ma S, et al (2016) In situ fabrication of AgI/AgVO₃ nanoribbon composites with enhanced visible photocatalytic activity for redox reactions. *Catal Sci Technol* 6:243–253.

Wang Y, Choi S, Zhao X, et al (2014) Polyol synthesis of ultrathin Pd nanowires via attachment-

based growth and their enhanced activity towards formic acid oxidation. *Adv Funct Mater* 24:131–139.

Wehbe N, Jaafar M, Guillard C, et al (2009) Comparative study of photocatalytic and non-photocatalytic reduction of nitrates in water. *Appl Catal A Gen* 368:1–8.

Wu H, Lin D, Zhang R, Pan W (2007) Facile synthesis and assembly of Ag/NiO nanofibers with high electrical conductivity. *Chem Mater* 19:1895–1897.

X

Xu H, Zeiger BW, Suslick KS (2013) Sonochemical synthesis of nanomaterials. *Chem Soc Rev* 42:2555–2567.

Xu Y (2005) Synthesis and characterization of silica coated CdSe/CdS core/shell quantum dots.

Xu Z, Lu G, Cai C (2017) Palladium nanoparticles stabilized by aqueous vesicles self-assembled from a PEGylated surfactant ionic liquid for the chemoselective reduction of nitroarenes. *Catal Commun* 99:57–60.

Y

Yadav M, Xu Q (2013) Catalytic chromium reduction using formic acid and metal nanoparticles immobilized in a metal–organic framework. *Chem Commun* 49:3327–3329.

Yan N, Yuan Y, Dyson PJ (2013) Nanometallic chemistry: deciphering nanoparticle catalysis from the perspective of organometallic chemistry and homogeneous catalysis. *Dalt Trans* 42:13294–13304.

Yang C, Meldon JH, Lee B, Yi H (2014a) Investigation on the catalytic reduction kinetics of hexavalent chromium by viral-templated palladium nanocatalysts. *Catal Today* 233:108–116.

Yang D, Li Y, Nie J (2007) Preparation of gelatin/PVA nanofibers and their potential application in controlled release of drugs. *Carbohydr Polym* 69:538–543.

Yang Q, Adrus N, Tomicki F, Ulbricht M (2011) Composites of functional polymeric hydrogels and porous membranes. *J Mater Chem* 21:2783–2811.

Yang W, Zhai Y, Yue X, et al (2014) From filter paper to porous carbon composite membrane oxygen reduction catalyst. *Chem Commun* 50:11151–11153.

Yoon J-W, Choi J-K, Lee J-H (2012) Design of a highly sensitive and selective C₂H₅OH sensor using p-type Co₃O₄ nanofibers. *Sensors Actuators B Chem* 161:570–577.

Yu L, Huang Y, Wei Z, et al (2015) Heck reactions catalyzed by ultrasmall and uniform Pd nanoparticles supported on polyaniline. *J Org Chem* 80:8677–8683.

Z

Zeng M, Yuan X, Yang Z, Qi C (2014) Novel macroporous palladium cation crosslinked chitosan membranes for heterogeneous catalysis application. *Int J Biol Macromol* 68:189–197.

Zhang C-L, Yu S-H (2014) Nanoparticles meet electrospinning: recent advances and future prospects. *Chem Soc Rev* 43:4423–4448.

Zhang S, Nguyen L, Zhu Y, et al (2013) In-Situ Studies of Nanocatalysis. *Acc Chem Res* 46:1731–1739.

Zhang Z, Shao C, Li X, et al (2010) Electrospun nanofibers of p-type NiO/n-type ZnO

- heterojunctions with enhanced photocatalytic activity. *ACS Appl Mater Interfaces* 2:2915–2923.
- Zhang Z, Yu Y, Wang P (2012) Hierarchical top-porous/bottom-tubular TiO₂ nanostructures decorated with Pd nanoparticles for efficient photoelectrocatalytic decomposition of synergistic pollutants. *ACS Appl Mater Interfaces* 4:990–996.
- Zhao D, Wang X, Yang S, et al (2012) Impact of water quality parameters on the sorption of U(VI) onto hematite. *J Environ Radioact* 103:20–29.
- Zheng B, Liu G, Yao A, et al (2014) A sensitive AgNPs/CuO nanofibers non-enzymatic glucose sensor based on electrospinning technology. *Sensors Actuators B Chem* 195:431–438.
- Zheng B, Qian L, Yuan H, et al (2010) Preparation of gold nanoparticles on eggshell membrane and their biosensing application. *Talanta* 82:177–183.
- Zhou X, Huang Y, Xing W, et al (2008) High-quality hydrogen from the catalyzed decomposition of formic acid by Pd–Au/C and Pd–Ag/C. *Chem Commun* 3540–3542.
- Zhu M, Wang C, Meng D, Diao G (2013) In situ synthesis of silver nanostructures on magnetic Fe₃O₄@C core-shell nanocomposites and their application in catalytic reduction reactions. *J Mater Chem A* 1:2118–2125.
- Zohoori S, Karimi L, Ayaziyazdi S (2014) A novel durable photoactive nylon fabric using electrospun nanofibers containing nanophotocatalysts. *J Ind Eng Chem* 20:2934–2938.